



University
of Glasgow

Shields, David (2020) *Bioengineered osteoinductive systems for surgical applications*. PhD thesis.

<https://theses.gla.ac.uk/79053/>

Copyright and moral rights for this work are retained by the author

A copy can be downloaded for personal non-commercial research or study,
without prior permission or charge

This work cannot be reproduced or quoted extensively from without first
obtaining permission in writing from the author

The content must not be changed in any way or sold commercially in any
format or medium without the formal permission of the author

When referring to this work, full bibliographic details including the author,
title, awarding institution and date of the thesis must be given

Enlighten: Theses

<https://theses.gla.ac.uk/>
research-enlighten@glasgow.ac.uk

Bioengineered Osteoinductive Systems For Surgical Applications

David Shields

MBChB MRCS(Ed) MSc(trauma surgery)



University
of Glasgow

Submitted in the fulfilment of the requirements of the Degree Doctor of Philosophy

College of Science and Engineering

School of Engineering

University of Glasgow

Glasgow, G12 8LT

November 2019

Thesis Abstract

Despite significant improvements in surgical implant manufacturing there remains a clinically unmet need for implantable bone regenerating scaffolds. Current clinical solutions such as the use of pelvic autologous bone graft give rise to additional symptoms and are unpredictable. An engineered customisable osteoinductive coating has been developed within this research group, however the translatable aspects have not yet been explored. As an orthopaedic surgeon with a clinical interest in complex trauma and limb reconstruction, an invested interest in the practical aspects in the application of this technology is maintained.

In this work, an engineered osteoinductive coating consisting of poly (ethyl acrylate) with fibronectin and bone morphogenetic protein 2 (BMP-2) is evaluated as a potential coating for surgical implantation. Firstly, it was found that the use of ethylene oxide to sterilise the system (on a variety of base materials) could be employed without significant detriment to the fibronectin network, however BMP-2 was not resilient enough to the process to warrant addition prior to sterilisation. The use of decellularised bone chips commercially available as a transport medium for the osteoinductive coating was explored using an *in vivo* critical defect model which demonstrated evidence of mature bone formation with BMP-2. *In vivo* experiments were carried out in the University of Glasgow Veterinary Research Facility and performed under personal (n°I44130F69) and project license (n°70/8638) issued by the Home Office under the Animals (Scientific Procedures) ACT 1986. A fully synthetic transport medium by way of a polymer (poly caprolactone) scaffold was investigated with mechanical compression testing and *in vitro* cell biocompatibility. Scaffold materials were found to accommodate cell adhesion and differentiation. Despite changes in scaffold pore size, density and addition of hydroxy apatite as a composite filler, mechanical properties did not reach those of current commercial products, specifically poly (methyl methacrylate) bone cement.

The findings of this work demonstrate potential translatable aspects of this osteoinductive scaffold. However further rigorous *in vivo* assessment of retained osteoinductive function following sterilisation is required, followed by analysis of safety and efficacy. Further work on the improvement on mechanical properties of a bioresorbable polymer scaffold are warranted.

Table of Contents

Chapter 1: Introduction

1.1 Material science and biological interaction

1.1.1 System materials

1.1.1.1 Poly (ethyl acrylate)

1.1.1.2 Poly (methyl acrylate)

1.1.1.3 Polycaprolactone

1.1.1.4 Fibronectin

1.1.1.5 Hydrogels

1.1.1.6 Hydroxyapatite

1.1.2 Biological factors

1.1.2.1 Bone extracellular matrix

1.1.2.2 Mesenchymal stem cells

1.1.2.2.1 Stem cells

1.1.2.2.2 Markers of osteogenic stem cell activity

1.1.2.3 Integrins and focal adhesions

1.1.2.4 Growth factors

1.1.2.4.1 Bone morphogenetic proteins

1.1.2.4.2 Vascular endothelial growth factor

1.1.3 Analysis techniques

1.1.3.1 Biomaterial characterisation

1.1.3.1.1 Topography

1.1.3.1.2 Chemistry

1.1.3.2 Mechanical properties

1.1.3.2.1 Stiffness

1.1.3.2.2 Strength

1.2 Legislation

1.2.1 EU Legislation

1.2.2 British standards

1.2.3 Regulations

1.3 Clinical applications

1.3.1 Non-union

1.3.2 Fusion

1.3.3 Critical bone loss

1.3.4 Osseointegration

1.4 Thesis aims and objectives

1.4.1 Aims

1.4.2 Objectives

Chapter 2: Ethylene Oxide Sterilisation

2.1 Introduction

2.2 Materials and methods

2.2.1 Materials

2.2.2 Methods and sample preparation

2.2.2.1 Spun samples

2.2.2.2 Fabrication of scaffolds

2.2.2.3 Plasma coated samples

2.2.2.4 Spray samples

2.2.2.5 Bone chips

2.2.2.6 Protein and growth factor

2.2.2.6.1 Fibronectin

2.2.2.6.2 Bone morphogenetic protein 2

2.2.2.7 Ethylene oxide sterilisation

2.2.2.8 Sterilisation control samples preparation

2.2.2.9 Atomic force microscopy

2.2.2.10 Enzyme linked immunosorbent assay

2.2.2.10.1 Fibronectin domains

2.2.2.10.2 Direct BMP-2

2.2.2.10.3 Normalisation

2.2.2.11 EO residual testing

2.2.2.12 X-ray photoelectron spectroscopy

2.2.2.13 Water contact angle

2.2.2.14 Cell differentiation analysis

2.2.3 Statistical analysis

2.3 Results

2.3.1 Atomic Force Microscopy

2.3.2 Enzyme Linked Immunosorbent Assay

2.3.2.1 Fibronectin

2.3.2.2 Direct BMP-2

2.3.3 Cell behaviour on EO sterilised surfaces

2.3.3.1 Fluorescence microscopy

2.3.3.2 Quantification of myotube formation

2.3.4 Addressing changes in PMA behaviour

2.3.4.1 Residual EO testing

2.3.4.2 Water contact angle

2.3.4.3 X-ray photoelectron spectroscopy

2.4 Discussion

2.5 Conclusions

Chapter 3: *In vivo* analysis of engineered osteoinductive surface coatings applied to decellularised bone chips

3.1 Introduction

3.2 Materials and Methods

3.2.1 Materials

3.2.2 Methods and sample preparation

3.2.2.1 Implant tube preparation

3.2.2.2 Plasma coating

3.2.2.3 Protein adsorption

3.2.2.4 BMP-2 adsorption

3.2.3 Surgery

3.2.4 Post-operative procedure

3.2.4.1 Quantitative analysis

3.2.4.2 Histological analysis

3.2.5 Statistical analysis

3.3 Results

3.3.1 Recovery

3.3.2 X-ray imaging

3.3.3 Calculated bone formation

3.3.4 Histology

3.4 Discussion

3.5 Conclusions

Chapter 4: Analysis of PCL and PCL/HA Composite Scaffolds

4.1 Introduction

4.2 Materials and methods

4.2.1 Materials

4.2.2 Methods and sample preparation

4.2.2.1 Mixing process

4.2.2.2 Validation of mixing technique

4.2.2.2.1 Resin polishing

4.2.2.2.2 Freeze Fracture

4.2.2.2.3 Scanning electron microscopy

4.2.2.3 Electron dispersive x-ray spectroscopy

4.2.2.4 Greyscale analysis

4.2.2.5 Scaffold design

4.2.2.6 Theoretical porosity analysis

4.2.2.7 Scaffold printing

4.2.2.7.1 PCL printing

4.2.2.7.2 Measurement of pore size

4.2.2.8 Control material preparation

4.2.2.8.1 Solid composites

4.2.2.8.2 Optipac® bone cement

4.2.2.8.3 Simplex® bone cement

4.2.2.8.4 Hydroset® Calcium Phosphate Bone Substitute

4.2.2.8.5 Osteoink

4.2.2.9 Functionalisation

4.2.2.10 Surface mineralisation assay

4.2.2.11 Cell culture

4.2.2.12 alamarBlue

4.2.2.13 Actin staining

4.2.2.14 Quantitative Polymerase Chain Reaction

4.2.2.14.1 RNA isolation

4.2.2.14.2 Reverse transcription

4.2.2.15 Alkaline phosphatase activity

- 4.2.2.16 Ethylene oxide
- 4.2.2.17 Mechanical analysis
 - 4.2.2.17.1 Stiffness
 - 4.2.2.17.2 Strength
- 4.2.3 Statistical analysis
- 4.3 Results
 - 4.3.1 Validation of mixing
 - 4.3.1.1 Scanning electron microscopy
 - 4.3.1.2 Greyscale analysis
 - 4.3.1.3 Electron dispersive x-ray
 - 4.3.2 Analysis of printing
 - 4.3.2.1 Theoretical versus physical pore dimensions
 - 4.3.2.2 Density and porosity
 - 4.3.3 Mechanical analysis
 - 4.3.3.1 Pure polycaprolactone
 - 4.3.3.2 Polycaprolactone & hydroxyapatite composite
 - 4.3.3.3 Plasma surface coating
 - 4.3.4 *In vitro* osteogenesis
 - 4.3.4.1 Cell metabolism
 - 4.3.4.2 Quantitative polymerase chain reaction
 - 4.3.4.3 Cell migration
- 4.4 Discussion
- 4.5 Conclusions

Chapter 5: Future Work & Thesis Conclusions

5.1 Future Work

5.2 Thesis Conclusions

Chapter 6: Appendix

6.1 List of reagents Chapter 2

6.2 List of reagents Chapter 2

6.3 List of reagents Chapter 2

6.4 Proposed method for subcutaneous mineralisation experiment

References

List of Figures

Figure 1 - Chemical formula of poly(ethyl acrylate)	22
Figure 2 - Chemical formula of poly(methyl acrylate)	23
Figure 3 - Chemical formula of polycaprolactone	24
Figure 4 - Diagrammatic representation of fibronectin.....	28
Figure 5 - MSC differentiation potential	33
Figure 6 - Stress strain curves.....	44
Figure 7 - X-rays of non-union	49
Figure 8 - X-rays of arthodesis.....	54
Figure 9 - X-rays of a large critical bone defect.....	55
Figure 10 - Failure of osseointegration	58
Figure 11 - Schematic of EO Sterilisation Process	61
Figure 12 - Scaffold Geometry.....	64
Figure 13- Illustration of custom plasma chamber.....	65
Figure 14 - Height phase and error AFM images of FN adsorbed on spun PEA before and after EO sterilisation	78
Figure 15 - Height phase and error AFM images of FN adsorbed on plasma PEA before and after EO sterilisation.	79
Figure 16 - Height phase and error AFM images of FN adsorbed on spun PCL + spun PEA before and after EO sterilisation.....	80
Figure 17 - Height phase and error AFM images of FN adsorbed on spun PCL + plasma PEA before and after EO sterilisation.	81
Figure 18 - Height phase and error AFM images of FN adsorbed on PMA before and after EO sterilisation.	82
Figure 19 - Height phase and error AFM images of FN adsorbed on a PCL scaffold + plasma PEA before and after EO sterilisation.	83
Figure 20 - Height phase and error AFM images of FN adsorbed on a PCL scaffold + spray PEA before and after EO sterilisation	84
Figure 21 - Height phase and error AFM images of FN adsorbed on a bone chip + plasma PEA before and after EO sterilisation.	85
Figure 22 - Schematic of ELISA target sites on fibronectin demonstrating domain type, growth factor binding (P5F3) and cell binding (HFN 7.1) sites.	86
Figure 23 - Mean absorbances.	87
Figure 24 - BCA standardisation of fibronectin density	88
Figure 25 - EO sterilised BMP presenting systems, versus non sterilised systems.....	89
Figure 26 - PMA sterilised before and after addition of fibronectin	91
Figure 27 - Spun PEA sterilised before and after addition of fibronectin, then BMP-2 compared to non-sterile sPEA control.....	91
Figure 28 - Plasma PEA sterilised before and after addition of fibronectin, then BMP-2 compared to non-sterile pPEA control.....	91
Figure 29 - Spun PCL and plasma PEA sterilised before and after addition of fibronectin, then BMP-2 compared to non-sterile glass control	91
Figure 30 - C2C12 differentiation of EO a) before and b) after adsorption of fibronectin.	92
Figure 31 - Graphs demonstrating changes in static WCA and hysteresis with and without EO sterilisation.....	94

Figure 32 - Static Water Contact Angles	95
Figure 33 - XPS Analysis.....	96
Figure 34 - Schematic of Mouse Radius Critical Defect Model	103
Figure 35 - Description of histology	109
Figure 36 - Summary X-ray and CT representation of critical defects.....	111
Figure 37 - Postoperative mouse weights.....	112
Figure 38 - X-ray and 3D reconstructed images of μ CT data	113
Figure 39 - Quantification of bone volume as an absolute figure and as a proportion of the entire defect	114
Figure 40 - Histological bone chip appearance	115
Figure 41 - Histological demonstration of bone formation with each additive component of the osteoinductive system	116
Figure 42 - Histological comparison with negative control	117
Figure 43 -Synostosis. A BMP-2 sample demonstrated heterotopic ossification	118
Figure 44 - Schematic of 3D printing scaffolds then mechanically tested and in vitro analysed	124
Figure 45 - Twin screw extruders with mixing cams used to heat, mix and extrude PCL and HA	127
Figure 47 - 'Pellet' of extruded PCL/HA composite fractured for SEM analysis	128
Figure 48 - Example toolpath for a single layer and multilayer 0-90° in BioCAD	130
Figure 49 - Toolpaths - overlaid extrusion demonstrating (i) line spacing (ii) extrusion width and (iii) theoretical gap c) 0/90 toolpath. Increasing line space and decreasing extrusion width increased theoretical gap, thus increasing pore size and porosity.....	130
Figure 50 - Examples of final scaffold prints	134
Figure 51 - Measurements made of pore size for 0-90 and 0-60.....	134
Figure 52 - CAD mould	135
Figure 53 - Optipac® bone cement mixing device and plastic moulds.....	136
Figure 54 - Schematic from manufacturer's literature. Mixing, vacuum release and preparation for injection is demonstrated.	136
Figure 55 - Schematic of compression testing	144
Figure 56 - Stress strain example.....	145
Figure 57 - 0.2% proof stress example.....	148
Figure 59 - Magnification series of nanoHA at 20 & 30%	149
Figure 60 - Magnification series of sintered HA at 20 & 30%	150
Figure 61 - EMS of Polished nanoHA and sintered HA.	151
Figure 62 - Greyscale analysis of visible from SEM images.....	152
Figure 63 - EDS Analysis following reduction of the gold palladium	153
Figure 64 - Magnified photo of scaffolds	154
Figure 65 - Measurements of pore size parameters	154
Figure 66 - 0-90 layer orientation with 0.8 gap.....	157
Figure 67 - Post mechanical analysis samples plastically deformed	159
Figure 68 - PCL graph demonstrating baseline characteristics of solid components.....	160
Figure 69 - Typical appearance of calcium phosphate scaffolds following mechanical analysis and corresponding stress strain curves.....	161

Figure 70 - Reduction of pore size	162
Figure 71 - Changing layer geometry	163
Figure 72 - Comparison of processing conditions on PCL.....	164
Figure 73 - Effect of EO processing on PCL stiffness and strength.....	165
Figure 74 - Comparison of 20% and 30% nano and sintered HA across geometries, solid material and PCL	166
Figure 75 - Effect of varying printing temperatures 3°C higher or 6°C lower	167
Figure 76 - OsteoImage flouresent imaging and absorbance of HA/PCL composite scaffolds with and without pPEA.....	168
Figure 77 - AlamarBlue absorption	169
Figure 78 - 7 day (RUNX2, ALP, OSX) and 28 day (osteopontin, osteonectin, osteocalcin) markers for osteoblast differentiation and mineralisation.....	170
Figure 79 - Actin staining of functionalised 0/90° and 0/60° scaffolds	171
Figure 80 - Modulus versus porosity.....	176
Figure 81 - Survivorship of Boneloc cement compared to modern (high viscosity) cement	179

List of Tables

Table 1 - Properties of PEA.....	22
Table 2 - Properties of PMA	24
Table 3 - Properties of PCL	25
Table 4 - Causes of non-union.	50
Table 5 - Categorisation of non-union by radiographic appearance.....	51
Table 6 – Plasma chamber pressures.....	66
Table 7 - Bone chip weights for each group.....	67
Table 8 -Samples tested to establish effect of EO process on BMP-2.....	70
Table 9 - Detectable remnants of EO using gas chromatography.....	93
Table 10 - Static WCA and hysteresis calculations	94
Table 11 - Mean area attributable to bonds	96
Table 12 – Summary of conditions investigated	98
Table 13 - Paraffinisation protocol	108
Table 14 - Design parameters for scaffolds.....	131
Table 15 - Scaffold printing parameters for each condition	132
Table 16 - Sample groupings for in vitro RNA expression.....	139
Table 17 - Change in pore dimensions due to printing process.....	156
Table 18 - Changes in pore size and volume	157
Table 19 - Density and Porosity of 0/90° scaffolds.....	158
Table 20 – Relationship between porosity.....	177
Table 21 - Chapter 2 reagents and sources.....	187
Table 22 - Chapter 3 reagents and sources.....	188
Table 23 - Chapter 4 reagents and sources.....	189
Table 24 - List of proposed reagents and sources	190
Table 25 – Proposed nanocoating application and 3D printing design.....	191
Table 26 – Proposed printer settings for scaffolds	191
Table 27 - Implantation schedule	194

Presentations

- Glasgow Meeting of Orthopaedic Research (GlaMOR), 2019 Beardmore Hotel, Glasgow
- International Orthopaedic and Trauma Symposium, Royal College of Physicians and Surgeons, Glasgow
- Scot meeting (national orthopaedic meeting), 2019, Crieff Hydro, Perthshire

Publications

- Nanoscale Coatings for Ultralow Dose BMP-2-Driven Regeneration of Critical-Sized Bone Defects. Z.A. Cheng, A. Alba-Perez, C. Gonzalez-Garcia, H. Donnelly, V. Llopis-Hernandez, V. Jayawarna, P. Childs, D.W. Shields, M. Cantini, L. Ruiz-Cantu, A. Reid, J.F.C. Windmill, E.S. Addison, S.Corr, W.G. Marshall, M.J. Dalby, M Salmeron-Sanchez. Advanced Science. 2018, DOI: 10.1002/adv.201800361

Manuscripts in draft

- Evolution of a customisable, supermacroporous scaffold for critical bone defects D.W Shields, V. Jayawarna, V.Llopis-Hernandez, M.Salmerón-Sánchez
- Sterilisation of polymer and protein based osteoinductive scaffolds D.W Shields, V.Llopis-Hernandez, M. Salmerón-Sánchez

Awards

- 1st prize oral presentation – SCOT meeting, September 2019 Dunblane Hydro Hotel, Perthshire
- 1st prize oral presentation – Glasgow Meeting of Orthopaedic Research (GlaMOR), March 2019 Beardmore Hotel, Glasgow
- 2nd prize poster presentation – International Orthopaedic and Trauma Symposium, May 2019, Royal College of Physicians and Surgeons, Glasgow

Acknowledgements

I would like to acknowledge the support of my primary supervisor Manuel Salmerón-Sánchez for his guidance through this particular research phase of my career. He has made every effort to create a bespoke approach for this PhD accommodating flexibility of working and facilitating regular meetings around my work and family life. I would like to further recognise the support of my second supervisor, Matt Dalby who's upbeat and pragmatic approach to life and research has maintained my perspective on life out with the lab.

My sincere gratitude to the MiMe (and now CeMi) biomedical engineering research group for their inclusion both academically and socially for a 'non-scientist' such as myself into their closely-knit group. In particular, I would to individually thank Cristina Gonzalez-Garcia, Vineetha Jayawarna and Virginia Llopis-Hernández who have been incredibly generous with their time and patience to teach and support me through experiments far beyond my comfort zone. In particular Virginia as a third supervisor has gone above and beyond the ordinary call of duty for a supervisor and her support both personally and professionally has been instrumental to me getting to the stage of a completed thesis.

To my clinical colleagues and friends who have accommodated my needs both in granting me time away from the workplace and being receptive to my venting over the last 3-4 years. You are too numerous to name individually, but I am indebted to your tolerance and hope I have the opportunity to repay the favour.

Specific recognition to NHS Lanarkshire throughout this research secondment during which the provision of research time has developed my abilities as a clinician, educator and time manager. I have gained new friends and long-term colleagues as a result and am indebted to you all.

Finally, and most importantly, my immediate family, parents and in-laws who have supported me practically and emotionally. It is fair to say that this thesis

has coincidentally coincided with some of the most difficult years in my life to date. Trying to balance family time alongside work, research and exercise has been unsustainable at times and I am grateful for them for bending over backwards to allow me to get this far. My wife Kathleen has borne the brunt of what remains of me at the end of each working day and has somehow sustained her life, career and shouldered the majority of our family responsibilities on her own, for which I am eternally grateful. To my sons Finn and Oscar, I look forward to being able to spend more time with you guys from now as watching you grow and learn to date has been nothing but a pleasure.

I would like to dedicate this thesis to our daughter Freya who despite not being here has taught me so much.

Author's Declaration

I hereby declare that the research presented within this thesis is my own work unless otherwise stated and has not been submitted elsewhere for any other academic degree.

1. Introduction

As an orthopaedic surgeon, with a focal interest in the management of complex trauma and its sequelae (e.g. critical bone loss) has led me to commence post-graduate research within the division of biomedical engineering. This project focuses around steps toward translation of this research group's specialist area of efficient binding and presentation of growth factors onto 3D scaffolds with a view to several potential clinical applications. Specific key areas of exploration are the effect of chemical (ethylene oxide) sterilisation, the utility of bone chips as a carrier medium and the potential utility of 3D printed polymers as a carrier medium. The system in particular discussed in this thesis investigates various base materials, coated in poly(ethyl acrylate), presenting fibronectin and growth factors, as a functionalised implant to deal with bone loss. This Chapter forms the basis of current literature on the concepts of material science, interaction with cell biology and the potential clinical applications focussing on osteogenic regeneration.

1.1. Material science and biological interaction

1.1.1 System materials

1.1.1.1 Poly(ethyl acrylate)

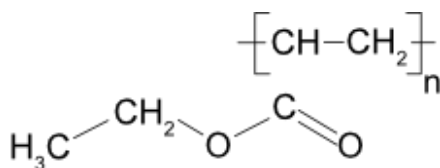


Figure 1 - Chemical formula of poly(ethyl acrylate)

Poly (ethyl acrylate) (PEA) is a hydrophobic polymer (Figure 1) which has favourable elastomeric characteristics at physiological temperature and has good biological compatibility with a number of cells including chondrocytes, osteoblasts, endothelial and neural cells (1). Its properties are outlined in Table1.

Property	Value
Chemical formula	$(\text{C}_5\text{H}_8\text{O}_2)_n$
Glass transition temperature ($^{\circ}\text{C}$)	-21
Amorphous density at 25°C (g/cm^3)	1.12
Molecular weight of repeat unit ($\text{g}/\text{mol}.$)	100.12
Molar Volume V_m (mol^{-1})	89.4 mL
Solubility Parameter δ ($\text{MPa}^{1/2}$)	18.5 - 19.2
Molar Cohesive Energy E_{coh} (mol^{-1})	30600 - 33000 J
Molar Heat Capacity C_p (mol K^{-1})	179 - 182 J
Entanglement Molecular Weight M_e (g mol^{-1})	7800 - 8600
Index of Refraction n	1.46 - 1.47
Van-der-Waals Volume V_{vw} (mL mol^{-1})	56.20

Table 1 - Properties of PEA (2,3)

PEA is formed by polymerisation of its base units as ethyl acrylate (EA) with either benzoin (4) or acrylic acid. This is done at room temperature often under ultraviolet light which forms copolymer sheets, which can be boiled in ethanol to remove low molecular mass substances before being dried in a vacuum. Work within this research group has also been done using a plasma chamber to polymerise PEA (pPEA) (5). This benefits from a thin layer of PEA (25-50nm) that can be applied to any material, which aids bioresorption and has since shown non-inferiority to traditionally spun PEA (6). Both spun and plasma PEA possess the ability to allow fibronectin (a plasma protein) to form physiological networks onto which growth factors (such as BMP-2 and VEGF) can bind.

1.1.1.2 Poly(methyl acrylate)

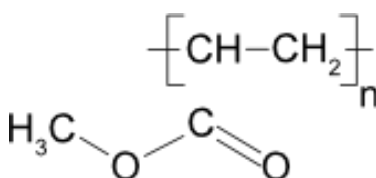


Figure 2 - Chemical formula of poly(methyl acrylate)

Poly (methyl acrylate) (PMA) is a hydrophobic polymer (Figure 2) which is chemically similar to but much softer than a polymer commonly used in clinical practice, poly(methyl methacrylate) (PMMA) (7,8). It is polymerised from methyl acrylate dissolved in chloroform or toluene however PMA preferentially dissolves in chloroform and can be separated from ethylmethacrylate which is a frequent co-polymer. PMA is a biologically compatible polymer, however recent work has demonstrated its inferiority to PEA when combined with fibronectin as a functionalising protein maintaining a globular conformation and slower cell migration (7,8). Its properties are outlined in Table 2.

Property	Value
Chemical formula	$(C_4H_6O_2)_n$
Glass transition temperature (°C)	10
Amorphous density at 25°C (g/cm ³)	1.22
Molecular weight of repeat unit (g/mol.)	86.09
Solubility Parameter δ	19.2 – 21.6 MPa ^{1/2}
Molar Volume V_m (mol ⁻¹)	106.15
Molar Heat Capacity C_p (mol K) ⁻¹	114.0
Entanglement Molecular Weight M_e (g mol ⁻¹)	10035
Van-der-Waals Volume V_{vw} (mL mol ⁻¹)	47.9

Table 2 - Properties of PMA (3,9)

1.1.1.3 Polycaprolactone

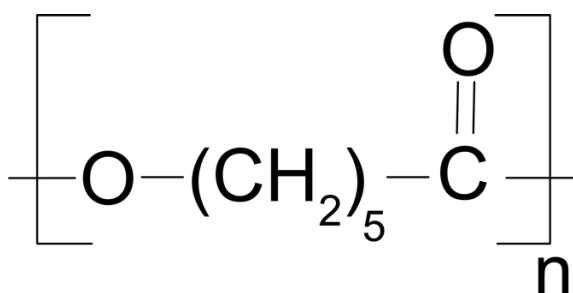


Figure3 - Chemical formula of polycaprolactone

Polycaprolactone (PCL) is a polyester composed of hexanoate repeat units (Figure3) and is synthesised either by polycondensation of hydroxycarboxylic acid or by ring opening polymerisation of ϵ -caprolactone to poly(ϵ -caprolactone) (9). At room temperature it is highly soluble in a number of solvents (chloroform, benzene, carbon tetrachloride), slightly soluble in others (acetone, ethyl acrylate) and insoluble in alcohols, petroleum, ether and water (10). Whilst PCL is miscible with other polymers, such as polyvinylchloride and polystyrene-acrylonitrile, it is mechanically compatible with others such as natural rubber, polypropylene and polyethylene.

Property	Range
Number average molecular weight ($M_n/g\ mol^{-1}$)	530–630 000
Density ($r/g\ cm^{-3}$)	1.071–1.200
Glass transition temperature ($^{\circ}C$)	60
Melting temperature ($^{\circ}C$)	56-65
Decomposition temperature ($/^{\circ}C$)	350
Inherent viscosity ($Z/cm^3\ g^{-1}$)	100-130
Intrinsic viscosity ($Z/cm^3\ g^{-1}$)	0.9
Tensile strength (s/MPa)	4-785
Young modulus (E/GPa)	0.21-0.44
Elongation at break (e/%)	20-1000

Table 3 - Properties of PCL (3,11)

Of particular interest in the biomaterial field, is the biodegradability of PCL, the rate of which depends on molecular weight, crystallinity and conditions of degradation (12). As a result the process takes several months to years, which would be compatible with a bone regeneration scaffold, as opposed to polylactides and polyglycolides which degrade within 2-4 months (13). Its properties are outlined in Table 3.

Of note, there is a difference between biodegradation of a compound, which is simply degradation in a biological environment, and bioresorption which refers to the active breakdown and complete elimination of the foreign material (14). PCL is readily degraded by living single cell organisms such as bacteria (firmicutes and proteobacteria) and fungi (penicillium and aspergillus) (15). Degradation in humans is more difficult due to a lack of enzymatic activity but still occurs by repeated hydrolysis of the polymer backbone with diffusion

of the monomers and oligomers into the surrounding tissue (14). As this begins at the surface and works down the material, this gives a predictable erosion characteristic which is essential for the ultimate translation of the system.

Throughout the literature, there is no research into the copolymerisation of poly(ethyl acrylate) (PEA) with PCL, however work has been done with polycaprolactone-b-polymethylmethacrylate which is a single molecule different to what ultimately the system used here (16,17). Despite this, the likely interaction between the base material PCL and PEA will likely be additive rather than true copolymerisation between the layers. This work focusses on true addition of PEA onto of pre-polymerised PCL.

1.1.1.4 Fibronectin

Fibronectin (FN) is an extracellular glycoprotein with a high molecular weight (approx. 440kDa) which has roles in cell adhesion, growth, migration and differentiation (18-21) by binding integrins, cell receptors. Fibronectin is crucial to development of mesoderm, neural structures and vasculature demonstrated by FN knockout mice failing to develop in utero (22). There are in excess of 20 forms of FN with 2 main forms in vertebrates, soluble fibronectin (produced by hepatocytes and found in blood plasma) and insoluble cellular fibronectin (secreted by fibroblasts initially as a soluble dimer and assembled into an insoluble matrix) (23).

FN is encoded by a single gene producing various protein dimeric structures consisting of 2 similar polypeptide chains linked with disulphide bonds at their C terminus (24,25) (Figure 4). These monomers are composed of 3 types of repeating units (type I, II and III) which themselves are built from predictable chains of amino acids; type I (approx. 40 amino acids), type II (approx. 60 amino acids), type III (approx. 90 amino acids) (26). These types are repeated as outlined in Figure 4, however 90% of the FN sequence comprises 12 type I repeats, 2 type II repeats and 15-17 type III repeats. Further extra domains and variable regions give rise to differences between the known FN variations, with these extra domains delineating between soluble plasma (pFN) and insoluble

cellular (cFN) isoforms. For the purposes of research in this piece of work, the utility of pFN as a surface protein on these biomaterial systems are exploited.

Each of the dimers possess regions called “domains” which interact with other extracellular proteins such as heparin, fibrin and other fibronectin molecules (given place to the process known as ‘matrix assembly’). Domains identified for cell adhesion via integrins have also been identified, most notably the 9th and 10th type III repeat (noted as III₉ & III₁₀), III₉ (the “synergy site”) binds to integrin $\alpha_5\beta_1$ and III₁₀ to $\alpha_v\beta_3$. The variable portion (of which is present in most cFNs, but only in 1 subunit of pFN) contains the binding site for $\alpha_4\beta_1$ (also known as Vascular Cell Adhesion Molecule) (27). Additional identified binding sites include binding sites for heparin on the C and N terminals, (28), collagen on I₆₋₉ & II_{1,2} (29) and fibrin on I₄₋₅ (30). Several self-binding sites have been identified, in particular I₁₋₅, III_{2,12,13} have been well described as self-interaction sites (where I₁₋₅ is described as the “self-assembly site”), with additional ‘cryptic’ sites becoming available with conformational cell mediated changes (e.g. I₁₂ & III_{1,7,10,14,15}). These binding sites are essential for matrix assembly of fibronectin, which is a complex cell mediated process called fibrillogenesis in which rolled up “globular” FN unravels due to flexibility in the type III repeats (which are flexible due to absence of disulphide bonds) and strong bonds between matrix assembly units (31,32).

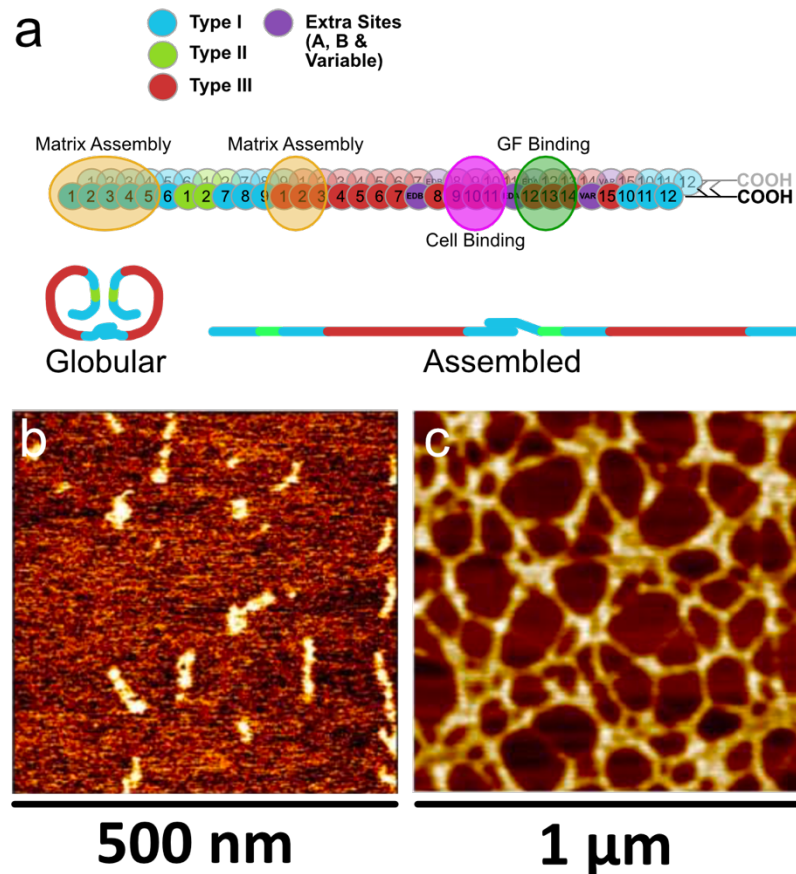


Figure 4 – a) Diagrammatic representation of fibronectin outlining repeat types, assembly & binding sites and conformations. Adapted from *A material-based platform to modulate fibronectin activity and focal adhesion assembly* F. A. Vanterpool, M. Cantini, F. P. Seib and M. Salmerón-Sánchez, *BioResearch. Open Access*, 2014, 3. Atomic force microscopy pictures of FN in a b) globular and c) assembled formation from *Material-driven fibronectin assembly for high-efficiency presentation of growth factors* V. Llopis-Hernandez et al, *Science Advances* 2016.

The use of fibronectin as a binding protein for growth factors (GFs) has been known for over a decade in which fraction groups can be used as either GF or integrin binding sites. For example platelet derived growth factor (PDGF) or hepatocyte growth factor (HGF) can bind to III₁₀ and vascular endothelial growth factor (VEGF), fibroblast growth factor (FGF), along with PDGF and HGF bind to III₁₃₋₁₄ (33). In particular interest to this work is the ability of bone morphogenetic protein 2 (BMP-2) to bind to FNIII₉₋₁₀, which is enhanced when the nearby FNIII₁₂₋₁₃ is exposed (34).

Whilst pFN is generally found in the plasma at bountiful concentrations of approximately 300 µl/ml, it is in a tightly bound globular inactive form and thus suboptimal for presentation. It is possible to use recombinant FN (rFN) to overcome this globular form and expose binding sites, this is expensive and complex (35,36). Recent work from the Salmeron-Sanchez bioengineering research group has shown that pFN can be assembled as a network spontaneously on polymer coatings and reveal the FNIII₉₋₁₀ and FNIII₁₂₋₁₄ binding domains (37,38) so called “material driven fibrillogenesis”. This work showed that the addition of FN to poly(ethyl acrylate) (PEA) exposed the binding sites compared to a control poly (methyl acrylate) (PMA), presented BMP-2 *in vitro* but also resulted in osteoblastic function and bone regeneration *in vivo*. Subsequent work has shown that thin layers of PEA can be assembled by plasma polymerisation without the need for solvents with no reduction in efficacy of fibrillogenesis or cell function (6).

This conversion of ravelled into unravelled FN, which then forms a mesh network exposes the binding domain to the ECM and thus can be utilised in tissue engineering.

1.1.1.5 Hydrogels

Hydrogels are polymeric materials with strong hydrophilic properties capable of holding large amounts of water in their 3D networks. They respond to a number of physical and chemical stimuli and changing their water content and becoming ‘swollen’ or ‘unswollen’ as a result. There are many ways of engineering hydrogels, for example simple one step processes such as polymerisation or cross-linking or more complex multistep methods. Depending on the method and base units used, different properties can be exploited, such as; mechanical strength, biodegradation, chemical response. The physical stimuli which causes swelling or deswelling include temperature, electric fields, magnetic fields, light, pressure and sound. In addition, chemical factors such as pH, solvents and molecular species can prompt accumulation or depletion of the hydrogel.

Hydrogels can be classified in a number of manners; polymeric composition, configuration, type of cross-linking, physical appearance, electrical charge, natural/ synthetic (39). Defining by polymer composition results in homopolymeric hydrogels with one subunit repeated, whereas copolymeric and multipolymeric hydrogels have multiple different monomers or multiple independent polymers respectively. Classification by configuration defines crystalline from semi-crystalline and non-crystalline. Chemically and physically crosslinked hydrogels exhibit permanent and transient junctions, where the latter results from chain entanglement or physical interactions (e.g. hydrogen bonds or hydrophobic). The physical appearance of a hydrogel is dependent upon the preparation technique but can form as a matrix, microsphere or film. Electrical charge of a hydrogels can be ionic, non-ionic, zwitterionic (both anionic and cationic) or amphoteric electrolyte (both acid and base groups). Finally, whilst synthetic hydrogels can be formed a large number of polymers, natural hydrogels tend to be formed from collagen, gelatine and polysaccharides (e.g. alginate).

As modern synthetic hydrogels have developed their capacity to absorb water has surpassed those of naturally found hydrogels such as polysaccharides and collagen gels. Synthetic hydrogels are chemically stronger than natural hydrogels, they have more formidable mechanical properties providing durability and potential for slower degradation rates. For example, presently in clinical practice, natural hydrogels are used in fluid resuscitation for patients who require a fluid transfusion for low blood pressure. However, they are rapidly metabolised within the intravascular compartment (blood vessels) and the water is dissipated beyond this compartment within 30 minutes and thus its efficacy is limited by its rapid degradation properties.

Hydrogels can be synthesised from their base units by:

- Chemical reaction to link the base units together
- Creation of free radicals from the main-chain using radiation, which then creating cross-links to recombine
- Physical interactions as crystals, entanglements or electrostatically.

The three general groups of materials required to create the gel matrix are a monomer (natural/synthetic/both), an initiator and a cross-linker. The process of polymerisation is exothermic and thus frequently additional diluents such as water are added, then washed off along with any impurities (residual monomer/initiator/cross-linker or by products of the reaction). There are many types of hydrogels, but they are mostly cross-linked polymers of: acrylate and acrylic acid or grafted starch-acrylic acid polymers.

1.1.1.6 Hydroxyapatite

Hydroxyapatite (HA) is a natural mineral of calcium and phosphate, with the formula $\text{Ca}_5(\text{PO}_4)_3(\text{OH})$ which crystallises into a hexagonal form becoming $\text{Ca}_{10}(\text{PO}_4)_6(\text{OH})_2$. It is a ceramic and therefore is stiff with an elastic modulus of 80-120 GPa but brittle at 0.6-1 $\text{MPa}\cdot\text{m}^{-1/2}$ in comparison to cortical bone which is less stiff at 7-30 GPa but has greater fracture toughness at 2-12 $\text{MPa}\cdot\text{m}^{-1/2}$ (40). HA is key to the mechanical properties of bone (41), but also acts as a reservoir of calcium for mineral homeostasis and acid-base homeostasis. In orthopaedic practice, we frequently use implants which are coated in HA to encourage osseointegration which is in part explained by the osteoinductive properties of HA (42).

1.1.2 Biological factors

1.1.2.1 Bone extracellular matrix

The extracellular matrix (ECM) refers to the 3D environment out with cells and includes the basement membrane and the interstitial space. It is comprised of a large number of macromolecules such as collagen, elastin and glycoproteins which provide mechanical support for cells and act as a medium through which communication can occur (24). The basement membrane is a thin fibrous structure delineating the boundaries of the ECM and comprises the basal laminae and reticular connective tissue. The interstitial space is filled with fibrous proteins and polysaccharides which cushion cells from mechanical

forces which are placed upon them and transmitted throughout the ECM (43). FN, as previously mentioned, is an extracellular matrix protein which binds to collagen and facilitates allowing cells to migrate through the extracellular matrix.

Bone has a remarkably high proportion of ECM with less than 5% of bone being comprised of cells. The ECM is crucial for mechanical support of the skeleton, providing protection and establishes insertions for muscles in order for bodies to move and function. Furthermore, the ECM acts as a reservoir for mineral storage and houses haemopoietic stem cells for maintenance of blood constituents. The proportions of ECM vary in humans throughout age, weight, gender, activity and disease. In normal bone, the ECM is approximately 30% organic (proteoglycans, glycosaminoglycans, glycoproteins, osteonectin, osteocalcin and collagen) (44). Collagen in bone is required to be stiff and improve tensile strength thus 90% of the collagen is type I. Proteoglycans help maintain the 25% water content. The remaining 70% of non-organic ECM is hydroxyapatite which further improved stiffness and strength, however, is liable to fracture due to its reduced toughness compared to collagen. Commercially, demineralised bone matrix (DMB) is available as an implant to augment autologous bone grafts theoretically delivering ECM including growth factors, however the contents are variable and only low quality clinical data exists (45).

1.1.2.2 Mesenchymal stem cells

1.1.2.2.1 Stem cells

Stem cells have the capacity to differentiate into a variety of cells types or indeed divide and remain as a stem cell. They are central to the development of new organisms but also exist in a quiescent state in order to provide new cell lineages for tissue repair and maintenance. There are many types of stem cells, embryonic stem cells (ESC) originally harvested from mice in the 1980s (46,47), adult stem cells (ASC). ESCs can be found in the several days old embryo (called a blastocyst) before they begin differentiation into their more specific germ layers for organ formation (48). Additionally amniotic and

placental cord cells are a rich resource of stem cells (49,50). These cells have a remarkable capacity for self-renewal and differentiation into a wide variety of cell lineages in response to suitable environments. ASCs were initially isolated from foetal gonadal tissue (51) but now can be isolated from a multitude of tissues, such as adipose, bone marrow and brain. Whilst similar to ESCs, the ability to self-renew and differentiate is more limited and are better suited to tissue specific use (52) which had be genetically programmed to act like ESCs (“induced pluripotent stem cells”, or “iPSCs”). Mesenchymal stem cells (MSCs) are a population of ASCs which were isolated from bone marrow originally by Friedentein (53) and demonstrated to proliferate in ectopic tissues, such as the kidneys. MSCs can differentiate into any cell of a mesodermal lineage (osteoblasts, chondrocytes, adipocytes - Figure 5) but also endodermal (myocytes and epithelial cells) and ectodermal (neurons) germ types (54). In order to meet the International Society for Cellular Therapy definition must express the markers CD73, CD90 and CS105. Additionally they must not express HLA-DR, CD9a, CD11b, CD14, CD19, CD34, CD45 and CD79a (55).

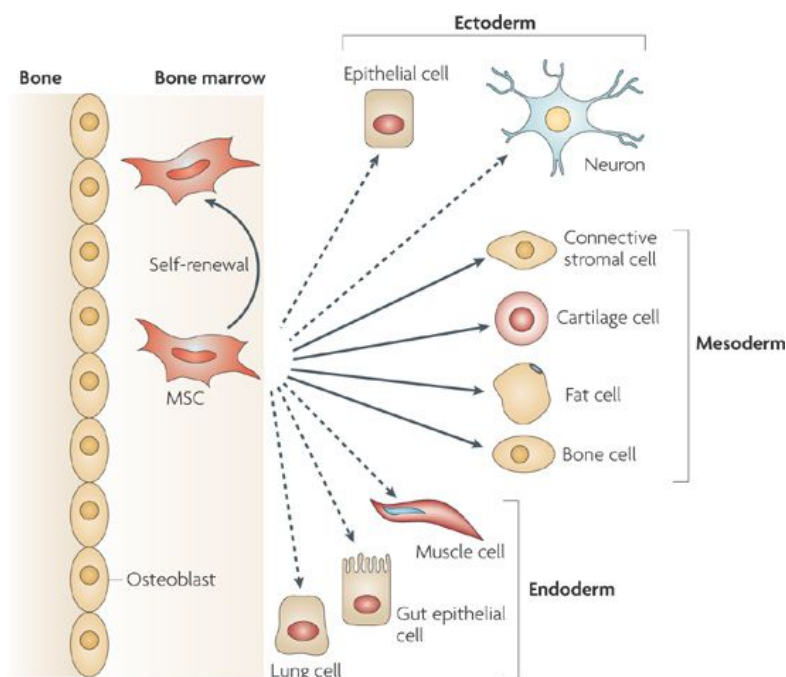


Figure 5 - MSC differentiation potential outlining the potential for a bone derived mesenchymal stem cell (MSC) to divide into numerous cell types. Mesodermal lineages are most appropriate to bone defects, specifically bone cells. Notably however, crucial to ongoing bone function is the presence of osteoclasts, which are derived from haemopoietic stem cells rather than MSCs. From Mesenchymal stem cells in health and disease. Ucelli & Pistoia, 2008, Mesenchymal Stem cells in health and disease, Nature Reviews Immunology volume 8; pages 726-736 (2008) (54)

MSCs are therefore key to tissue engineering and consideration of their activity is paramount to the function of an engineered implant, as well as for the study of the future implant *in vitro*. *In vitro* analysis necessitates the use of a variety of markers to indicate the ability for MSCs to adhere, differentiate, proliferate and function. Whilst microscopy and cell counting can be used to evaluate cell numbers, and live-dead staining can give information on the number of cells undergoing apoptosis, little more information can be inferred from these techniques. Markers of cell activity are more specific and relevant measures of engineered tissues.

1.1.2.2.2 Markers of osteogenic stem cell activity

This project is primarily concerned with bone regeneration, and the use of mineralisation as an end marker of cell activity is useful and clinically relevant. In patients with fractures or bone defects, we monitor the formation of mineralised bone via x-ray as an indicator of ongoing cell activity and correlate this with mechanical stability and return to function. However, mineralisation, which is cell mediated organised deposition of bone mineral (primarily calcium phosphate) into the extracellular matrix, does not begin to occur until beyond the 28 day mark (56). The following markers which have been associated with an end point of bone formation have been identified at various time points.

Early markers of bone formation (<14 days)

i) Runt-related transcription factor is (RUNX2) is a protein encoded by a single gene in osteoblasts, it suppresses pre-osteoblast proliferation and is intimately involved in osteoblast differentiation (57). RUNX2 is crucial to the progression of cell differentiation in a osteoblast lineage and thus knockout mice without RUNX2 show complete absence of bone formation (58).

ii) SP7 transcription factor, also known as Osterix (OSX) is an osteoblast specific protein encoded by the gene SP-7 and plays a key role in sheparding MSC differentiation toward osteoblast lineages

rather than chondrocytes. The suppression of OSX via knockout seems to block the osteoblast lineage resulting in MSC differentiation into chondrocytes and production of cartilage (59,60). This is particularly relevant as we know from clinical studies that bones which do not go on to heal with mineralised bone exhibit large amounts of chondral tissue in the gap. Of particular interest is that the implantation of cells which overexpress OSX has been shown to heal critical sized defects (59).

iii) Alkaline Phosphatase (ALP) is a homodimeric enzyme responsible for the dephosphorisation of phosphate-based compounds, such as calcium phosphate. It has a multitude of roles throughout the body and clinically is often used as a marker of bone turnover. It is unclear therefore why the presence of ALP in the first 2 weeks of MSC differentiation has been associated with formation of mineralised tissue at a later time point (59-62). The main so called “booster hypothesis” is that the presence of ALP increases local concentration of inorganic phosphate which ultimately combines with calcium to mineralise the organic component of bone ECM (62).

Late markers of bone formation (14-28 days)

i) Osteopontin (OPN) is a small integrin binding ligand, n-linked glycoprotein (SIBLING) which is coded by the SPP1 gene. It is expressed by relatively immature osteoblasts and its association with bone mineralisation is dependent upon OSX and RUNX2 (61). The function of OPN is not fully understood but is seen in ectopic calcification states (e.g. pulmonary fibrosis) and is thought to regulate mineral crystal growth as a mineralisation inhibitor (56). OPN ultimately binds to a variety of cells via integrins $\alpha_4\beta_1$, $\alpha_9\beta_1$ and $\alpha_9\beta_4$ on t-cells, mast cells and osteoclasts to activate cell differentiation and stimulate bone turnover.

ii) Osteocalcin (OCN) is a hormone excreted solely by mature osteoblasts and encoded by Bone Gamma-Carboxyglutamate Protein (BGLAP) receptor (63). It has a key role in the wider homeostasis of

calcium and additionally insulin and testosterone synthesis. OCN can be used to monitor mineralisation levels in bone mineralisation disorders such as osteoporosis. Using OCN as a marker of osteoblast activity demonstrates that they are functioning in a more holistic endocrine manner.

iii) Osteonectin (ON) is a bone glycoprotein with a high affinity for collagen, calcium and phosphate. It is integral to extracellular matrix formation prior to mineralisation to anchor calcium crystals to the organic components the ECM. In contrast to OCN, ON is produced by a wide variety of cells including fibroblasts, chondrocytes and epithelial cells (64). Knockout mouse not expressing ON have demonstrated reduced bone mineral density, indicating its role in mineralisation (65).

1.1.2.3 Integrins and focal adhesions

Integrins are transmembrane macromolecular proteins consisting of an α and β subunits which are non-covalently bound. Being trans-membranous, they act as adhesion receptors for ligands and function as signalling molecules for both mechanical and chemical pathways between the intracellular extracellular environments, having roles in 'outside-in' and 'inside-out' signalling pathways (66,67). The α unit consists of a ' β -propeller' domain, a thigh, knee, 2 calf units and an intracellular tail. The propeller domain has 7 repeat units, some of which conformationally changes when bound to Ca^{2+} and affect ligand binding. The β subunit is made from 4 repeats of epidermal growth factor, and a cytoplasmic tail, but also has an ion sensitive ligand binding site (which is inhibited by calcium but activated by Mn^{2+} and Mg^{2+}) so called metal ion-dependent adhesion sites (MIDAS) (68). Each unit therefore has a complex ligand sensitive extracellular structure, a single pass transmembranous portion and an independent cytoplasmic portion. The cytoplasmic portions of the α and β subunits undergo dimerization in response to ligand binding at the head units, causing intracellular signalling pathways (69,70). There are several classes of protein adaptors which have intracellular interactions with the integrin tails; structural adaptors (e.g. talin or tensin which bind to the cell

cytoskeleton), scaffolding adaptors (e.g. kindlin and paxillin which bridge with focal adhesions) and catalytic adaptors (focal adhesion kinase, which propagate signal transduction).

Ligand signalling from integrins can result in the formation of focal adhesions which are large multiprotein structures which form mechanical links between the ECM and the cell by incorporating the integrin with multiple intracellular 'anchoring' proteins such as actin (71). In 2D *in vitro* work, focal adhesions are found on the base of the cell, and thus are considered as the foot of the cell (72). Focal adhesions are highly dynamic and evolve over time, undergoing a process of initiation, clustering, growth, maturation and finally disassembly in response to mechanical stress (66-68). Integrin and focal adhesion activity are key to the biomedical engineering principles within this project, as the integrin binding site of FN is geographically close to that of the expressed growth factors. This co-localisation means that when MSCs detect growth factors, immediate integrin mediated binding to a protein network can occur which facilitates cell differentiation and activity.

1.1.2.4 Growth factors

Growth factors (GFs) are biological molecules which regulate fundamental cell functions. The term growth factor is probably now a misnomer as the same hormones/proteins have been found to not just stimulate cell proliferation and tissue growth, but individual cell growth, differentiation, tissue healing and even cell death. A more correct term for a signalling molecule is cytokine (from Greek for 'cell movement') where growth factors could be considered a subgroup involved in cell/tissue growth. There are a multitude of growth factors associated with bone growth; insulin-like growth factor (IGF) 1&2, bone morphogenetic proteins (BMPs), platelet-derived growth factor (PDGF), transforming growth factor beta (TGF- β), fibroblast growth factors (FGFs), parathyroid hormone-related peptide (PTHrP), vascular endothelial growth factor (VEGF). Beyond these GFs, bone morphology responds to more general cytokines, such as growth hormone (GH) and androgens (testosterone, oestrogen, dihydrotestosterone, oestradiol),

parathyroid hormone, thyroid hormone, calcitonin, cortisol and calcitriol (vitamin D).

1.1.2.4.1 Bone morphogenetic proteins (BMP)

Bone Morphogenetic Proteins (BMP) (or osteogenic proteins) were noted by Urist in the 1960s (73) and fall under the superfamily of TGF- β (with the exception of BMP-1 which is a metalloprotease) (2) and as with many GFs, have roles out with post-natal bone growth, such as cartilage, neural and cardiac development. BMPs act through serine/threonine kinase receptors, which have type I and II subtypes of which there are 3 subtype variations of each (74-79). This gives rise to approximately 20 varieties of BMP with varying roles in chondrogenesis and osteogenesis (80) with the exception of BMPs 8,9, 10 and 11 (which are responsible for reproductive, adipose, blood vessel and cardiac development respectively), There are only 2 types of recombinant BMPs (rhBMP) approved for use in humans, rhBMP-2 and rhBMP-7 and are most relevant to the work presented here. BMP acts via bone morphogenetic protein receptors (a typical type 1 transmembrane protein, belonging to the serine/threonine-specific protein kinase class) transducing signal via SMADS (transcriptional factors for TGF- β), signaling receptive mesenchymal stem cells into bone (or cartilage) forming cells. The response of cells appear to be dependent upon local concentrations of BMP, with low levels giving rise to angiogenesis, and higher concentrations resulting in chondro- and osteogenesis (81). Notably, BMP-3 and BMP-13 have been found to be inhibitors of bone formation (82). BMP-2 (83) and BMP-5, BMP-6 and BMP-7 (84) are associated with potent *in vitro* and *in vivo* osteogenic activity, and only this subset are associated with de novo bone formation (85). The specific preclinical study of BMP-2, BMP-4 and BMP-7 demonstrated bone regeneration in critical defect models (86-88). The clinical application of BMP-7 for non-unions (and subsequently spinal fusion) was approved by the Food and Drug Administration (FDA) in 2001 as "OP-1" (Stryker, Illinois). Following this, BMP-2 has been used in for spinal fusion and then for acute tibial fracture fixation. Initial approval was via the

Humanitarian Device Exemption, in which products can be brought to market without clinical evidence of efficacy (89). These proteins are however eluted from a collagen matrix (80) at high doses and this product has had an FDA caution applied (90-92) following a series of unanticipated events. Despite this, clinical trials have concluded that the use of BMPs in non-union surgery perform as effective as the current gold standard of autologous bone grafting (93-96), however have increased cost. The regular use of BMPs would likely be dependent upon reduction in production costs, demonstration of reduced clinical symptoms, or improved cost efficacy (e.g. reduction in healthcare episodes).

Many research groups continue to demonstrate the utility of BMPs in tissue engineering (97-99), although no single method of tissue delivery has been identified. The administration of BMP in solution is inferior to its combination with an appropriate carrier (100). Therefore the use of such a carrier has been the subject of repeated investigation (101). A range of ceramics and non-ceramics (or composites) as both scaffolds and particulate materials have been investigated.

The predominant ceramic in the literature is hydroxyapatite, which can be used as a carrier on its own (102), however the slow degradation rate is a disadvantage (103). The addition of β -TCP as a biphasic calcium phosphate ceramic increases bioresorption rates and improved bioactivity (104). This combination of BMP with the osteoinductive effects of HA/TCP is proposed as the main advantage of calcium phosphate ceramics as carriers for BMP (105). More recently, clay (laponite) has been demonstrated as a particulate material capable of encapsulating bioactive molecules (106) and safely harness BMP-2 to induce bone formation (107).

A wide variety of non-ceramics have been explored including synthetic materials, natural materials and titanium. Poly lactic acid was the first synthetic polymer to be investigated, however its degradation products are too acidic for tissue survival (101,108,109). Synthetic hydrogels, such as PEG derived gels, have been shown to be suitable signalling protein transport medium, along with the ability to present integrin binding sites. (110) These PEG hydrogels can infer favourable *in vitro* behaviour when presenting BMP-2

(108), however the problem remains that the PEG degradation products cause inflammatory responses which reduce stability of the *in situ* BMP (109,111). Natural polymers, such as fibrin, collagen or alginate can assist cell function by mimicking *in vivo* cell signalling (112). Fibrin, which is currently utilised clinically as a glue, has been shown to be effective not only in bone formation, but in GF retention (113). Collagen, which is the most abundant connective tissue in humans, is biocompatible, however as with the issues noted by the FDA, retention of the GF is a persistent issue and side effects occur as a consequence. Alginate gels have been demonstrated to utilise BMP-2 receptors to fill critical defects *in vivo* (114,115) and can be further enhanced by the addition of chitosan (116).

Titanium is a metal commonly used in orthopaedic surgery, given its stiffness properties, which are closer to bone than other implanted metals such as stainless-steel or cobalt-chrome (117). Early work of 'treating' titanium with BMP (118) has advanced to the use of thin coatings of HA (119,120) or fibrin (121)., however the models described by these models are that of osseointegration rather than critical defects.

1.1.2.4.2 Vascular endothelial growth factor (VEGF)

Vascular Endothelial Growth Factor (VEGF) was originally detected in 1983 in intrabdominal tumours, associated with fluid accumulation and was initially coined vascular permeability factor (122). As a growth factor, it is thought to be integral to vasculogenesis (blood vessel system formation in utero) and angiogenesis (growth of new blood vessels to an established system). Not surprisingly it was discovered in tumours, as once a tumour gets to a certain size, in order to survive, they must develop their own blood supply otherwise they undergo necrosis (typical to glioblastoma multiforme). VEGF is now categorised under the PDGF family and has 5 subtypes; VEGF-A, VEGF-B, VEGF-C, VEGF-D, PIGF. VEGF-A is the main GF involved in angiogenesis by increasing endothelial mitosis, migration and lumen/fenestration formation. VEGFB-D and PIGF are primarily functional in foetal vasculogenesis.

These GFs cause transphosphorylation of specific tyrosine kinase receptors (VEGFRs), which are present in high levels in vascular endothelial

cells. VEGF increases in expression in tissue, which is in a low oxygen environment, circulating to local endothelia and stimulating angiogenesis. Bone defects, in particularly larger ones such as critical defects, depend heavily on recruiting blood supply via angiogenesis from surrounding muscle as part of the inflammatory and regenerative process (123).

1.1.3 Analysis techniques

1.1.3.1 Biomaterial characterisation

The physiochemical properties of biomaterials determine how proteins and cells behave when in their proximity (124). Cells respond to chemical, mechanical and topographical properties (125). A measured approach to the characteristics of a biomaterial is essential in understanding its utility, measuring its consistency and predicting the impact it has on the microcellular environment.

1.1.3.1.1 Topography

The surface morphology of a material is intimately connected to its mechanical and chemical properties. Topography is a variation from the mean baseline of a material and a variety of methods can be used to visualise the topographical appearance of a material. Commonly available methods are optical, electron and atomic force microscopy. Optical microscopy is cheap, accessible and quick but resolution is limited to the 400-700nm wavelength of light. Electron microscopy has a much higher resolution due to the wavelength of an electron being much smaller and can focus of magnifications of up to x2 million. Atomic force microscopy (AFM) is a commonly used method of analysis in biomedical engineering in which an oscillating tip taps along the surface of a material and the changes in tip height/wavelength is detected by a laser and visually represented digitally. This method has a high resolution on a nanoscale and can also infer information on mechanical properties of the surface by nanoindentation.

1.1.3.1.2 Chemistry

Surface chemistry is the study of chemical bonds and reactions on a material surface. Chemical interaction between materials, proteins and cells are central to the function of biomaterials. Surface chemistry is intimately linked to the elements of a material and environment and can act differently than the bulk material. Commonly used methods of analysing the elemental makeup of a surface include x-ray photoelectron spectroscopy (XPS), water contact angle (WCA) and energy-dispersive X-ray spectroscopy (EDS), with over 40 further described tests including surface plasmon resonance (SPR) and Fourier-transform infrared spectroscopy (FTIR) (126). XPS is a quantitative analytical tool which emits a series of x-rays in a vacuum at a surface and measures the kinetic energy and number of electrons escaping from the top 10nm (98). This can be used to measure the composition, chemical and electronic states of the material (99). The angle at which the x-rays are projected at the surface (take off angle) dictates the depth of penetration and analysis.

EDS acts in a similar manner to XPS however projects electrons at a surface (often in conjunction with electron microscopy) and measuring the number and energy of x-rays emitted from the surface (100). These energies and x-ray counts can be compared to studied databases and give quantitative elemental compositions within a visually targeted area on a material surface.

WCA is a less specific but more accessible method of surface chemistry quantification which is specifically used for addressing wettability of a material (99). A number of methods variations exist, however specified volume of water is dropped onto the surface, and the angle formed at the base is measured to describe the wettability of the material inferring net behaviour of a surface, not just chemical hydrophobicity, but roughness and geometry (101).

1.1.3.2 Mechanical properties

Response of cells to mechanical stimulus has long been established as a key influencer in cell proliferation and activity (102,103). This is particularly evident in the musculoskeletal system where the mechanical environment will stimulate cell lineage direction and thus the type of tissue which will form

(122,124,127). Bone is strong, flexible and semi rigid, and a mismatch between mechanical properties of any implant and bone can give rise to a stress resulting in a yield or fracture and loss of integrity of the mechanobiological environment.

1.1.3.2.1 Stiffness

Stiffness is a deflection in response to force, most commonly evaluated by compression testing, in which a stiff material is more resistant to deflection for a given load. It is a factor of stress (force per unit area, N/m^2) and strain (change in length per original length (106)). Stiffness is often represented as Young's Modulus (stress/strain) for a given direction within the linear elastic portion of a stress-strain curve (Figure 6).

1.1.3.2.2 Strength

Strength is a resistance to deformation of a material. Two areas of strength can be considered; yield point and ultimate strength (Figure 6). The yield point of a material is the point at which a material exits its elastic region and will no longer return to its original shape. The force required to reach the yield point is a practical measurement of strength, as an implant should not breach this point. Alternatively, the 'ultimate strength' can be used as a point beyond which less force is required to cause the same strain, however implants are designed to avoid getting to this point under physiological load. Given the

consideration of scaffolds in this work as implants, the yield point will be used as the definition of strength.

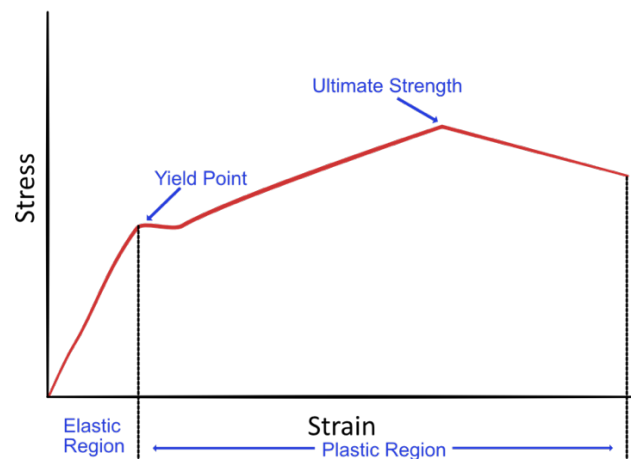


Figure 6 - Stress strain curve. All materials have an elastic and plastic region as a progressive force is applied in which deformation follows a uniform trend and then returns to their original form following cessation of load. The ratio of stress and strain in this region is the definition of elastic modulus (or Young's Modulus, E), which is a measure of stiffness. The steeper the line in this segment, the less deformation for a given force is observed and thus stiffer the material is. Beyond the elastic limit (at the 'yield point') materials undergo an irrecoverable dimensional change which is highly variable depending on their mode of failure.

1.2 Legislation

In the UK, the implantation of medical devices is subject to a number of legislative processes from the EU and British standards. From a terminology perspective both processes divide 'active' medical device from non-active medical devices by the need for an external source of power (e.g. a battery). These active medical devices are subject to European Union (EU) directive 90/385/EEC (128). As this is not the case for this system, focus remains on legislation and standards for the implantation of non-active medical devices.

1.2.1 EU Legislation

The EU directive under which the non-active biological implants studies in this work, is 93/42/EEC (129) published in June 1993 and updated in 2003 defines a medical device as *“any instrument, apparatus, appliance, material or other article, whether used alone or in combination, including the software necessary for its proper application intended by the manufacturer to be used for human beings for the purpose of:*

- *diagnosis, prevention, monitoring, treatment or alleviation of disease*
- *diagnosis, monitoring, treatment, alleviation of or compensation for an injury or handicap*
- *investigation, replacement or modification of the anatomy or of a physiological process*
- *control of conception*

and which does not achieve its principal intended action in or on the human body by pharmacological, immunological or metabolic means, but which may be assisted in its function by such means” (129)

Much of the 44 page legislation deals with bringing such a device to the market after the manufacturing process, with a view to legislating the award of a conformity marking ‘CE’ which is required to sell a device which was manufactured within the European Economic Area (EEA) whether that sale occurs within or out with the EEA. Areas relevant to this research are the general requirements, classification and sterilisation. This legislation states in detail that the device must be designed and manufactured in such a way that its purpose does not compromise the clinical condition or safety of patients. In addition, the manufacturer must ensure the device is inherently stable, has protection (if necessary) relating to risks which cannot be eliminated and finally inform users of any residual risks which should be considered to not outweigh the benefits. Throughout transport, storage or its declared lifespan (“use by” period dictated by the manufacturer) devices must also not be adversely affected to the degree it causes an issue with patient safety. Further to this,

the legislation stipulates that the product must be manufactured to guarantee its characteristics regarding not just toxicity, but compatibility with biological tissues.

In this legislation, medical devices are classified according to their site of use and intended duration of use; transient (<60 mins), short term (>60 mins, <30 days) or long term (>30 days). For the systems discussed in this thesis, the aim will intend to be beyond 30 days. An 'invasive device' is defined as *"A device which, in whole or in part, penetrates inside the body, either through a body orifice or through the surface of the body"*. It further clarifies a 'surgically invasive device' as *"An invasive device which penetrates inside the body through the surface of the body, with the aid or in the context of a surgical operation"* and 'an implantable device' as one which is *"totally introduced into the human body"*. The systems our research group use for bone regeneration are considered 'active therapeutic devices' as *"any active medical device, whether used alone or in combination with other medical devices, to support, modify, replace or restore biological functions or structures with a view to treatment or alleviation of an illness, injury or handicap"*. Invasive devices are ones which *"have a biological effect or to be wholly or mainly absorbed"*, i.e. an engineered osteoinductive system, is considered a Class III medical devices.

Regarding sterilisation, Section 8 of Annex 1 ('General Requirements') stipulates that the device must be manufactured to eliminate or reduce risk of infection to both patient, user and third parties. This includes; sterilising in an appropriate manner (without specifying techniques), packaging in a sterile manner, use of single use packaging which will remain sterile until use.

Out with the application of legislation to this research, the remainder of the document details the manufacturer's responsibilities in quality assurance, testing, verification and postproduction monitoring of the device, including mandatory training.

1.2.2 British standards

There are numerous British standards set out by the British Standards Institution (BSI) for implants in the UK. BS7251 refers to joint prostheses, BS7252 to metallic implants, BS7253 to non-metallic implants and BS3531 covers orthopaedic implants involving osteosynthesis, which may seem most relevant to this research. However, the 15 current sections (and 34 withdrawn/superseded) refer to permanent metal implants (plates, screws, pins, staples and nails), rather than polymers or biodegradables and has no additional relevant material within them.

1.2.3 Regulation

Within the UK, the Medicine and Healthcare products Regulatory Agency (MHRA) are the assigned governmental body who administer and enforce the law on medical devices. They operate within the '*Medical Devices Regulations 2002 (SI 2002 No 618, as amended)*' and the '*General Product Safety Regulations 2005 (SI 2005 No 1803)*'. They conduct surveillance of marketed products and assess allegations of non-compliance and investigate medical devices associated with adverse events.

The MHRA can act with various enforcement powers to restrict the supply of medical devices under the above acts, or indeed under the '*Consumer Protection Act (1997)*' and '*Consumer Rights Act (2015)*' carrying maximum penalties of unlimited fines and 6 months imprisonment.

1.3 Clinical Applications

The ultimate aim for this project and its funders is to develop means of translating of bone regeneration systems into human patients. There are several main domains in which bone regeneration systems could be applied in humans and animals, the main domains of which are outlined in this section.

There are a number of circumstances in which a patient may lose a significant amount of bone, with the tolerance of a patient to withstand the loss of bone depending on a multitude of factors. When discussing bone loss, the natural history of most causes (i.e. traumatic fractures) is macrophage and osteoclast driven resorption of bone debris prior to regeneration of new bone (130,131). This is to say that all fractures have varying degree of bone substance loss, however as long as spontaneous healing of the bone occurs then this bone loss is negligible. For the purposes of this review, bone loss is considered to be *'the loss of a significant amount of bone in the absence of spontaneous healing'*. The ability for a patient to tolerate bone loss depends on the bone which has suffered insult, for example weight bearing bones such as the tibia and femur have a significant functional impact, whereas non load bearing bones such as the fibula can have little to no symptoms with large defects. Secondly, the activity level which an individual undertakes has a substantial effect on whether the bone loss goes unnoticed or not. As such, a collarbone (clavicle) fracture which doesn't heal and results in bone resorption may quickly become pain free and unnoticeable in an elderly patient with low functional daily demands (132), whereas a badminton enthusiast may be significantly disabled by even a small defect.

1.3.1 Non-union

In the above examples, simple fractures are given as a cause of the bone loss, however in reality it is rare for a bone to not complete bony union resulting in a 'non-union'. This occurs in approximately 5-10% of fractures (133) and up to 30% of high risk fractures (134-138). There are a multitude of definitions of non-union, often described radiologically, but in practical terms they all agree that it is the lack of bone bridging the fracture site and resulting in mechanical incongruence throughout the bone (Figure 7).

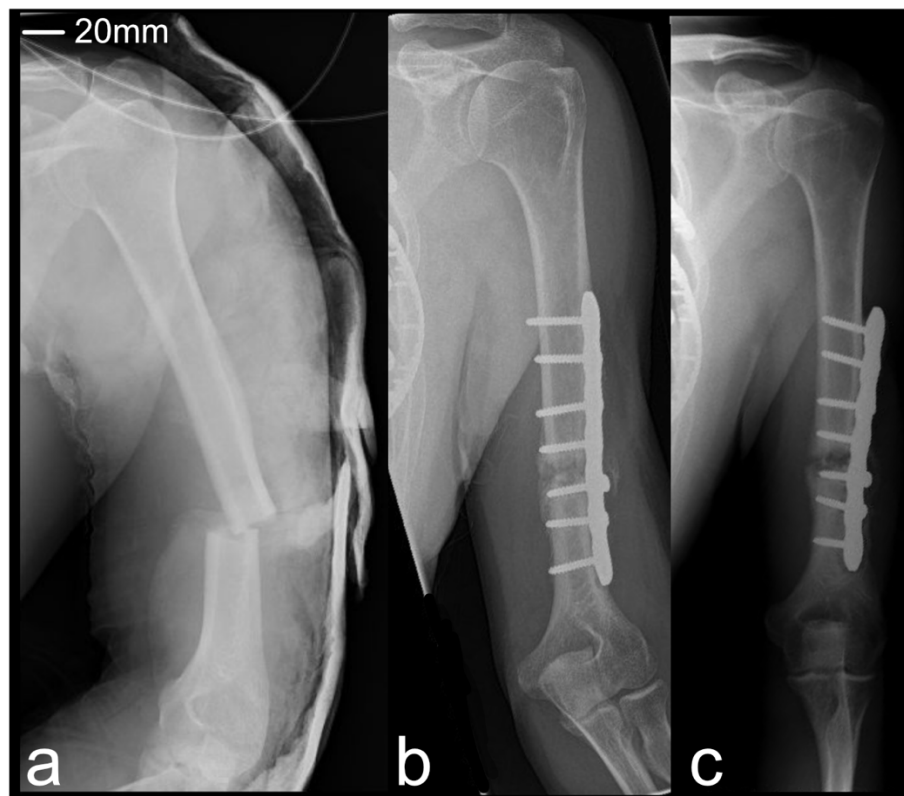


Figure 7 – Non-union. This series of X-rays demonstrate a) an acute humeral fracture, b) managed with open reduction and internal fixation (ORIF) with plate and screws. C) several months following fixation, a lucent gap develops at the fracture site indicative of osteolysis and non-union (pictures courtesy of NHS imaging archives).

Union therefore is a time dependant process, and different bones in different biological/mechanical circumstances in different patients will heal at different rates (117,118). Defining non-union in clinical practice can be difficult as it involves an element of experience in whether a bone, given time, would eventually heal or whether it is quiescent in its healing process. A clinician

often needs to make a judgement once an adequate period of time has passed for that particular injury as to whether healing is slow ('delayed union') or not going to occur ('non-union). Non-union is then pragmatically defined as a fracture which has not healed and will not do so without intervention.

A non-union may occur for numerous reasons, which are broadly divided into mechanical and biological factors shown in Table 4.

Mechanical	Biological
Excess mobility	Poor perfusion
Excess rigidity	Infection
Excess gap	Pathological process - e.g. malignancy
	Smoking/malnutrition
	Endocrinology: diabetes, hypothyroidism, hypoparathyroidism, hypogonadism

Table 4 - Causes of non-union categorised by mechanical and biological aetiologies (119).

To aid clinical planning, the causes are often also categorised by the bone's resultant appearance (usually radiographically with X-rays or computed tomography (CT) scans), whether there has been a good response to healing or not (Table 5). Often there are large volumes of callus laid down, but not in an organised enough manner to bridge the fracture gap known as 'hypertrophic non-union'. Alternatively, if there would appear to be little or no new bone formation with rounding off of the bone ends and a persistent gap, this is described as 'atrophic non-union' (139). The caveat to this diagnosis, is that there is often fibrous tissue bridging the gap (not seen on x ray) which gives a variable degree of mechanical stability, which would be described as a 'fibrous non-union' the mechanical adequacy of which would dictate the patient's symptoms. A good example of this would be a base of 5th metatarsal

fracture, where the fracture frequently results in a fibrous non-union which is functionally sufficient and thus patients quickly get back to normal function.

Hypertrophic	Atrophic
Excess mobility	Poor vascular supply
Excess gap	Infection
	Excess rigidity
	Pathological process (e.g. lymphoma)
	Smoking/malnutrition
	Endocrinological; diabetes, hypothyroidism, hypoparathyroidism, hypogonadism
	Medications; steroids, non-steroidal anti-inflammatory drugs (NSAIDS), bisphosphonates, chemotherapy

Table 5 - Categorisation of non-union by radiographic appearance.

Whilst the focus of the functional deficit could correctly be perceived as an ineffective mechanical stability in a non-united bone, the relevance to critical bone defect becomes apparent following surgery. As outlined above, during the failed healing process, a large amount of bone and bone fragments are resorbed by osteoclastic activity. The principle of surgery is to debride any fibrous tissue and non-healing bone ends away until 'fresh' and bleeding bone ends can be opposed and held together in a mechanically sound manner to facilitate new bone healing. The combination of osteoclast resorption and surgical resection inevitably results in loss of length of bone. Similar to the tolerances discussed above, different degrees of shortening in united bones are tolerated differently depending on the bone, function and personal circumstances of the patient. However as a rule of thumb, upper limb long bones tolerate shortening well (140) and weight bearing lower limb long bones

can compensate for 10mm of shortening by tilting the pelvis (123). Whilst shoe raises can be used to help compensate for this in some patients, many patients with reasonable function levels or young age could be better managed by restoration of bone length, alignment and rotation.

In Scotland, approximately 1000 non-unions occur per year, with an even gender distribution, with a preponderance for upper limb over lower limb (141). Much of orthopaedic fracture surgery is aimed at minimising chance of non-union in the early days following injury, as late surgery to correct non-union is less predictable and results in sub optimal symptomatic relief. A recent study indicated that when tibial fractures don't heal, an average of 36% will require more than one operation to establish union with up to 5 procedures required to achieve a union rate of 7% (142).

Establishing techniques to ensure rapid bone union could minimise patient pain, improve function and thus quality of life. Furthermore, minimising hospital visits and facilitating patients' return to hobbies and work has potentially unmeasurable effect on morale.

The wide range of case types give health care costs within the NHS reported to be between £7000 and £79000 per case (143-145). Given the estimated caseload of 19/100000 population, or 53 cases in Scotland per year, this has significant fiscal impact on healthcare provision (124). In particular, the West of Scotland population suffers from high incidences of obesity and type 2 diabetes, which both increase the chance of non-union and complicate subsequent surgery (146-148).

As indicated above, the principles of management of non-union depend on which category it falls under. It is worth noting there are some prerequisites which must be addressed in order to successfully manage any bone healing namely the absence of infection & preservation of blood supply. Beyond this, the 'Diamond Concept' of bone healing covers the 4 core areas which need to be present; osteogenic cells, growth factors, osteoconductive scaffolds, a favourable mechanical environment (149-151). The management of hypertrophic non-union which is rarely a problem with the biological presence of blood supply/cells/GFs and as such is managed by a change of mechanical environment, usually by decreasing strain often with surgery. Atrophic non-

unions can be more difficult to define a causative factor, however in the presumption infection has not ensued (via surgery or open fractures) then either poor biomechanics (too rigid), poor vascular supply or paucity of cells/growth factors are left (139). All of these factors are hard to fix surgically, and perhaps in these cases bioengineered scaffolds may have a role.

1.3.2 Fusion

Perhaps a simpler and more predictable model for application of a bioengineered bone regeneration would be in arthrodesis (joint fusion). These common procedures are performed for alleviation of pain and improved stability of a joint which is non-functional usually due to arthritis (inflammatory, traumatic, degenerative, post infective) or less frequently for neuromuscular disorders (152). Arthritis causes pain by a number of mechanisms, but essentially the damaged articulations rub off each other giving direct pain/stiffness and a secondary inflammatory reaction due to debris formation. The principle of arthrodesis is that the mobility of the joint is causing functional or nociceptive detriment to a patient, thus removing the joint and joining its articulating ends with bone eliminates movement (Figure 8). Whilst this minimises pain, the trade-off is a loss of function (movement) at the joint, however this patient group frequently neglect to use the joint on account of pain, and surgery acts to accelerate the natural history of arthrodesis of the arthrosed joint.

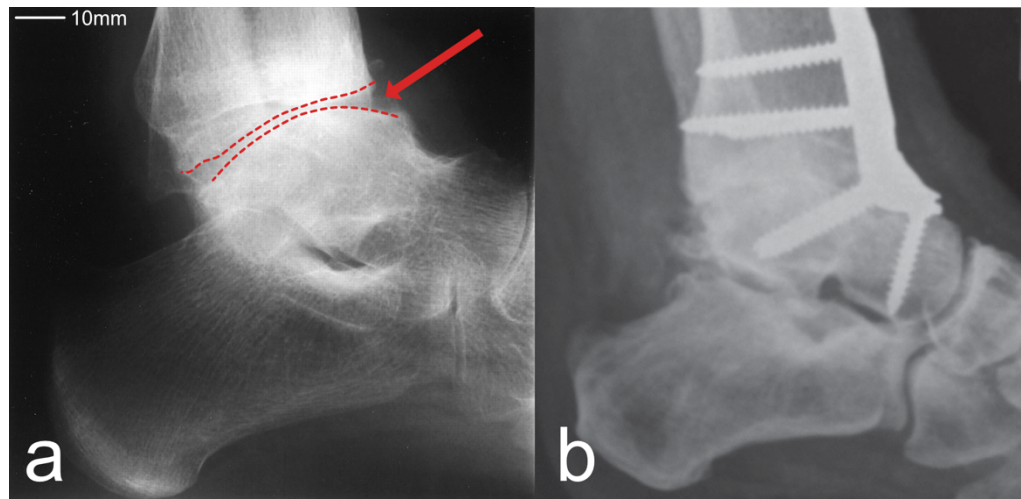


Figure 8 – Arthrodesis. Lateral view X-rays of a) an arthritic ankle joint (dotted lines) and with loss of joint space (arrow). b) Following plate fusion the joint line is eradicated and replaced with mineralised bone (153).

An alternative to fusion would be arthroplasty (joint replacement) which removes the worn joint lining and replaces it with synthetic materials. Arthroplasty maintains range of motion and improves pain, however there are few joints in which this is consistently effective for the right indications e.g. hips, knees, and shoulders (154,155).

_____ Rates of fusion failure varies between in the literature depending on the joint, patient, technique and surgeon, but is between 0 and 20% (138,156,157). For instance, a patient who suffers from rheumatoid arthritis has florid intraarticular inflammatory synovium, so typically has a high chance of fusion. In contrast, a patient who is diabetic or has a lifelong history of smoking with poor vascular supply has a much poorer chance of fusion, particularly if it is a distal joint (e.g. an interphalangeal joint).

Whilst failure to fuse is generally infrequent, it causes significant morbidity due to persistent pain and reduced function, such as a failed ankle fusion impacting on other joints which have been compensating. Additionally, any repeat attempts to fuse the joint are less fruitful due to reduced blood supply, loss of bone stock and frequently disuse osteopenia. These repeat surgeries often require autologous bone graft which causes pain, irritation and risk of infection at the donor site. If osteoinductive materials can be introduced into the surgical fusion site to promote fusion, particularly in high risk cases, then patients would benefit from more predictable surgery with lower donor site morbidity and fewer healthcare episodes. Recent evaluation of multiple

clinical studies has demonstrated that the use of polymers rather than traditional metals can give favourable outcomes in degenerate spinal disease (158).

1.3.3 Critical Bone Loss

As discussed above, the loss of bone can be as a result of a number of pathologies, with even the simplest of fractures resulting in macrocytosis and bone resorption. The relevance of bone loss is related to both the aforementioned acceptable functional loss of bone but also critical bone defects. A critical bone defect (Figure 9) is one which will not heal without intervention, somewhat similar to an established non-union, however has not gone through the biological attempts and failure to heal (although ultimately a critical bone defect will result in a non-union).



Figure 9 – X-rays of a large critical bone defect. This patient developed a deep bone infection Following surgical removal of infection, a substantial critical defect of the tibia (stabilised with external fixation). Note surgical clips within the defect following plastic surgical intervention to cover a soft tissue defect(pictures courtesy of NHS imaging archives).

The amount of bone lost from a bone in order to create a critical defect depends on the bone, the local environment (e.g. co-morbidities) and species of animal, for example, a 2.5mm defect in a mouse radius has been shown to be a critical defect (159) yet it is not until >10mm does a human tibial diaphysis run a risk of not healing (160), is the long bone with the highest risk of non-union. Due to the large number of variables, critical defects are not easily defined nor predicted (161). Critical bone defects occur following trauma (such as severe open fractures with bone loss or devitalised), following tumour surgery (where large amounts of bone are resected due to invasive disease or the required margin of normal tissue excised with tumours) or occasionally through infective osteomyelitis. The present strategies in these circumstances are to use engineered bioinert implants (such as titanium or stainless steel) or attempt regeneration of bone, the choice in which depends on individual patient requirements. There are a multitude of implants available to accommodate bone loss which can incorporate joint replacements (arthroplasty) and if the end of the bone is sacrificed or for a segmental defect intercalary implants may be used. For bone regeneration, the strategy is to stabilise a gap with a mechanical environment which facilitates micromotion and callus, whilst maintaining as much growth factor, scaffold and osteogenic cell activity as possible. This can be obtained with plates and screws to 'bridge' the gap (often with osteoinductive scaffold, such as bone chips or autograft), by shortening the limb to close the gap and slowly lengthening the bone ("distraction osteogenesis"), or maintaining the length and moving a 5-10cm block of vascularised bone slowly through the gap to fill it ('transport osteogenesis') (162).

There are however limitations of the surgical methods of dealing with critical bone loss. For longevity, we rely upon osseointegration at the bone implant interface, which gives problems with bone stock for coupling and ultimate loosening if it fails. Even modern titanium implants have a mechanical limit when they are used in a load bearing capacity so are subject to metal fatigue and fracture after a given number of cyclical loads (163,164). The above described bone regeneration techniques often require external fixation frames which are adjusted on a daily basis by the patient over many months. Not only

is this a painful and slow process, leaves scarring, runs high rates of infection but also can eventually fail to unite (165-167). These long and complex processes require close outpatient monitoring and make it difficult for patients to maintain employment, thus have significant fiscal implications for patients and healthcare systems.

In the acute critical defect scenario, where the bone has not yet undergone the biological cessation of attempts to heal seen in non-union, the implantation of engineered scaffolds which mimic the diamond concept domains would be beneficial. These scaffolds could have the potential to encourage new bone formation with predictable rates of union and ultimately shorten patients' healthcare episodes.

The use of an acute critical defect model in mice described in this work, aims to explore the efficacy of functionalised scaffolds (6,168,169). This model exploits the fact that a mouse can remain fully functional with the absence of its radius. The resection of 2.5mm of a mouse radius will not spontaneously heal, thus establishing the role of the model in acute bone defects (168). The quantitative outcome measure in this model is mineralisation within the defect however as the formation of functional bone is more than the presence of minerals, a measure of the utility of the forelimb would be a useful additional measure. Functional measures are not possible in this model, not only because the observation in mouse behaviour is impractical, but also the forelimb maintains normal function due to the presence of an ulna. The use of mice may not entirely reflect human defects, given their lack of Haversian canals (170), and difference in relative bone size (171). Mouse models however remain attractive given their relative low cost, ease of handling and ability to genetically manipulate them. Knock-out mice could be used to simulate the utility of functionalised scaffolds in 'high-risk' fracture and defect scenarios, such as diabetes or immunosuppression.

1.3.4 Osseointegration

The insertion of implants has been in practice since 1938 when Vitalium inserted spacers into knees to relieve wear within compartments of the knee (172). Then in 1940, Campbell and Boyd created a resurfacing implant for the distal femur as a treatment for knee arthritis however integration of the prosthesis was problematic (173). In subsequent decades, orthopaedic implants have divided into 2 distinct groups: implants which couple with the body via bone-cement and cement-implant interface ('cemented'), or implants which integrate with bone directly ('uncemented'). Uncemented implants have undergone evolution in terms of surgical technique (where maintenance of bone stock and rigid fixation are key) but also in implant design, with load bearing wedge designs for rigid fixation and combinations of porous, trabecular and hydroxyapatite coatings.

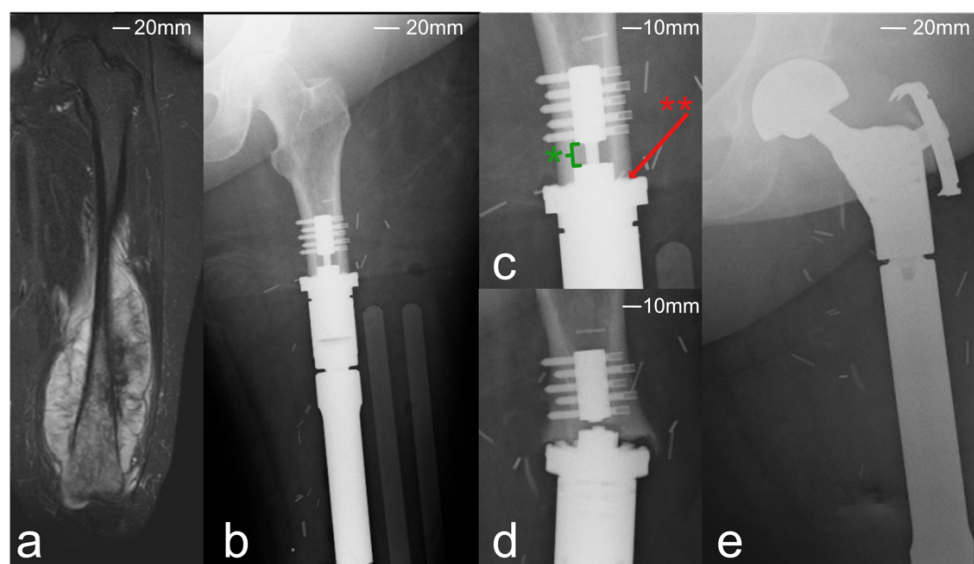


Figure 10 - Failure of osseointegration. a) Patient with a tumour of the left femur (chondrosarcoma) which was surgically excised and b) replaced with a femoral implant. c) The interface between the implant and bone is limited by a short trunnion () which is liable to fatigue failure unless the bony on-growth is achieved at the opposition site (**). d) Failure of bone on-growth and biological coupling resulted in fatigue fracture of the implant trunnion and e) entire replacement of the femur (pictures courtesy of NHS imaging archives).*

Integration of uncemented implants continues to fail in over 10% of cases (174) resulting in subsidence of implants, loosening, dislocation and destruction of bone stock which makes revision surgery challenging. Prompt bone on-growth or in-growth of bone (depending on prosthesis design) is therefore required to

integrate implants (Figure 10) and an osteoinductive bioengineered material coating could be applied in this circumstance. Recently fibronectin coatings have been applied to stainless steel and demonstrated a favourable environment for osteointegration (175).

1.4 Thesis Aims and Objectives

1.4.1 Aims

The aim of this doctoral thesis is to investigate aspects of the PEA/FN/BMP-2 osteoinductive nanocoating which are key to future translational research. It has already been established that plasma polymerisation of PEA is key to this technology's utility in 3D applications.

1.4.2 Objectives

1. Explore the effect of ethylene oxide as a sterilisation on the osteoinductive capabilities of the technology at 3 key stages. Sterilisation could occur of base polymers alone followed by intraoperative addition of FN and BMP-2. Alternatively, the system could have FN or FN+BMP-2 adsorbed then sterilised. Therefore, the first objective is to establish if there is an effect of protein sensitive (ethylene oxide) sterilisation at each of these key steps. (Chapter 2)
2. The utility of functionalising (with PEA, fibronectin and BMP-2) a currently used bone substitute (decellularised bone chips) will be tested as the first controlled *in vivo* 3D experiment of this technology (Chapter 3).
3. Moving on to a fully synthetic system, the merits of a customisable 3D printed scaffold will be evaluated using biocompatible PCL from a mechanical and biological perspective (Chapter 4).
4. PCL is a relatively soft polymer therefore the addition of HA will be investigated to potentially improve mechanical properties of PCL and induce osteogenesis (Chapter 4).

Chapter - 2 Sterilisation of Fibronectin + BMP-2 Osteoinductive Systems

2.1 - Introduction

In order for any implantable medical device to progress to translational evaluation, their resilience to recognised sterilisation techniques must be evaluated. Given the temperature and sensitivity and potential effects of polymer crosslinking associated with autoclaving and gamma irradiation, ethylene oxide (EO) was put forward as the most biologically sensitive sterilisation technique. Ethylene oxide (EO) sterilisation is the most commonly used technique for medical devices in the UK (unpublished data, Andersen Caledonia LTD). It has particular advantages in deep penetration of porous scaffolds and those sensitive to heat or crosslinking. The industrial scale process is outlined in Figure 11.

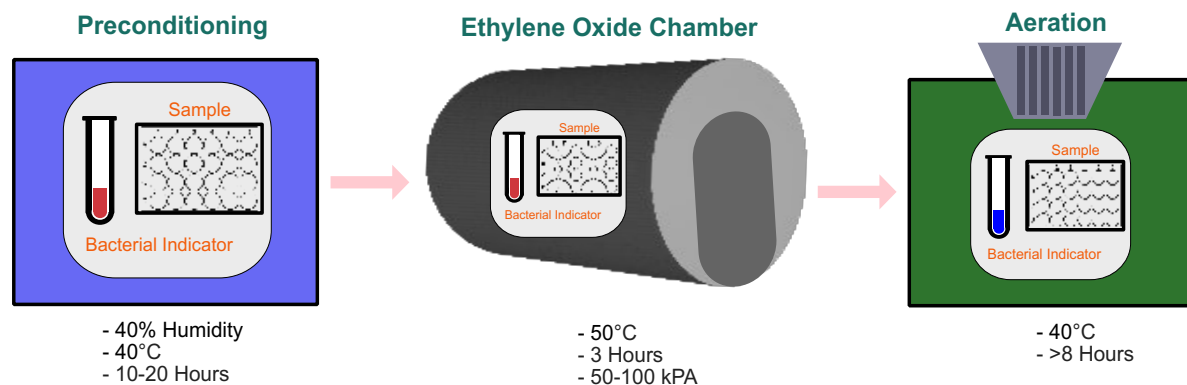


Figure 11 - Schematic of EO Sterilisation Process. A warming and humid preconditioning phase to expose bacteria from spore form is performed before transfer to a specialised EO chamber along with a control bacterial indicator. Products are exposed to the volatile EO gas for several hours in a slight vacuum before transferred to an aeration chamber to evacuate remnants of the noxious gas. At this point, bacterial indicators (*bacillus atrophaeus*) are confirmed as dead before products are distributed.

This Chapter investigates the effect of EO sterilisation on a) different materials' ability to induce a FN network ('material driven fibrillogenesis'), b) established FN networks and c) present BMP-2. Quality of FN network is assessed by atomic force microscopy showing fibrillogenesis present in all samples where

expected with persisting fibronectin (FN) network despite the penetrance of the volatile gas. Cell binding and growth factor domains were available upon the FN networks as demonstrated by ELISA for FN added before and after sterilisation.

Subtle changes in behaviour of materials following EO were noted leading to the exploration of surface chemistry changes using x-ray photoemission spectroscopy and water contact angles. These demonstrated constitutional changes in PMA which are favourable to formation of FN networks.

Finally, the sterilised systems show that MSK progenitor cells differentiation on base polymers and FN which have been exposed to EO.

Specific acknowledgement in this Chapter to Dr Virginia Llopis-Hernandez for her role in advising and guiding experimental techniques.

2.2 Materials and methods

2.2.1 Materials

A list of materials and manufacturers can be found in appendix 6.1

2.2.2 Methods and sample preparation

2.2.2.1 Spun samples

Poly(methyl acrylate) (PMA), poly(ethyl acrylate) (PEA) and poly(capro lactone) (PCL) polymers were synthesised via radical photopolymerisation of methyl acrylate, and ethyl acrylate. This was performed using ultraviolet light and 1% benzoin as a photo initiator. PEA and PMA were dissolved into solution using toluene with 4% PEA and 6% PMA. PCL was dissolved in chloroform as a 10% solution. 12 mm glass coverslips were cleaned by 30 minutes sonication in absolute ethanol followed by a triple rinse in absolute ethanol and drying at 60 °C. Solutions were pipetted onto the glass coverslips in 100 µl aliquots then spin coated for 30 seconds at 3000 rpm with an acceleration of 3000 rpm/second² using (SPIN200i, Polos). Excess solvent was removed in a 2-hour vacuum oven process at 60 °C for PMA and PEA, and 50 °C for PCL.

2.2.2.2 Fabrication of scaffolds

PCL scaffolds were prepared using RegenHU Discovery 3D with a heated extruder screw 72 °C and 0.45 MPa pressure into a class 2 hood with an ambient temperature of 26 °C. Filaments were extruded using a 0.5 mm nozzle into strands of thickness of 0.3 mm. Extrusion line were 0.5 mm apart in the y-axis and 0.5 mm in the z axis giving a pore dimension of 0.2 mm x 0.2 mm. The layers were stacked at 90 ° to one another for 4 layers giving a total scaffold dimensions 5x5x1.2 mm (Figure 12). Scaffolds were stored in a clean dry environment at room temperature.

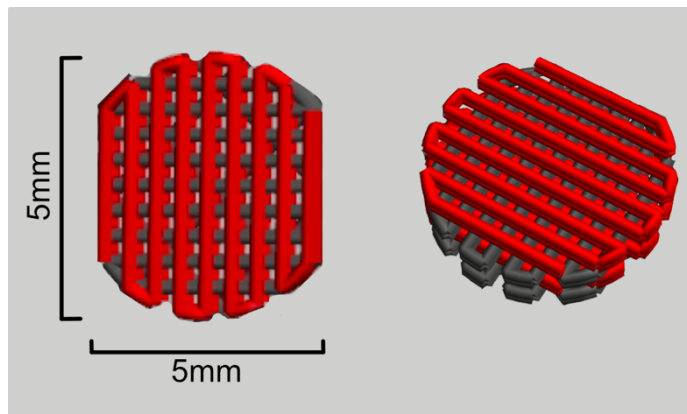


Figure 12 - Scaffold Geometry. Printed scaffolds were designed to fit within each well of a 24 well plate giving outer dimensions of 5x5x1.2 mm.

2.2.2.3 Plasma coated samples

12mm glass coverslips were cleaned by 30 minutes sonication in absolute ethanol followed by a triple rinse in absolute ethanol and drying at 60 °C. These were inserted into a clean plasma chamber (Figure 13) and a vacuum slowly formed before introduction of radiofrequency (RF) to initiate an ‘air plasma’ treatment (no monomer introduced) at 50 W for 5 minutes to clean the samples and prime the surfaces for interaction with the impending polymerisation. The air was shut off after 5 minutes and vacuum allowed to increase once again before the formal plasma polymerisation. The vacuum was adjusted for a final time, the EA monomer introduced into the chamber and plasma state was formed using a static radiofrequency. The monomer valve was adjusted periodically to maintain a consistent vacuum of 1.2×10^{-1} mbar (+/- 0.2×10^{-1}) (Table 6). This was maintained for 15 minutes at 50 W then RF ceased and vacuum slowly reduced via a filtered air source as per previous work in this field (6).

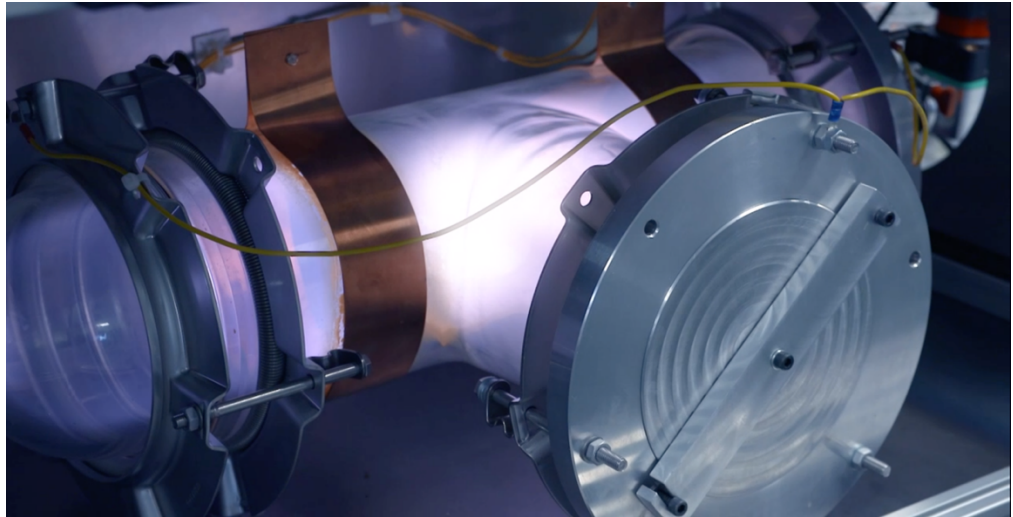
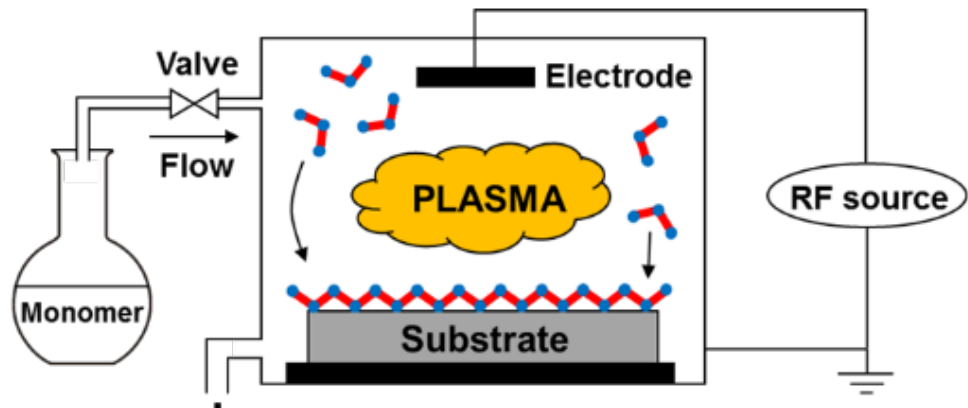


Figure 13- Illustration of custom plasma chamber from Nanoscale Coatings for Ultralow Dose BMP-2-Driven Regeneration of Critical-Sized Bone Defects, Cheng et al, *Advanced Science* 2018 6:2(5) and photo of plasma induced state. Materials are introduced into a shelf in the 15l reactor chamber and vacuum is generated in the region of $1-2 \times 10^{-1}$ mbar. Then an electrical potential difference is created within the vacuum via 2 capacitively coupled copper rings and maintained using an RF source. This creates a plasma state throughout the chamber, into which ethyl acrylate monomer is introduced which spontaneously polymerises coating any exposed materials. The duration and plasma intensity dictate the thickness of coating

Sample base material	Pressure 1 (pre-plasma) (mbar)	Pressure 2 (air-plasma) (mbar)	Pressure 3 (post air-plasma) (mbar)	Pressure 4 (polymerising plasma) (mbar)
Glass Slips	1.1×10^{-2}	$1.2-1.3 \times 10^{-1}$	1.0×10^{-2}	$1.5-1.7 \times 10^{-1}$
Spun PCL	1.2×10^{-2}	$1.0-1.2 \times 10^{-1}$	1.0×10^{-2}	$1.6-1.8 \times 10^{-1}$
PCL Scaffold	2.0×10^{-2}	$1.2-1.3 \times 10^{-1}$	1.1×10^{-2}	$1.5-1.8 \times 10^{-1}$
5mm bone scaffolds	1.1×10^{-2}	$1.2-1.3 \times 10^{-1}$	1.0×10^{-2}	$1.5-1.7 \times 10^{-1}$
Control. (PCL Scaffold + Glass)	8.3×10^{-3}	$1.0-1.2 \times 10^{-1}$	7.0×10^{-3}	$1.2-1.4 \times 10^{-1}$
BMP EO Samples	1.5×10^{-2}	$1.2-1.4 \times 10^{-1}$	1.4×10^{-2}	$1.5-1.8 \times 10^{-1}$
Samples for Water Contact angle and residual EO testing	2.2×10^{-2}	$1.1-1.4 \times 10^{-1}$	1.6×10^{-2}	$1.5-1.7 \times 10^{-1}$

Table 6 – Plasma chamber pressures for each PEA polymerisation process were maintained within a consistent and narrow pressure range between sample preparations.

2.2.2.4 Spray samples

Scaffolds were spray coated with 8% PEA (Sigma-Aldrich, Missouri, USA) with a pressure of 130 mmhg. This pressure and nozzle were calibrated to extrude 5 mls of 100% ethanol in 55 seconds, a level previously used within the research group . A petri dish was sprayed lightly with the PEA solution to adhere samples to it in order for them to remain in position (as the petri dish is propped up at 90 °). The samples were then sprayed at 15 cm for 15 seconds on each side with the above calibrations and excess solvent removed in a vacuum oven for 2 hours at 60 °C.

2.2.2.5 Bone chips

Following fibronectin absorption, the bone chips were aliquoted by weight into 10 even groups using a microbalance (Pioneer PA64, Ohaus)(Table 7). Given the random nature of bone formation, this was the best way to infer volume of bone however does not necessarily mean the surface area is equal, this was estimated visually when dividing the bone chips into groups. As the groups were initially divided in 2 blindly, any surface area inconsistencies were randomly divided between the groups.

Sample	1	2	3	4	5	6	7	8	9	10	Mean Weight (μg)
PreEO FN (μg)	18.9	16.9	15.0	17.4	15.6	18.6	15.6	15.8	17.3	15.0	16.6
PostEO FN (μg)	15.7	16.6	19.0	17.6	15.5	17.2	16.2	17.0	15.4	15.1	16.5

Table 7 - Bone chip weights for each group. Mann-Whitney U test for this non-parametric data, the groups are not statistically different ($p=0.968$)

2.2.2.6 Protein adsorption

2.2.2.6.1 – Fibronectin (FN)

The method of protein coating was the same for whether it was adsorbed prior to EO sterilisation or afterward. Human plasma FN was prepared in Dulbecco's Phosphate Buffered Solution (contents per litre; 8 g sodium chloride, 0.2 g potassium phosphate, 1.15 g sodium phosphate, 0.2 g potassium chloride) to 20 $\mu\text{g}/\text{ml}$ from stock solution of 1.42 mg/ml. Samples prepared on glass slips were placed on parafilm and 200 μl of fibronectin added to the sample and left covered for 60 minutes. Scaffolds (including bone chips) were immersed in the FN solution in a vacuum using a vacutainer for 60 mins. At 60 minutes the FN solution was removed and stored for future normalisation using unadsorbed FN where appropriate. Finally, a wash with DPBS and then MilliQ water was performed before drying the samples with nitrogen.

2.2.2.6.2 - Bone Morphogenetic Protein-2

1% w/v BSA in MilliQ water was inactivated in a 65 °C bath for 10 mins, to block non-specific binding sites, then filtered and added to samples for 30 minutes. Following triple wash with Dulbecco's Phosphate Buffered Solution (DPBS) the samples were incubated with BMP-2 (which displaces albumin due to a higher dissociation constant) at 50 ng/ml in DPBS -- (-calcium -magnesium) for 60 minutes and unadsorbed BMP-2 removed and kept at -80 °C. A final wash with DPBS -- was performed then samples dried with nitrogen flow.

2.2.2.7 Ethylene oxide sterilisation

Samples were placed in polystyrene 24 well plates and low temperature EO sterilisation was carried out at the Andersen Caledonia LTD facility (UK). This process (Figure 11) consisted of preconditioning process where the samples were warmed and humidified to expose any bacterial spores. The batch was then transferred to the EO chamber where it was exposed to the EO gas for >90 minutes at a controlled temperature of 45-50 °C (this upper limit was dictated to avoid approaching the melting temperature of PCL). Finally, the samples were aerated and allowed to cool in order to remove the remaining gas over an 8-hour period. To establish efficacy of treatment, *Bacillus atrophaeus* colonies were placed amongst the batch being sterilised and then cultured for 7 days following sterilisation to confirm sterility of the batch. EO sterilisation exposure takes 90 minutes, however this work aimed to investigate the pragmatic effect of EO sterilisation on an industrial scale. Therefore a 90-minute EO exposure in the laboratory (adopted in published literature to date) and experimental evaluation thereafter is a less relevant outcome than the 7-10 day EO sterilisation process widely used in industry. For these experiments, samples were prepared, sterilised and evaluated upon release from the facility, >7 days from preparation.

2.2.2.8 Sterilisation control sample preparation

The industrial EO sterilisation process takes 7 days from preparation of the samples to analysis. Control samples were prepared at the same time as the intervention with the exception of protein adsorption which was added 'fresh' on the day of analysis therefore giving the control samples a theoretical advantage over the intervention samples.

2.2.2.9 Atomic force microscopy (AFM)

AC/tapping mode was used on dried samples mounted with glue onto glass slides. AFM was carried out using a JPK Nanowizard 4 (JPK Instruments), in air using a tip resonating at 75kHz with a force constant of 3 N/m (RFESPA-75 Material 0.01-0.025 Ohm-cm Antimony (n) doped Si, Cantilever: T=2.8µm, L: 225 µm, W: 35 µm, f₀: 75kHz, K: 3N/m, Bruker). The phase signal was set 0 and a resonant frequency 5-10% lower than the resonant frequency. Images were analysed using Nanowizard (version 5 for Linux). Representative images were obtained for height, phase and error signals.

2.2.2.10 Enzyme linked immunosorbent assay (ELISA)

2.2.2.10.1 Fibronectin domains: growth factor binding domain (P5F3) & cell binding domain (HFN7.1)

3 samples representing each condition were incubated in 1% BSA in DPBS for 30 minutes as a blocking buffer, then incubated with the primary antibody in Dulbecco's Phosphate Buffered Solution (DPBS) for 60 minutes at room temperature (1:2000 in 1% BSA/DPBS for P5F3 and 1:330 in 1% BSA/DPBS for HFN7.1). Samples were then washed with 0.5% Tween20 in DPBS 3 times before incubation with the conjugated secondary antibody (1:10000 horseradish protein anti-mouse IgG product 62-6520 in 1% BSA/DPBS) for 60 minutes at room temperature in the dark. The samples were again washed 3 times with 0.5% Tween20 in DPBS and transferred to new 24 well plates and incubated with the substrates in the dark (Color Reagent A - Stabilized Peroxide Solution, lot P100349, Part No. 895000. Color Reagent B -Stabilized Chromogen

Solution, lot P100353, Part No. 895001). After 20 minutes, N sulfuric acid (lot P100333, Part No. 895032) was added as a stop solution. Triplicates of 100 µl of the solution of each sample were added to high binding flat bottomed 96 well plates (Costar, Corning, Maine USA) and absorbance measured by a plate reader using Skanit (software version). The plate underwent a 5 second constant medium velocity shake then absorbance was measured at 450 nm and 570 nm. The 570 nm reading was subtracted from the 450 nm reading to normalise for visual imperfections in the plates and a mean of the 9 readings per condition (3 readings for each of the 3 samples per condition) were plotted.

2.2.2.10.2 Direct BMP-2

To evaluate the effect of the sterilisation process on BMP-2, 6 groups were used (Table 8).

<i>Sample No.</i>	<i>PEA type</i>	<i>Intervention</i>
1	Plasma	EO Sterilisation
2	Spun	EO Sterilisation
3	Plasma	1-week room temperature
4	Spun	1-week room temperature
5	Plasma	Nil (control)
6	Spun	Nil (control)

Table 8 -Samples tested to establish effect of EO process on BMP-2 availability. All samples had PEA adsorbed as detailed, then fibronectin adsorbed and dried prior to final adsorption of BMP-2.

Both plasma polymerised and spun PEA had FN and human BMP-2 adsorbed in order to test the resilience of a complete growth factor presenting system to EO sterilisation. In order to account for potential degradation of BMP-2 over the 1-week sterilisation duration, control samples were engineered on the same day as the intervention samples in addition to fresh samples on the day of analysis.

After FN was coated at 20 µg/mL for 1 h, the surfaces were blocked with heat inactivated 1% BSA/DPBS for 30 min, followed by adsorption of 50ng/ml BMP-2 (355-BM, R&D Systems) in DPBS for 1 h. Unadsorbed FN and BMP-2 was kept for BCA and ELISA analysis respectively. The surfaces were washed and blocked again with 1% BSA for 30 min. Next, primary antibodies against BMP-2 (ab14933, rabbit polyclonal, 1:2000, Abcam) were added onto the surfaces and incubated for 1 h.

After washing for 3 × 5 min with 0.5% Tween in PBS (5 mins agitation per wash), a biotinylated anti-rabbit antibody (BA-1100, 1:10000, Vector Laboratories) was added onto the surfaces and incubated for 1 h. The samples were then washed again for 3 × 5 min with PBS, and a streptavidin-HRP solution (DY998, R&D Systems, lot 293996) was added and incubated for 20 min. After a final 3 × 5 min wash with Tween PBS, the samples were transferred to a clean 24 well plate and a substrate solution was added onto the surfaces and the samples were incubated in the dark for 20 min, followed by the addition of a stop solution. Triplicates of the resultant coloured solution were placed into a low bind 96 well plate. The absorbance of the coloured solution was read at 450 nm and 540 nm and the data was used to determine the relative adsorption of BMP-2. All preparations were performed at room temperature.

2.2.2.10.3 Normalisation ELISAs

Following preparation of samples for sterilisation or controls, the supernatant was removed and stored at -80°C. Each sample has variations in surface topography and area, thus variations in the amount of FN adsorbed onto each surface varies. In order to account for this potential variation in mass of fibronectin (and subsequent BMP-2) adsorbed, normalisation was undertaken using analysis of this supernatant following incubation period. For fibronectin adsorption a bicinchoninic acid assay (BCA) was undertaken and for unadsorbed BMP-2, a sandwich ELISA was undertaken.

Fibronectin - Bicinchoninic acid assay (BCA)

A working solution comprising reagent A, B and C were mixed at room temperature with a ratio of 25:24:1. 100 µl of unadsorbed fibronectin were thawed to room temperature from -80°C and added to 50 µl of PBS (tablet) in a 96 well plate. A fresh sample of fibronectin was mixed to a concentration of 20mg/ml and used to make a standardisation curve as per manufacturer's instructions (40 µg/ml, 20 µg/ml, 10 µg /ml, 5 µg /ml, 2.5 µg /ml, 1.25 µg /ml, 0.025 µg /ml, 0.312 µg /ml, 0.156 µg /ml, 0.078 µg /ml). 150µg of the working reagent was added to each sample (including standardisation samples) and incubated for 2 hours. Following incubation, the samples were cooled to room temperature and placed in a photospectrometer (Multiskan FC, ThermoFisher) and analysed using SkanIt (version 4.1 for Windows). A 5 second orbital shake was performed with a 1mm amplitude and absorbance was measured at 562nm.

Points were plotted to create the standardisation curve using a scatter graph and a polynomial trend line plotted. This trend line was used to calculate the mass of FN adsorbed for each sample and divided by volume per sample giving the mass adsorbed onto each glass slip.

BMP-2 sandwich ELISA

The capture antibody was diluted in PBS (tablet) and used in 100 µl aliquots to coat the inside of a 96 well plate and incubated overnight in a 96 well plate at room temperature. The wells were then washed 3 times with a wash buffer with evacuation of wash buffer between steps using suction. The wells were then blocked using 300 µl of reagent diluent and incubated at room temperature for 1 hour. Three further washes were completed before adding 100 µl triplicates of each sample, and additional concentrations of BMP-2 at 3ng/ml, 1.5 ng/ml, 0.75 ng/ml, 0.375 ng/ml, 0.188ng/ml, 0.0938 ng/ml, 0.0469 ng/ml and 0ng/ml to form a standard curve for the given BMP-2 under typical conditions for this experiment. The plate was covered with an adhesive strip and incubated at room temperature for 2 hours. The wells were washed once again 3 times with wash buffer before addition of 100 µl of detection antibody

to each well. Another 2 hour incubation at room temperature was performed and a triple wash performed again. 100 µl of Streptavidin horse radish protein was added to each well and incubated at room temperature in the dark for 20 minutes. Triple wash was repeated and 100 µl of substrate solution was added to each well and incubated for 20 minutes in the dark before addition of 50 µl of stop solution. The plate was tapped to mix, and the plate placed into a spectrophotometer for analysis of absorbance at 450 nm with wavelength correction at 570 nm.

The standardisation curve was plotted using a scatter graph with a polynomial trend line. The graph equation was then used to accurately plot each of the absorbencies to give a BMP concentration for supernatant. Taking into account the varying volumes of supernatant, this was deducted from the known concentration and volume added during the preparation phase and the resultant mass of BMP-2 was calculated.

The mean mass of BMP-2 adsorbed between conditions was compared statistically to account for any variation in end result (direct BMP-2 ELISA and cell differentiation analysis).

2.2.2.11 EO residual testing

Triplicates of spun PEA and PMA were prepared as per 3.1.2.2.1 and plasma polymerised PEA as per 3.1.2.2.3. Samples were sterilised using lower temperature EO. Following the aeration phase of the EO process, samples were temporarily frozen at -20°C until testing setup was prepared. Extraction time was kept to a minimum to avoid escape of EO from the sample, as mandated in ISO10993-7.

Routine extraction was undertaken using an emersion technique in a gas tight container into which deionised water was added to fill the container to 90% its capacity. The container sealed and incubated at 22°C overnight. 1ml of the extraction solution was transferred to a vial using a calibrated pipette. Gas chromatograph testing was performed using a Perkin Elmer Gas Chromatograph following procedure W177, Medistri SARL (Domdidier, Switzerland).

2.2.2.12 X-ray photoelectron spectroscopy (XPS)

10 replicates of spun PMA were sterilised using EO and 10 replicated of non-sterilised PMA were analysed. XPS data collection was performed at the EPSRC National Facility for XPS ('HarwellXPS'), operated by Cardiff University and UCL, under contract No. PR16195. X-ray photoelectron spectroscopy (XPS) was performed on a Thermo Fisher Scientific NEXSA spectrometer fitted with a monochromated Al $K\alpha$ X-ray source (1486.7 eV), a spherical sector analyser and 3 multichannel resistive plate, 128 channel delay line detectors. All data was recorded at 72W and an X-ray beam size of 400 x 200 μm . Survey scans were recorded at a pass energy of 200 eV, and high-resolution scans recorded at a pass energy of 50 eV. Data was recorded at pass energies of 200 eV for survey scans and 50 eV for high resolution scan with 1 eV and 0.1 eV step sizes respectively. Electronic charge neutralization was achieved using a Dual-beam low-energy electron/ion source (Thermo Scientific FG-03). Ion gun current = 150 μA . Ion gun voltage = 45 V. All sample data was recorded at a pressure below 10^{-8} Torr and a room temperature of 294 K. A take-off angle of 90° to the surface was used.

Results were compared to archived XPS results for spun PEA and compared to published values (3). Changes in peak position and areas under peaks were calculated using CasaXPS (v2.3.19 for Windows, Casa Software LTD).

2.2.2.13 Water contact angle (WCA)

Two sets of triplicates of plasma PEA, spun PEA and spun PMA were prepared as per the protocols detailed in 3.1.2.2.1 and 3.1.2.2.3 and placed in polystyrene 24 well plates. One set was sterilised using EO and the other kept at room temperature. Samples were analysed using an Attension Theta Optical Tensiometer (Biolin Scientific, Gothenburg, Sweden) and Attension v2.2 analytical software. Young-Laplace surface tension modelling used ($\gamma_{sv} = \gamma_{sl} + \gamma_{lv} \cos\theta_v$). Static contact angles (SCA) were calculated using 3 μl of milliQ

dispensed at 1 $\mu\text{l/s}$ with video recording of 30 frames per second, droplet deposition 90 degrees to the surface. Once initial droplet stability was excluded, the mean of left and right sided angles was averaged over a minimum of 15 seconds. The needle was then advanced into the droplet and milliQ water infused until the contact points of the droplet moved, with the advancing angle defined as the was defined as the last contact angle measured before movement. Receding angle was calculated by subsequent withdrawal of fluid until contact points again moved, with receding angle defined as the last contact angle measured before movement. Contact angle hysteresis was then defined as the advancing angle minus the receding angle ($\theta_A - \theta_R$).

2.2.2.14 Cell differentiation analysis

This experiment was performed in 2 runs with C2C12 mouse myoblasts, with passage number 3 for samples with FN adsorbed pre-sterilisation and passage 4 for samples with FN adsorbed post-sterilisation. The method was well established within our laboratory and is used to evaluate biocompatibility of materials. Cells were added to a media of modified DMEM (4.5 g/l glucose + L-glutamin + pyruvate) with 20% FBS and 1% antibiotic solution (penicillin & streptomycin) in vented flasks for 5 days with change of media after 3 days, until a confluence of >70% was achieved. Although samples were maintained sterile from the EO process, prior to addition of cells they were placed alongside controls in a class 2 sterile hood under UV light for 15 minutes placed in a 24 well plate. Cells were washed with DPBS and trypsinised using trypsin/EDTA. The cells were resuspended in media with 1% ITS and cultured in the 24 well plates for 5 days with media changed after 3 days.

At the end of the 5 day period the media was removed, samples were washed with DPBS and fixed with 4% formaldehyde in DPBS in 4°C for 30 minutes. The formaldehyde was washed off twice with DPBS and cells were permeabilised with 0.1% triton X-100 solution in DPBS for 5 minutes. The samples were washed with DPBS and a blocking buffer (1%BSA and 0.5% Triton/DPBS) was added as a blocking buffer for 30 minutes at room temperature. The samples were incubated in the primary mouse anti-myosin

antibody (MF-20) diluted to 1:200 in 0.5% BSA for 60 minutes at room temperature. Two washes with 0.5% Tween 20/DPBS were performed and then a further 60 minutes of incubation with the secondary antibody (Cy3 anti-mouse) dilution. Two washed with 0.5% Tween 20/DPBS were performed and then a further 60 minutes of incubation at room temperature in the dark with the secondary antibody (CY3 anti-mouse) diluted to 1:250 in 0.5% BSA. The samples were washed 3 final times before mounting the samples using a drop of mounting media with DAPI (nuclear stain) and a coverslip.

Fluorescence microscopy was performed using a Zeiss Z1 AX10 and MicroManager (version 1.4 for windows, Open Imaging Inc, UCSF). Using x10 magnification, 4 regions in each of 3 samples per condition were selected at random and a DAPI filter then DSRed filter used to capture nuclei and corresponding myotubes respectively. Interactive Learning and Segmentation Toolkit (ilastik, v1.2.2 for Macintosh , open source) was used to create a segmented binary area images of the myotubes and using Fiji Image J (v1.52i for Macintosh, open source, National Institutes of Health, USA) the mean number of nuclei underlying myotubes was calculated as an indicator of cells differentiating on the sample.

2.2.3 Statistical analysis

For non-inferiority sampling, experience in the analysis of FN and BMP dictates that rejection of the null hypothesis (the addition of these proteins has no effect) has been observed with triplicates of each condition. Therefore, unless specified otherwise, sampling has been performed in triplicates.

Data was analysed using Graphpad Prism (version 6 for Macintosh, GraphPad Software, La Jolla California USA) with normal distribution tested using the Shapiro-Wilk normality test then comparison of means carried out using t-test or Mann-Whitney U test for parametric and non-parametric data respectively. Where multiple comparisons were performed an ANOVA analysis or Kruskal Wallis test was used for parametric and non-parametric data respectively, with application of Bonferroni or Dunn's correction for incidental significance. A p-value of <0.05 was considered statistically significant.

2.3 Results

2.3.1 Atomic force microscopy (AFM)

Fibronectin conformation and fibrillogenesis was qualitatively assessed using atomic force microscopy at random areas throughout the samples. In the ‘ac tapping’ mode used, AFM visually represents 3 modes of interaction between a material surface and the machine tip; height, phase, error. Height measured is the topographical changes (peaks and troughs) on the samples and is measured in nanometres. Phase gives information on material properties by representing interactions between the tip and surface (e.g. stiffness, electrostatic) and is measured in degrees. Error notes a difference in signal on material as the tip taps back and forward across the samples, measured in millivolts. The presence of interconnecting fibrils with height in the order of several nanometers, throughout the surface confirms FN fibrillogenesis. Networks were shown (on height, phase and error measurement) as previously demonstrated on spun PEA samples (glass and PCL, figures 14 & 16 respectively), no visible networks as expected on plasma PEA samples (glass or PCL, Figure 15 & 17 respectively). There were however networks present on sterilised PMA which was not anticipated (Figure 18) (176). This was repeated with newly prepared PMA and fibronectin to confirm fibrillogenesis. Based on the results of this new behaviour of PMA, surface chemistry analysis was undertaken using XPS and water contact angles. PCL scaffolds were imaged with difficulty (Figure 19), and as previously, no FN network was detectable. Spray PEA (Figure 20) on PCL scaffolds, however, were visible, demonstrating the ability of FN to spontaneously form networks on 3D printed (medical grade) PCL, key to future translational applications. Finally, some bone chips were visualised using AFM (Figure 21), however given the instability of the chips and the acute changes in topography, images were limited. Once again, the FN network was not visible.

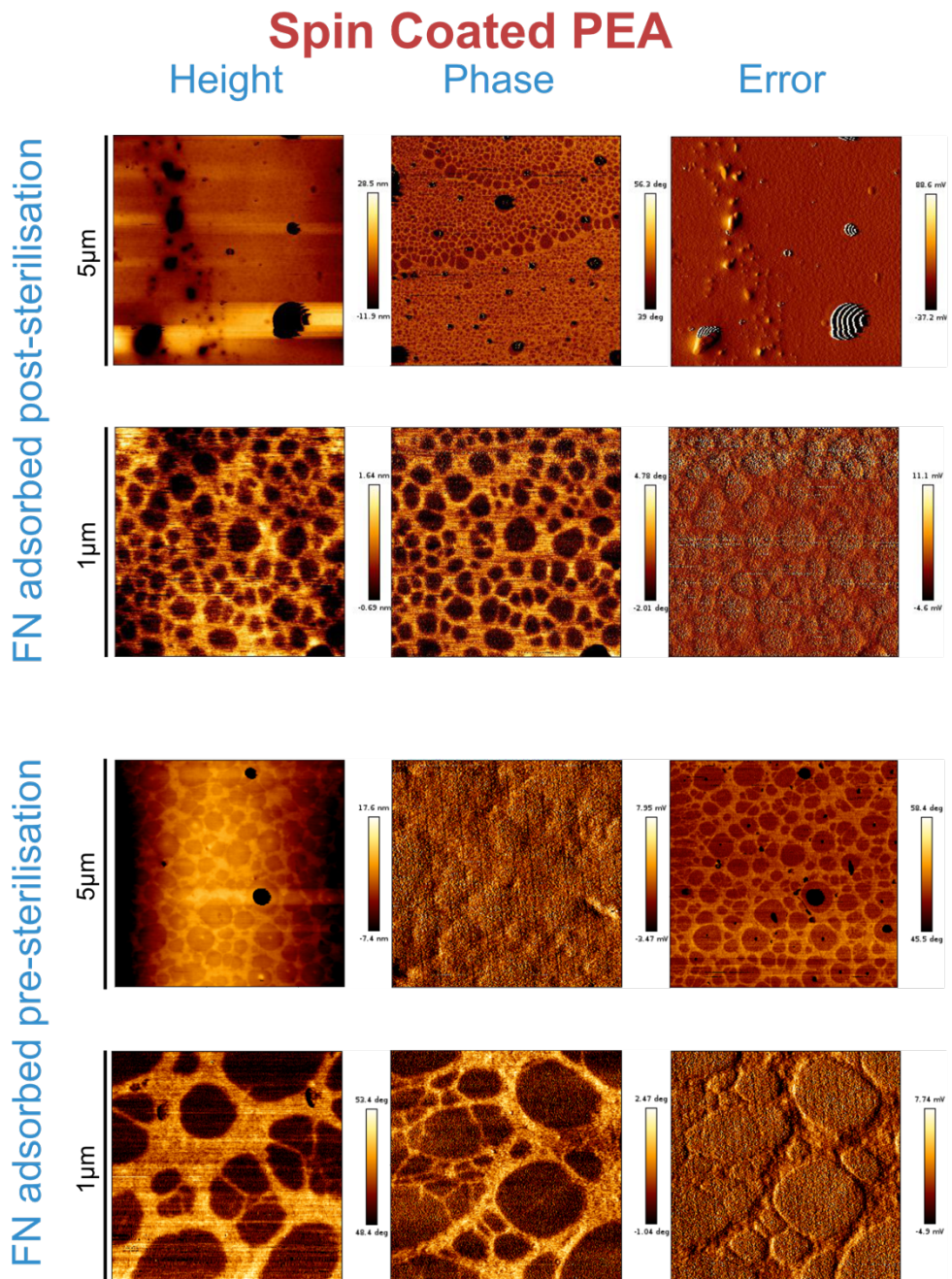


Figure 14 – Height phase and error AFM images of FN adsorbed on spun PEA before and after EO sterilisation. The presence of fibronectin network demonstrates material driven fibrillogenesis on sterilised PEA and resilience of the established protein fibronectin networks to EO sterilisation.

Plasma Coated PEA

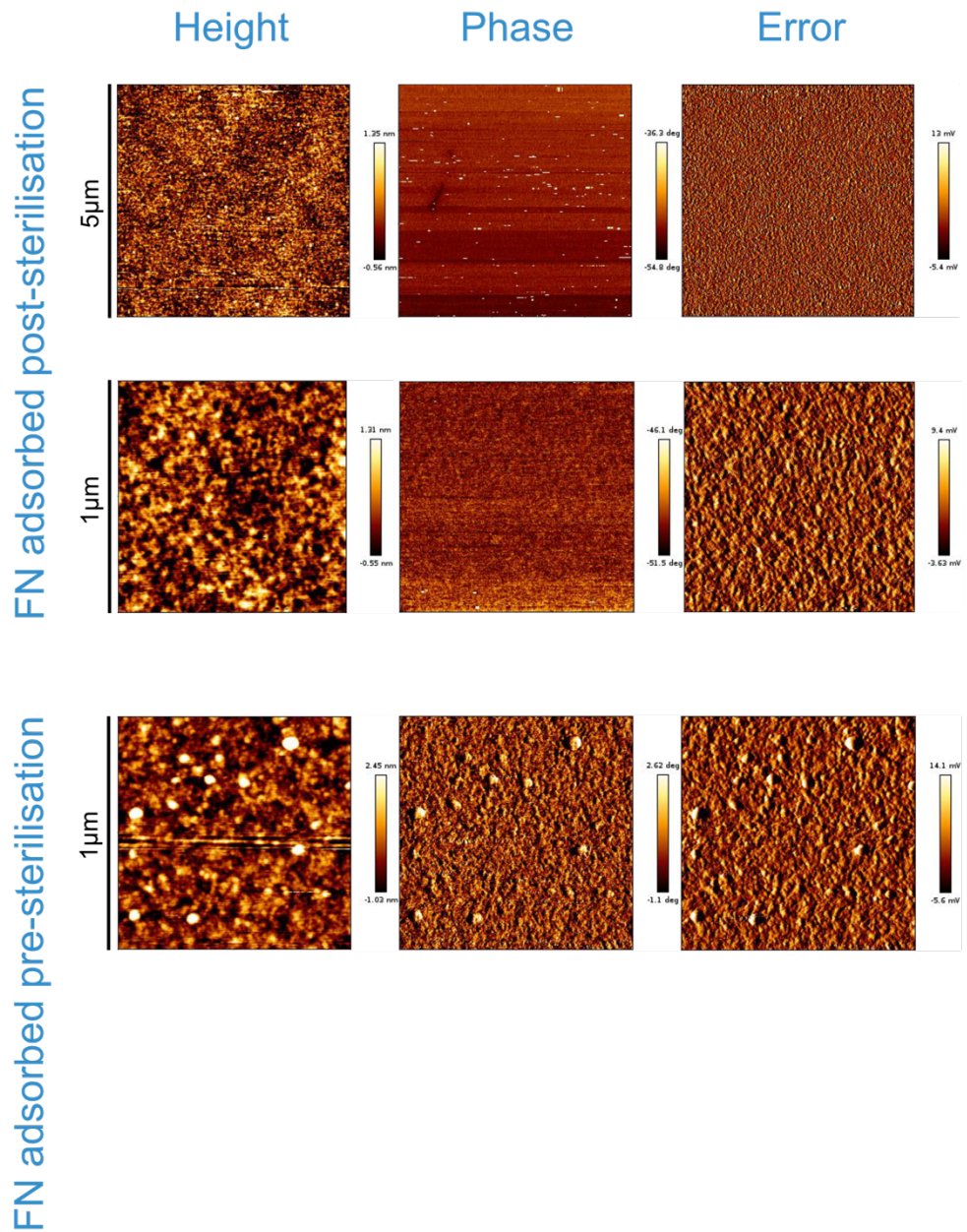


Figure 15 - Height phase and error AFM images of FN adsorbed on plasma PEA before and after EO sterilisation. Whilst no assembled network can be visualised, this has previously been demonstrated to be functionally present and hypothesised to be rough dense networks of FN (6,177). Not meaningful images were obtained at 5 μm .

Spin Coated PCL + Spin Coated PEA

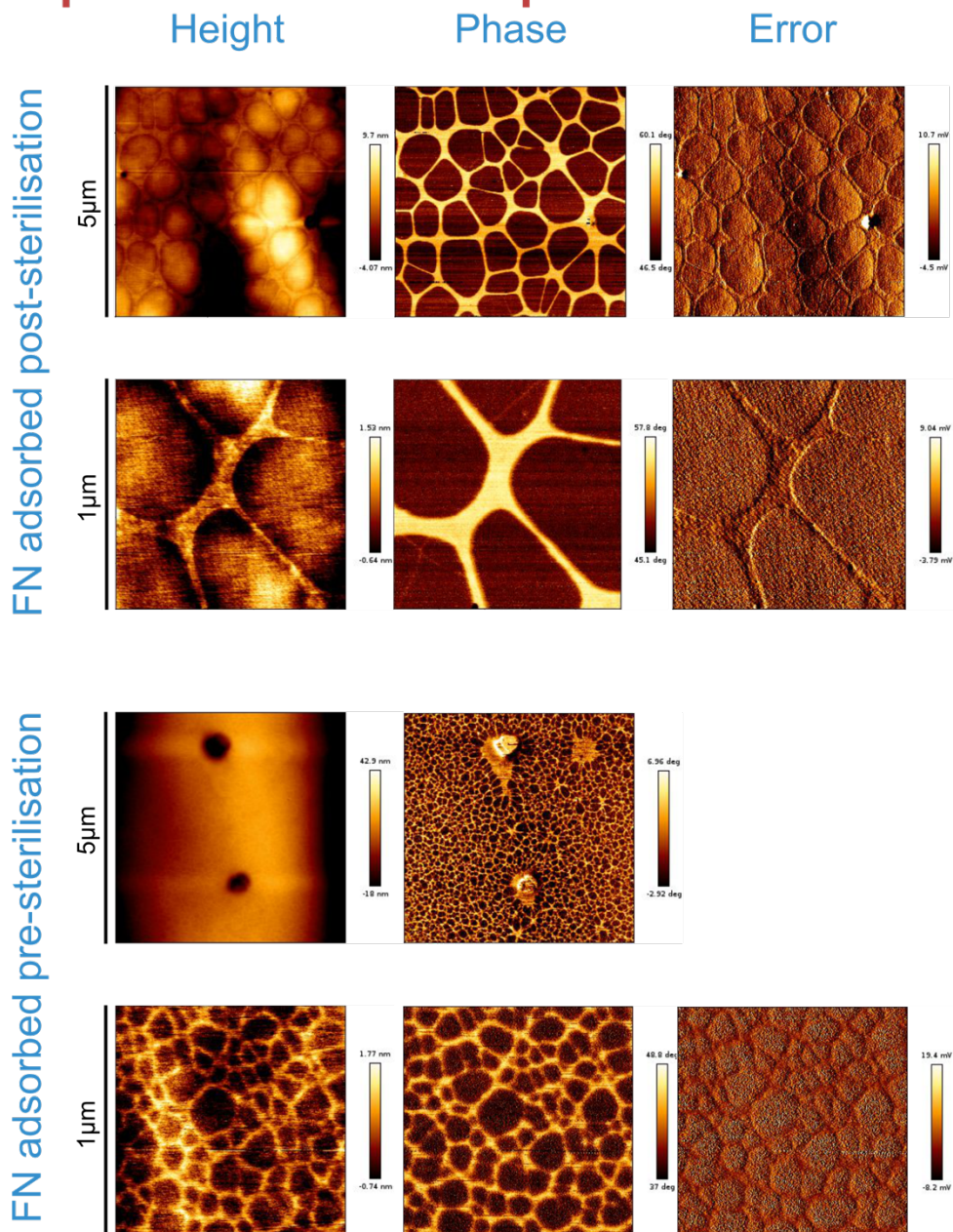


Figure 16 – Height phase and error AFM images of FN adsorbed on spun PCL + spun PEA before and after EO sterilisation. The presence of fibronectin network demonstrates material driven fibrillogenesis on sterilised PEA spun onto a PCL base layer and resilience of the established protein fibronectin networks to EO sterilisation. This condition is particularly useful to ongoing translation, as PCL is a useful biodegradable polymer in tissue engineering.

Spin Coated PCL + Plasma PEA

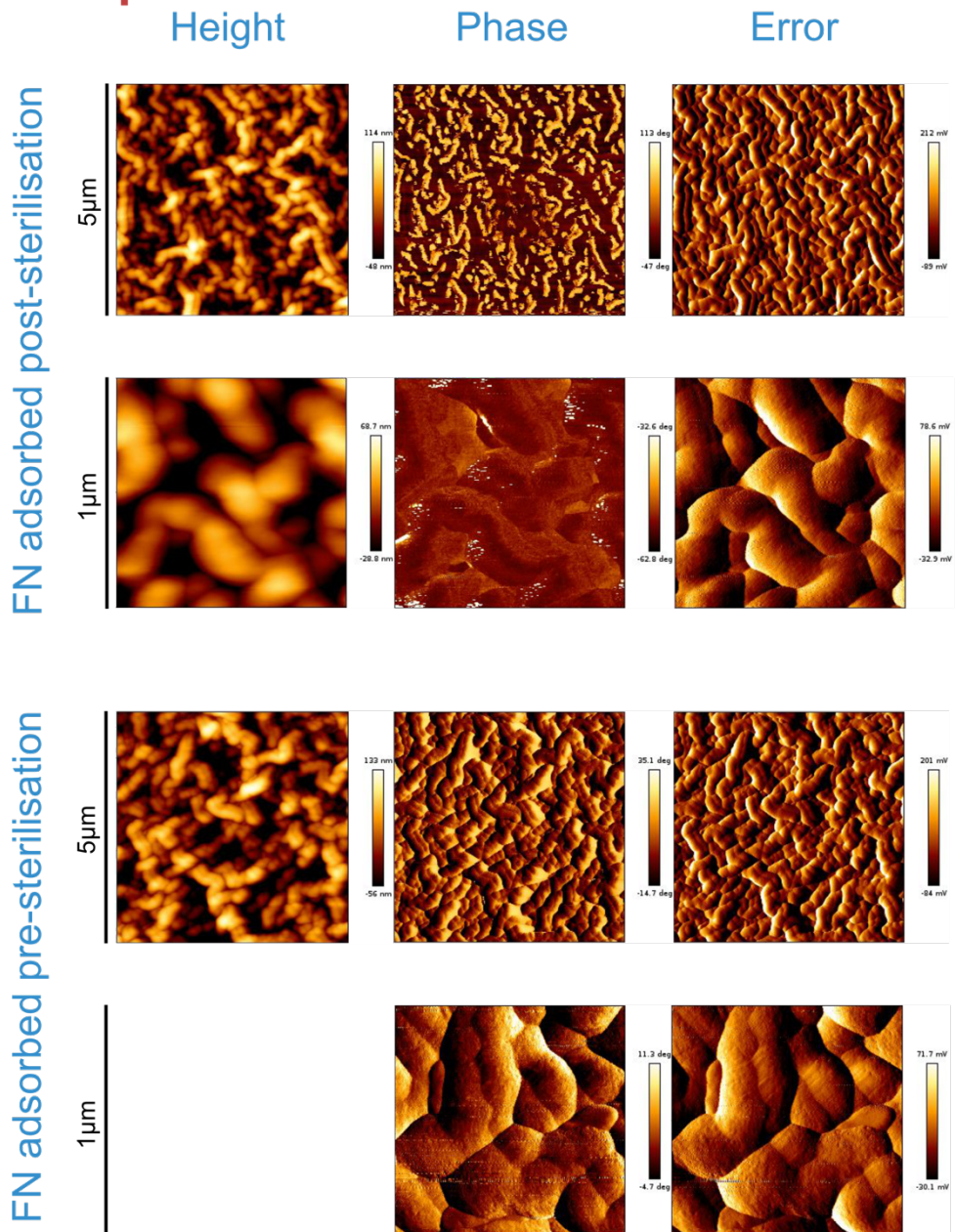


Figure 17 – Height phase and error AFM images of FN adsorbed on spun PCL + plasma PEA before and after EO sterilisation. Whilst no assembled network can be visualised, this has previously been demonstrated to be functionally present and hypothesised to be rough dense networks of FN (6,177).

Spin Coated PMA

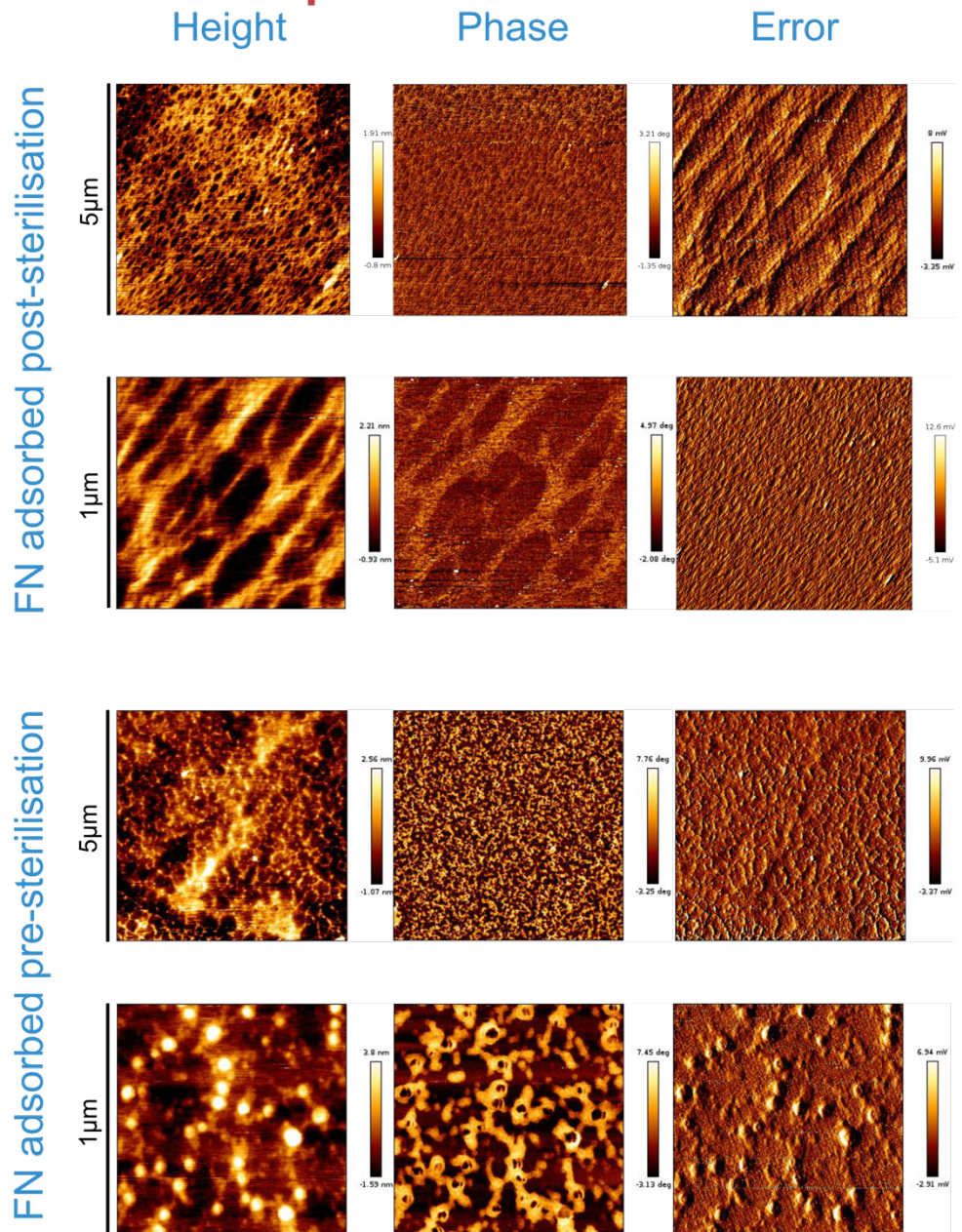


Figure 18 - Height phase and error AFM images of FN adsorbed on PMA before and after EO sterilisation. Typically, FN when adsorbed onto PMA it maintains a globular formation, which is not useful as a GF presenting medium (158,159). This was replicated when FN was adsorbed pre-sterilisation and the globular formation maintained following exposure to the EO process. However repeatedly it was demonstrated that when PMA was exposed to the EO process, and FN was adsorbed post-sterilisation, material driven fibrillogenesis was observed.

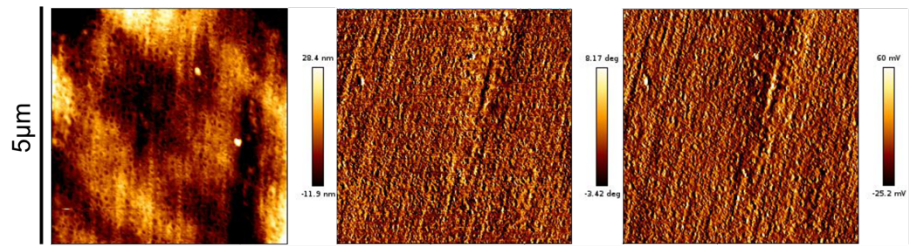
PCL Scaffold + Plasma PEA

Height

Phase

Error

FN adsorbed post-sterilisation



FN adsorbed pre-sterilisation

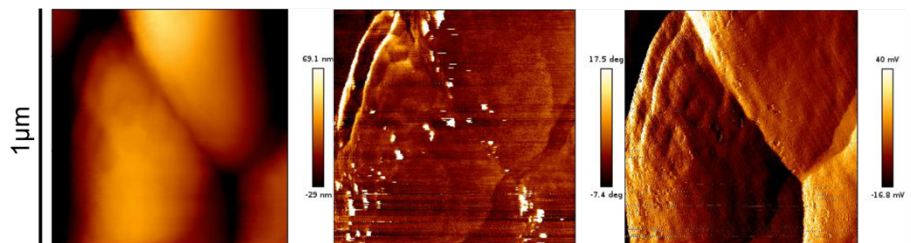
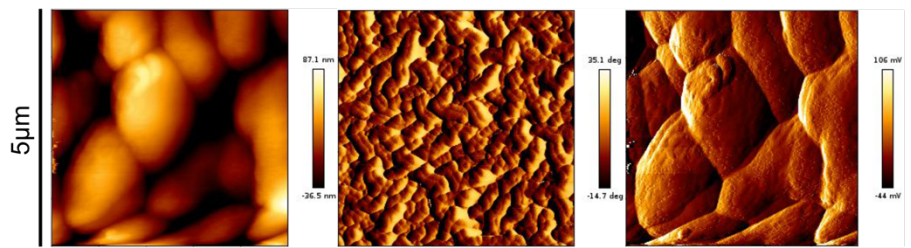


Figure 19 – Height phase and error AFM images of FN adsorbed on a PCL scaffold + plasma PEA before and after EO sterilisation. PCL scaffolds were glued down and were difficult to image due to relatively mobile surfaces. When finally, stable enough to be scanned, no assembled network can be visualised as would be expected with a plasma polymerised PEA network.

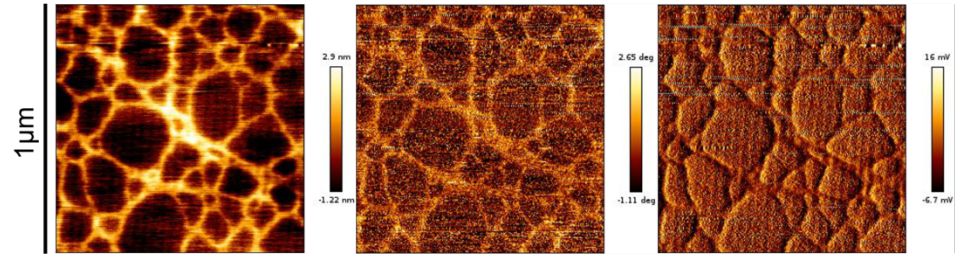
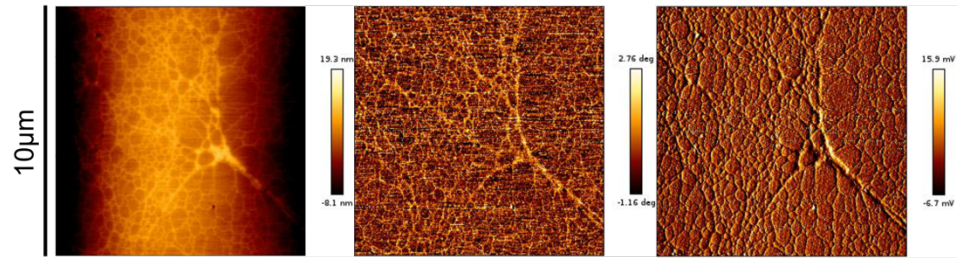
PCL Scaffold + Spray PEA

Height

Phase

Error

FN adsorbed post-sterilisation



FN adsorbed pre-sterilisation

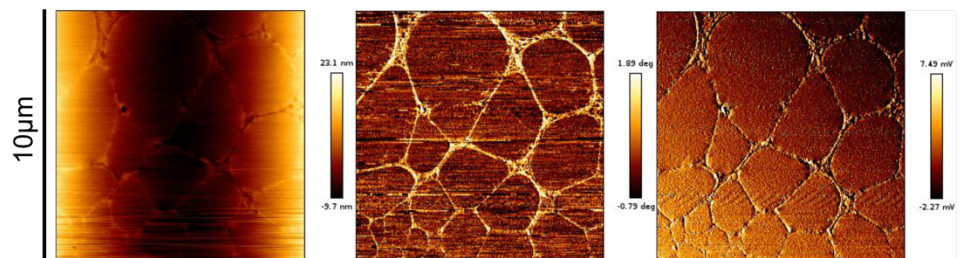


Figure 20 – Height phase and error AFM images of FN adsorbed on a PCL scaffold + spray PEA before and after EO sterilisation. Similar to spun PEA, material driven fibrillogenesis still occurred on sterilised PEA and established FN networks were resilient to EO sterilisation. No meaningful images were obtained at 1 μm.

Bone Chip + Plasma PEA

Height

Phase

Error

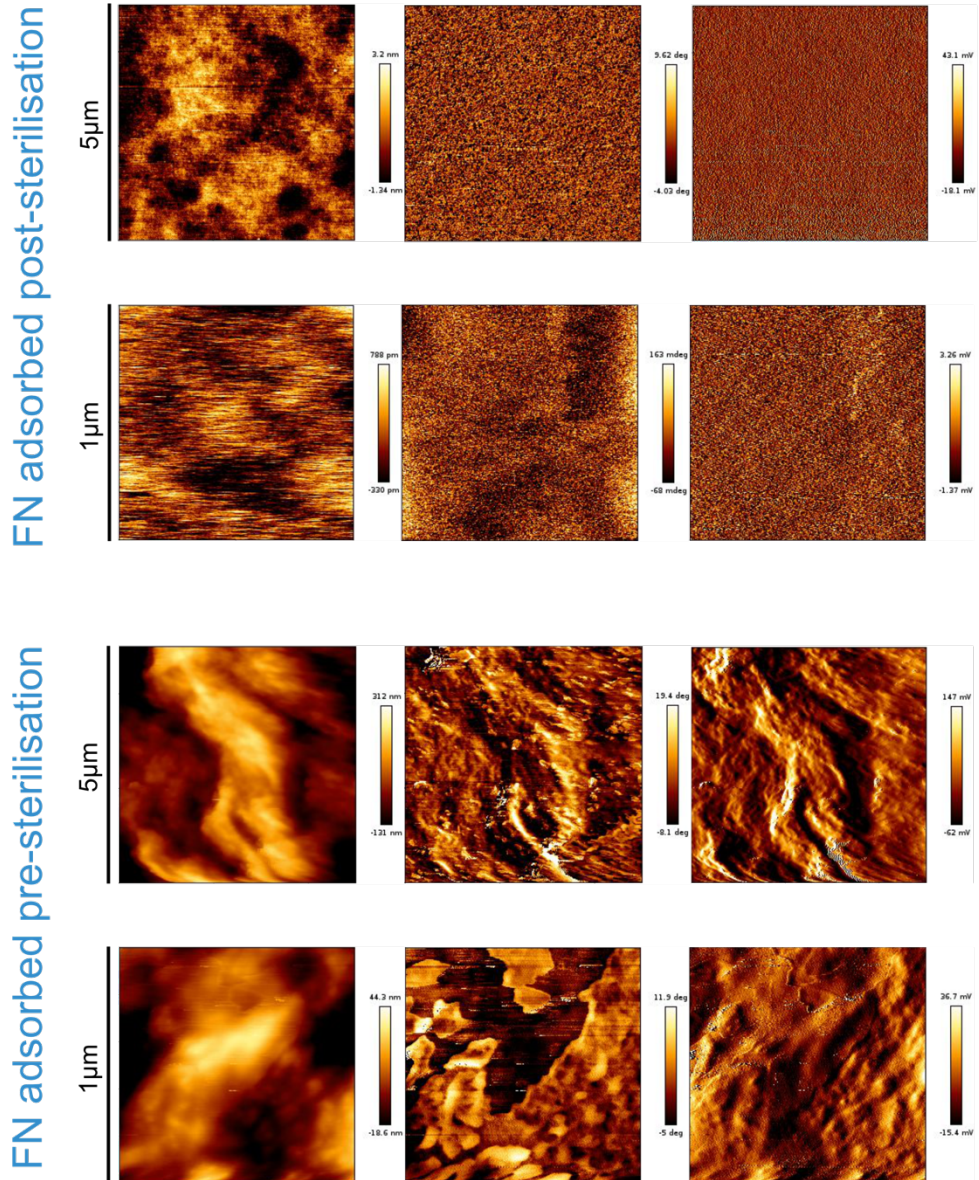


Figure 21 – Height phase and error AFM images of FN adsorbed on a bone chip + plasma PEA before and after EO sterilisation. Gaining stable images of bone chips which are inherently irregular in shape and mobile is difficult and did not show networks following plasma polymerised PEA. The baseline features however are similar to the only published data on AFM for bone chips (160).

2.3.2 Enzyme linked immunosorbent assay (ELISA)

2.3.2.1 – Fibronectin domains

The two relevant domains within the FN complex could be affected by EO sterilisation, the cell binding and growth factor domains. Unavailability of available domain could be due to destruction of the protein or lack of fibronectin network formation (Figure 22). To assess the fibronectin domains available on the networks visualised on AFM (and those not encountered but presumed present for plasma samples) an ELISA was performed. HFN7.1 and P5F3 monoclonal antibodies were directed against FNIII₉₋₁₀ (integrin and cell binding sites) and FNIII₁₂₋₁₄ (growth factor binding sites) respectively.

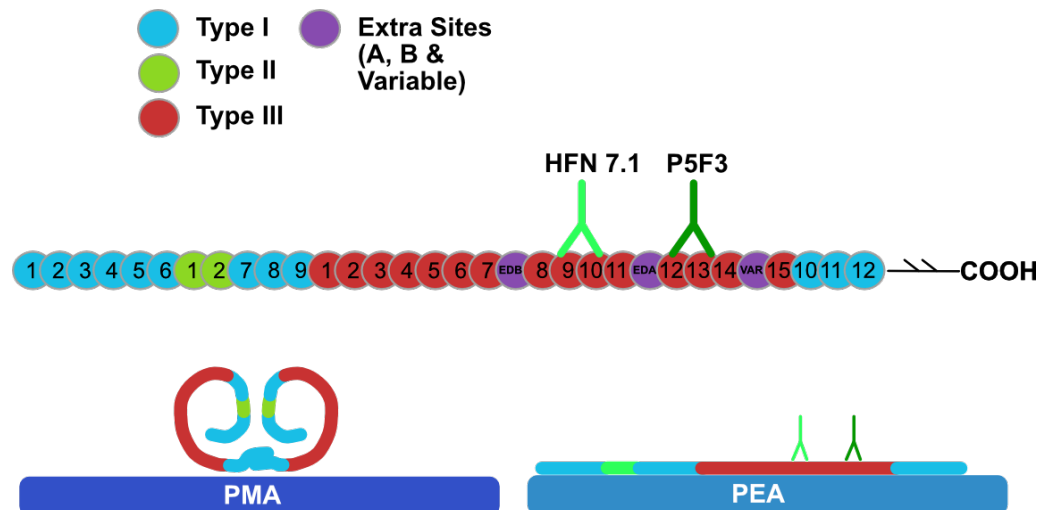


Figure 22 – Schematic of ELISA target sites on fibronectin demonstrating domain type, growth factor binding (P5F3) and cell binding (HFN 7.1) sites. On PMA, fibronectin remains in a curled ('globular') formation resulting in unexposed binding domains, whereas PEA results in unravelling and interconnectivity of fibronectin into networks ('fibrillogenesis') which exposes binding domains which can be evaluated with targeted antibodies.

PMA, spun PEA and plasma PEA had statistically fewer availability of growth factor domains than the glass control however not their matched non-sterilised controls (Figure 23a). Polymers/bone chips coated with FN prior to EO showed no statistical difference between any sample and matched controls for growth factor domain availability. (Figure 23b).

Sterilised polymers/bone chips showed PMA, plasma PEA on glass and scaffold had statistically fewer cell binding domains than glass and their matched controls (Figure 23c). When coated with FN prior to sterilisation PMA and plasma PEA had significantly fewer cell binding domains than controls (Figure 23d). For PMA this is expected due to the globular on FN formation previously demonstrated on PMA (8).

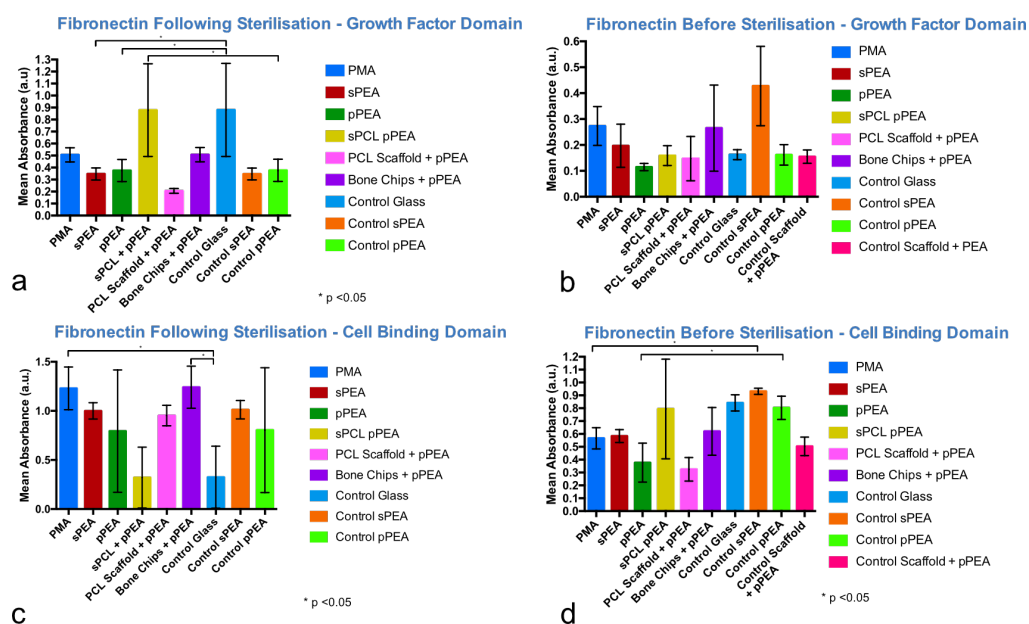


Figure 23 - Mean absorbances. These indicate availability of growth factor binding domain (a&b) and cell binding domain (c&d) for EO prior to fibronectin (a&c) and EO following fibronectin (b&d). Fibronectin adsorbed before sterilisation showed more predictable binding site availability than when base materials were sterilised then fibronectin adsorbed. Of note, the relative availability of cell binding domains on PMA was significantly increased when PMA was exposed to EO. Lines delineated standard deviation.

2.3.2.1.1 – Normalisation of fibronectin adsorbance using BCA analysis

To address any potential difference in number of binding sites due to difference masses of FN adsorbed between samples, the remaining mass of FN was calculated using a BCA quantitative analysis. This confirmed that statistically similar masses of FN were added to each samples (Figure 24a and 24b).

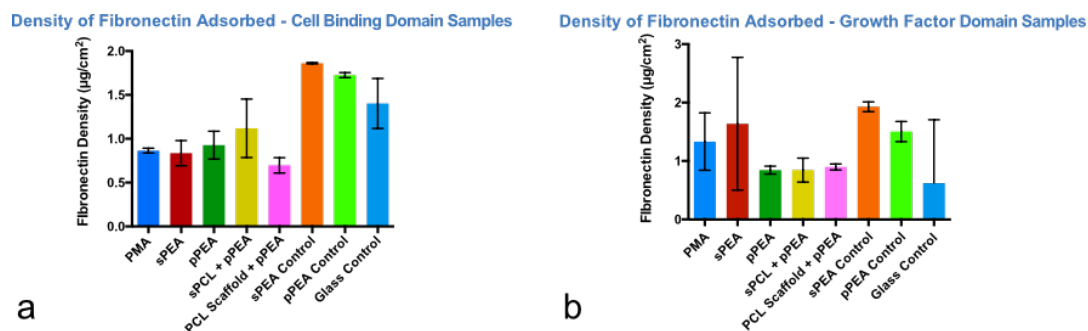


Figure 24 – BCA standardisation of fibronectin density adsorbed onto each sample demonstrating no statistically significant difference in amount of fibronectin adsorbed prior to a) HFN 5.1 or b) P5F3 analysis.

2.3.2.2 - Direct BMP-2 ELISA

As BMP-2 is an individual component of the osteoinductive system, in order to evaluate the effect of the EO sterilisation process on BMP-2 specifically a direct ELISA was performed. Given that the medical grade industrial sterilisation process takes 1 week, a control group which was not sterilised but kept at room temperature was employed to test the hypothesis that degradation of BMP-2 would be related to time rather than EO exposure.

The results demonstrate significantly reduced availability of BMP-2 following 1 week with and without EO exposure, when compared to fresh controls (Figure 25)

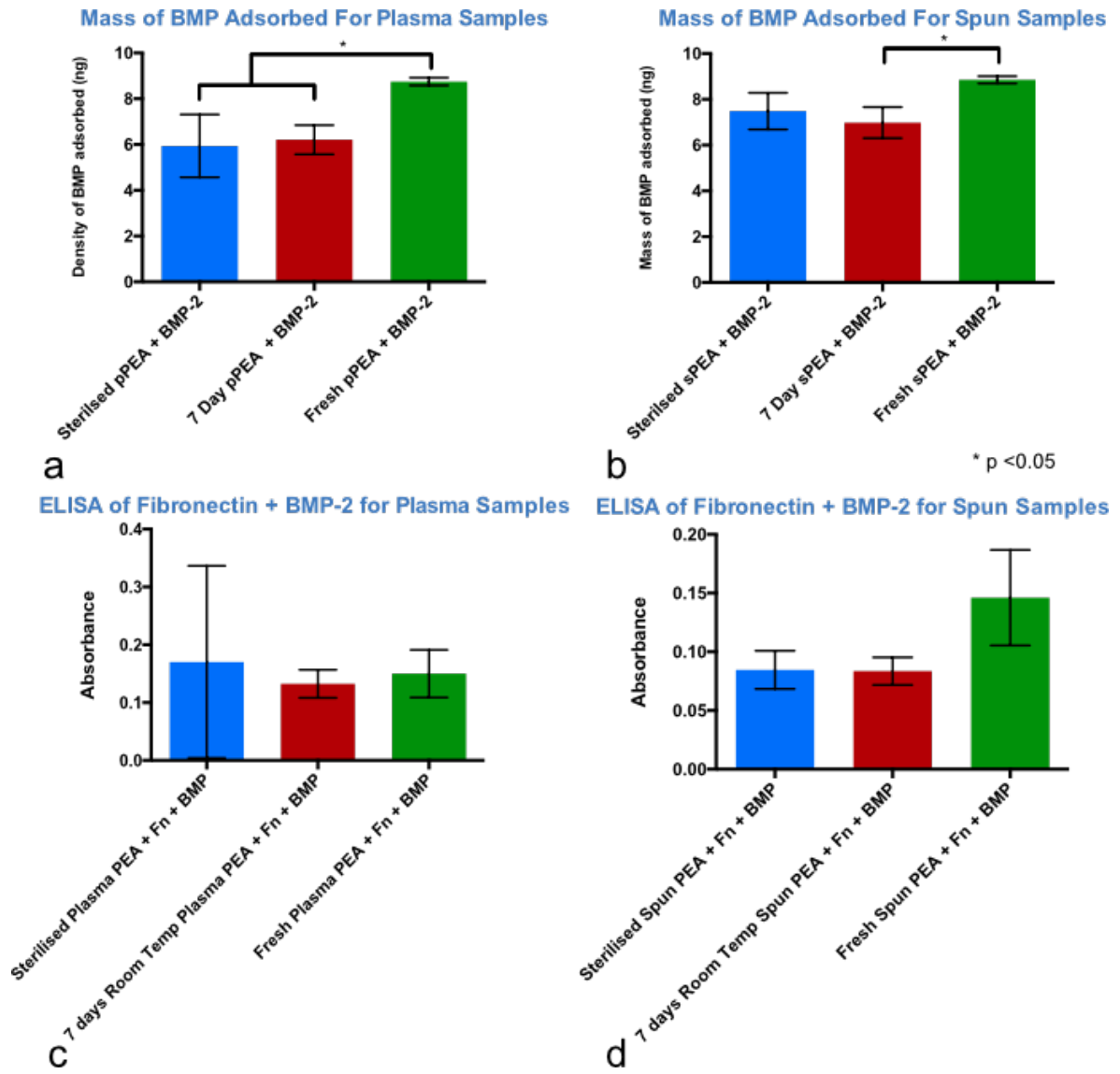


Figure 25 – EO sterilised BMP presenting systems, versus non sterilised systems (7 days at room temperature and freshly prepared samples). Quantification of BMP-2 mass indicated that more BMP-2 was adsorbed onto freshly prepared samples (a & b). Despite this, there was no statistically increased availability of BMP-2 on direct ELISA (c & d). Comparison comparing.

2.3.3 Cell behaviour on EO sterilised surfaces

Given the good availability of cell binding and growth factor domains, the readiness for cells to differentiate upon the sterilised polymers +/- sterilised fibronectin was evaluated. The cell lineage used was C2C12 mouse myoblasts, commonly used for *in vitro* studies as they are precursor cells which only when exposed to the correct physiological cues will differentiate into myoblasts and form (actin rich) fibroblasts. This can be due to their exposure to a soluble drug or physiochemical trigger or GF such a epidermal growth factor (161).

2.3.3.1 Fluorescence microscopy

C2C12 cells differentiation following day 5 culture were visualised with green myosin staining and blue nuclear staining.

In general, there was not a large cell response but adequate for analysis. In keeping with behavioural changes noted previously, PMA which had EO prior to FN adsorption demonstrated myocyte differentiation compared to control and samples which had FN adsorbed prior to EO (Figure 26). PEA, both spun (Figure 27) and plasma (Figure 28) had similar volumes of myocyte differentiation to freshly compared controls. There was a subjective reduction in myocyte differentiation in PCL samples coated with plasma PEA (Figure 25).

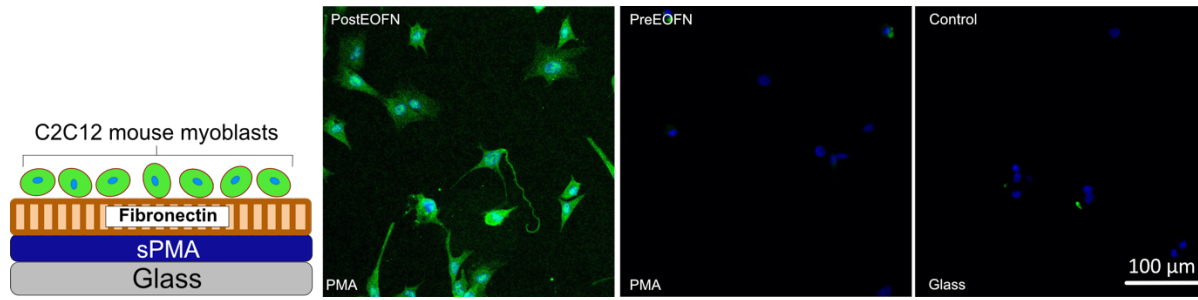


Figure 26 - PMA sterilised before and after addition of fibronectin, then BMP-2 compared to non-sterile glass control. Larger numbers of mature myotubes are demonstrated on PMA surfaces which had been exposed to EO gas prior to adsorption of FN.

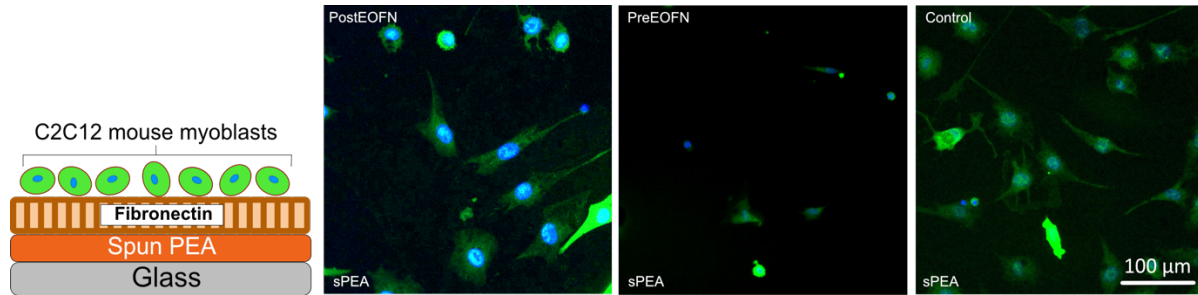


Figure 27 - Spun PEA sterilised before and after addition of fibronectin, then BMP-2 compared to non-sterile sPEA control. Differentiation into myotubes occurred at a similar rate across all 3 conditions

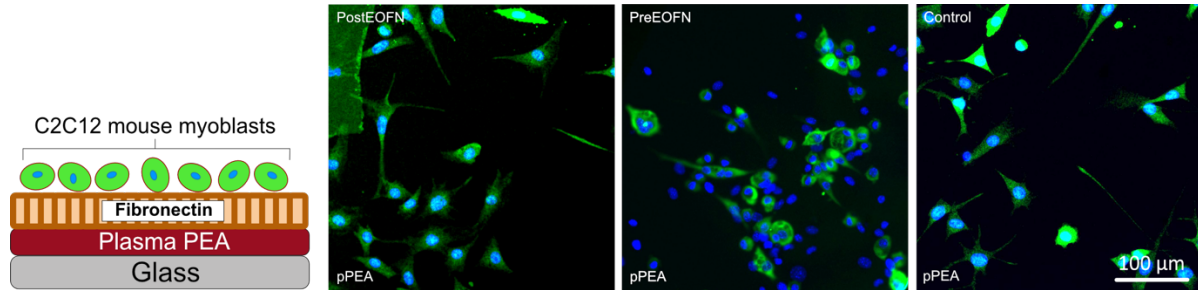


Figure 28 - Plasma PEA sterilised before and after addition of fibronectin, then BMP-2 compared to non-sterile pPEA control. Differentiation into myotubes occurred at a similar rate across all 3 conditions.

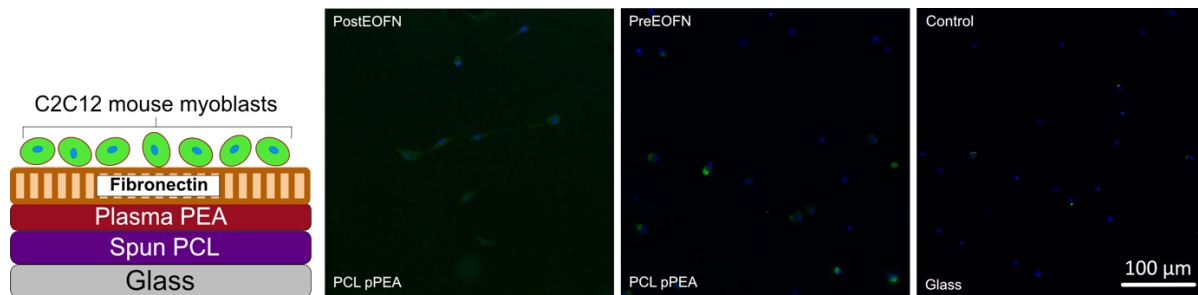


Figure 29 - Spun PCL and plasma PEA sterilised before and after addition of fibronectin, then BMP-2 compared to non-sterile glass control. Differentiation into myotubes at a statistically similar rate across all 3 conditions. Of note, imaging was limited by glare through the thick layers of PCL and PEA.

2.3.3.2 Quantification of myotube formation

Proportion of cell nuclei differentiating into myotubes expressed as a percentage are demonstrated in Figure 30. Fibronectin adsorbed onto unsterilized PMA demonstrated statistically lower rates of cell differentiation rates than PEA samples, which is expected due to the tendency of fibronectin to remain in globular formation on this material. Base materials which were sterilised prior to the adsorption of FN all outperformed glass indicating preferential cell differentiation in response to the inductive coating.

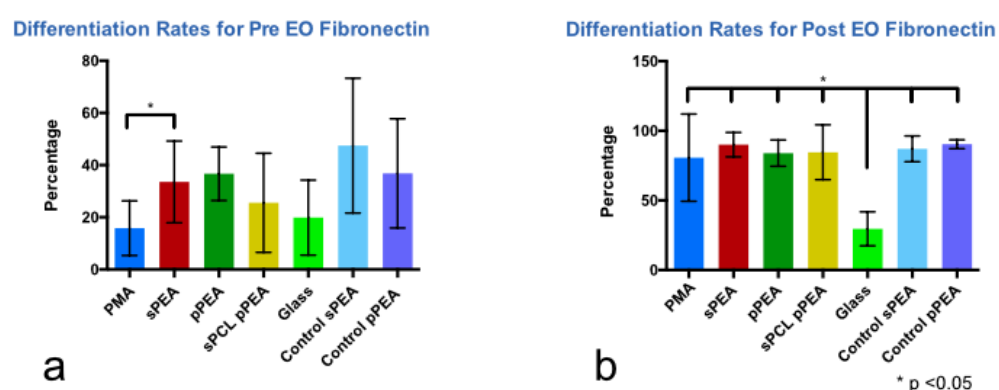


Figure 30 – C2C12 differentiation of EO a) before and b) after adsorption of fibronectin. BMP-2 was adsorbed fresh on all occasions. Sterilised FN had lower differentiation rates on PMA compared to remaining conditions as expected due to the globular conformation of FN. When base materials were exposed to EO prior to addition of FN, they all outperformed the negative glass control, including PMA, further demonstrating a behavioural change in EO sterilised PMA. Bars demonstrate standard deviation.

2.3.4 Understanding changes in PMA behaviour

PMA which was exposed to EO gas unexpectedly demonstrated spontaneous fibrillogenesis rather than maintaining its globular formation. To ensure this was not due to the presence of remaining EO gas, residual testing was undertaken. Furthermore, the surface chemistry of PMA before and after EO sterilisation was commenced using water contact angles and XPS and compared to PEA.

2.3.4.1 Residual EO Testing

The presence of residual EO was hypothesised to potential alter chemistry at the interface between PMA and FN. Therefore, gas chromatography was undertaken after immersion in deionised water demonstrating no remaining ethylene oxide (Table 10).

EO in extract concentration (µg/ml)	EO weight in whole sample (mg)	ECH in extract concentration (µg/ml)	ECH weight in whole sample (mg)
<0.09	<0.018	<6.00	<0.12

Table 9 - Detectable remnants of EO using gas chromatography. The level of residual EO fell below the tolerance of the gas chromatography machine, meaning residual ethylene oxide is unlikely to be responsible for changes in PMA behaviour. *ECH – ethylene chlorohydrin

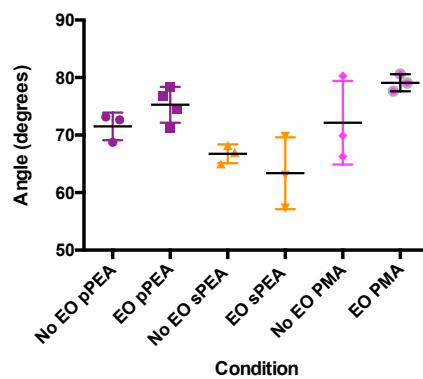
2.3.4.2 Water Contact Angle

An additional reason for the change in behaviour of PMA when exposed to EO gas was a change in surface chemistry. A simple series of water contact angles (WCA), including advancing and receding angles were collected on triplicates of sterilised spun PMA and compared to spun and plasma PEA for reference. Whilst these samples did not reach statistical significance, there was a tendency for the water contact angle to increase in PMA and hysteresis to decrease, of a magnitude not observed in PEA (Table 11 and Figure 31).

Condition	Mean Static Water Contact Angle (degrees)		Advancing Angle (degrees)		Receding Angle (degrees)		Hysteresis	
	No EO	EO	No EO	EO	No EO	EO	No EO	EO
pPEA	71.51	75.27	84.42	74.82	40.62	43.25	43.80	31.56
sPEA	66.75	63.37	107.35	96.97	30.80	33.99	76.51	62.98
PMA	72.14	73.10	96.06	86.86	22.24	33.98	73.82	52.88

Table 10 - Static WCA and hysteresis calculations pre and post sterilisation. No notable changes in mean static angle, with all samples increasing receding angle, reducing both advancing angle and hysteresis.

Water Contact Angles - Pre and Post Sterilisation



Hysteresis - Pre and Post Sterilisation

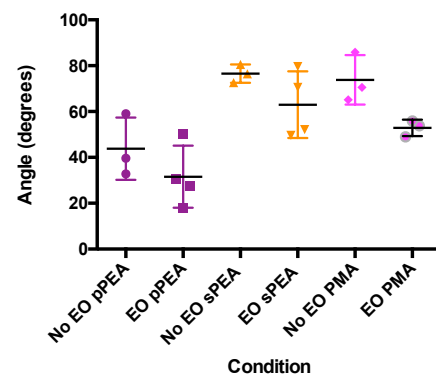


Figure 31 - Graphs demonstrating changes in static WCA and hysteresis with and without EO sterilisation. No significant change between intervention and matched controls (Kruskal-Wallis test, $p > 0.05$)

Examples of static water contact angles of pPEA, sPEA and PMA are demonstrated in Figure 32.

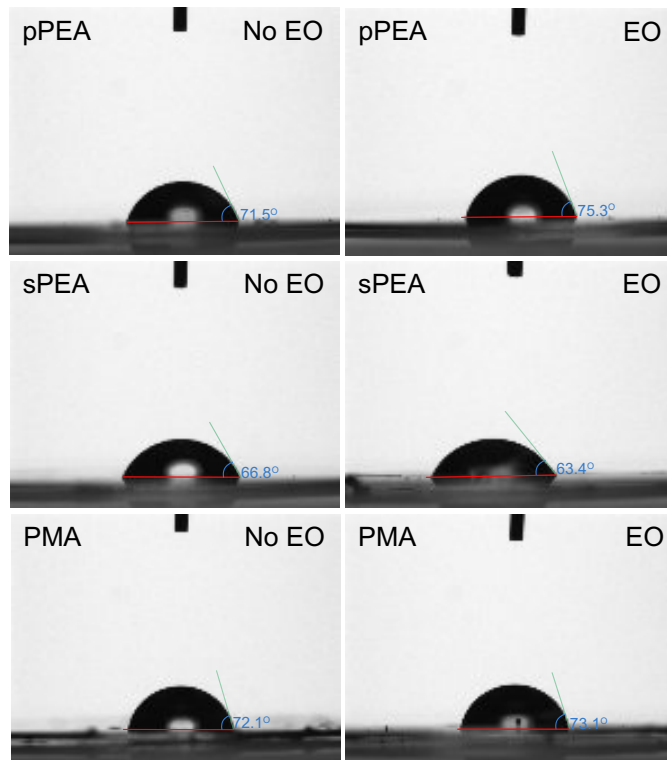


Figure 32 - Static Water Contact Angles. Relatively high angles typical of PEA were noted, less so with plasma PEA due to much thinner and rougher coating.

2.3.4.3 X-ray Photoelectron Spectroscopy (XPS)

The trend in WCA change led to further investigation and quantitative analysis of surface chemistry via binding energy assessment with XPS. This demonstrated a transition in surface chemistry of PMA toward that of PEA following exposure to EO. Exploration of contributing bond types revealed the formation of additional C-C bonds at the expense of C-O bonds (Figure 33).

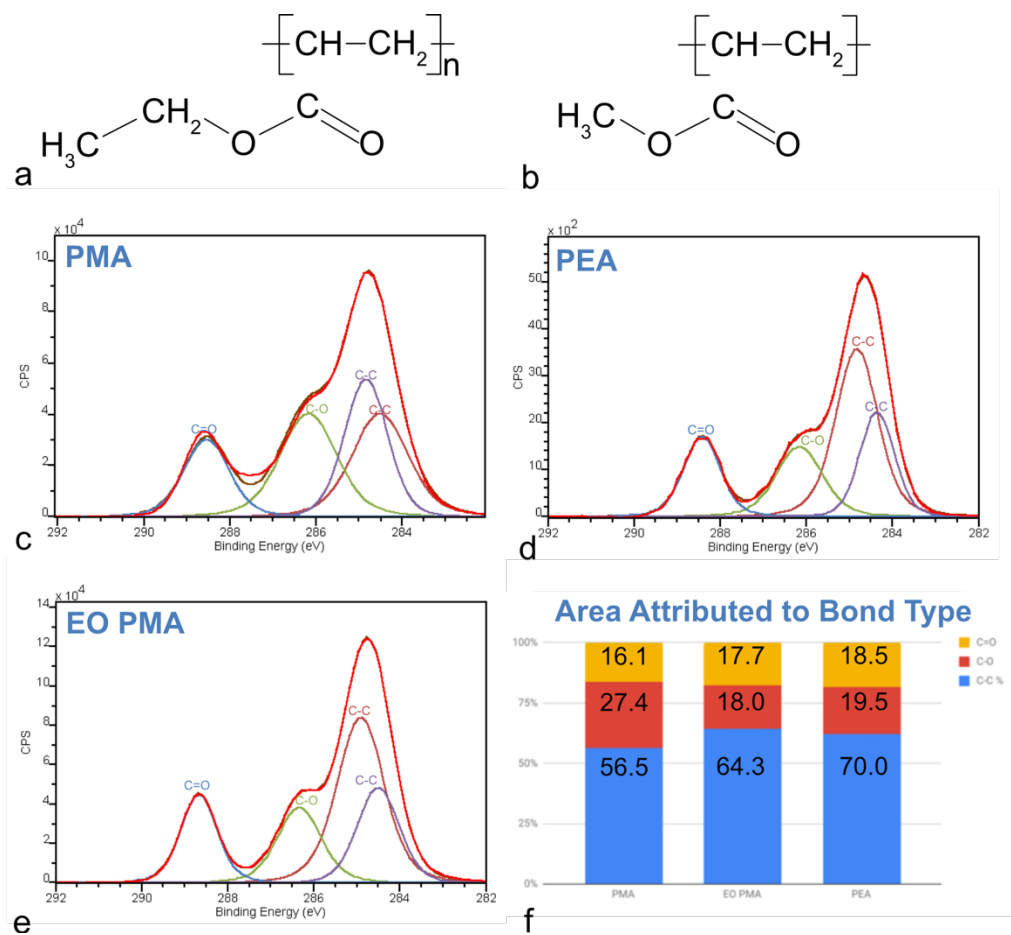


Figure 33 – XPS Analysis. The chemical formulas of a) PEA and b) PMA differ only by a single methylene group. Curves comparing binding energies of c) PMA d) PEA and e) sterilised PMA. The counts per second (CPS) at specific binding energies for recognised bonds are labelled and amalgamated into a net curve (red). Subtle changes in binding energies when PMA was sterilised demonstrated a net curve shape similar to PEA. This could explain the change in behaviour seen when FN is adsorbed onto sterilised PMA. f) The area under each attributable bond type was calculated indicating the EO process affects the net number of C-O bonds to C-C bonds.

The mean areas under curves attributed to each bond type is an established manner of exploring chemical formulae. When compared to the literature, EO sterilised PMA has surface bond energies more similar to PEA than PMA (Table 12).

Condition	Mean Area Under Curve (%)			Expected from database		
	PMA	EO PMA	PEA	PMA	EO PMA	PEA
C-C	56.47	65.31	61.99	52	N/A	62
C-O	27.41	18.02	19.50	25	N/A	21
C=O	16.12	17.68	18.52	24	N/A	18

Table 11 - Mean area attributable to bonds compared to published literature (127). EO PMA is closer in net bond energy type to PEA than PMA

2.4 Discussion

There is limited published data on the effect of EO sterilisation on engineered products designed for bone formation. Doherty *et al* found that a minimum time of 60 minutes EO exposure was required to sterilise demineralised bone, however beyond this duration the structure and osteoinductive features of the bone diminished (178). BMP has had limited investigation into the effects of EO. Reindeer BMP has reduced activity with EO sterilisation when compared to gamma irradiation in 1 study. Finally, a single study on bovine BMP showed no reduction in effect using EO sterilisation (180). There were no major differences in dwell time, temperature or carrier medium (collagen or gelatin) in these studies.

This Chapter demonstrates the resilience of PEA and fibronectin networks to ethylene oxide as a sterilisation technique, remaining effective despite exposure to temperature changes (20-50°C), volatile gas and humidity over a 7-10 period. The particular cycle of sterilisation chosen is on an industrial scale with large capacity and uses low temperature which avoids breaching the melting temperature of PCL. Given the multiple stages of manufacturing of this bioengineered system (base material preparation, polymerisation & addition of PEA, adsorption of FN, addition of BMP-2) and presently unknown commercial manufacturing process, the ideal point at which it would be sterilised is not known. However, PEA has been demonstrated to be stable for long durations once polymerised onto surfaces, therefore is it unlikely that it would be sterilised prior to this step.

The system was tested across a variety of applicable base materials/polymer (Table 13).

Glass	Scaffolds
Spun PMA	PCL Scaffold + plasma PEA
Spun PEA	PCL Scaffold + spray PEA
Plasma PEA	Bone chips + plasma PEA
Spray PEA	
Spun PCL + spun PEA	
Spun PCL + plasma PEA	

Table 12 – Summary of conditions investigated

The same samples were then tested following adsorption of FN networks to test stability of a fibrillose network. AFM was employed to describe surface conformation (2.3.1). ELISA was performed on adsorbed FN networks to demonstrate availability of cell binding/integrin domain growth factor binding domains (2.3.2.1) and BMP-2 presentation (2.3.2.2). Changes in PMA behaviour was noted following sterilisation and evaluated using gas chromatography and surface chemistry analysis (2.3.3). Finally, *in-vitro* cell differentiation confirmed persistent cell differentiation when seeded upon the EO sterilised samples.

AFM is a common method for characterising the surface of protein surfaces and has been used extensively within our research collaboration to visually confirm network formation of fibronectin as it exists *in vivo*. Fibronectin fibril thickness, length and connectivity varies significantly depending upon the surface onto which it is adsorbed.

Previous work has shown that it remains in a globular non-functional formation on unsuitable surfaces such as PMA (Figure 4). Conversely, it spontaneously forms extensive functional networks upon spun PEA several nanometers in thickness. FN on plasma PEA often do not demonstrate fibres on AFM due to

their long thin characters, however, have been demonstrated previously to be present and functional. This is firstly due to the rough topography of plasma PEA making it difficult to distinguish FN from PEA, and secondly due to the dense FN network formed on plasma PEA (6,177). Fibronectin adsorbed onto samples with spun and spray PEA demonstrated network formation following sterilisation of the polymer and persistent network structure following sterilisation. These networks had changes in topology (notably larger fibrils with wider interconnections) which indicate a change in surface interaction between the sterilised polymer and FN. This change in topology was not investigated further given the subsequent retained function of FN demonstrated in ELISA and cell behaviour. FN adsorbed onto non-sterilised PMA remained globular in conformation, however unexpectedly networks were repeatedly seen on FN adsorbed onto sterilised PMA.

ELISA analysis using antibodies directed against the cell binding domain and growth factor domain was employed to assess functionalisation of the fibronectin. The mass of FN adsorbed was compared using BCA analysis (Figure 24) demonstrating no significant difference between mass of FN adsorbed onto samples prior to the ELISA protocols. FN which was added to sterilised base materials (Figure 23) showed cell binding domain activity as expected with PEA samples comparable to positive controls, however again sterilised PMA was able to functionalise PMA with presence of cell binding sites. Growth factor domain activity was less consistent with growth factor domain results, showing strong performance from the negative controls. Sterilised fibronectin networks performed equivocally to positive controls with the exception of PMA and plasma PEA. The globular conformation with PMA is expected to not present domains however the plasma PEA unexpectedly did not present as many cell binding sites as anticipated which may have been a product of lower dose of PEA used than previously published evidence (6). ELISA targeted against BMP-2 was performed on spun PEA+FN+BMP-2 and plasma PEA+FN+BMP-2. Samples were EO sterilised and compared to freshly prepared controls and also samples not undergoing the EO process which were kept at room temperature. This tested the hypothesis that any reduction in BMP-2 presence would be due to time rather than sterilisation. Standardisation

showed that more BMP-2 was absorbed onto the fresh samples which went on to have slightly more BMP available after the 7 day process, however did not reach statistical significance.

Mouse myoblasts were cultured and seeded onto PMA, spun PEA, plasma PEA and spun PCL+ plasma PEA which had been sterilised either before or after addition of FN. After 5 Days cells stained for nuclei and actin demonstrated inferior differentiation of cells upon non sterilised PMA (Figure 30). The other sterilised samples performed statistically similar to fresh controls. When base polymers were sterilised then FN adsorbed, they all encouraged cell differentiation at a higher rate than the negative control and equivocal to the positive controls. Mouse myoblasts were used as to test of cell adhesion, survival, proliferation and function on sterile FN, and are commonly used in our laboratory. Mesenchymal stem cells were considered as an alternative to investigate the effect on this cell type and ultimately function measured by mineralisation. However, the hypothesis being tested was generic cell fate rather than specific cell function, which was adequately answered by the use of these cells, with mineralising MSC function to be explored *in vivo* at a later time point.

As detailed above, once sterilised, PMA formed networks which showed functional domains and drove stem cell differentiation. It was postulated that this change in behaviour of fibronectin on sterilised PMA may be due to remnant ethylene oxide within the sample or due to a change in the surface chemistry as a result of the EO process. Gas chromatography confirmed the absence of remaining ethylene oxide following the sterilisation process. Static water contact angles changed following sterilisation however not significantly so (Figure 31). Interestingly, XPS analysis revealed marked changes in the curve shape and binding energies of PMA following EO sterilisation, such that they bore more of a resemblance to PEA (Figure 33). More carbon backbone (C-C) bonds were seen at the expense of ester (C-O) bonds (Figure 33) resulting in an altered surface chemistry and could explain the spontaneous fibrillogenesis seen with PMA.

2.5 Conclusions

A non-inferiority study is difficult to achieve in a lab setting, in particular with delicate experiments such as ELISAs. However, this Chapter has demonstrated surface characteristics consistent with material resilience to low temperature EO treatment. Furthermore, the networks formed demonstrated function through ELISA and cell differentiation studies, enough to warrant further exploration with *in-vivo* experimentation.

The serendipitous finding of surface chemistry changes with PMA is interesting, but not likely to be of any translational benefit.

Other modes of sterilisation such as autoclave, plasma treatment and ethanol are effective, however are harsher in terms of chemical or heat properties. Similarly, when considering the future clinical 3D applications of polymer-based scaffolds, UV would not penetrate into 'shadows' and gamma irradiation causes crosslinking of polymers. Therefore, this Chapter outlines how ethylene oxide is not just an effective sterilisation technique for this technology, but also a viable method to proceed with in order to meet UK and EU standards for medical devices.

This work has demonstrated sterilisation of polymer and subsequent addition of FN would result in maintained FN network assembly and function. However, this post sterilisation addition of FN would require extra processing steps in a sterile facility. Therefore, given that the adsorption of FN prior to sterilisation demonstrated a maintained functional network, this is a more suitable coating combination for to be sterilised. One outstanding question was whether there would be a measurable difference between binding site availability with sterilised FN on polymer compared to sterilised polymer with subsequent addition of FN. It was, however, decided that from an industrial perspective, the complete polymer and FN combination being sterilised was more suitable, and thus the retained function was satisfactory to draw conclusions upon.

Chapter 3 - *In vivo* analysis of engineered osteoinductive surface coatings applied to decellularised bone chips

3.1 Introduction

A critical sized bone defect is an absence of bone which will not heal spontaneously due to the volume of bone lost and will progress to an atrophic non-union. They are commonly encountered after resection of bone for cancer, infection or occasionally as a consequence of implant failure or trauma. Bone regeneration across a critical bone defect in an *in vivo* model is a crucial stage in translation of a technology into human clinical use. This not only proves the efficacy of the underlying engineered system but takes into account the practical aspects of implantation of a bioengineered device. There are a multitude of reasons as to why a proven *in vitro* system may not translate to an effective *in vivo* model; infection, blood supply, mechanics, immunological defect (systemic and local) (181-183). Whilst orthopaedic surgery aims to minimise these factors, an effective engineered system will grow bone despite suboptimal blood supply and mechanical environment. In current clinical practice, we frequently use bone chips either autologously or as allograft, however their performance is unpredictable. Previous work has utilised plasma polymerisation as a method of coating 3D structures in PEA translating a 2D to a 3D system (6,169).

This Chapter shows that canine bone chips (decellularised bone minerals) as a scaffold can be covered using plasma PEA, then fibronectin can be adsorbed allowing the presentation of subsequently adsorbed BMP-2 and ultimately regenerate bone in an *in vivo* model.

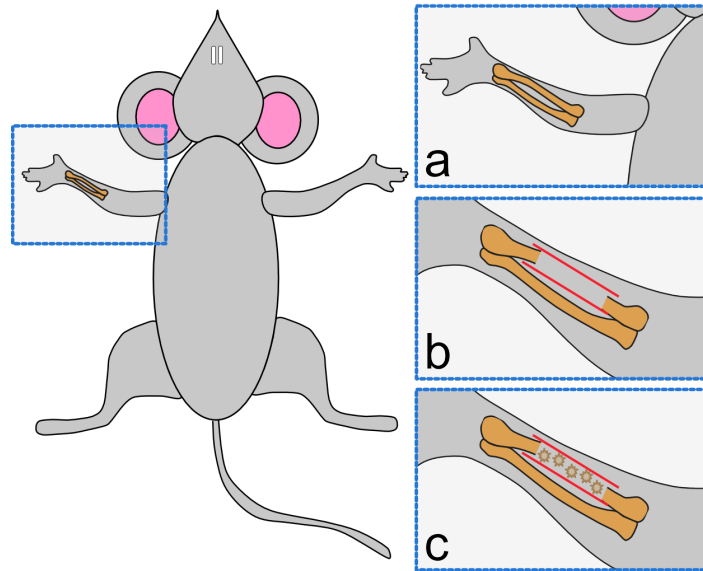


Figure 34 - Schematic of Mouse Radius Critical Defect Model demonstrating a) right forearm before bone resection b) bone resection and tube position c) tube complete with experimental condition, in this case decellularised bone chips. Adapted from Plante I, Stewart MKG, Laird DW. Evaluation of Mammary Gland Development and Function in Mouse Models. *Journal of Visualized Experiments*, 2011 July 21;(53):e2828 (184).

A murine critical defect model (Figure 34) is employed by creating a 2.5 mm segmental defect in the right radial diaphysis (approximately 0.8 mm diameter) which has been demonstrated as a critical sized defect (168). The stability of the forelimb is maintained by continuity of the ulnar averting the need for external fixation. A polyimide tube is then inserted containing the test materials, in this case functionalised bone chips.

The use of an *in vivo* model to test biomaterials accounts for variations untested by *in vitro* studies such as inflammation or immunological reaction. This is a key step of translational work and this technically challenging, yet conceptually simple model builds upon *in vitro* evidence gathered so far. The use of bone chips as opposed to custom 3D scaffolds is explored here as an adaption of current surgical techniques, is technically possible (due to the small size of chips) and in theory the presence of calcium phosphate has reported osteoinductive properties (185,186).

Specific acknowledgement in this Chapter to Dr Cristina Gonzalez-Garcia for training in the animal model and assistance with surgery.

3.2 Materials and methods

3.2.1 Materials

A list of materials and manufacturers can be found in appendix 6.2

3.2.2 Methods and sample preparation

Conditions tested in this Chapter; uncoated bone chips, bone chips with plasma PEA nanocoating, bone chips with plasma PEA and FN, bone chip with plasma PEA FN and BMP-2.

3.2.2.1 Implant tube preparation

Polyimide tubes of diameter 800 μm and 4 rows of 200 μm perforations were cut to 4mm lengths and cleaned by sonication in absolute ethanol followed by a triple rinse in absolute ethanol and autoclaved for 30 minutes.

3.2.2.2 Plasma coating

Plasma coating occurred 1 week prior to surgical implantation. Canine bone chips were obtained from Veterinary Tissue Bank (Wrexham UK) which are donated and processed to eliminate all biological material and contamination. This was achieved in a class 7 clean room with removal of bone marrow and fats via agitation and centrifugation with pyrogen free water, deproteinization in 3% hydrogen peroxide, decontamination in 70% isopropanol and extensive rinsing in sterile pyrogen free water. Finally, chips were freeze dried and gamma irradiated. Bone chips were placed into a clean plasma chamber and a vacuum slowly formed before introduction of radiofrequency (RF) at 100 watts to initiate a plasma reaction. Ethyl acrylate monomer was introduced into the chamber, a plasma state induced at 100 watts at a pressure between 1.3×10^{-1} and 1.6×10^{-1} mbar, which was maintained for 30 mins before cessation of plasma state and vacuum released via an air filter. To ensure the bone chips

remained sterile, they were placed under UV light 254nm in a class 2 sterile hood for 30 minutes. Under sterile conditions, tubes were filled with the plasma treated and negative control bone chips.

3.2.2.3 Protein adsorption

FN was adsorbed the evening before surgery. Human fibronectin solution was prepared in DPBS ++ to 20 ug/ml from stock solution of 1.42 mg/ml and placed into vacutainers. Perforated tubes with bone chips (+/- plasma PEA) were placed in vacutainers and a vacuum formed to incubate bone chips in the FN and allow solution to diffuse inside the bone chips. Incubation was carried out overnight in an incubator at 37°C. Samples were then double washed and stored in DPBS++ at 4°C.

3.2.2.4 BMP-2 adsorption

1% w/v BSA in MilliQ water was inactivated in a 65 °C water bath for 10 mins then filtered and added to samples for 30 minutes. Following wash with DPBS the samples were incubated with BMP-2 at 5 µg/ml in DPBS ++ for 60 minutes in vacuum via a vacutainer. Implants were then removed from the vacutainer and placed in Eppendorf tubes and kept at room temperature until implantation within the next 4 hours.

3.2.3 Surgery

Experiments were carried out in the University of Glasgow Veterinary Research Facility and performed under personal (n°I44130F69) and project license (n°70/8638) issued by the Home Office under the Animals (Scientific Procedures) ACT 1986. Appropriate training on cadaveric specimens prior to *in vivo* experimentation was undertaken. Intervention groups were randomised to minimise bias by any improvement in surgical technique during the series of operations.

C57BL/6 male mice, 8 weeks old were accustomed to the animal facility for 1 week prior to surgery. Mean mouse weight preoperatively was 24.9g (SD 1.56g, range 21.8g – 28.3g) with statistical similarity across all conditions. On the day of surgery mice were anaesthetised with isoflurane 3 litres/minute in air then weighed and the skin of the right forelimb removed using hair removal cream. The forelimb was sterilised using betadine solution and a sterile field created with drapes and sterile tape. Mice were transferred to the surgical table and their faces placed in a constant flow of isoflurane at 2-3 l.min⁻¹ titrated to effect. Intra peritoneal buprenorphine and carprofen were administered. A heating mat was used with a non-adhesive belt deployed to maintain positioning. A dorsoradial incision was made with a scalpel and blunt dissection using a periosteal elevator was performed to expose the radius. A 2.5 mm mid-diaphyseal resection of bone was undertaken using a custom manufactured double blade bone cutter with replaceable blades to ensure a precise resection without damaging the ulna. The bone ends were cleared of soft tissue and the 4 mm implant (selected by an assistant due to a predetermined quasi-random schedule, with operator blinded to the group) was slid over the proximal and distal aspects of the remaining radius. Lavage with 0.9% saline was performed and the muscle opposed. The skin was closed with interrupted absorbable 5-0 vicryl suture and the mouse transferred to a warm recovery tank.

3.2.4 Post-operative procedure

Post operatively mice were transferred to a recovery cage with warm fresh bedding and soft diet then transferred to individually numbered cages to conceal allocation. Daily weights and observations were recorded for the following 7 days. Food was made available on a daily basis and bedding was changed weekly as part of routine care in the animal facility.

After 1 week of recovery an *in vivo* computed tomography (CT) scan was performed under isoflurane anaesthetic to confirm implant position (SARRP, Perkin Elmer 0820 detector panel, Xstrahl Life Sciences) and Murplan (Xstrahl Life Sciences).

8 weeks following surgery the mice were euthanised using high dose phenobarbital intraperitoneal injection. The right forelimb was skeletonised, then excised and immersed in formalin for 48 hours before a triple wash with PBS and stored in 70% ethanol. Samples were removed from 70% alcohol and X-Ray Computer Tomography (CT) scans were performed using the Bruker Skyscan 1172, using an SHT 11 Megapixel camera and a Hamamatsu 80 kV (100 μ A) source. The sample was mounted vertically on a portion of dental wax and positioned 71.24mm from the source. No filter was applied to the X-Ray source and a voltage of 50kV was applied for an exposure time of 380ms. The images generated were 2664 x 4000 pixels with a resolution of 2.97 μ m per pixel. A total of 1800 images were taken in 0.2° steps around one full 360° rotation of the sample with the average of 2 frames taken at each rotation step.

3.2.4.1 Quantitative analysis

CT data was visualised using CTAn (version 1.12 for windows, SkyScan, Bruker) with the bone defect defined as the 2.5mm segment between native bone ends in the radius of which the central 2mm was studied. This region was exported as a 'volume of interest' and opened using CTvol (version 2.2 for windows, Skyscan, Bruker). A threshold was used to define areas of density consistent with bone mineralisation and applied to all samples. The volume of mineralised bone was calculated using a threshold attenuation range set to 70-255 for all images. A despeckling process was applied for black and white to remove noise from the images. BatchManager was then used to measure the volume of radio dense material within the 2 mm field giving a measured value for mineralised material in the defect.

Visual 3D reconstructions were then developed using CTvox (version 3.3 for windows, SkyScan, Bruker). The images produced by the μ CT are based on the level of attenuation through the sample, which is dependent on the thickness of the material and its absorption coefficient. Following this analysis, groups were revealed for combination and comparison of data. Negative and positive controls were not approved as data for this experimental arm were already available (6).

3.2.4.2 Histological analysis

Following μ CT the forelimbs were decalcified in Krajian's Solution (sodium citrate dihydrate, formic acid and deionised water) for 72 hours with change of solution every 24 hours. Limbs were mounted in paraffin with the below paraffinisation protocol detailed in Table 15.

Reagent	Duration
70% Ethanol	2 hours
90% Ethanol	2 hours
100% Ethanol no.1	2 hours
100% Ethanol no.2	2 hours
100% Ethanol no.3	2 hours
Amyl Acetate no.1	2 hours
Amyl Acetate no.2	2 hours
Amyl Acetate no.3	2 hours
Paraplast wax no.1	4 hours
Paraplast wax no.2	4 hours

Table 13 - Paraffinisation protocol used to dehydrate and mount mouse tissue into paraffin blocks for histological analysis.

Samples were then mounted in paraffin blocks, osteotomised into 5 μ m slices and mounted on microscopy slides. Slides were deparaffinised and rehydrated in histo-clear and reducing concentrations of ethanol then deionised water. Samples were incubated in Mayer's hematoxylin solution for 8 minutes then Scott's for 1 min as a blue nuclear stain. Incubation in fast green solution was performed for 30 seconds to highlight connective tissue then rinsed off in acetic acid for 3 seconds. Finally, slides were immersed in 1% safranin-O for 5 minutes as a nuclear counterstain (to convert the green connective tissue to

red) before dehydration through sequentially increasing concentrations of ethanol then histo-clear.

Slides were fixed with DPX synthetic resin and coverslips applied. Digital microscopy images were captured using an EVOS FL Auto (Life Technologies) and Evos FL (v 1.4 for Windows, Thermofisher). Images were captured at x20 magnification and stitched using the Stitch Image Grid plugin for image J(187). Images were cropped to the tube section demonstrating proximal and distal radius and the defect within (Figure 35).

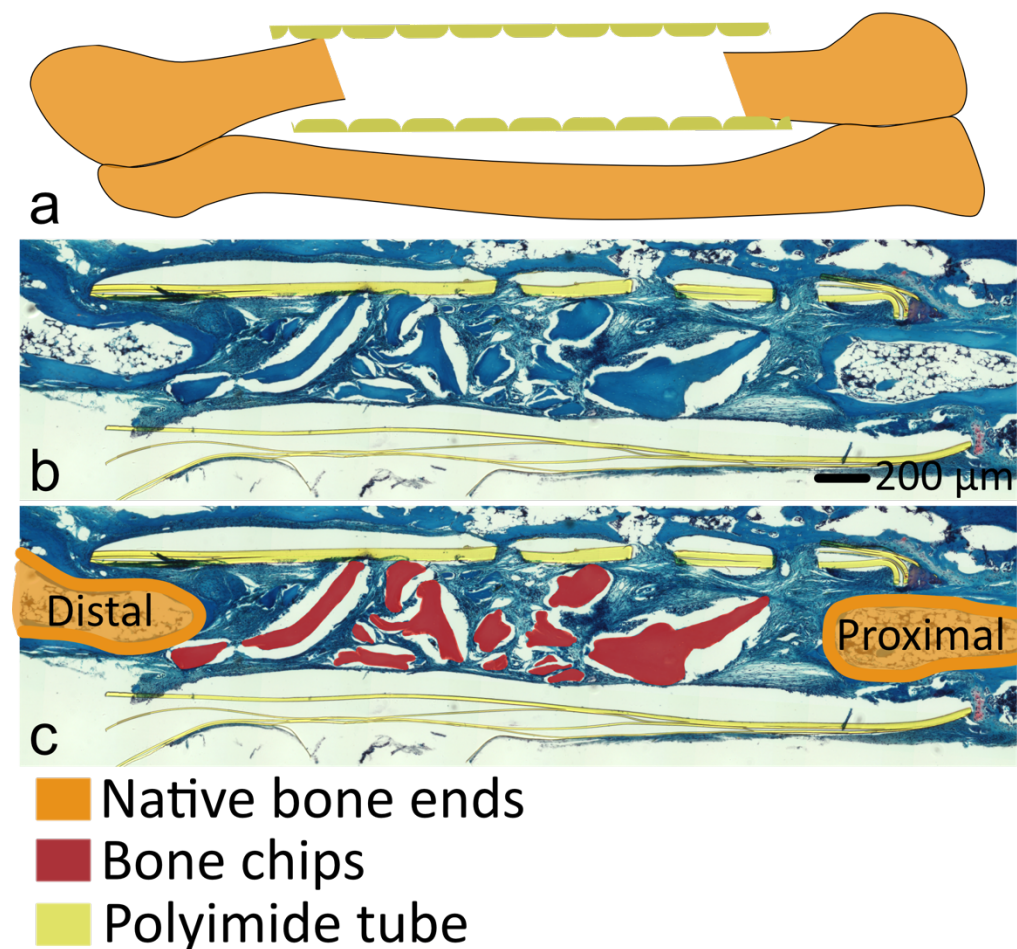


Figure 35 - Description of histology. a) schematic of resected radial diaphysis with polyimide tube bridging defect. b) stitched histological image c) histological image with overlaid descriptors.

3.2.5 Statistical analysis

4 mice per condition were authorised for use. Data was analysed using Graphpad Prism (version 6 for Macintosh, GraphPad Software, La Jolla California USA) with normal distribution tested using the Shapiro-Wilk normality test then comparison of means carried out using t-test or Mann-Whitney U test for parametric and non-parametric data respectively. Where multiple comparisons were performed an ANOVA analysis or Kruskal-Wallis test was used for parametric and non-parametric data respectively, with application of Bonferroni or Dunn's correction for incidental significance. A p-value of <0.05 was considered statistically significant.

3.3 Results

Summary of results

Quantitative inspection of the CT images was encouraging that bone bridging between osteotomised ends was more consistent between all samples presenting BMP-2 on bone chips. Samples not presenting BMP-2 showed islands of bone chips with little consistent bone growth between bone chips. Quantitative analysis was affected by artefact created by residual bone chips. As such, the no statistical difference in mineralisation was observed.

Histological appearance was more reassuring that the bone chips had been functionalised with better integration of bone chips as can be observed in Figure 36.

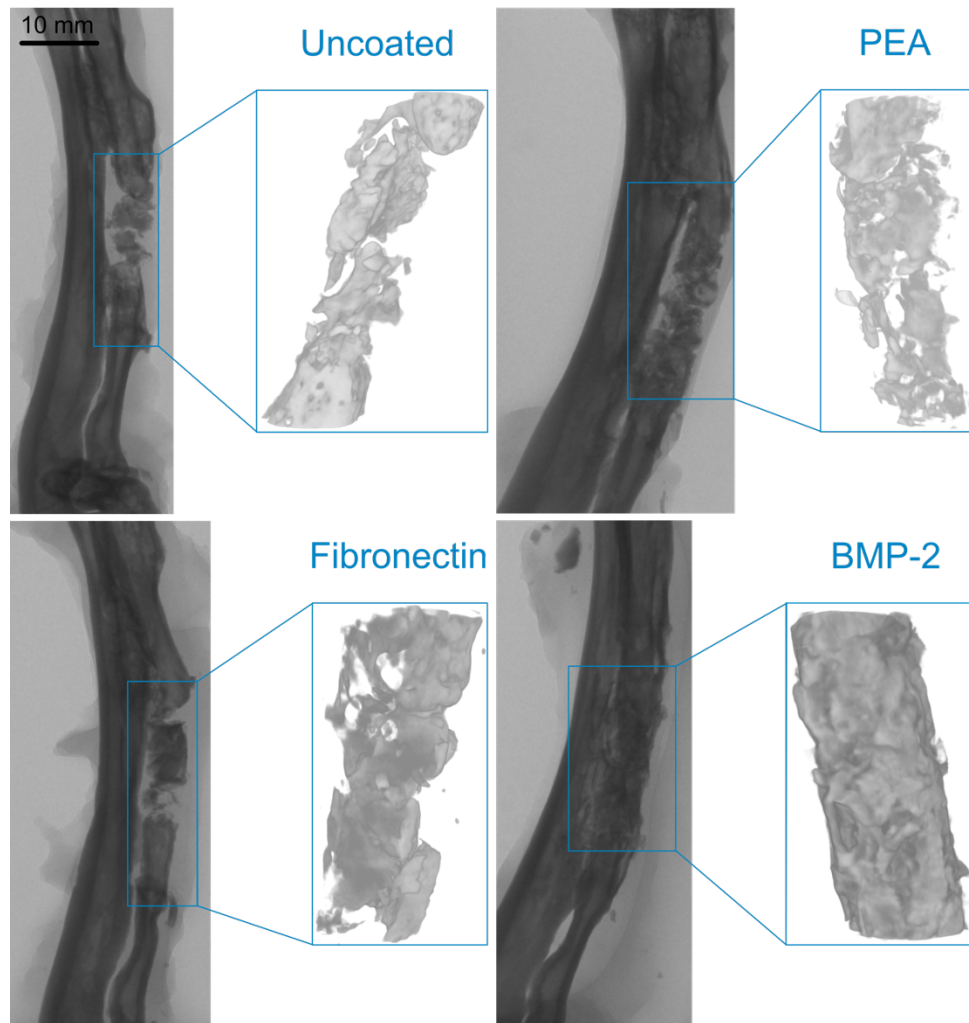


Figure 36 – Summary X-ray and CT representation of critical defects. Mineralised bone remained evident for the entirety of the 8 week live experiment making quantitative comparison difficult. However qualitative bone formation was convincing both radiologically and histologically.

3.3.1. Recovery

All mice regained $\geq 95\%$ of their pre-operative weight (Figure 37) by the end of week 1. 2 mice gnawed through their sutures and required wash out and re-suturing day 1 post operatively. Three mice exhibited signs of persistent pain and were euthanised. This left the number of remaining mice with; uncoated bone chips (n=4), PEA (n=3), PEA+FN (n=3), PEA+FN+BMP-2 (n=4). These remaining made satisfactory post-operative recovery with recommencement of diet, made satisfactory recovery from surgery and spontaneously began moving about the cage from day 1 post operatively. No mice beyond those euthanised exhibited any unresponsiveness, vocalisation upon handling or facial swelling.

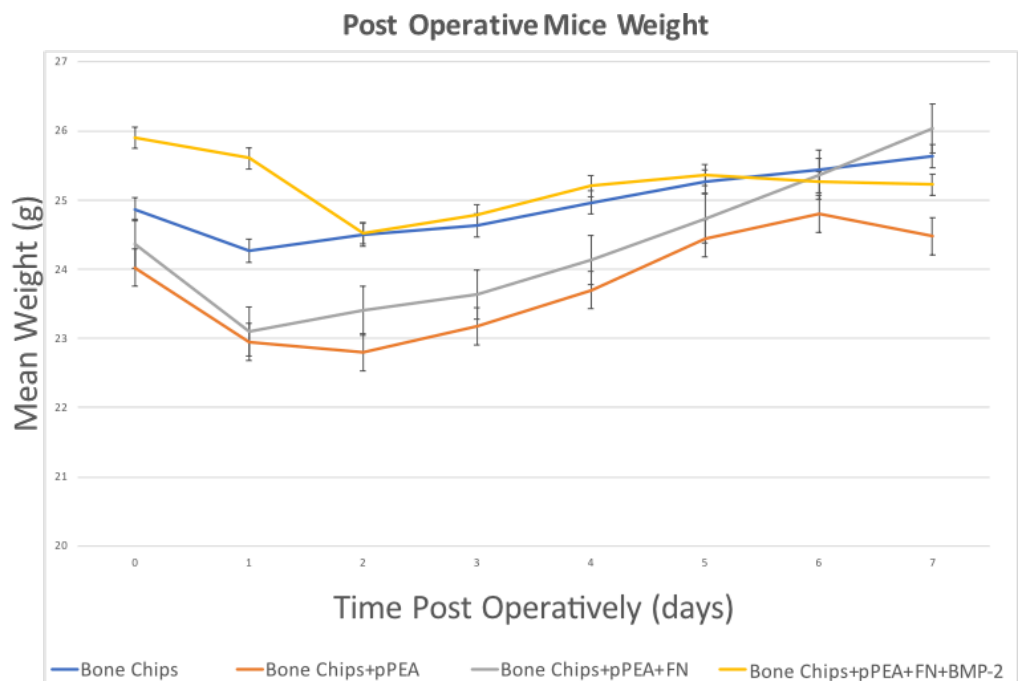


Figure 37 – Mean postoperative mouse weights with standard error lines. All mice analysed made a prompt recovery in terms of behaviour and weight. Legend denotes mouse number. Mouse weight loss is strongly associated with ill health. The encouraging return to weight and behaviour negates causation of reduced bone formation due to ill health.

3.3.2 X-ray imaging

Difficulty was encountered when interpreting imaging to differentiate between impacted bone chips and true biological mineralisation between islands of bone. Bone chips remained in all samples with little or no evidence of mineralised bridging between uncoated bone chips. PEA and PEA+FN coated samples demonstrated inconsistent deposition of mineral between chips. BMP-2 coated chips exhibited more consistent bone formation, with integration of bone chips and appearances consistent with bone remodelling seen in clinical practice (Figure 38).

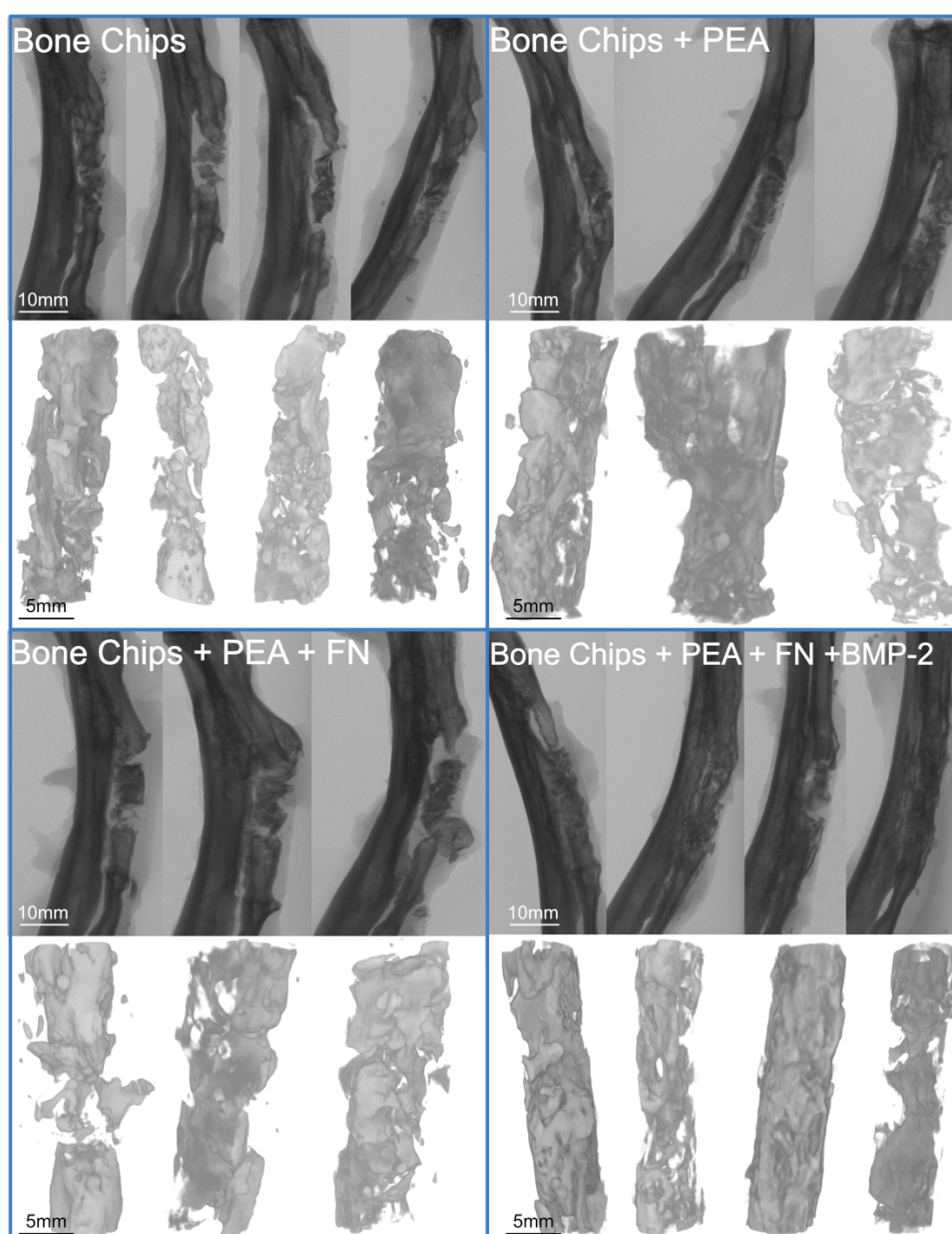


Figure 38 - X-ray (above) and 3D reconstructed images (below) of μ CT data. BMP-2 sample demonstrated mineralised bone bridging between bone chips indicative of functionalisation of the bone chips.

3.3.3 Calculated Bone Volume

Quantitative analysis of mineralisation within the defect was confounded by the presence of bone chips. Statistical comparison showed no statistical difference in total mineral volume or as a proportion of the defect (Figure 39). Our previously published data demonstrated that an empty tube gives 0.25 mm³ of bone formed.

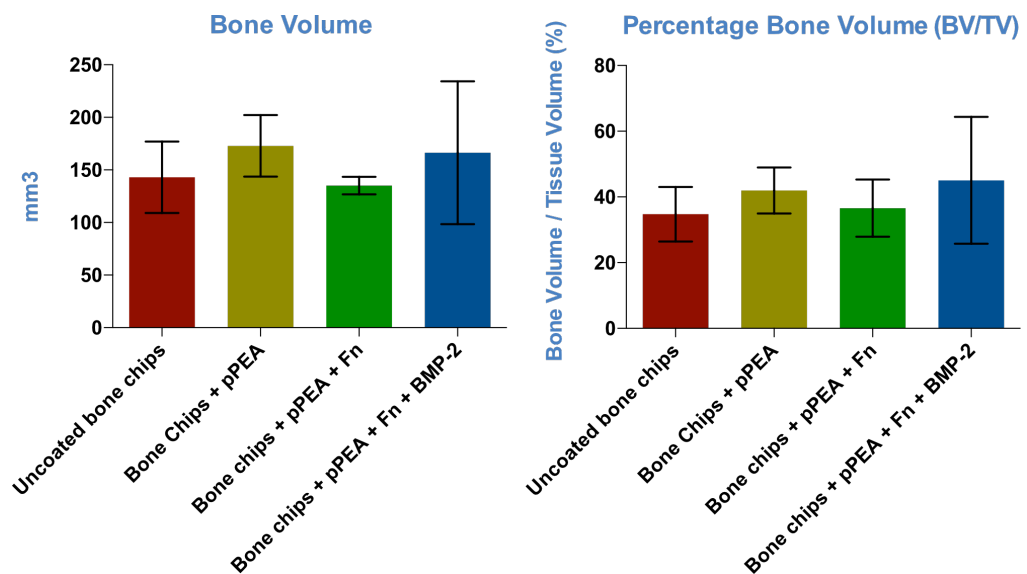


Figure 39 – Quantification of bone volume as an absolute Figure and as a proportion of the entire defect. No statistically increased in bone volume was noted between groups, due to the confounding presence of mineralised bone chips. However the subjective bridging of bone demonstrated between chips (Figure 34) is of more value than net bone presence. The ‘baseline’ bone volume between groups is impossible to control, as the bone chips are heterogenous in morphology and can be compressed when introduced, potentially giving rise to wide confidence intervals.

Clinically the volume of mineralised bone is not sufficient for confirmation of defect union. The pattern of bone formation (existence and direction of trabeculae) and interconnectivity of fragments are more sensitive markers of union and mechanical integrity. Therefore, in clinical practice, measurements are more subjective based on x-ray appearance and patient reported symptoms (pain and stability during function). To investigate further, histological analysis was performed to detail response on a cellular level. A

computational analysis of chip interconnectivity was also considered; however, this resource was not available given the complexity of the data field.

3.3.4 Histology

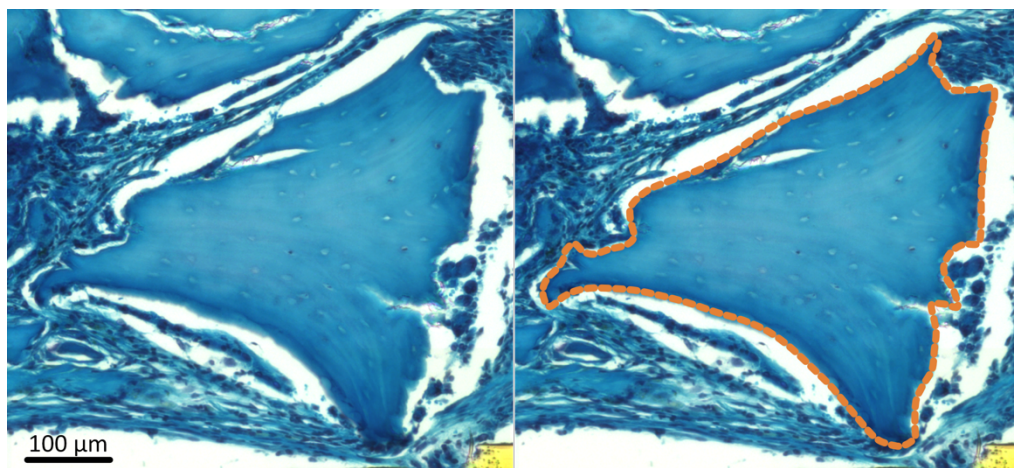


Figure 40 - Histological bone chip appearance (orange outline).

Bone chips appear as blue stained predominantly extracellular matrix (Figure 40) indicating that cells could migrate and differentiate within the chip. This is seen in normal bone biology in which cells move throughout lacunae in response to mechanical, chemical and intercellular signalling to maintain bone (and biochemical) homeostasis. Few nuclei exist compared to osteoblasts seen out with the chip indicating an earlier lineage. The gap surrounding this area is likely gap left where bone minerals were decalcified previously noted by Bertolai *et al* (188).

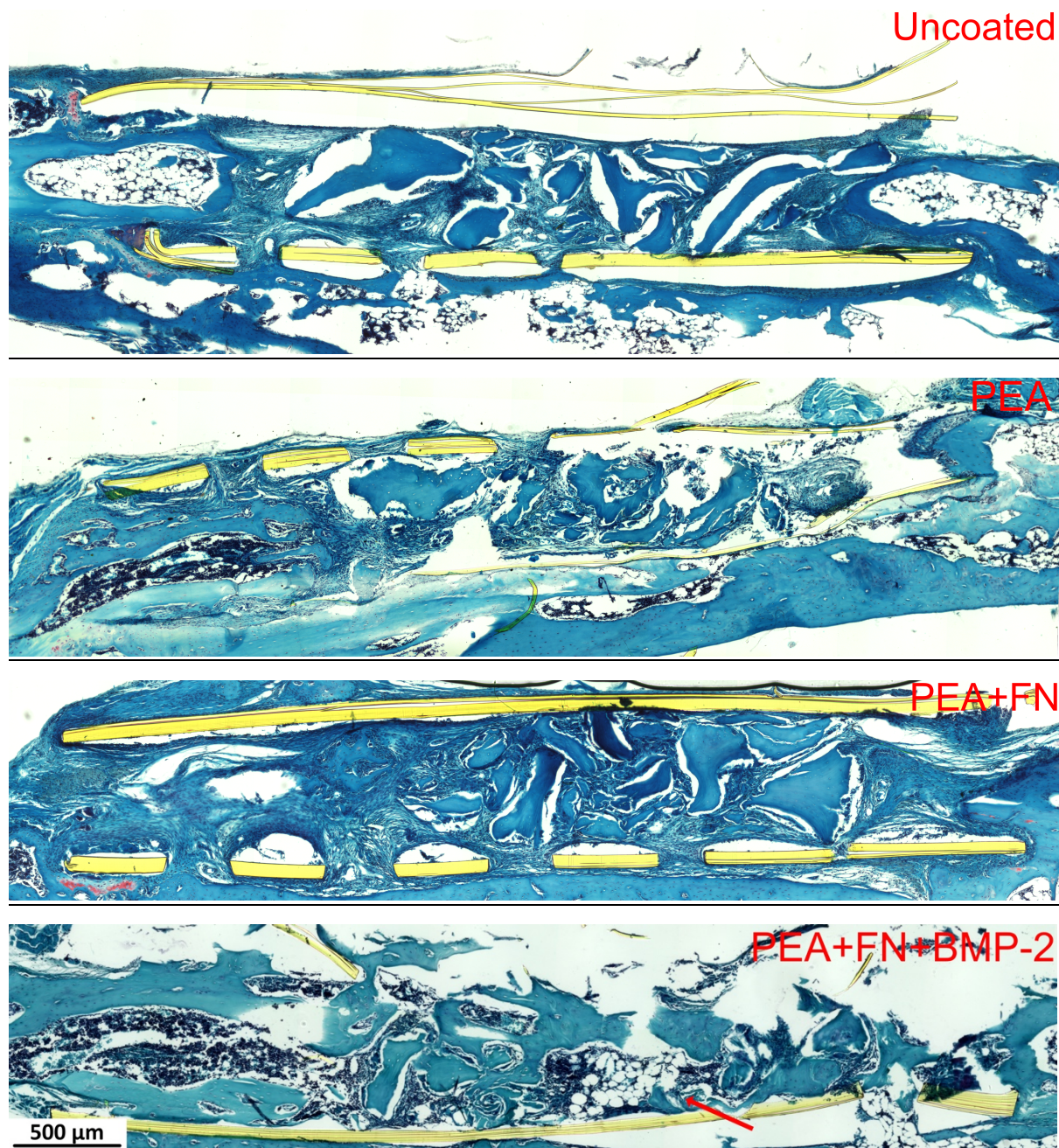


Figure 41 - Histological demonstration of bone formation with each additive component of the osteoinductive system. The addition of FN and BMP-2 demonstrated closer integration of bone chips within the early bone regenerate. Furthermore, the BMP-2 samples demonstrate mature bone flowing throughout the sample (red arrow).

All samples demonstrate cellular activity within the defect and an absence of fibrocytes stained red with safranin-O (Figure 31). Following decalcification, the cellular activity within the bone chips is evident, however are closer integrated in samples containing FN and BMP-2. The BMP-2 group demonstrated mature trabecular bone marrow formation of bone centrally

within the defect (arrow). More dense cellular activity flowing contiguously with bone ends incorporating bone chips.

When compared to our previous experience in this model, results are markedly different to the negative control. (Figure 42).

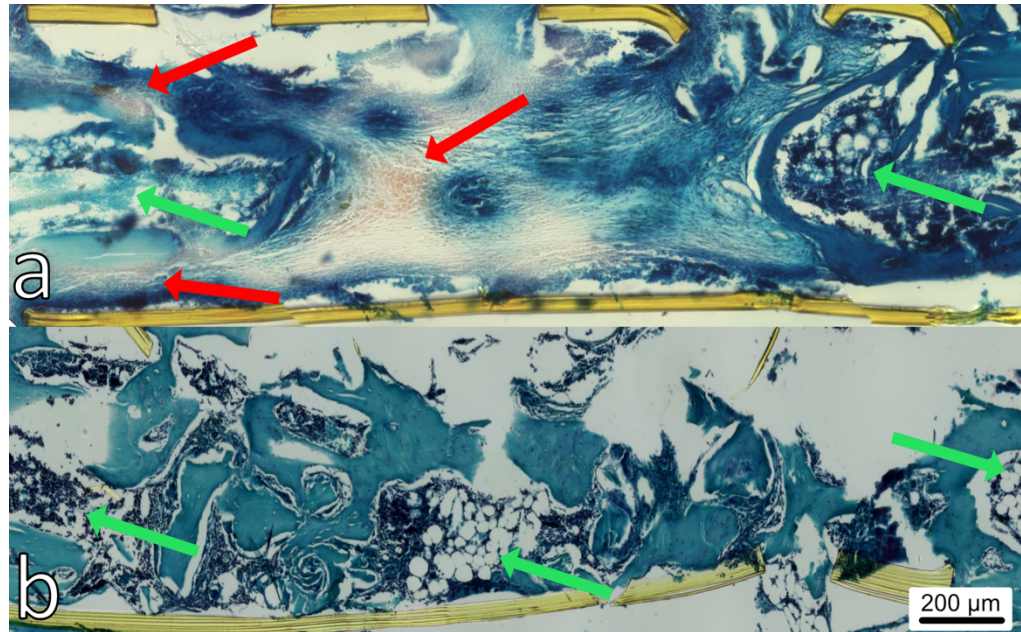


Figure 42 – Histological comparison with negative control. a) polyimide tube coated with PCL from our previously published data(6) showing the natural history of a critical defect with bone marrow in native bone ends (green arrows) with the defect full of linearly arranged fibrous tissue and fibroblasts stained (red arrows) b) BMP-2 sample from this experiment demonstrating mature bone marrow formation within the defect.

The presence of heterotopic ossification (HO) was noted through the tube perforation in one of the BMP-2 samples (Figure 43) causing osseous bridging between the radius and ulna (“synostosis”). This is an encouraging demonstration of the potency of the technology but is concerning regarding some clinical applications. For example, the use of bone substitutes near joint (“periarticular”), specifically near the elbow, are liable to HO. Additional concern is raised with the use of a bone regenerative technology which could cause a surplus of bone growth, in areas with limited space to grow, e.g. use in fusion of the cervical spine which is in tight proximity to blood vessels to the brain, trachea and oesophagus. One of the key advantages of this system is the restrained local presentation of the GF at ultralow doses.

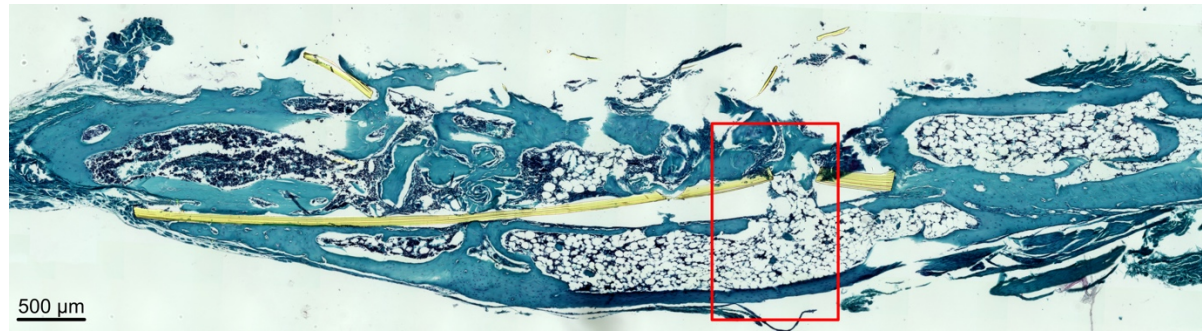


Figure 43 – Synostosis. A BMP-2 sample demonstrated heterotopic ossification resulting in “synostosis” between the neo-radius and ulna (red box). This pathological bone growth is typical to aggressive healing responses and is not likely coincidental in the BMP-2 sample. This is both an encouraging demonstration of the technology, but also a concerning reminder that dosage of BMP-2 administered can cause negative effects. If this were to happen clinically, there would be pain and inability to rotate the forearm/wrist.

3.4 Discussion

Mice analysed in this study regained their preoperative weight within 7 days of surgery, and no wound infections were noted, nullifying the hypothesis that any inferior bone production would be due to inferior biology.

As x-rays are cheap and accessible in clinical practice, they are the current standard for inferring information on bone union. The interpretation of x-ray appearances in this experiment required consideration of the bone chip appearance on X-ray, which is similar to that seen in humans, however bone chips appear proportionately bigger. Rather than considering appearance volume of mineralised material, more emphasis is placed on mineralised interconnectivity of bone chips which ultimately is what gives mechanical stability.

The measurement of mineral formation is negated by the large volume of pre-existing mineral in the defect. It was not possible to quantify the volume of bone chips accurately prior to implantation as the chip fragments were liable to falling out and compacting within the tube during implantation. Furthermore, *in vivo* scanning was not comparable in image quality to the highly detailed μ CT scanning of explanted forelimbs. A repeat experiment with larger numbers may prove a more adequately powered study and account for low numbers and wide standard deviations. The mean percentage bone volume in this experiment was 35% across the non-BMP-2 samples and mean with BMP-2 was 45%. A power calculation (β power =0.8, α significance=0.05, superiority margin $\delta=0.1$) to demonstrate this increase as significant demonstrates a requirement of 514 mice per arm, which would require 2056 animals to repeat this experiment and gain statistically significant results (in the presumption the bone volume percentage results remained the same). This does not include 'loss to follow up' (in this case, animal death) which was 19% in this experiment. Therefore, an additional at least another 400 mice would be required to mitigate for this. This would result in a large animal experiment and even notwithstanding the financial cost, would not satisfy the replacement, reduction and refinement principles of animal experimentation.

This is the first experiment of its kind, with no similar comparison in the published literature so histological appearances were not easily hypothesised. Uncoated bone chips and pPEA coated chips demonstrated little in the way of difference histologically with limited integration of chips with cells, however there was cell activity in the tube and this combined with clinical observation of the animals over the 8 week period confirmed the biocompatibility of the combination. The addition of fibronectin revealed closer integration between the base scaffold material (bone chips) and the surrounding cells, which is in keeping with *in vitro* experimentations (175,189). Finally, the addition of BMP-2 also demonstrated the appearance of closer integration with cells, contiguous flow of bone cells through the chips and defect with the appearance formation of mature bone (however it's not possible to define if this is functioning bone marrow). Given the above referenced literature on the beneficial effects of a simple fibronectin coating which would eventually result in bone integration, it could be hypothesized that BMP-2 has a role in expediting the bone regenerating process. Although the addition of BMP-2 vastly increases the cost of the system, a quicker healing bone defect would reduce repeat hospital visits, minimise time for muscle wasting (improving ultimate function) and potentially speed up return to work time. All of these clinical outcomes have an effect on the overall cost of treatment and cost analysis via a clinical trial may demonstrate an offset in the cost of the BMP-2.

Qualitative images, both microCT and histological, demonstrated more mature bone formation flowing throughout the defect. This visual measure is most clinically relevant, as pattern of bone formation is more important than volume of bone formed. However, unlike this experiment, in clinical practice the progression of bone formation is observed over a series of time points. Consideration of how to quantify these findings was considered, e.g. computational analysis of connections formed between bone chips, or surveying of clinicians to validate these observations, however neither of these avenues came to fruition.

A variety of murine *in vivo* models exist to test orthopaedic implants in a simulated human environment utilising cranial, femoral, radial and ulnar bone (190-194). The critical defect model used in this experiment has

previously been validated in 2D (169) and 3D (6) models, however prior to this work the use of bone chips within a murine diaphyseal critical defect has not been attempted. It was unclear whether the bone chips would have a large osteoinductive effect within the 8 week period and cause bridging union of the 2.5mm defect as has been shown with cranial models (159). Conversely the bone chips were not thought to be mechanically contributing to forelimb function and therefore may have been resorbed (195). These questions could have been answered with the use of a high resolution *in vivo* μ CT scanner at the midpoint of the experiment, which was not available to us, via serial observations of the bone chip volume. The quantitative analysis at a single end timepoint resulted in no significant difference between groups, which is to be expected in the absence of complete union or resorption. By putting bone graft in the defect, it stands to reason that the critical defect model therefore is no longer a critical defect and evaluation of the merit of a BMP-2 system falls to subjective observation of mineralisation quality and histology (the former of which is the current clinical standard). It has yet to be explored in this model whether increasing doses of BMP-2 would increase the healing rate, or indeed does the system have capacity to present more BMP-2 nor at which time point during adsorption does the fibronectin become saturated with BMP-2. This point is difficult to address given the irregular topography of bone chips, and it is not clear what actual dose of BMP-2 is being administered via the chips. 5 μ g/ml was used in this experiment (with unadsorbed BMP-2 being removed as part of the implant preparation). To give this context, Llopis-Hernandez *et al.* used 75 μ g/ml within a hydrogel used in their use of the same model, thus there may be scope to increase BMP-2 dosing further. The clinically available InductOs uses 12mg as a single dose to treat human non-unions and fusions, this is 160 times the dose from Llopis-Hernandez *et al.* used in mice, however the typical human is 3000 times heavier.

Previous experience of investigating this technology *in vitro* and *in vivo* has shown promising results of 2 dimension applications (169), and has subsequently been validated in 3D with the progression to plasma polymerisation (6). The use of plasma coated bone chips is therefore a potential avenue of natural progression into 3D applications which are

currently used in clinical practice and are bioresorbable (188). Subsequent to this work, we have implemented the osteoconductive technology in clinical cases of non-union and fusion in small animals in collaboration with the Small Animal Hospital at the University of Glasgow, in which synthetic bone minerals (Reprobone[®], Ceramisys, Sheffield, England) are sterilised and coated with FN and BMP-2 then implanted in bone defects, with encouraging clinical results to date (6).

There are several limitations of this experiment, not least the aforementioned interference of bone graft in a critical defect model. The study is short and could be better timed by serial high-resolution imaging, rather than a pre-determined time frame based upon our experience of this model in other experiments. Ideally this would have been performed at a regular interval (e.g. fortnightly) until bridging union was achieved in some samples, then the endpoint could have been more relevantly determined and a pattern of bone chip integration could have been described. The nature of *in vivo* experimentation mandates that we use as few animals as possible to draw a conclusion, however larger numbers (>2400 as outlined above) would allow more observations and give more statistical power with which to qualify which implant condition was most osteoinductive. This was addressed by a powering the study based upon previous experience in this model but given the unknown pattern of mineralisation prior to this specific experiment, an estimation of minimum numbers required to demonstrate a statistical improvement. The current clinical standard of bone chips or synthetic HA use as allograft is to combine with blood or bone marrow as a source of stem cells and growth factors, therefore the exclusion of this additive process detracts from this experiment's alignment with current clinical practice (196). The implant tube neatly contained the bone chips in a fixed region, whereas in reality the defects operated upon in clinical practice are 'uncontained' by anything other than surrounding muscle compartments and metal ware. Although plasma polymerisation was used with adsorption of FN and BMP-2 in a vacuum, it was not possible to confirm whether the inside of the bone chips were functionalised or not.

Future work investigating the utility of functionalised bone chips could involve longer follow up, ideally with detailed *in vivo* imaging at regular time points. Varying doses of BMP-2 could be investigated to minimise manufacturing costs, but more importantly negate unnecessary inflammatory response and heterotopic ossification which are important complications of bone regenerative surgery. Quantification techniques of how penetrative the addition of PEA and adsorption of FN and BMP-2 could be explored further. Finally, future *in vivo* work could be developed in other bone regenerative archetypal models (joint fusion, cancellous defect), potentially in larger animals where the bone chips are relatively smaller and could be combined with bone marrow.

3.5 Conclusions

The use of an ultra-low dose BMP-2 adsorbed onto FN and PEA on decellularised bone chips did not give rise to quantitative conclusions. Further *in vivo* evaluation by way of larger animal trials is not likely to satisfy animal welfare criteria in its current form. Qualitative histology provides new insight into the use of functionalised bone chips in this model, and raises caution as to the potential for heterotopic ossification.

Chapter 4 - 3D Composite Scaffolds For Delivery of Engineered Nanocoating

4.1 Introduction

This Chapter investigates the utility of 3D printed PCL scaffolds as a delivery mechanism for the BMP-2 osteoinductive nanocoating. Scaffold geometry is intimately related to mechanical properties, however pore size, shape and connectivity have an association with cell activity. The practical aspects associated with fused filament fabrication (FFF) printing of PCL scaffolds with a view to use as an implantable bioresorbable device are presented. Whilst PCL was selected for its thermoplastic properties, biocompatibility and favourable resorption characteristics, like most polymers its relatively low modulus and strength led to attempts in improvement using hydroxyapatite as part of a composite filler within the PCL material matrix. Additionally, the biological osteoinductive properties of HA addition were investigated with MSC culture and qPCR. Two types of HA were available for experimentation; sintered ('R') HA and nanoHA.

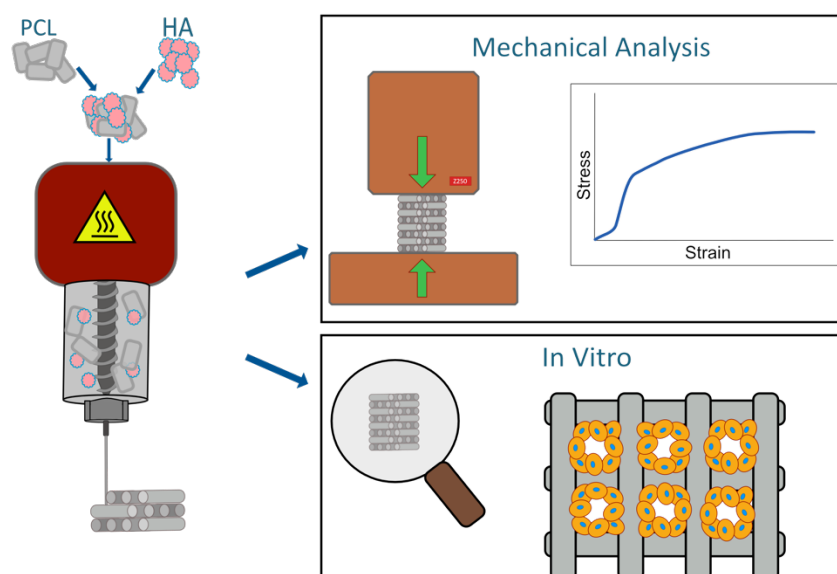


Figure 44 - Schematic of 3D printing scaffolds then mechanically tested and *in vitro* analysed. PCL and HA were mixed using pharmaceutical grade laboratory equipment then added to a fused filament (thermoplastic) 3D printer and extruded as composite scaffolds. These scaffolds underwent mechanical compression testing and *in vitro* analysis of functionalisation and biocompatibility.

Homogenous mixing of a monomodal filler (e.g. HA) into matrix is key to optimise the properties of a composite, in particular with spherical fillers such as HA which creates an amorphous material with limited stress concentration.

The balance of matrix to filler ratio is key to optimising any composite in which a low filler volume composite would maintain low modulus whilst inducing setting contraction. Excessive amounts of filler can cause brittle properties due to filler-filler contact or leaking of filler from the matrix. Filler contents higher than 30% volume as they clogged even the largest 3D printer extrusion needle. Therefore, it was possible only to test 20% and 30% volumes in both nanoHA and RHA throughout a range of scaffold geometries. Theoretically, higher filler contents should result in increased stiffness, however improvement in strength is less predictable and is dependent on interaction between the HA and PCL. Finally, scaffolds were compared to current industry standards for bone substitute materials currently used in clinical practice.

In vitro cell behaviour was evaluated on various scaffold geometries and composite types given the reported cellular response to HA composite scaffolds (197-199). This was performed with human MSCs (MSC101) and osteoinductive activity was measured at 7 and 28 days following seeding onto functionalised scaffolds. RNA analysis via qPCR demonstrated osteoblast activity DNA activity consistent with progression toward bone formation, however the addition of various HA volumes or particle sizes did not infer an osteoinductive advantage. This is not in keeping with published results on addition of HA, which is reported to have osteoinductive properties, however there may be an associated publication bias.

Specific acknowledgement in this Chapter to Dr Vineetha Jayawarna for assistance in with 3D printing, sample preparation and *in vitro* cell work.

4.2 Materials and Methods

4.2.1 Materials

A list of materials and manufacturers can be found in appendix 6.3.

4.2.2 Methods and sample preparation

4.2.2.1 Mixing process

Mass and density of HA filler (f) and PCL matrix (m) were used to calculate volume % using the formula $(W_f/\rho_f)/(W_f/\rho_f)+(W_m/\rho_m)$ where W_f - filler weight, ρ_f - filler density, W_m - matrix weight, ρ_m – matrix density. Medical grade PCL nanoHA nano and sintered (“RHA”) were weighed using microbalance (Pioneer PA64, Ohaus). Volume calculated batches were then pre-blended in a rotating 5l drum within a batch blender (AB-015, Pharmatech, Denver) for 20 minutes in the pharmaceutical materials lab in the University of Strathclyde. The mixture was then slowly added to a parallel co-rotating twin-screw extruder (Process 11, Thermo Scientific, Massachusetts) to compound the material with a melting temperature of 70 °C, pressure < 100 bar. 11x440mm screws were used with 2 mixing 55mm barrel segments and progressive cam angles (Figure 45). Compounded material was collected in 3 mm filament form, allowed to cool and pelletised into 1mm pellets using a pelletiser (Thermo Scientific)

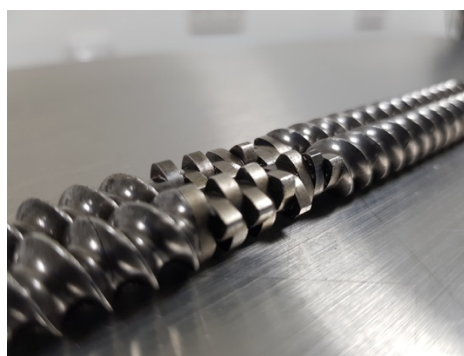


Figure 45 – Twin screw extruders with mixing cams used to heat, mix and extrude PCL and HA. The screw segments extruded melting composite through the cams which progressively mixed the compound before the remaining screw length extruded composite into a receptacle.

4.2.2.2 Validation of mixing technique

Visual inspection of homogeneity of mixing and filler/matrix interaction was carried out using SEM. Methods used were mounting in PMMA then polishing, and freeze fracture.

4.2.2.2.1 – Resin polishing

2 replicates of each solid samples and mounted using coloured clips (Figure 46) in poly (methyl methacrylate) PMMA which was set overnight in moulds. PMMA blocks were removed from moulds and polished using progressive orbital sanding with silicon carbide grinding papers, water cooled using 240, 400, 600, 800 and 1200 grit. Fine polishing was carried out using 6-micron and 1-micron diamond paste for 30 minutes each.

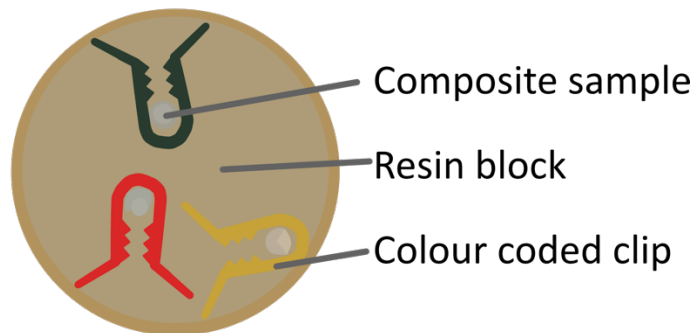


Figure 46 - PCL/Composites mounted in PMMA blocks with coloured clips for polishing. Excess PMMA was then polished down to expose composites for SEM analysis.

4.2.2.2.2 Freeze fracture

Single pellets of nano and R hydroxyapatite at 20% and 30% volume percentage were immersed in liquid nitrogen then struck with a mallet to create a horizontal fracture (Figure 47)

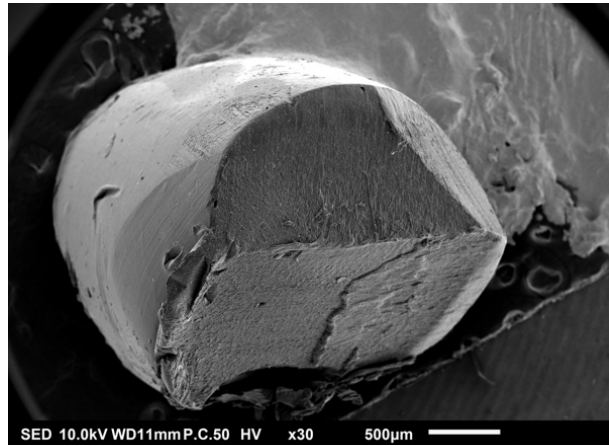


Figure 47 - 'Pellet' of extruded PCL/HA composite fractured for SEM analysis. Suitably flat fracture planes can be established for using this method onto which detailed SEM can be performed.

4.2.2.2.3 Scanning electron microscopy (SEM)

Samples were mounted onto subs with silver glue, and carbon/silver tape and coated in 20 nm of gold palladium (Au/Pd) at a ratio of 60:40 using a 25 mA sputter current on a turbomolecular pumped coater (Quorum Q150T ES). Mounted samples were placed into a 10 kV volton scanning electron microscope (Jeol JSM-IT100). Each sample had a scouting scan then representative areas selected to give a x1000, x5000 and x10000 magnification.

4.2.2.3 Electron dispersive X-ray spectroscopy (EDS)

Electron Dispersive X-ray Spectroscopy(EDS) was performed using a Zeiss Sigma VP field emission scanning electron microscope, in a high vacuum (<1000pa) of air. Aperture was set to 60um, electrons were emitted using a tungsten filament at 20 kV and 1 nanoamp with an analytical working distance of 8.5 mm. SmartSEM API (v5.06 for windows, Zeiss) was used for image acquisition and EDS analyses performed with Aztec (v3.3 SP1, Oxford Instruments). Specimens were aligned and a magnification series (x500, x1000, x5000) were obtained with the latter used for point elemental analysis and mapping.

4.2.2.4 Greyscale analysis

To quantify the volume percentage of HA within the PCI matrix, SEM images at x5000 were captured. These were converted to 8-bit images and a threshold process to values between 90 and 255 using Image J (Fiji, version 2.0.0-rc-69/1.52i for Mac). A noise despeckling process of small particles performed to remove single pixel noise and particle percentage quantified using the analyse particles feature in Image J.

4.2.2.5 Scaffold design

Scaffolds were designed using BioCAD (version 1.1 for windows, Regen HU, Switzerland) before exporting to BioCAM (version 1.1 for windows, Regen HU, Switzerland). Beyond simple geometry of layers, a number of variables required optimisation for each scaffold design and material; melt tank temperature, screw extrusion chamber temperature, extrusion speed, nozzle diameter, extrusion width, line spacing, layer repetition, different layout geometries (2 angle, e.g. 0/90° and 4 angle, e.g. 0/45/90/135°). BioCAD works differently than most CAD programs where completed models are retro engineered to be built up layer by layer, whereas BioCAD designs are designed on a layer by layer basis with much simpler geometries. All scaffolds were layered up in a circular outline with continuous extrusion 'snaking' throughout the layer (figures 48 and 49). Samples undergoing *in vitro* cell analysis extrusion patterns were repeated until scaffolds were 4x2.4 mm and compression testing samples 11x15 mm, the design and printing parameters of which are detailed in tables 17 and 18 respectively.

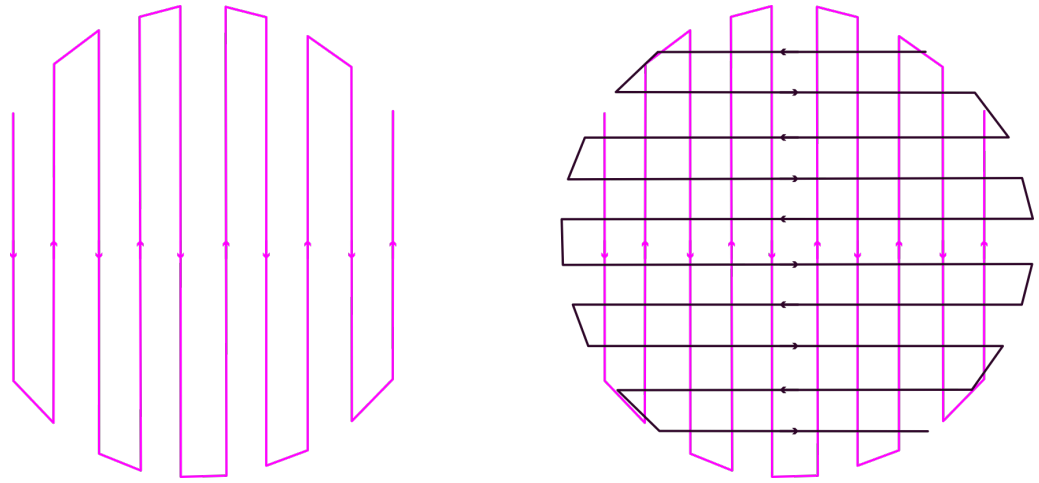


Figure 48 - Example toolpath for a single layer and multilayer 0-90° in BioCAD with overlaid arrows delineating direction of extrusion. Alternate layers were repeated (pink then black) until predetermined scaffold geometries were acquired.

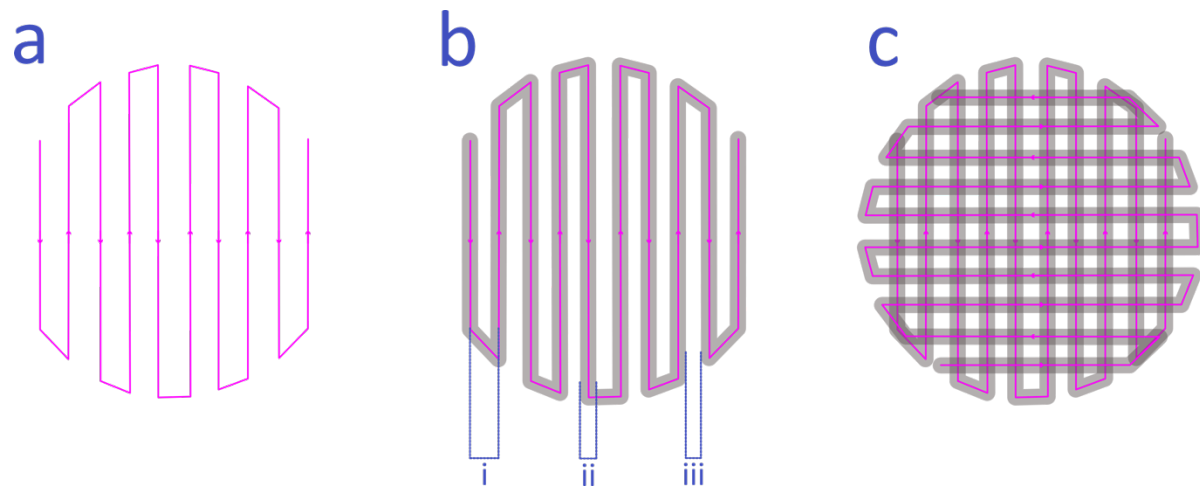


Figure 49 – Toolpaths. a) Example toolpath for a single layer in BioCAD b) Overlaid extrusion demonstrating (i) line spacing (ii) extrusion width and (iii) theoretical gap c) 0/90 toolpath. Increasing line space and decreasing extrusion width increased theoretical gap, thus increasing pore size and porosity.

Scaffold Type	Layer Orientation (°)	Layer Repetition	Line Spacing (mm)	Nozzle diameter (mm)	Extrusion Width (mm)	Theoretical Horizontal Gap (mm)	Theoretical Vertical Gap (mm)
PCL single layer	0,90	No	1.0	0.51	0.3	0.7	0.3
PCL 0-90	0,90	Double	1.0	0.51	0.3	0.7	0.6
PCL 0-60	0,60	Double	1.0	0.51	0.3	0.7	0.6
PCL 0-45-90-135	0,45,90,135	Double	1.0	0.51	0.3	0.7	0.6
PCL 0-90 0.7 spacing	0,90	Double	0.7	0.51	0.3	0.4	0.6
PCL 0-60 0.7 spacing	0,60	Double	0.7	0.51	0.3	0.4	0.6
PCL 0-90 0.8 spacing	0,90	Double	0.8	0.51	0.3	0.5	0.6
PCL 0-60 0.8 spacing	0,60	Double	0.8	0.51	0.3	0.5	0.6
PCL pPEA	0,90	Double	1.0	0.51	0.3	0.7	0.6
Reused PCL	0,90	Double	1.0	0.51	0.3	0.7	0.6
PCL 0.33 Needle	0,90	Double	1.0	0.33	0.25	0.75	0.5
Low Temp 20% nano	0,90	Double	1.0	0.51	0.3	0.7	0.6
High Temp 20% nano	0,90	Double	1.0	0.51	0.3	0.7	0.6
20% nano 0-90	0,90	Double	1.0	0.51	0.3	0.7	0.6
30% nano 0-90	0,90	Double	1.0	0.51	0.3	0.7	0.6
20% R 0-90	0,90	Double	1.0	0.51	0.3	0.7	0.6
30% R 0-90	0,90	Double	1.0	0.51	0.3	0.7	0.6
20% nano 0-25-90-135	0,45,90,135	Double	1.0	0.51	0.3	0.7	0.6
20% R 0-25-90-135	0,45,90,135	Double	1.0	0.51	0.3	0.7	0.6
Osteoink	N/A*	Double	1.0	0.51	0.3	0.7	0.6

Table 14 - Design parameters for scaffolds across the range of geometries and composites tested. Layer orientation, repetition and line spacing were varied with nozzle diameter and extrusion width used to accommodate the target filament width.

Scaffold Type	Melting Temperature(°C)	Screw Extrusion Temperature(°C)	Extrusion Pressure (MPa)	Extrusion Speed (mm.s ⁻¹)
PCL single layer	68	69	0.40	8
PCL 0-90	68	69	0.40	8
PCL 0-60	68	69	0.40	8
PCL 0-45-90-135	68	69	0.40	8
PCL 0-90 0.7 spacing	68	69	0.40	8
PCL 0-60 0.7 spacing	68	69	0.40	8
PCL 0-90 0.8 spacing	68	69	0.40	8
PCL 0-60 0.8 spacing	68	69	0.40	8
PCL pPEA	68	69	0.40	8
Reused PCL	68	69	0.40	8
EO Sterilised PCL	68	69	0.40	4
PCL 0.33 Needle	68	69	0.40	8
Low Temp 20% nano	96	98	0.45	6
High Temp 20% nano	102	105	0.45	6
20% nano 0-90	102	100	0.45	6
30% nano 0-90	102	100	0.45	6
20% R 0-90	102	100	0.45	6
30% R 0-90	102	100	0.45	6
20% nano 0-25-90-135	102	100	0.45	6
20% R 0-25-90-135	102	100	0.40	6
Osteoink	N/A*	N/A*	0.4	8

*Table 15 - Scaffold printing parameters for each condition. After a series of failed prints, the most stable melting and extrusion temperatures, pressure and speed are detailed. *Pressure extrusion only*

4.2.2.6 Theoretical porosity analysis

To investigate mechanical properties as a product of porosity and density, triplicates of 0/90° and 0/60° at 1.0mm 0.8 and 0.7mm line spaced scaffolds were printed and weighed using a microbalance (Pioneer PA64, Ohaus). Porosity was calculated from the means for each condition using the formula:

$$\text{Porosity} = 1 - \left(\frac{\rho_{\text{Scaffold}}}{\rho_{\text{Material}}} \right) * 100$$

$$\rho_{\text{Material}} = 1.145\text{g/cm}^3$$

$$\rho_{\text{Scaffold}} = \frac{\text{Mass}}{\text{Volume}} = \frac{\text{Mass}}{\pi r^2 h}$$

Where ρ =density, r = radius of scaffold, h = height of scaffold.

4.2.2.7 Scaffold printing

4.2.2.7.1 PCL Printing

PCL and composite scaffolds were 3d printed using a RegenHU Discovery 3D (Regen Hu, Switzerland) into a class 2 hood with an ambient temperature of 20-24 °C. Samples were printed (using parameters outlined in tables 17 and 18 and demonstrated in Figure 50) onto adhesive tape on microscopy slides and allowed to cool before removal. Scaffolds were stored in a clean dry environment at room temperature.

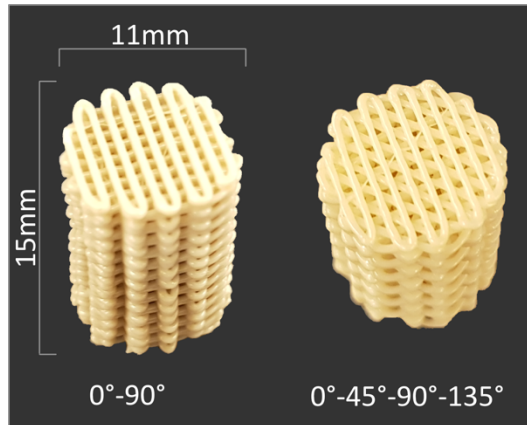


Figure 50 - Examples of final scaffold prints. Dimensions were consistently 11x15mm however layup pattern and thus density, pore size and shape varied between sample type.

4.2.2.7.2 Measurement of pore size

To explore the difference between the theoretical dimensions of 3D printed scaffolds, scaffold of pure PCL and PCL/HA composites were printed and allowed to cool for >24 hours. Microscopic photos of the top, side and cross section were taken (Stemi 2000-C, Zeiss). Images of a scale bar at appropriate magnification were used to calibrate image analysis software (Fiji Image J, v1.52i for Macintosh, open source, National Institutes of Health, USA) and 10 replicates of each measurement per sample were taken of representative pores in the sample (Figure 51).

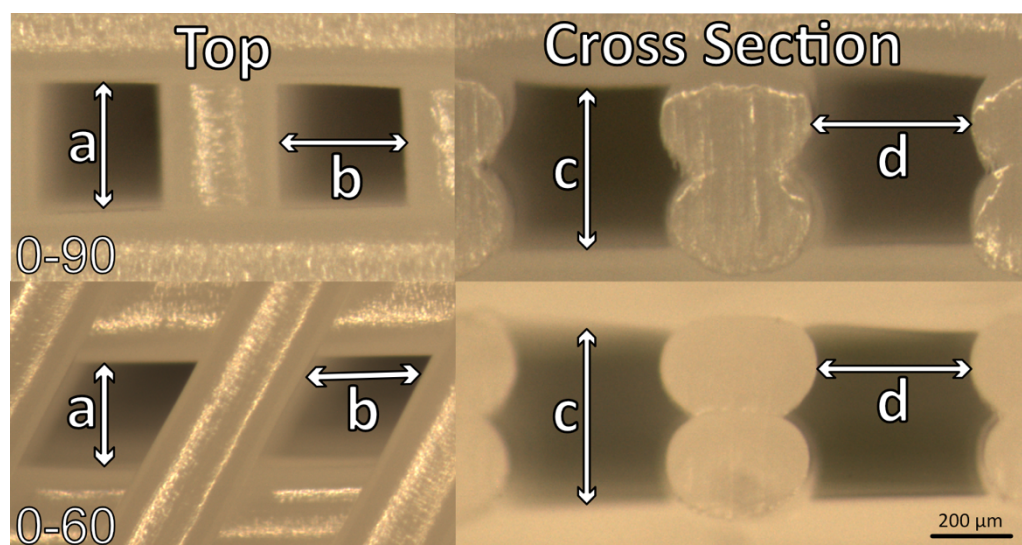


Figure 51 - Measurements made of pore size for 0-90 and 0-60 (parallelogram). a) length b) width c) height d) internal width.

4.2.2.8 Control material preparation

Solid samples were formed using custom 3D printed moulds with internal cylindrical dimensions of 11 mm x 17 mm. They were designed using Tinkercad (Autodesk Inc), sliced using Cura (Ultimaker B.V) and formed using polylactic acid (Colorfila, BCN3D, Barcelona) via a 3D fused filament fabrication printer (SigmaMax, BCN3D, Barcelona) (Figure 52). Following curing, moulds were sliced and snapped to remove PLA mould from solid samples, which were then cut down to 15 mm length to account for setting contraction prior to mechanical testing.

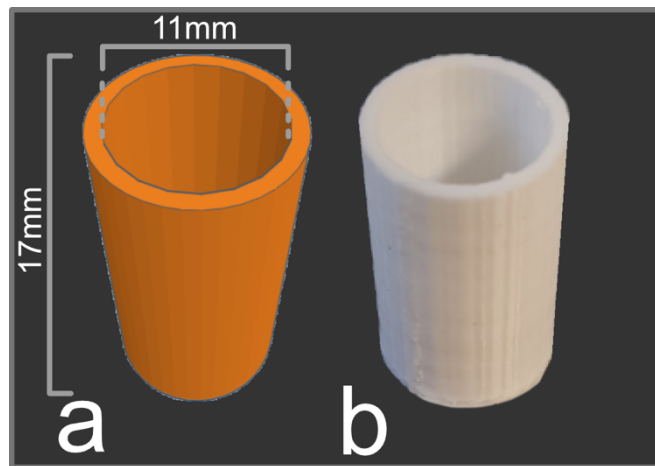


Figure 52 – CAD mould. a) CAD mould design and b) 3d Printed PLA mould with internal diameter 11mm and external diameter 17mm. Moulds intentionally made long to allow for solid material expansion/meniscoid retraction which was then machined down to 15mm to give comparable dimensions to the 3D printed scaffolds.

4.2.2.8.1 Solid composites

Granules of PCL, 20% nanoHA/PCL and 20%RHA/PCL were inserted into the mould and placed into an oven at 70 °C. The mould was topped up until full then allowed to cool at room temperature. Moulds were left for >24 hours before testing then scored and split free from the composites.

4.2.2.8.2 Optipac® bone cement

Optipac® Refobacin® Bone Cement R (Biomet Orthopaedics, Switzerland) was mixed the proprietary vacuum mixing system (Optivac®) in which liquid monomer (along with N,N-dimethyl-p-toluidine as an initiator, benzyl peroxide as a catalyst, hydroquinone stabiliser and green dye) is added to the polymer powder (including barium sulphate and gentamicin) (Figure 53). Under vacuum, the cement was mixed for 30 seconds as per manufacturer's instructions (Figure 54) until a homogenous mix achieved, then vacuum seal broken and injected into the moulds at RT and allowed to set for 24 hours before testing.



Figure 53 – Optipac® bone cement mixing device and plastic moulds. Monomer (green) is added to the white polymer powder within the canister under vacuum then manually mixed.



Figure 54 – Schematic from manufacturer's literature. Mixing, vacuum release and preparation for injection is demonstrated.

4.2.2.8.3 Simplex® bone cement

Simplex® bone cement (Stryker, Freiburg, Germany) was prepared as above by adding the liquid monomer (with N,N-dimethyl-p-toluidine, benzyl peroxide and hydroquinone) to the polymer powder (including barium sulphate and erythromycin cement) and mixed for 30 seconds until homogenous. Cement was poured into the mould and allowed to set for 24 hours at RT.

4.2.2.8.4 Hydroset® Calcium Phosphate Bone Substitute

Hydroset® (Stryker, Freiburg, Germany) was reconstituted as per the manufacturer instructions by mixing HA powder with liquid (which is subject to industry secrets), placed into the provided syringe for low pressure injection into the mould and allowed to cure between 18 and 22°C for 30 minutes.

4.2.2.8.5 OsteoInk

OsteoInk (RegenHu, Switzerland) is a commercially available HA/TCP suspension specifically designed for the Discovery 3D bioprinter. It is supplied in a 5cc cartridge. The cartridge and pressure adapter were added to pressure extrusion module of the printer. Scaffolds were designed as per the mechanical scaffold method described in 4.2.2.5 and extruded at 0.4MPa onto glass. The scaffolds were cured at 37 degrees for 48 hours until solid before removal.

4.2.2.9 Functionalisation

Samples for *in vitro* analysis were functionalised using plasma PEA, fibronectin and BMP-2. Plasma was carried out as previously in 2.2.2.3 using air plasma then EA polymer introduced into a plasma state for 15min 50watts at a pressure of $1.5-2.0 \times 10^{-1}$ mbar before cessation of plasma state and vacuum release via air filtration.

Human fibronectin was diluted to 20mg/ml in DPBS and adsorbed in a vacuum for 60 minutes, then washed with DPBS and MilliQ water.

1% w/v BSA in MilliQ was inactivated and added to samples for 30 minutes before triple wash and adsorption of BMP-2 at 50ng/ml in DPBS. After 60 minutes, the BMP-2 solution was removed before wash with DPBS.

4.2.2.10 Surface mineral assay

To assess adequate coverage of HA/PCL composites with plasma PEA a surface mineralisation assay was undertaken with the hypothesis being the demonstration of reduced mineral detection would indicate effective PEA coating. The OsteoImage™ kit (Lonza, Basel, Switzerland) uses a fluorescent staining agent specific to HA, unlike the non-quantitative von Kossa stain against phosphates or Alizarin red against calcium. Duplicates 0/90° scaffolds with double layering and 1.0 mm spacing and were printed as per variables in tables 17, 18 and Figure 48, using 30% nanoHA, 30% R HA and PCL as a baseline for normalisation. 0.2 ml of staining reagent was added to each well and incubated at RT in the dark for 30 minutes. The staining reagent was then removed and discarded before a triple 5 minute rinse with diluted wash buffer. Following removal of the 3rd wash, 1ml of wash buffer was added to each well. Microscopy photos were obtained of the scaffolds. Fluorescence was measured using a photospectrometer (Thermo Scientific) with excitation and emission wavelengths set to 492 nm and 520 nm respectively.

4.2.2.11 Cell culture

Primary human mesenchymal stem cells (Promocell) were thawed from stock and expanded using high glucose DMEM supplemented with 1.9% v/v penicillin/streptomycin, 1-% v/v FBS, 0.1% sodium pyruvate and non-essential amino acids. Cells were cultured at 37°C with media changed every 3-4 days. Only cells up to the 3rd passage were used. After confluence achieved, cells were rinsed with PBS trypsinised using EDTA/trypsin and added to UV sterilised

scaffolds in a tissue culture treated 48 well plate in 300 μ l quotients to encourage adhesion to the scaffolds. After 1 hour, media was topped up to 600 μ l, then changed twice weekly until the 28 day timepoint. For 3 scaffolds, a positive control was used by the addition of 25 ng/ml of BMP-2 was added for each media change (Table 19).

Sample No.	Composite	Layer Geometry	Scaffold Coating	Media
1-3	Pure PCL	0-90	pPEA, FN, BMP-2	Standard
4-6	Pure PCL	0-60	pPEA, FN, BMP-2	Standard
7-9	20% nano HA	0-90	pPEA, FN, BMP-2	Standard
10-12	30% nano HA	0-90	pPEA, FN, BMP-2	Standard
13-15	20% R HA	0-90	pPEA, FN, BMP-2	Standard
16-18	30% R HA	0-90	pPEA, FN, BMP-2	Standard
19-21	Pure PCL	0-90	pPEA, FN, BMP-2	Osteogenic

Table 16 - Sample groupings for in vitro RNA expression. Pure PCL scaffolds with 2 geometries were compared to one another and different compositions of HA/PCL. PCL with osteogenic media was used as a positive control.

4.2.2.12 Alamar blue

Cell viability on various scaffold pore sizes was analysed using alamarBlue[®] assays, which demonstrate a colorimetric change in proportion to cell activity. Active cells reduce blue resazurin to fluorescent red resofurin. Following 14, 21 and 28 days of cell culture, triplicates of scaffolds were removed from 48 well plates and washed with DPBS. 60 μ l of alamarBlue (BioRad, California, USA) was added to each well, alongside positive and negative reagents and incubated for 4h at 37°C and 5% CO₂. The supernatant from each scaffold was

removed and divided into 2 wells in a flat bottom 96-well plate (Costar, Corning, Maine USA) and colour change measured using a photospectrometer (M200, Tecan, Männedorf, Switzerland) with absorbance wavelengths of 570nm and 600nm. The percentage reduction in alamarBlue reagent was calculated using:

$$\% \text{ reduction of alamarBlue} = \frac{\text{experimental RFU value} - \text{negative control RFU value}}{100\% \text{ reduced positive control RFU value} - \text{Negative control value}} * 100$$

RFU = relative fluorescence units

4.2.2.13 Actin staining

Visualisation of cell attachment and migration of scaffolds was performed using actin staining. Following 24 days of cell culture, 0/60 and 0/90 PCL scaffolds (functionalised with plasma PEA, FN and BMP-2) were washed with DPBS and fixed using PBS/10%formalin(v/v) at 37°C for 15 minutes. The fixative was removed and cells permeabilised with 0.5% triton X-100 solution in PBS(+ 10.3gsucrose, 0.292gNaCl, 0.06gMgCl₂ and 0.476ghepes) for 5 minutes at 4°C. Triton solution was removed and PBS1%(w/v)BSA was added then incubated at 37°C for 15 minutes before removal and addition of phalloidin (1:500 with PBS1%(w/v)BSA) and incubation phalloidin was removed. Finally, three 5 minutes washes with PBS/0.5%(v/v)Tween before vectroshield-DAPI was applied onto the scaffolds and visualisation using a fluorescent microscope (Zeiss Z1 AX10 and MicroManager version 1.4 for windows, Open Imaging Inc, UCSF).

4.2.2.14 Quantitative polymerase chain reaction (qPCR)

4.2.2.14.1 RNA isolation

RNA was isolated using RNeasy (Qiagen) media washed off with DPBS then 350 µl buffer solution and 70% ethanol. Samples were transferred to filtering membrane collection tubes and centrifuges at 10,000 rpm for 1 minute and excess fluid discarded. 350 µl of buffer was centrifuges through for 1 minute

at 10,000rpm before addition of 80 µl of DNase/buffer (7:1) and incubated at room temperature for 15 minutes. 350 µl was then added to the collection tube and centrifuged at 10,000 rpm for 1 minute. The flow through was discarded and 500 µl buffer added then centrifuged as before. 80% ethanol was then centrifuged at 10,000 rpm through for 2 minutes before a 5 minute drying centrifuge at 30,000 rpm. Finally, 14 µl of RNase-free water was added to the filtering membrane and a 1 minute 30,000 rpm centrifuge into a fresh collection tube was performed to elute the RNA.

A NanoDrop 1000 spectrophotometer (Thermo Scientific) was calibrated and 1.5 µl of each sample was added sequentially and concentration (ng/µl) of RNA calculated (NanoDrop Spectrophotometer v3.8 for windows).

4.2.2.14.2 Reverse transcription

Genomic DNA elimination reaction components were formulated using 2 µl of gDNA Wipeout buffer 1 µg of template RNA from 4.2.2.10.1 and made up to 14 µl using RNase-free water before controlled incubation in a thermal cycler (ProFlex PCR, Thermofisher) at 42 °C for 30 minutes then rapidly cooled to 4 °C. 1 µl of reverse transcriptase, was added to 5 µl of RT buffer and RT buffer (4:1), then mixed with the genomic DNA elimination reaction components and transferred to the thermal cycler for 30 minutes at 42 °C, then 95 °C for 3 minutes and finally rapidly cooled to 4 °C and stored at -20 °C. The 7 day samples were analysed for expression of alkaline phosphatase (ALP), runt-related transcription factor (RUNX2) and transcription factor sp-7, also known as osterix (OSX), which are markers of early bone formation. 28 day samples were analysed for gene activity for osteopontin (OPN), osteonectin (ON), which are non-collagenous glycoproteins expressed in extracellular bone matrix and osteocalcin (OCN) which is a less specific hormone related to osteoblast activity.

4.2.2.15 Alkaline phosphatase activity

0-90 scaffolds were printed as per 4.2.2.6, functionalised as per 4.2.2.8 and cultured with MSCs as per 4.2.2.9 for up to 28 days. At time points 7, 14, 21 and 28 days, triplicates of scaffolds were washed with DPBS – twice. 500 µl of ice cold Tris-HCL was added and kept at -80 °C.

After 28 day culture, all samples were thawed and sonicated for 2x10 seconds at 5 W, then centrifuged at 10,000g for 5 minutes to extract protein from the scaffold/cell complex. A standard curve was made by serial dilution of 50 µl BSA triplicates with 150 µl BCA working reagent, then 150 µl BCA working reagents (A, B & C at ratios 25:24:1) was added to 50 µl of Tris-HCL as a 'blank' reading, and to 50 µl of each sample before incubation at 37°C for 2 hours in a 96 well plate (Costar 3596, Corning, USA). Colourmetric reading of results were obtained using a photospectrometer (Infinite M200PRO, Tecan, software, Tecan i-control v3.8.2 for Windows) with a 5 second shake and reading at wavelength 562nm. Mean blank results were deducted from the absorbances, a standard curve was plotted with a polynomial trend line then combined with to calculate protein concentration (mg/ml) for each sample.

Substrate solution was produced from 500 µl 1M NaCO_3 , 2ml 5xdiethanolamine buffer, 7.5 ml MilliQ water and 34µl of 4-methylumbelliferyl phosphate disodium salt (MUP) solution. A standardisation curve of ALP was prepared from stock 1 U/µl solution to a concentration of 0.025 U/µl (in MilliQ water) then further diluted in DPBS to 0.01 U/µl and used to create a series of standard triplicate (from 5 mU/µl to 0.078125 mU/µl) of which 25µl was added to 100 µl substrate. Blank triplicates were created from 25 µl Tris-HCL and 150 µl of substrate. 25 µl of each sample was added to a 96 well plate (Costar 3596, Corning, USA) with 100µl of substrate the incubated in the dark at 37°C for 1 hour. Fluorescence was read using the same photospectrometer with an excitation at 360 nm and emission of 465 nm.

Mean blank values were deducted from absorbances and the standard curve formula again used to calculate the units/µl of ALP in each sample. This was represented graphically, and the proportion of protein attributable to ALP

(mU of ALP per mg protein) calculated by division of ALP by concentration of protein.

4.2.2.16 Ethylene oxide

Ethylene oxide sterilisation was carried out at Andersen Caledonia LTD using the same parameters as 2.2.2.7 in which a preconditioning humidification in 35-41% conditions at physiological temperatures of 38-41 °C occurred for 16 hours. Following this exposure to EO gas at 49 °C for 3 hours occurred before evacuation of gas and aeration for 8 hours at 38-43 °C.

4.2.2.17 Mechanical analysis

15x11 mm samples were orientated vertically in a Zwick/Roell Z250 with a load capacity of 250 KN load cell and controlled using testControl v6.01, under a constant force with wide bearing plates so no slippage or surface friction was observed so further supports were not required (Figure 55). The deformation range was set from 0-10 mm and digitally calibrated to a zero state. 1 mm per minute of compression was achieved and the corresponding force to achieve said compression was recorded and tabulated using testXpertII v2.1.

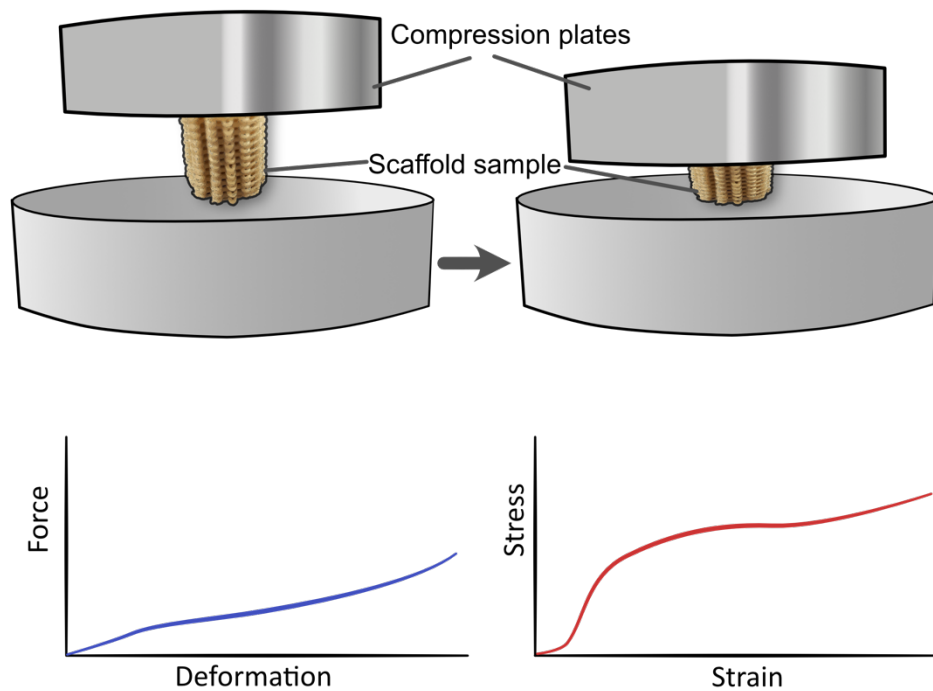


Figure 55 - Schematic of compression testing. The load cell calculates the force required to cause a deformation. The stress force per area is then plotted against strain (change in length per original length).

Standard force (N) was measured for each standard travel (mm). Surface area was calculated using the formula $A=\pi r^2$. Strain was calculated by change in length/original length (in this case 15mm). Stress (MPa) was calculated using force per unit area, in this case $N/(\pi r^2)$. Stress strain graphs were plotted using Microsoft Excel For Macintosh (version 15.32, Microsoft Inc.) (Figure 56).

4.2.2.17.1 Stiffness

Young's modulus (E) for each condition calculated by establishing a linear trend line in the elastic region of each material's stress strain curve (linear defined as an R^2 value >0.999) and dividing stress by strain (Figure 56).

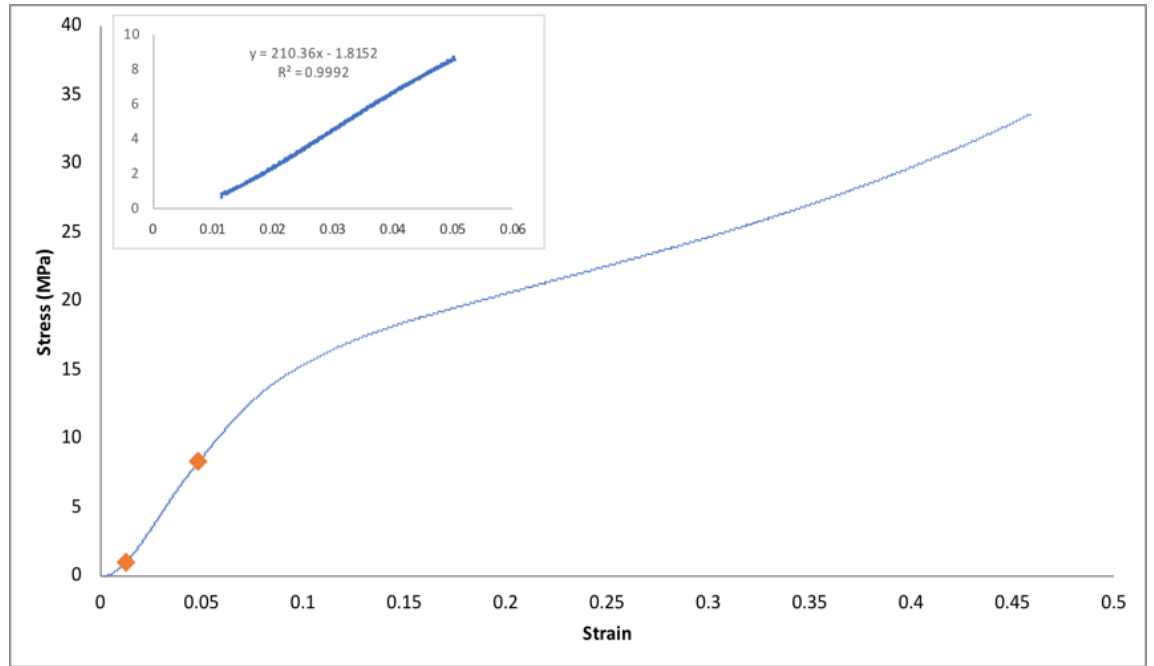


Figure 56 - Stress strain example. The stress (MPa) is calculated for each sample base upon scaffold geometry and deformation. These formed a typical appearance with an elastic and plastic zone. The most linear segment within the elastic zone (orange diamonds) was verified with an R^2 calculation for the line. The formula for this line is used to calculate the Young's modulus).

4.2.2.17.2 Strength

Due to the broad curvature of the yield point, a 0.2% proof stress model was used to determine strength of the samples. This point is nominally accepted as the point at which a material leaves the elastic stage and enters plastic deformation stage. The line used for Young's modulus was continued to the horizontal (strain) axis, then translated by 0.2% (Figure 57). The point transected by the curve was then defined as the yield point for each sample and stress value used accordingly.

For samples which demonstrated an evident yield point (i.e. pure calcium phosphate) this point was used as the strength measurement.

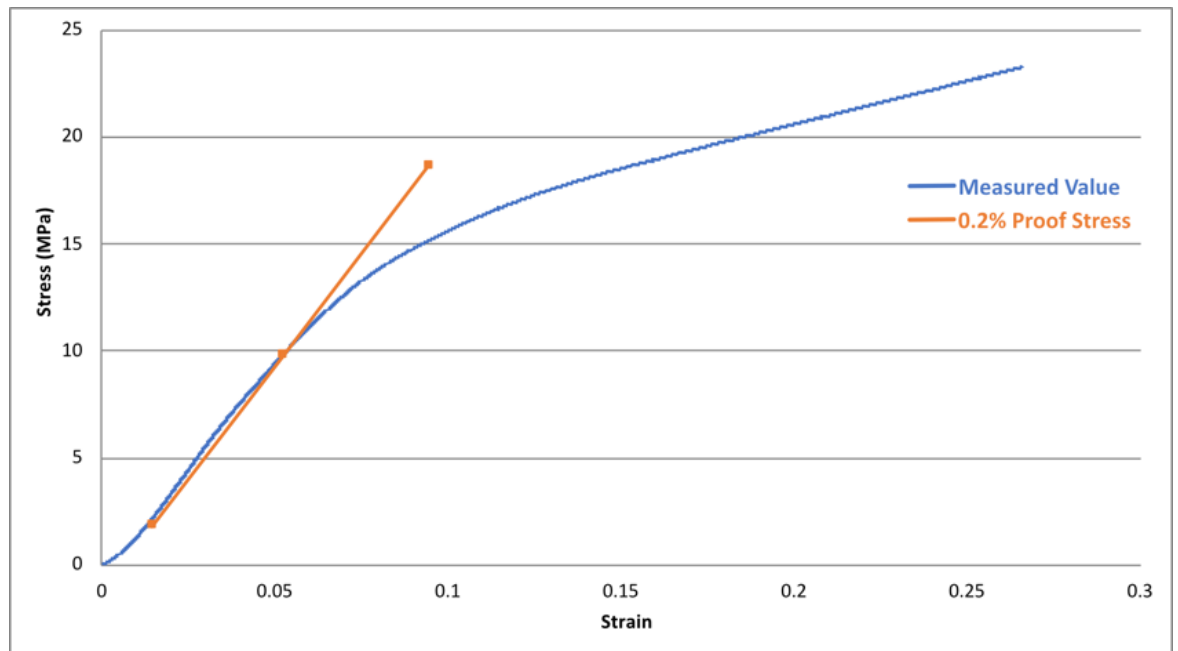


Figure 57 - 0.2% proof stress example. The yield point was used to define the strength of a material, at which point it transforms from an elastic to a plastic state. The issue often arises where visually, this point is not clear. The 0.2% proof stress method is an established definition, in which the line used to define the Young's modulus, is translated along the x-axis by 0.2% and the stress value at which this line transects the measurements on the stress strain curve (middle orange diamond) is the definition of the yield point.

4.2.3 Statistical analysis

Data was analysed using Graphpad Prism (version 6 for Macintosh, GraphPad Software, La Jolla California USA) with normal distribution tested using the Shapiro-Wilk normality test then comparison of means carried out using t-test or Mann-Whitney U test for parametric and non-parametric data respectively. Where multiple comparisons were performed an ANOVA analysis or Kruskal Wallis test was used for parametric and non-parametric data respectively, with application of Bonferroni or Dunn's correction for incidental significance. A p-value of <0.05 was considered statistically significant.

4.3 Results

Summary of Results

Due to differences in mass, volume and thermal properties between HA and PCL, creating a homogenous mix proved challenging. It quickly became evident that hand mixing was not plausible and therefore mechanical mixing and heated twin screw mixing and extrusion was performed. The quality of this mix was evaluated using SEM to ensure the mix was homogenous (avoiding clustering) and to give visual information on the interface between HA and PCL. Calculated theoretical weight percentages translated into measured volume percentages. Initial concerns that the difference in density between PCL granules and HA would cause sedimentation of HA (at the bottom of the mixture, in the mixing extruder, or in the heat tank at the beginning of the 3D printing process). This was not observed upon visual inspection of the composites with SEM, which demonstrated even distribution of HA particles throughout the matrix and confirmed as calcium phosphate particles by EDS. There was however limited integration between the HA filler and PCL matrix.

These results demonstrate that, ultimately all 3D printed porous scaffolds were mechanically inferior to solid versions of the same materials and exhibited much lower moduli and strength than commercial products, specifically *Simplex* and *Refobacin* poly (methyl methacrylate) (PMMA) bone cements. With the addition of HA as a composite material showed increased strength and stiffness in solid models which was not replicated in porous scaffolds. Further improvements in mechanical properties were seen by decreasing porosity, however when gaps reduced below 0.4mm MSCs were unable to migrate. Similarly, when gaps were larger (>1mm) then cells in the 2D environment were unable to bridge gaps.

Theoretical scaffold design in single layers showed promising pore size and porosity. However, the nature of thermal fused filament fabrication meant that, when printed the filaments 'sagged' forming ovoid shapes rather than cylindrical, reducing pore structure.

Increasing layup geometry complexity did not improve mechanical properties. The addition of HA did not improve mechanical properties with the best scaffold achieving approximately 10% of the stiffness of metaphyseal bone. Reassuringly however, processing parameters (such as reusing PCL, plasma treatment and EO sterilisation) did not result in reduced mechanical properties of scaffolds.

In vitro activity was noted in MSCs seeded onto functionalised scaffolds, indicating differentiation into an osteoblastic lineage. No statistical difference was identified between pure PCL and the additions of either type or volume of HA.

4.3.1 Validation of mixing

4.3.1.1 Scanning electron microscopy (SEM)

SEM of base materials was undertaken to assist post mixing identification. It revealed more consistency in sintered HA particulate diameter (approx. 5 μ m). NanoHA clustered inconsistently and was seen as individual particles (<200 nm) up to clusters approximately 1 μ m in diameter (Figure 58).

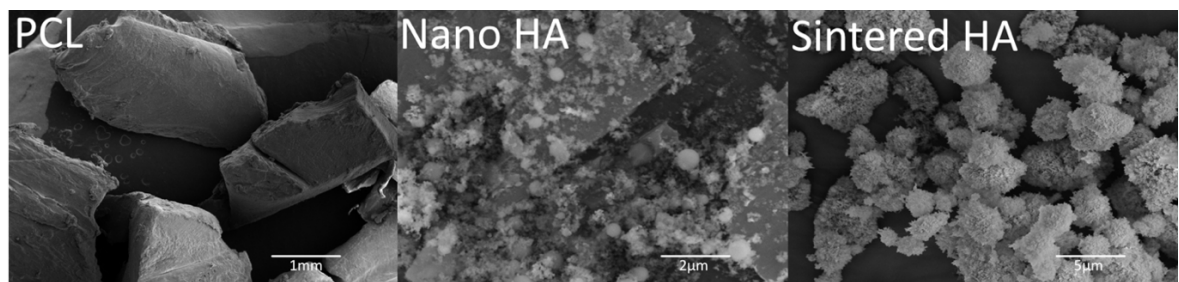


Figure 58 - SEM of PCL, nanoHA and sintered HA. Nano HA is comprised of small particles of differing sizes, which aggregate together. Sintering HA (“RHA”) forms larger particles which are more easily defined.

SEM of fractured nanoHA demonstrated evenly distributed HA with variations in size as observed in the plain material (Figure 59). The HA did not integrate well with particles which may be an artefact of proportionally different contraction properties of HA and PCL when frozen, but voids would be expected to refill upon return to warm temperature, therefore is likely to reflect a true limited interaction between polymer and ceramic. At the greater

30% volume, HA was unable to be retained within the matrix and more voids were demonstrated, indicating that 30% is perhaps beyond the retention capacity for this composite.

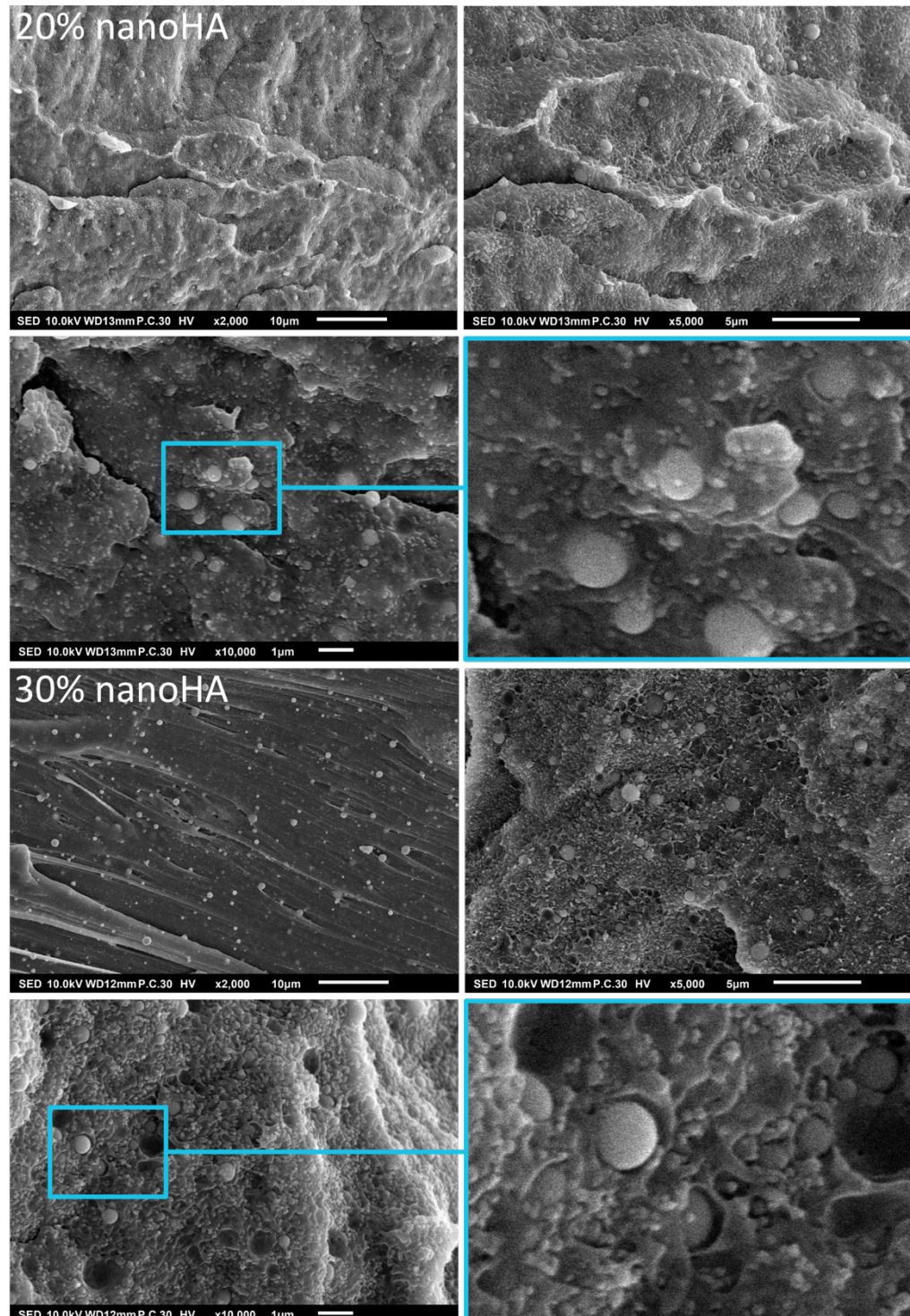


Figure 59 - Magnification series of nanoHA at 20 & 30%. HA particles are evenly distributed in both composites. There is limited integration between phases and at the high volume of HA (30%) voids were demonstrated where HA was unable to be retained by the PCL matrix.

Sintered HA also displayed even distribution and maintained particle diameter however lack of interaction with the matrix was even more pronounced (Figure 60). Fewer voids were encountered at higher volumes of HA in sintered HA when compared to nanoHA, however this could be a product of the poorer interaction with the matrix.

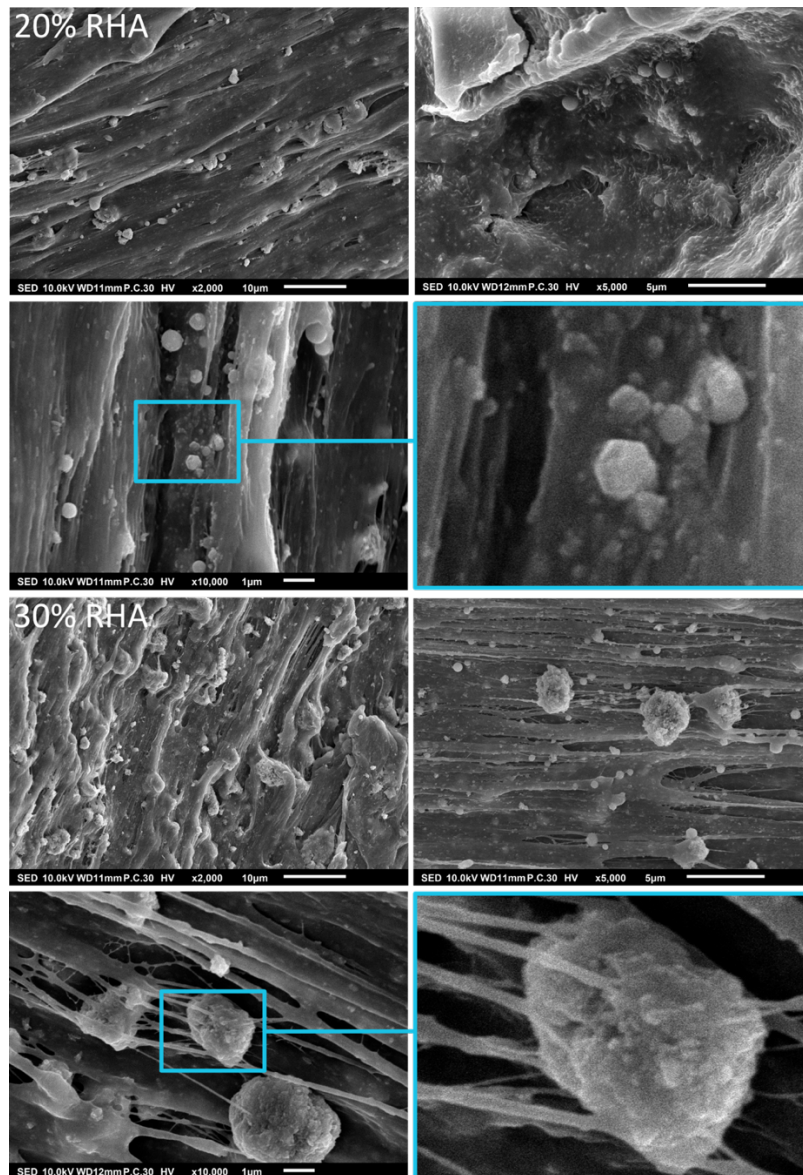


Figure 60 - Magnification series of sintered HA at 20 & 30%. The HA was again well mixed and distributed throughout the PCL matrix. At both 20% and 30% the HA did not integrate confluent within the composite

The interaction of HA following polishing was investigated with SEM to compare to current literature (200). It was apparent that this particular composition was liable to thermal changes associated with the process. As such, large volumes of HA were lost and so distribution of HA was not able to be commented upon, however in the interest of comparison to published data, remnant HA was imaged and studied (Figure 61). It was evident that the margins of polished HA were not well bound to surrounding PCL in either nano or sintered grades.

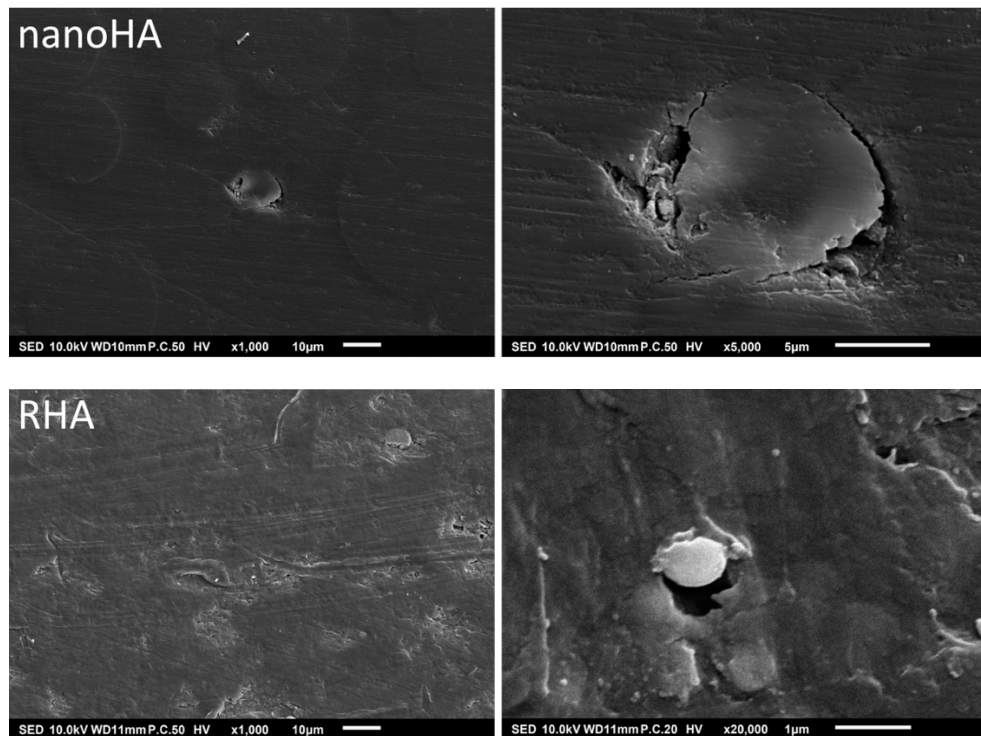
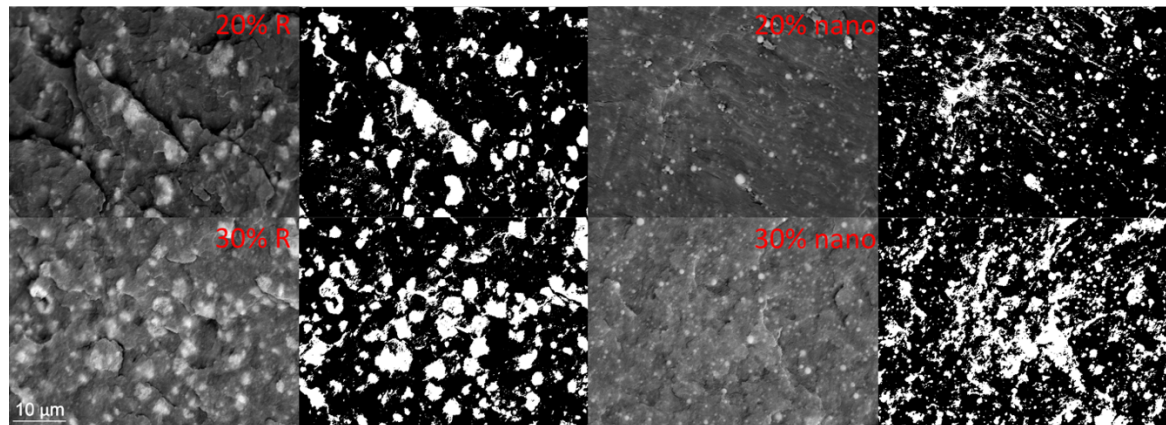


Figure 61 – EMS of Polished nanoHA and sintered HA. These show circumferential voids, indicating poor integration between the materials previously demonstrated in the literature (191).

4.3.1.2 Greyscale analysis

To quantify mix proportions, binary images were created of x5000 magnification SEM images of PCL/HA composites. This accurately represented the index picture and calculated similar volume percentages to those predicted from theoretical calculation (Figure 62).



Sample	Calculated (%)
20% nano	18.60
30% nano	31.13
20% R	18.04
30% R	27.95

Figure 62 - Greyscale analysis of visible from SEM images. Binary surface analysis of composited to visually demonstrate distribution and identify percentage of filler on composite surface. With exception of 30% nano, calculations are underestimated proportions, indicating the limit of this technique as a surface analysis tool, but also the propensity to underfill composite with the filler.

4.3.1.3 Electron dispersive x-ray (EDS)

EDS analysis at x5000 typically has a depth of analysis of 3-5 μm and quantified the white particles to be predominantly calcium and phosphate in chemistry. Some carbon and oxygen were detected which can be explained by a thin layer of polymer overlying the particles. Element mapping demonstrated defined calcium and phosphate in sintered samples however are more diffuse in nanoHA, indicating grinding of the HA particles which are more finely dispersed amongst the matrix (Figure 63).

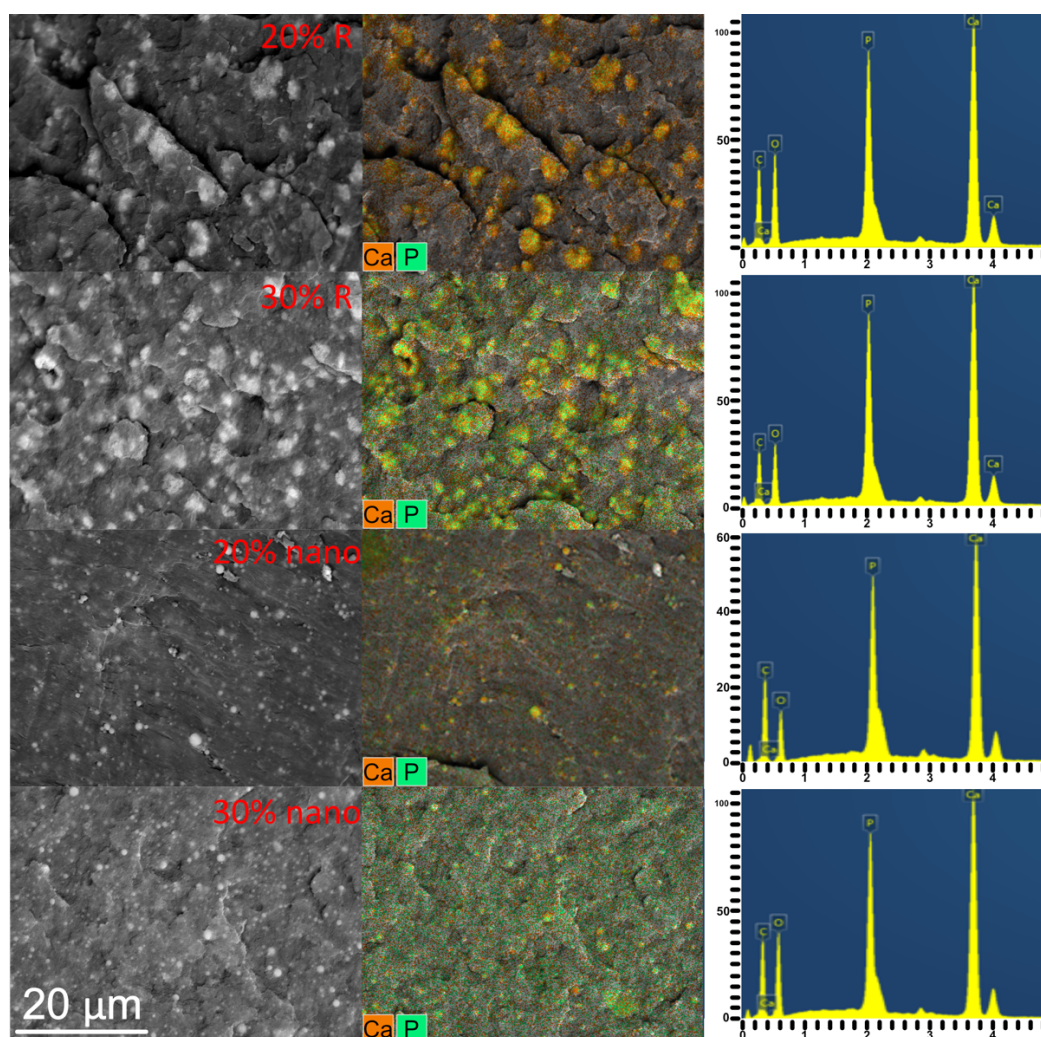


Figure 63 - EDS Analysis following reduction of the gold palladium. Original image, overlaid calcium and phosphorus signal and point analysis graphs (y-axis intensity (cps), x-axis energy (keV)). Sintered HA tends to form more easily described particles, formed of calcium and phosphate, whereas nanoHA remains more diffusely distributed.

4.3.2 Analysis of Printing

4.3.1.1 Theoretical versus physical pore dimensions

PCL samples were printed, calibrated magnified photos taken of the top, side and cross section (Figure 61). These were measured using Image J (figures 64 and 65).

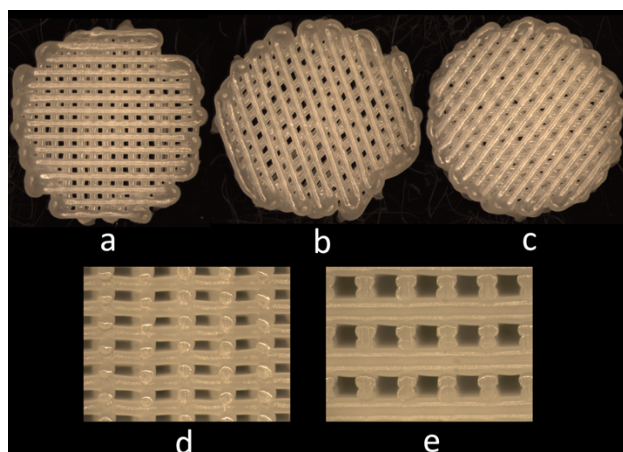


Figure 64 - Magnified photo of scaffolds a) 0-90° layup b) 0-60° layup c) 0-45-90-135° layup d) single layer repetition e) double layer repetition. Density is visibly increased with 0-45-90-135° and cross sectional pore size is clearly larger with double layering.

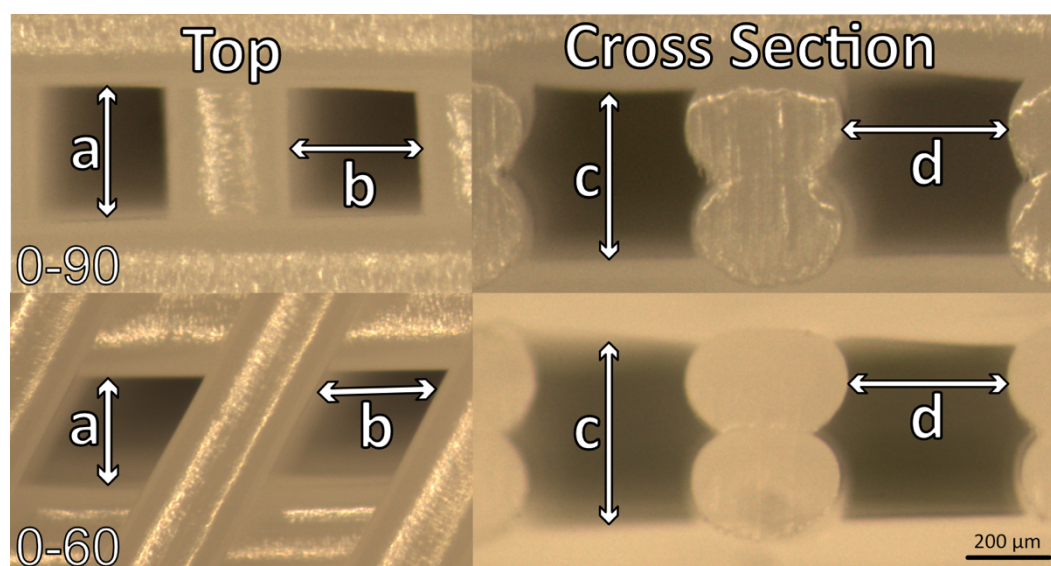


Figure 65 - Measurements of pore size parameters. a) length b) width c) height d) internal width

Absolute reduction in pore size was observed across all prints indicating scaffold sagging as opposed to cooling contraction (Table 20). When compared to theoretical pore sizes there was an exponential reduction in

pore volume from theoretical measurements (Table 21). There is probably also an increasing effect of sagging with smaller gaps as filaments get closer and radiate heat to one another. Additionally, there are fewer air gaps for heat to be dissipated, causing longer heat retention and more time to remain liquid and be subjected to weight of subsequent layers. Reassuringly there was no measurable difference in sagging and thus pore size with the addition of hydroxyapatite (Table 21). Anecdotally, this is a result of slowing down the print speed to give each filament strip time to cool between layers. Ultimately, double layering was adopted for ongoing printing as whilst they exhibited proportionally quite a large loss of volume (mean 54% and 39% for the 0.5mm and 0.33mm needle respectively) these had consistently the largest remaining volume with a mean of 0.16mm^3 (range $0.14\text{-}0.17\text{mm}^3$).

Size (mm), SD												
	Theoretical	Measured	Theoretical	Measured	Theoretical	Measured	Theoretical	Measured	Theoretical	Measured	Theoretical	Measured
	0-90 single (mm, SD)		0-90 double (mm, SD)		0-60 (mm, SD)		0-60 0.8 (mm, SD)		0-60 0.7 (mm, SD)		0-90 0.8 (mm, SD)	
a) Length	0.7	0.68, 0.01	0.7	0.5, 0.01	0.4	0.5, 0.03	0.5	0.24, 0.02	0.4	0.34, 0.01	0.5	0.33, 0.02
b) Width	0.7	0.66, 0.02	0.7	0.5, 0.02	0.4	0.5, 0.03	0.5	0.25, 0.03	0.4	0.35, 0.02	0.5	0.34, 0.02
c) Height	0.3	0.26, 0.02	0.6	0.6, 0.02	0.6	0.6, 0.05	0.6	0.51, 0.02	0.6	0.55, 0.02	0.6	0.56, 0.01
d) Internal width	0.7	0.61, 0.05	0.7	0.5, 0.03	0.4	0.5, 0.02	0.5	0.20, 0.03	0.4	0.19, 0.02	0.5	0.30, 0.03
Simplified volume (a*b*c, mm³)	0.15	0.12	0.29	0.14	0.29	0.17	0.15	0.06	0.10	0.03	0.15	0.11
	0-90 0.7 (mm, SD)		0-90 0.33 needle (mm, SD)		20% nanoHA (mm, SD)		30% nanoHA (mm, SD)		20% R HA (mm, SD)			
a) Length	0.4	0.34, 0.01	0.75	0.65, 0.02	0.7	0.54, 0.03	0.7	0.55, 0.03	0.7	0.57, 0.03		
b) Width	0.4	0.35, 0.02	0.75	0.63, 0.02	0.7	0.58, 0.03	0.7	0.57, 0.03	0.7	0.58, 0.04		
c) Height	0.6	0.55, 0.02	0.5	0.42, 0.03	0.6	0.52, 0.03	0.6	0.52, 0.04	0.6	0.53, 0.04		
d) Internal width	0.4	0.19, 0.02	0.75	0.54, 0.02	0.7	0.54, 0.02	0.7	0.55, 0.02	0.7	0.56, 0.01		
Simplified volume (a*b*c, mm³)	0.10	0.07	0.28	0.17	0.29	0.16	0.29	0.16	0.29	0.17		

Table 17 - Change in pore dimensions due to printing process. (Samples were printed using pure PCL, with a 0.5mm needle and double layering unless stated otherwise). Absolute reduction in pore size was observed across all prints indicating scaffold sagging as opposed to cooling contraction.

% loss in size/volume						
	0-90 single	0-90 double	0-60	0-60 0.8	0-60 0.7	0-90 0.8
a) Length	2.76	28.07	18.41	33.52	41.01	12.04
b) Width	5.62	27.26	22.08	32.02	38.28	6.89
c) Height	14.20	12.24	6.64	7.42	15.78	8.23
d) Internal width	13.12	27.04	31.67	39.57	51.28	41.81
Simplified volume (a*b*c, mm ³)	21.26	54.08	40.64	58.16	69.34	24.84
	0-90 0.7	0-90 0.33 needle	20% nano	30% nano	20% R	
a) Length	14.71	13.75	22.44	21.19	18.67	
b) Width	12.39	15.61	17.87	18.32	17.74	
c) Height	8.21	16.61	13.98	13.06	11.55	
d) Internal width	52.66	27.59	23.49	22.11	20.09	
Simplified volume (a*b*c, mm ³)	31.41	39.1	45.21	44.03	40.83	

Table 18 - Changes in pore size and volume as a percentage of theoretical size. All samples had their theoretical pore volume reduced by at least 20%, impacting the super-macroporous nature of the scaffolds. Note, repeated failures to print 30% R rendered the printer unable to print further samples for analysis.

The directional ‘drag’ effect of building up a layered scaffold frequently caused warping of the layer below in a slight ‘zig-zag’ pattern (Figure 66).

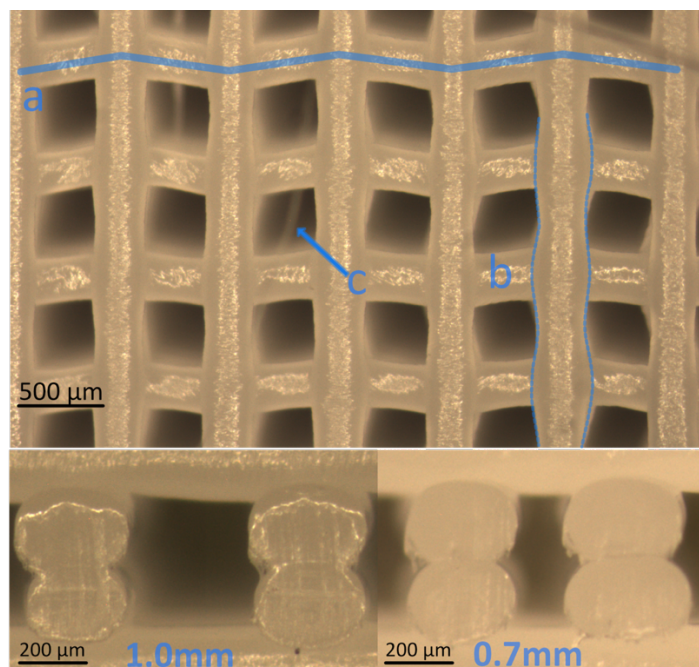


Figure 66 – Above: 0-90 layer orientation with 0.8 gap. A) warping of layers b) stretching/uneven contraction of filament and c) stringing deeper in the scaffold. Below: Difference in cross-sectional pore area as a result of reducing line spacing.

4.3.2.2 Density and porosity

Printed scaffolds were weighed with density calculated from known values to represent porosity as a percentage (Table 22).

Scaffold	Line Space (mm)	Mean Mass (g)	Density (g/cm ³)	Porosity (%)
0/90°	1.0	0.81	0.57	50.45
	0.8	0.95	0.66	42.04
	0.7	1.23	0.87	24.43

Table 19 - Density and Porosity of 0/90° scaffolds. Whilst pores are large in these scaffolds are large, the overall porosity is relatively low, indicating dense material. As a reference, poly-urethane foams have a porosity of >97% (201), whereas cortical bone has a porosity of 3.5% and 7-16% in the metaphysis of the femoral neck (196,197).

4.3.3 Mechanical Analysis

Scaffolds were tested in compression with progressive loads to achieve 1mm of deformation per minute until 10mm deformation was achieved. Whilst scaffolds are certainly anisotropic, compressive loads are the most important in defect surgery, particularly in lower limbs. Bones are subject to compressive and tensile strength and occasionally bending/torsional moments however these can be modified with metal ware used to implant scaffolds, plates and screws for example are strong in tension but weak in compression.

Scaffolds were all tested to failure beyond their elastic limit with PCL folding in the centre of the cylinder consistently, whereas composites all compressed more evenly (Figure 67).

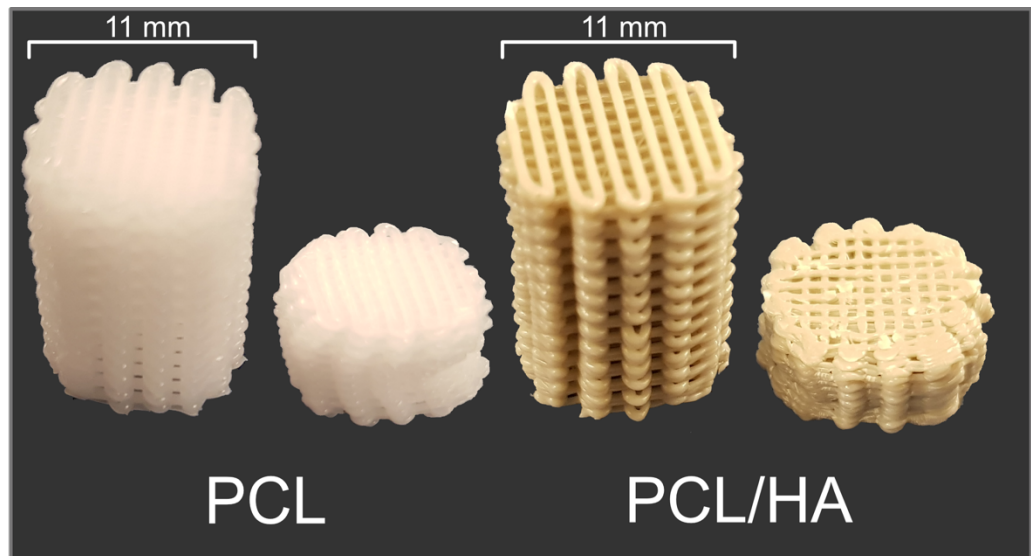


Figure 677 - Post mechanical analysis samples plastically deformed. PCL samples consistently buckled in the midportion of the scaffold and retained a degree of elasticity. Composite scaffolds had a more homogenous compression which remained plastically deformed.

4.3.3.1 Pure polycaprolactone

Baseline material strengths were obtained with solid material prepared into 11x15mm cylinders. Solid PCL as an example of maximum achievable properties of PCL, Hydroset® and Osteoink as examples of pure hydroxyapatite (Osteoink also contains tricyclophosphate). Optipac® and Simplex® are examples of commercially available bone cement which is the most applicable polymer implanted as an interface with bone. Of note, the modulus of metaphyseal bone ranges from 0.1-2GPa, cortical bone is approximately 20GPa (202) and ultra-high molecular weight polyethylene (UHMWPE) which is used as a bearing surface in arthroplasty has a modulus of 500-600MPa (203). Compressive strength cortical bone is 100-200MPa with cancellous bone weaker at 2-20MPa. Solid PCL was statistically indifferent to hydroset in stiffness and similar to both calcium phosphate compounds in terms of strength (Figure 68), however the mode by which they exited the elastic region was markedly different (Figure 69). The addition of HA did not achieve the

statistical significance which would be expected from addition of the nanofiller. As outlined before, this is most likely due to failure at the interface.

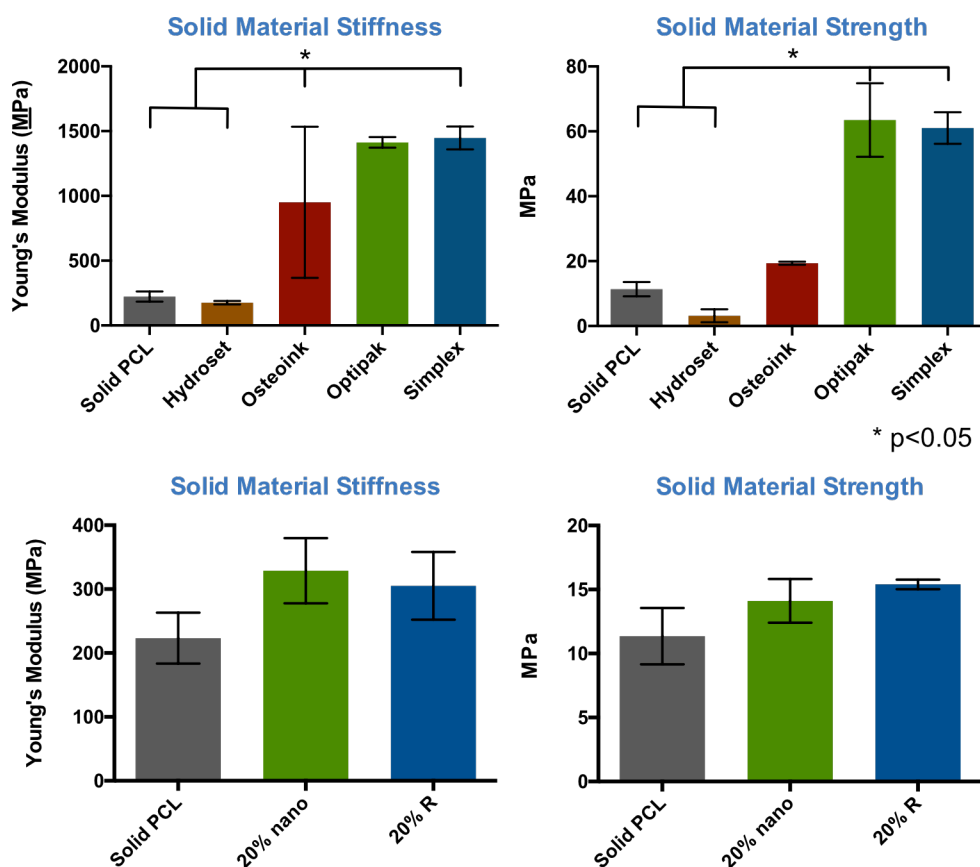


Figure 68 - PCL graph demonstrating baseline characteristics of solid components. Hydroset and Osteoink are commercial calcium phosphates. Optipak and Simplex are commercial bone cements which are the current standard for load bearing polymer (204,205)

From numbers alone, it may be possible to conclude that the mechanical properties of PCL were similar to calcium phosphate products, however the mode of failure was markedly different (Figure 70). PCL like most polymers (and indeed the remaining conditions in this Chapter) underwent progressive failure and a broad transition from elastic to plastic regions. Conversely, Hydroset® and Osteoink crumbles (figures 70a and 70b). These varied modes of failure demonstrate the different properties expected between ceramics and polymers. Whilst polymers typically are soft, they are more ductile and have a more predictable mechanical profile. Ceramics, however, have a tendency to be stiffer but much less tough, so they resist deformation

effectively, but then can fail catastrophically. The combination of these 2 materials should give similar properties to the PCL matrix, but with added stiffness associated with ceramics.

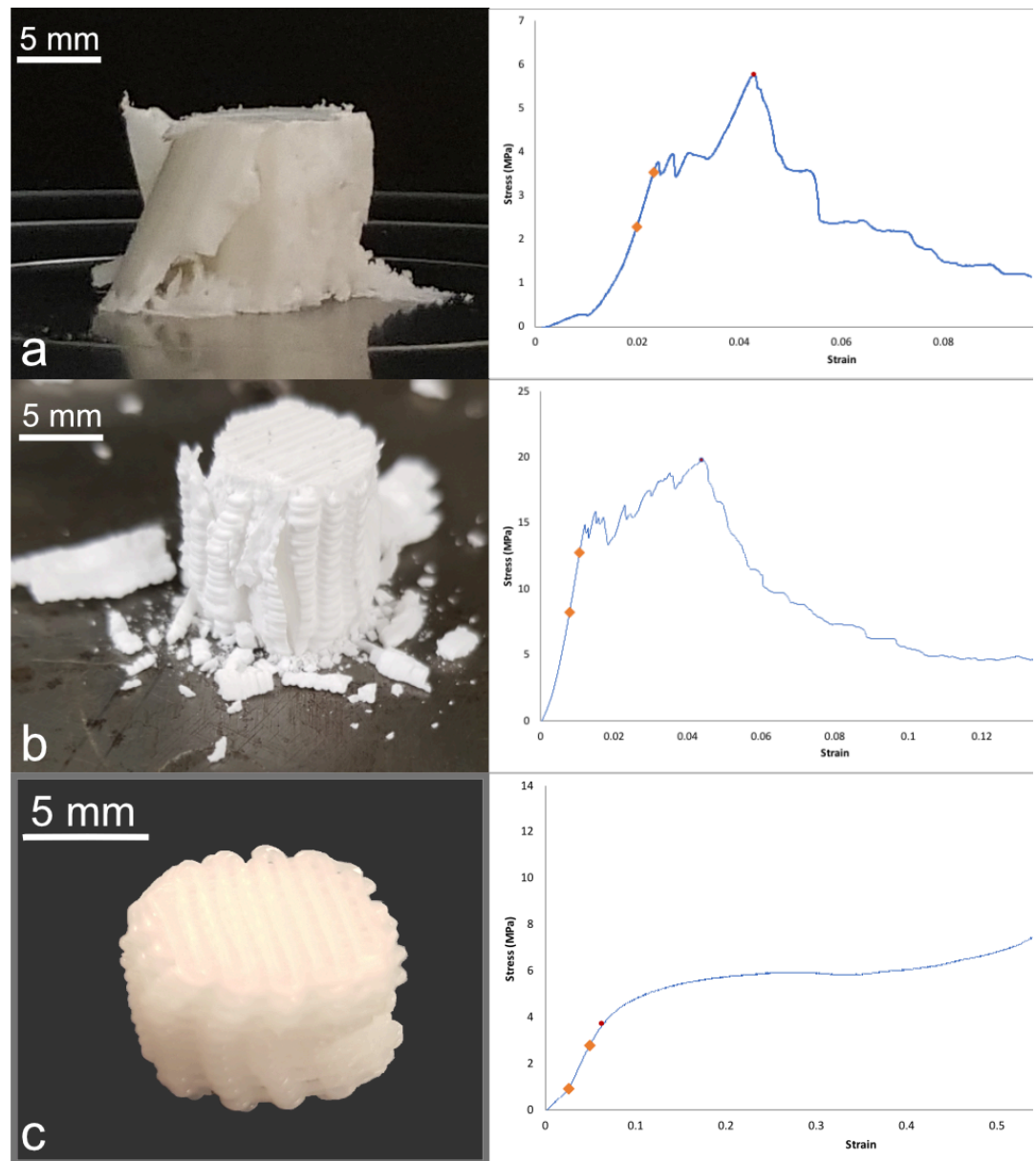


Figure 69 - Typical appearance of calcium phosphate scaffolds following mechanical analysis and corresponding stress strain curves. a) Hydroset® b) Osteoink. Orange diamonds – portion of elastic behaviour used for modulus calculation. Red circles – point defined as strength c) typical visual and stress/strain appearance of a pure PCL scaffold.

Exploring the effect of reducing pore size via single layer repetition and reducing filament width using a smaller nozzle diameter demonstrated no statistical difference in mechanical features (Figure 70). There was a trend to increased strength and stiffness with wider filaments which was adopted for remaining conditions.

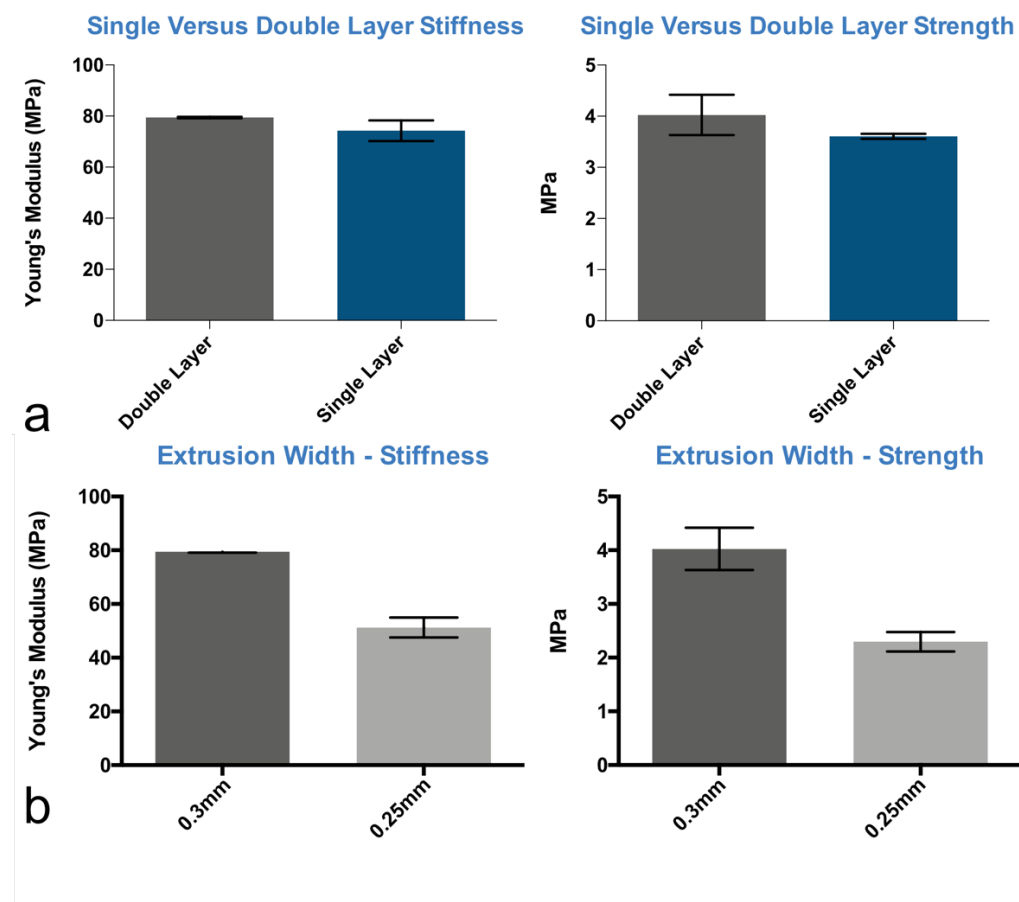


Figure 70 – Reduction of pore size via a) single layer printing and b) wider filaments. Increasing to a double layer (therefore increasing pore size) did not reduce stiffness, therefore became the preferred print design. Reducing filament with reduced stiffness and also resulted in more print failures so was not perused any further.

Continuing with 0.5mm extrusion widths and double layering, the fibre orientation (“layup”) was tested with increasing complexity from orthogonal orientation, to 0-60° and 0-45-90-135° demonstrating no difference across conditions and still significantly weaker than solid material (Figure 71). This is perhaps unsurprising as there are the same number of layers in a vertical stack

so resistance to compression is unlikely to differ, however other forms of mechanical testing may show a difference, particularly torsional moments.

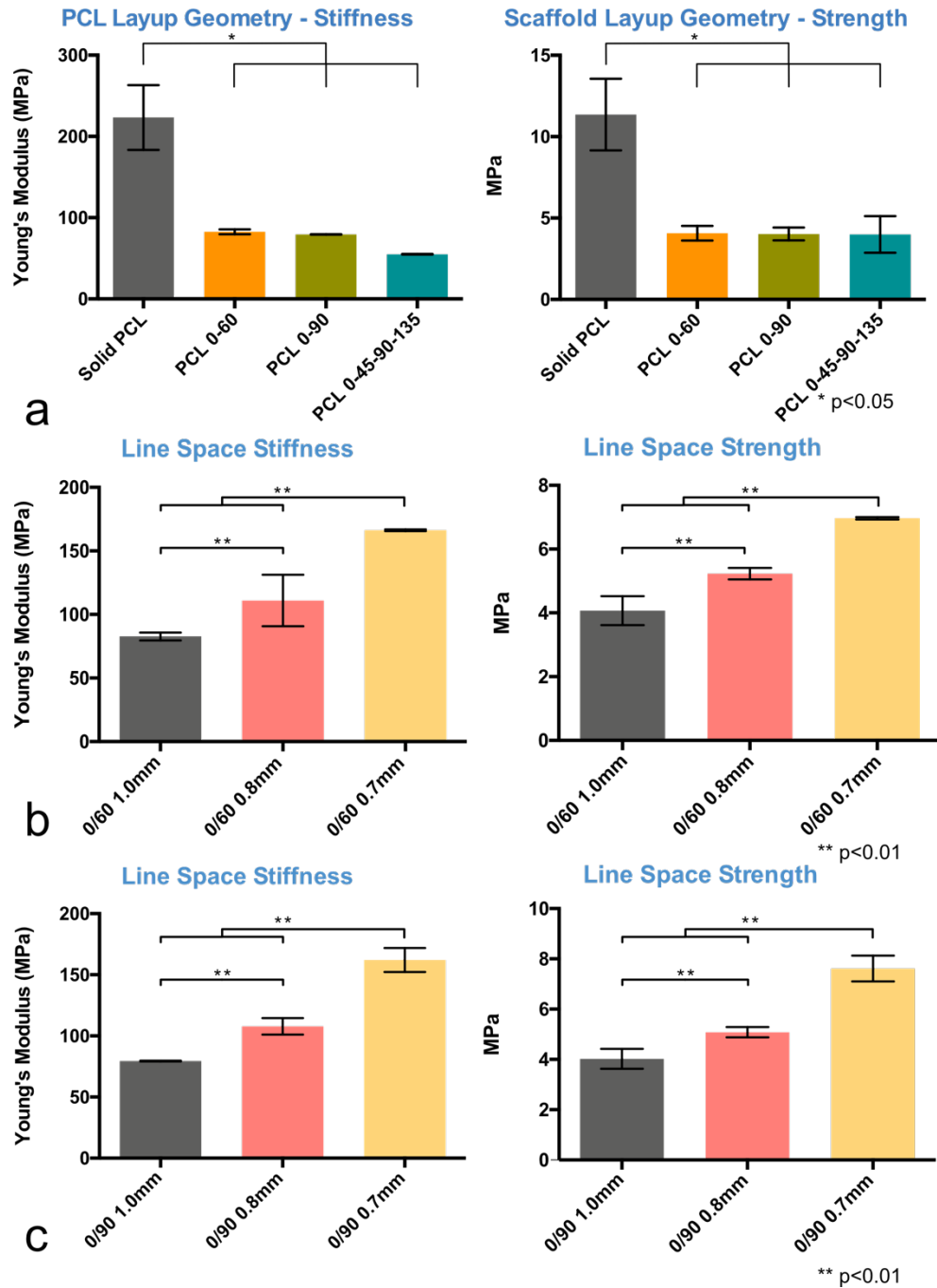


Figure 71 – Changing layer geometry. a) increasing layer complexity did not increase stiffness or strength, therefore 0-45-90-135° was abandoned given the inferior pore size and connectivity. Decreasing the gap between extrusion lines for a) 0-90° and b) 0-60° progressively increased strength, with strong statistical significance. Reducing line space caused increasing print failure rate and was associated with large reduction in pore size (Table 21).

A statistical improvement in mechanical properties was observed by reducing the distance between filaments (Figure 71). Porosity analysis of 0.7mm gap gives rise to actual widths of between 190 and 350 μ m and drops to the minimum acceptable size for a super-macroporous (206) and customisable scaffold, thus reducing space for flow of nutrients and waste as well as cell proliferation. Furthermore, the printing of narrow width scaffolds requires much slower printing speeds and a higher print failure rate.

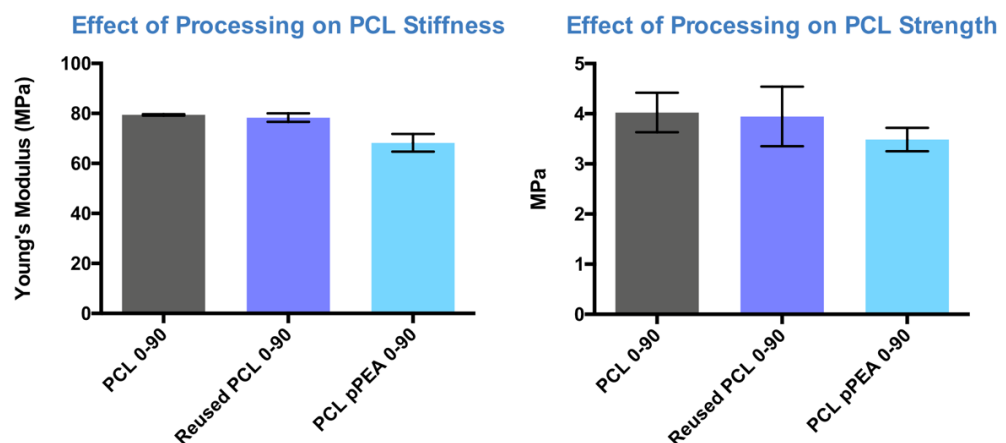


Figure 72 – Comparison of processing conditions on PCL. Reuse of PCL and post plasma polymerisation of PEA did not statistically reduce mechanical properties.

Important aspect of manufacturing such as reuse of PCL and mechanical features after plasma treatment were investigated (Figure 72) revealing resilience of the PCL to repeated melting and plasma polymerisation.

Continuing on from Chapter 2, scaffolds were printed and sterilised using ethylene oxide and compressed revealing no change in stiffness (Figure 73). A key area of the utility of PCL as a potential scaffold medium onto which PEA/FN/BMP-2 can be carried into critical defects, is its ability to withstand sterilisation. It was hypothesised that crosslinking, or subtle changes in chemistry (as seen with PMA) could cause significant mechanical impairment, and it was encouraging to see the PCL resilient in this manner. Some studies however have demonstrated improved mechanical properties with sterilisation techniques (207).

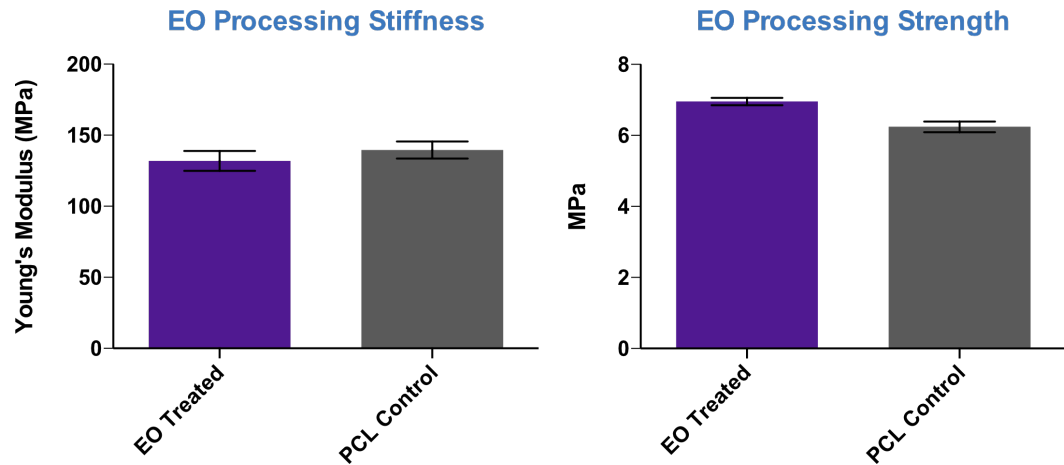


Figure 73 - Effect of EO processing on PCL stiffness and strength. Of note, printing software updates were applied prior to printing of these samples, so were matched with a new control PCL. These statistically similar measurement are encouraging translational results indicating maintained structural integrity of the PCL if it were to be sterilised before implantation.

4.3.3.2 Polycaprolactone and hydroxyapatite composite

HA was added to a matrix of PCL and validated as an evenly mixed composite. Concerns regarding integration between the filler and matrix could explain the lack of improvement in mechanical properties on compression testing irrespective of type of HA or volume percentage (Figure 74).

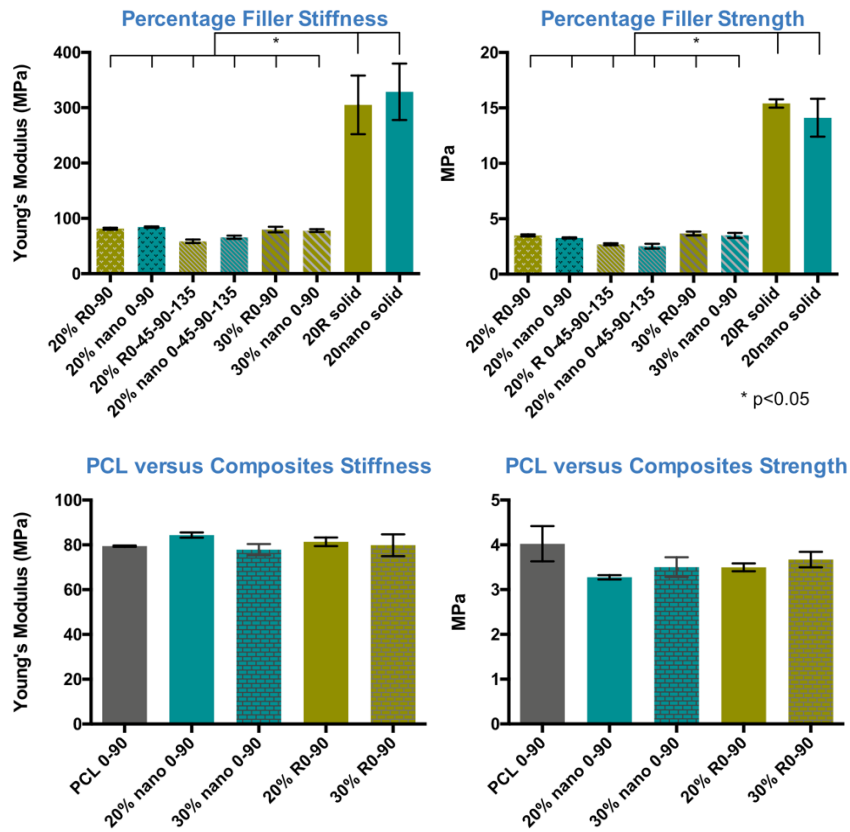


Figure 74 – Comparison of 20% and 30% nano and sintered HA across geometries, solid material and PCL. All porous composite scaffolds were statistically less stiff and weaker than their solid counterparts. When pure PCL scaffolds were compared to composite scaffolds of all types, no significant increase in mechanical properties were observed.

Taking 20% nano as an example of varying melting temperature it was apparent that varying the melting temperature (as indicated in Table 17) within the tank and extruder has an impact on ultimate strength and stiffness. Low temperature (96 °C tank temperature and 98 °C extrusion temperature) had lower absolute value than standard and higher temperature, (102 °C temperature for both, 100 °C and 105 °C extrusion temperature respectively) (Figure 75).

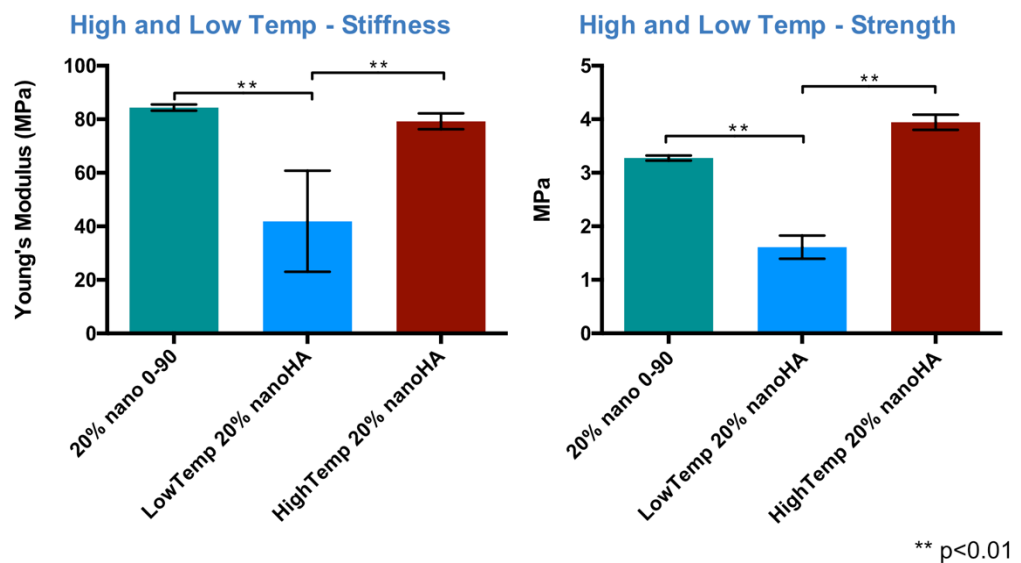
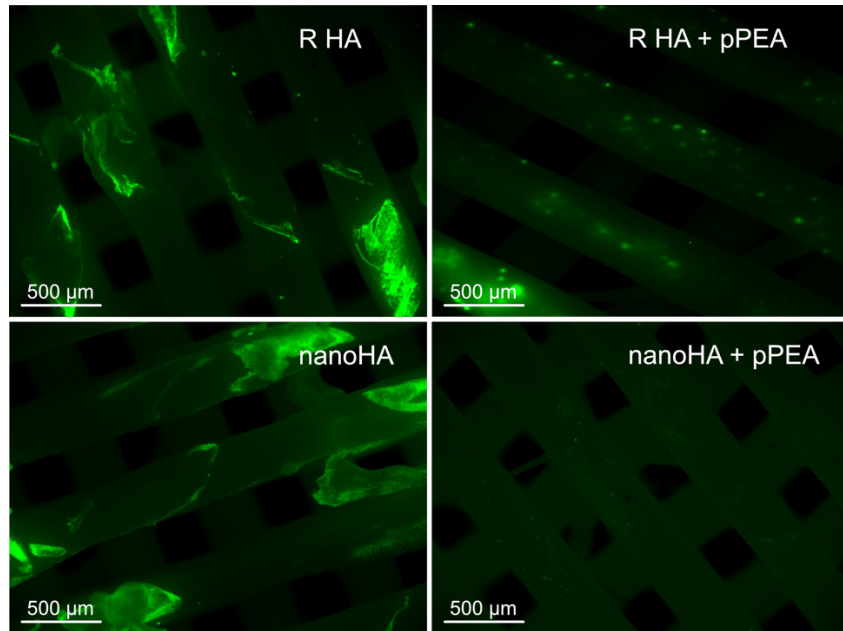


Figure 75 - Effect of varying printing temperatures 3°C higher or 6°C lower. Reducing print temperature significantly reduced both stiffness and strength whilst increasing temperature did not cause inferior properties. This may be due to incomplete melting of composite and aggregation during prints resulting in stress risers and fault lines throughout the composite.

4.3.3.3 Plasma surface coating

To assess the adequacy of plasma PEA coating an OsteoImage™ mineralisation assay was undertaken on uncoated and coated scaffolds (Figure 76).



Surface HA before and after plasma PEA application

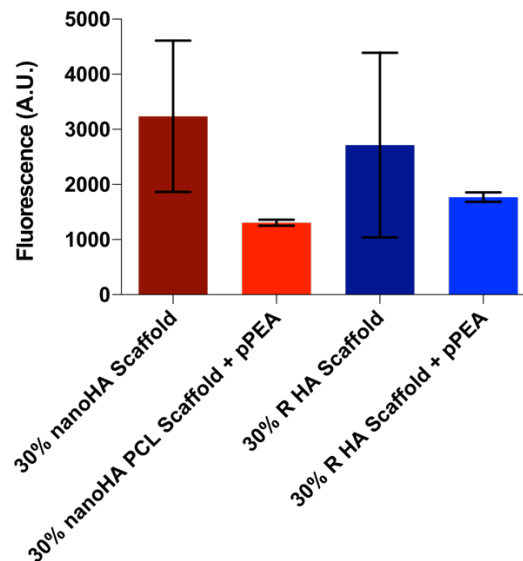


Figure 76 - OsteoImage fluorescent imaging and absorbance of HA/PCL composite scaffolds with and without pPEA. This assay detects surface mineralisation, therefore low fluorescence is indicative of adequate coverage. There is a trend toward lower signal from plasma PEA coated samples, however due to wide confidence intervals, this did not reach statistical significance. A repeat experiment with larger numbers was proposed, however given the expense of the experiment, these results, albeit not statically validated, were accepted that coverage with PEA was adequate. *Data and images in collaboration Dr Vineetha Jayawarna.

There is less signal from HA in the nano group indicating broader coverage, and the images quantitatively demonstrates nanoHA has a more confluent coating (Figure 74). This may be explained by some peaks of HA being prominent above the PEA coating, although the trend is encouraging that the coating is adhering.

4.3.4 *In vitro* osteogenesis

4.3.4.1 Cell metabolism

To explore the effect of various pore sizes and layup upon cell metabolism, an AlamarBlue assay was carried out on 0/90° and 0/60° scaffolds with 0.1mm, 0.8mm and 0.7mm line spacing at 14, 21 and 28 days (Figure 77).

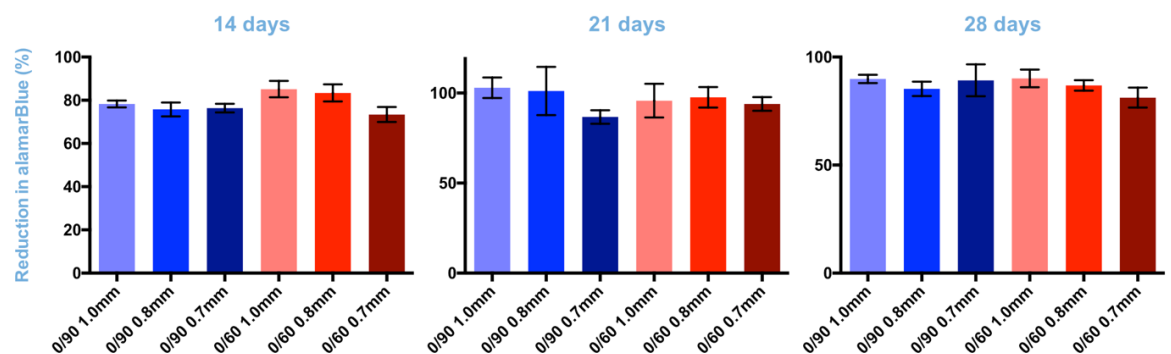


Figure 77 - AlamarBlue absorption. At 2, 3 and 4 weeks persistent cell metabolism was noted, but no scaffold geometry resulted in statistically increased cell activity at any timepoint.

Whilst an increasing proportion in reduction of alamarBlue was noted over time (denoting increasing total cell metabolism), there was no statistical difference between pore sizes at any time point (Figure 75).

4.3.4.2 Quantitative polymerase chain reaction (qPCR)

To evaluate the biological compatibility of scaffolds the PEA/FN/BMP-2 osteoinductive system, mesenchymal stem cells were seeded onto scaffolds of different geometry (0/60° and 0/90°) as well as various composites fillers

(20%/30% of both nano and sintered HA) which were then plasma coated with PEA and had FN and BMP-2 adsorbed. Quantitative polymerase chain reactions (qPCR) for intracellular markers associated with bone formation was carried out at 7 and 28 days (Figure 78).

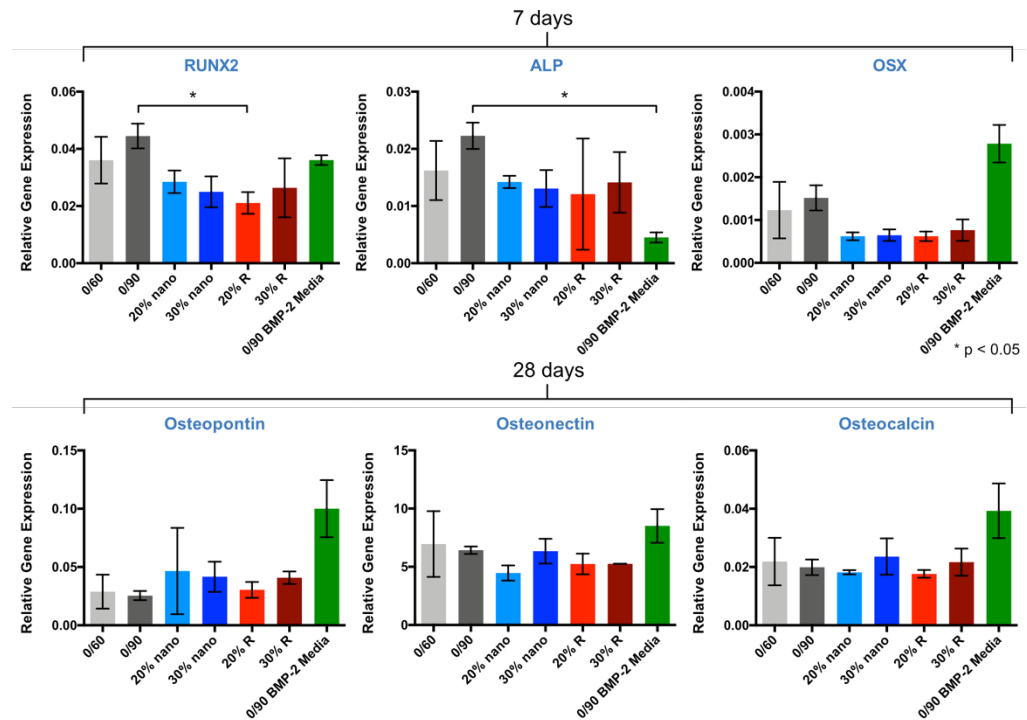


Figure 78 - 7 day (RUNX2, ALP, OSX) and 28 day (osteopontin, osteonectin, osteocalcin) markers for osteoblast differentiation and mineralisation on functionalised scaffolds. All conditions have plasma coated PEA, FN and BMP-2. Cells seeded onto functionalised 0/90° scaffolds showed significantly increased markers of early bone cell activity, however this was negated by week 4. A positive control (by addition of biweekly BMP-2) was created, which showed no statistical difference in effect, indicating that there was saturation of effect of the BMP-2 within the osteoinductive scaffolds.

Markers for osteoblast differentiation and function were present in pure PCL samples and the full variety of HA type and concentration. Osteogenic media (biweekly addition of 25 ng/ml BMP-2) was used as a positive control. MSCs showed active differentiation and mineralising activity across all materials, however no material demonstrated statistical superiority. Thus, the hypothesised osteoinductive effect of HA was not replicated in this experiment. This could be explained by the presence of a small layer of polymer covering the surface of the HA nullifying its effect. Longer studies or more physiological conditions (i.e. *in vivo*) the surface polymer may have the

potential to undergo surface hydrolysis or cell mediated degradation (macrophages/osteoclasts), exposing the HA and improving osteoinductive function of the system. Additionally, these *in vitro* experiments are carried out in a non-mechanostimulated environment, which *in vivo* is crucial for bone cell activity.

4.3.4.3 Cell migration

Given the lack of *in vitro* difference between pore sizes, and the trend toward improved mechanical properties with reduced pore size the ability of MSCs to proliferate and migrate on functionalised 0.7mm line spaced scaffolds was visualised. MSCs were seeded onto 0/90° and 0/60 scaffolds which were functionalised with plasma PEA, FN and BMP-2. When compared to controls at this time point cells were able to bridge pores in both of the geometries (Figure 79).

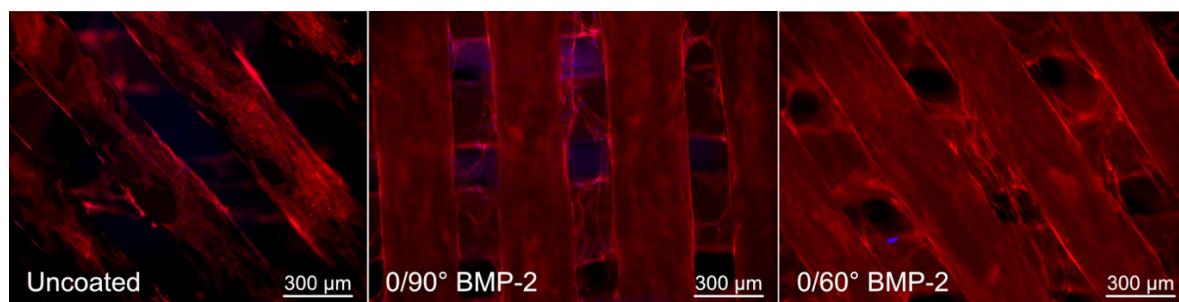


*Figure 79 - Actin staining of functionalised 0/90° and 0/60° scaffolds following 24 days of cell culture. It is evident that in both these geometries cells are able to bridge the pore gap *in vitro* with culture media in the gap. The acute corners created by 0-60° geometry give the cells a smaller gap which could be bridged. *In vivo* this situation would be substantially different, as the gaps would not be filled with media, but a more fibrinous structure following infiltration with blood, plasma or extracellular matrix. *Images in collaboration with Dr Vineetha Jayawarna*

4.4. Discussion

The purpose of this Chapter was to investigate the use potential utility of 3D printed bioresorbable polymers as a carrying transport medium for nanoscale osteoinductive coatings into bone defects. Any scaffold must be; biocompatible, bioresorbable, mechanically sound for its environment and have adequate porosity (208). Given that PCL is inherently biocompatible and resorbable, the key aspects of development here is the ability to produce scaffolds with predictable geometric and mechanical features. Whilst there are a variety of shortcomings of the described scaffolds, one of the encouraging features was resilience to reuse and EO sterilisation. The baseline mechanical characteristics of solid PCL (Figure 68) were similar to that previously documented (209).

A minimum pore size of 100 μm is required in order to allow cell migration and the flow of nutrients and waste (210). However, larger pore sizes of $>250\mu\text{m}$ was demonstrated by Murphy as optimal for cell attachment, proliferation and migration (211) and potentially even better with super-macroporous scaffolds (212). Pore size was evaluated a multitude of parameters in order to gain sufficient size taking into account the limiting factors encountered with the fused filament fabrication (sagging, stringing, filament contraction etc). The sagging and filament contraction could be addressed with sacrificial moulding processes using PEG hydrogels or water soluble polymers (e.g. polyvinyl alcohol), to support the construction of larger pores (213,214), however in the case of bone scaffolds, the modulus would not only be concerning low for mechano-stimulation, but also workability to couple with the bone (e.g. with plates and screws).

Scaffolds were engineered with pores of adequate size for cell activity, (so called 'super-macroporous') but also for through flow of the plasma state for addition of PEA, and submersion of FN/BMP-2 adsorption. Pore size and shape have been investigated previously and whilst nano and micro porous scaffolds are associated with better cell adhesion (184) macroporous pores are required for cell mobility and angiogenesis (185, 186).

The difference between theoretical pore shape and size was found to be different to that measured on the prints (Tables 20 & 21, Figure 66). Maximum width may be the optimal indicator of dimensionality and the volume measurement used is simplified and does not take into account the bulbous nature of the filament. Furthermore, whilst the sagging nature causes narrowing, the filaments appear to narrow in centre between coupling points with the filaments above and below. This is seen quite commonly in fused filament fabrication and is a product of stretching of the polymer from the nozzle after each contact point with the orthogonal row below. As such, the limitation of this method is that we used measurements and mathematical calculations for straight edge shapes (square, parallelograms, cuboids) for pores which are curved and more complex internally. Ideally volumetric measurements would be calculated using 3D imaging; however, the polymer is radiolucent and computed tomography isn't sensitive enough to accurately delineate between air and polymer. A contrast agent could be introduced into the scaffold to counteract this; however, this is a resource we do not have access to. Computational analysis, such as finite element analysis may be able to develop this model further and could give information on porosity and connectivity also.

Whilst the behaviour of the polymers and composites exhibited typical elastic and plastic phases before failure (215), the increased porosity (decreased density) resulted in reduced mechanical features, which has been noted previously by Rezwani with composite scaffolds, who saw that this inverse relationship did not occur with metallic scaffolds, however metallic scaffolds were associated with inferior biological integration (216).

Other types of 3D printing compatibility with plastics could be considered, such as selective heat laser or sintering, which offer high resolutions, however print times are significantly slower and large volumes of waste occur (217). Furthermore, the addition of HA as a composite to sinter together would confound the printing process. Photopolymerisation is another method of high-resolution 3D printing, however, requires light sensitive polymerisation of monomers from a resin vat, of which we could find no

reported techniques in this. The use of fused filament fabrication with multiple nozzles has the added benefit of multiple material prints, thus theoretical combination of polymers and hydrogels.

Printing with PCL revealed a relatively low Young's modulus when compared with cortical bone (20 GPa stiffness and 200 MPa strength), however reached the lower end of cancellous bone strength at 4 MPa and almost adequate stiffness of 80 MPa. This is still 20 times as stiff other composite scaffolds which were printed with poly(lactic co-glycolic) acid and 10% nanoHA (214).

Despite the refinement of an adequate mixing technique to distribute the filler evenly throughout the matrix, the addition of nano or sintered hydroxyapatite had no predictable trend or statistical effect on mechanical properties measured. It would have been expected that increasing proportions of HA would have seen a change in stiffness, however this was not encountered, and we reached the maximum capacity of the printer at 30%. This is in contrast to Domingos *et al* who used single layers with 20% nanoHA (and synthetic micro HA) noting a 32% improvement in mechanical strength (218). This lack of integration may be due to the natural hydrophobicity of HA or indeed due to the different thermal properties of the two materials. This interfacial interaction documented within the literature as a key determiner of composites' ability to withstand stress. There are many modes in which failure at the interphase occurs; hydrophobic mismatch, thermal stresses, electrostatic, interfacial friction (192,193). Most likely in this situation, hydrophobic or thermal mismatch (in particular due to the thermoplastic processing) would be most probable (194). Given the different particle features of nanoHA and sintered HA, they may have lacked integration for different reasons. Sintered grade HA had a more even mix and consistent particle size however doesn't physically combine well and demonstrated voids where the particles fell out, possibly due to hydrophobicity or a thermal mismatch. NanoHA is a much finer powder and has a tendency to cluster, which may create weaknesses where the matrix had not incorporated it.

The materials used here were found to be biocompatible, as expected from previous studies (219,220) however this work is unique in its use of functionalised coating and MSCs rather than differentiated osteoblasts. MSCs exposed to HA are reported to have increased cell response, particularly with the finer nano grade particles. This behaviour was not demonstrated in MSCs in this work. This is likely an effect of the incorporation of HA within the PCL matrix. PCL is not easily degraded actively by MSCs and therefore the cells were likely not exposed to masses of HA large enough to cause stimulation and increased osteoid formation. With a longer exposure during an *in vivo* experiment, the surface hydrolysis of PCL would expose the underlying HA and promote differentiation of MSCs along the osteoblast lineage. *In vivo* evaluation would perhaps be a more appropriate method of evaluate further, as the environment would give rise to surface hydrolysis but also give information on the effect of cell mediated breakdown of PCL by host cells not present with *in vitro* studies (e.g. eosinophils, macrophages etc). Therefore, further experimentation using nanoHA mixed into a composite would be beneficial in observing any effect of HA incorporated into the PCL matrix. Further work on improvement in integration of HA with PCL could be investigated, for example by embedding in silicon or plasma treatment of HA to improve wettability properties.

When considering the optimal layup geometry for scaffolds, there was no significant improvement in mechanical (or indeed cell activity) when varying from the simple 0-90° layup and 0.3mm extrusion diameter (Figure 70). Reducing the line spacing had an exponential reduction in pore size, which could impact *in vivo* performance. They were also significantly more difficult to print, and preparation took much longer per sample. In a lab based scenario these are minor considerations, however given that these scaffolds are being investigated with a view to critical defects in humans which are frequently in excess of 10 times the size of the scaffolds, reliability and speed of prints are a significant manufacturing consideration. Narrower filament width did show a trend toward improved mechanical properties (from 79.5MPa to 162.0MPa and 4.0MPa to 7.6MPa for stiffness and strength respectively in the case of 0-

90°) which did not achieve statistical significance, but did get beyond to the minimum target stiffness of cancellous bone (100-2000)MPa. Therefore, progressing with smaller widths would be worth evaluating *in vivo*, however narrow prints were even more unreliable with the addition of HA, adding to their limitation. A correlation between pore size and cell activity has not been explored in this Chapter, but has been previously described (211). This *in vitro* work may however be less relevant in an *in vivo* applications, as the observation of MSC behaviour in isolation in cell media is different to the activity of multiple cells acting in synergy within an inflamed post-implantation environment in which haematoma, fibrin, and a multitude of inflammatory mediators act simultaneously and evolve over several weeks. Therefore, ongoing *in vivo* evaluation is warranted to explore which of the geometries and compositions are potentially more effective in clinical scenarios.

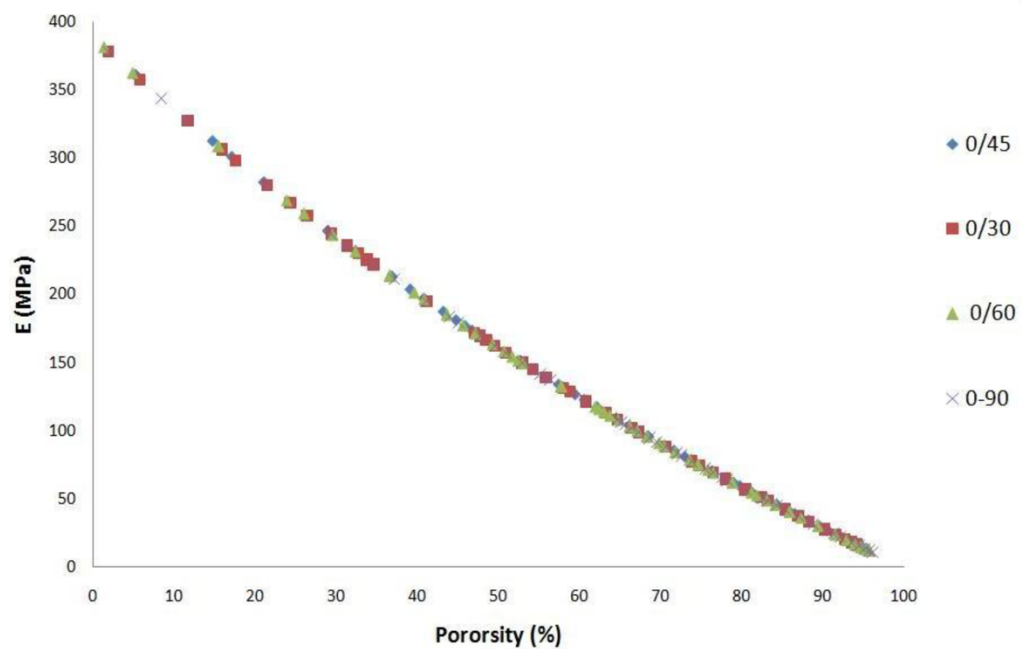


Figure 80 - Modulus versus porosity from Chuan et al (221). As expected, increasing porosity and (thus decreasing) density reduces modulus, and is independent of scaffold lay up geometry for 3D printed PCL scaffolds. This validates the results found in this work.

Study	Material	Fabrication Method	Geometry	Porosity (%)	Compressive Modulus (MPa)	Compressive Strength (MPa)
This work	PCL	Fused Filament	0/90	50.4	79.4	4.0
This work	PCL/30%nanoHA	Fused Filament	0/90	50	77.9	3.5
Hutmacher(220)	PCL	Selective Laser Sintering	0/90	61	41.9	3.1
Lam(181)	PCL	Fused Filament	0/60/120	68	2.4	1.0
Lam(181)	PCL/20%TCP	Fused Filament	0/60/120	68	6.8	1.0
Zein(222)	PCL	Fused Filament	0/90	55	69.2	3.32
Zhou(223)	PCL	Fused Filament	0/60/120	65	2.7	1.5
Zhou(223)	PCL/TCP	Fused Filament	0/60/120	65	9.3	3.1

Table 20 – Relationship between porosity. Comparison of this work with published literature of PCL scaffolds +/- HA printed via fused deposition revealed lower porosity but greater stiffness to previous studies. We know from this work, that cells were still able to proliferate, migrate and demonstrate osteogenic activity despite the lower porosity.

Kim et al used a combination of macro and micro porous scaffolds using PCL and up to 20% hydroxyapatite. However whilst the porosity was relatively large (77-78%) this figure is misleading, as the macropores were relatively small (<185um) therefore much of the porosity was attributed to poorly connected micropores (199). Zhou and LAM added TCP which more than tripled the modulus and doubled the strength (Table 23). This wasn't observed in our samples and may be related to the different physicochemical properties of TCP and HA.

There are several limitations to making definitive conclusions based on the experimental design and outcomes of this Chapter. The integration of HA into the PCL matrix was only visibly inspected after thermally interfering treatments (i.e. freeze fracture and polishing) and given the different properties of the phases, this may not be a true reflection of what is happening in the composite scaffolds. The nature of fused filament fabrication requires heating and extrusion of material through a fine nozzle limited the volume of HA we could introduce into the implant. Further increasing of HA content may

have increased the properties (or given further evidence that the HA doesn't integrate well with PCL), however visual inspection of the composite revealed voids at 30% HA, therefore increasing filler content may have been futile even if the printer could cope.

The scaffolds were only tested in compression, which is a primary mode of use for a bone scaffold, however they are also subject to bending, tensile and rotational forces which were not formally explored (224,225). However, it was clear that scaffolds are anisotropic, and can peel apart with tensile force and to a lesser degree with rotational force. Current orthopaedic implants, particularly those which would be used to fix scaffolds, for example plates & screws, can be applied in a fashion to augment the limited tensile and rotational properties of the implants however it is more difficult to account for cyclical compression seen for example in large tibial defects.

Mechanical analysis was undertaken at room temperature and therefore a non-physiological state. It is important that material, particularly polymers, are tested in a range of physiological conditions, with specific relevance to those which have a glass transition temperature close to or straddled by the difference between room temperature and the internal body. In this case, the glass transition temperature of PCL is well below that investigated (-60°C). Irrespective, the orthopaedic community and patients have been subject to significant complications associated with implants materials which fail as a result of difference between laboratory based studies and clinical cases. For example, Boneloc[®] cement which was extensively tested at room temperature to have preferential mixing and mechanical properties. However when implanted into an environment of 37°C , the cement became rubbery and early failure of thousands of joint replacements (226-229) and up to 65% within 3 years (230)(Figure 81) (three quarters of modern hip replacements are expected to last 15-20 years) (231).

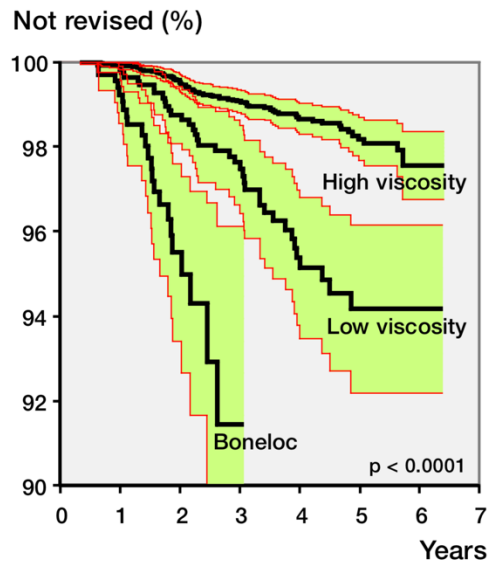


Figure 81 - Survivorship of Boneloc cement compared to modern (high viscosity) cement(232). This demonstrates the importance of market monitoring (by the MHRA in the UK) to pick up and identify catastrophic failure of medical devices.

Following implantation of any orthopaedic device, the subsequent inflammation and blood flow immerses the implant in physiological fluids of varying viscosity depending on the state (blood, inflammatory fluid, seroma etc). Due to limited facilities being available, these scaffolds were tested only in their dry state and therefore the effect of hydrodynamics is not described. In particular comparison has been made to commercially available calcium samples which may perform vastly differently in a more hydrated state.

A variety of limitations of FFF 3D printing have been discussed and the discrepancy between theoretical measurements and physical prints described (sagging, stringing, filament stretching). Many of these issues are well known within the 3D printing 'community' but are relatively scarcely discussed within the scientific literature or biomedical engineering. Investigating in detail here is helpful for this application, and whilst not original they are large considerations when we consider the precision with which the osteoinductive nanocoating. Given the broad range of porosities seen in the human body and engineered scaffolds described in the literature, cell biology is relatively flexible meaning, if we can get the porosity in the right region the cells are likely to adapt to a range of environments.

Further mechanical analysis of scaffolds would be beneficial as baseline characteristics of PCL and PCL/HA composites. Toughness and hardness are properties which influence the “workability” of a scaffold, and how easy it can be modified intraoperatively (e.g. can be trimmed down or screwed into). Creep resistance (the ability to resist deformation under a constant load) is a key feature of any porous scaffold in order to maintain pore shape and size, as well as resist compression in the longer term. Fatigue failure (failure of a material due to repetitive loading under stress levels below ultimate tensile strength) in flexible implants is relevant but less important than creep resistance, particularly in a load sharing arrangement. Mechanics may be improved in future by changing from HA to bioglass (233,234), however this would be at the expense of the hypothesised cell activity associated with HA. Now that baseline mechanical properties have been established for the materials, finite element analysis could be performed to predict mechanical behaviours and allow more cost and time efficient planning of scaffold design (217). Alternatively, should adequate mechanical properties not be achievable, the implant could be coupled with commercial load bearing implants (e.g. plates and screws) then poly(lactic-co-glycolic acid) to improve workability of the implant (235).

Testing in physiological fluids (e.g. saline) would give some information in hydrodynamic activity of the scaffolds, but also degradation over time. Similarly, the addition of hydrogels into the pores during the 3D printing process may alter mechanical properties but could have vast benefits in terms of controlling the microenvironment as a transport medium for cells or additional growth factors (e.g. VEGF).

To improve the integration between HA and PCL, the incorporation of HA into silicon could be investigated or improve wettability of HA with plasma. This would exclude one of the main areas which could be limiting the integration of HA at the interphase. Further investigation into electrostatic, or thermal mismatch would be difficult. In particular thermal incompatibility may be terminal for the utility of PCL/HA composites via 3D printing of these scaffolds.

4.5 Conclusions

There are a multitude of subtractive and additive fabrication processes available to engineers to manufacture implants. As 3D printing is a slow and relatively expensive process, the only practical application is to utilise its flexibility and use in modern orthopaedics is for use in custom designed implants. The scaffolds investigated in this Chapter fall short of the mechanical properties required for independent implantation as a delivery device in load bearing critical defects. They may have application as a load sharing device (i.e. derive mechanical support from an alternate device such as an intramedullary nail) and progressively become more resistant to deformation as mineralisation occurs. In the absence of mechanical or biological benefit, the *in vitro* results from this chapter do not support the use of HA filler. Having predictable time frames for mineralisation and resistance to deformation would be key to use in this circumstance and could be the subject of investigation for future development.

5. Further Work and Conclusions

5.1 Future Work

The primary purpose of this research is to translate an established engineered osteoinductive nanoscale coating into potential clinical applications. Thus far, it has been demonstrated that the BMP-2 presenting system is resilient to sterilisation, functional at low doses when applied to bone chips and can be applied to custom 3D scaffolds. What has not been able to be established is the optimal pore size or geometry, nor the perceived value of adding hydroxyapatite. Chapter 4 demonstrated equivocal mechanical and *in vitro* cell behaviour between 0/90° or 0/60° pore geometries, 0.7mm or 0.4mm pore width, and nano or sintered hydroxyapatite. Consequently, further work will involve *in vivo* experiments method which could establish whether there is preferential ectopic mineralisation induced by the nanoscale coating using a selection of pore shapes and sizes to help draw conclusions on which may be best for cell adhesion migration and nutrient delivery. This is different to the *in vitro* work developed in Chapter 4 by the nature of the 3 dimensional inflammatory extracellular environment which can aid cell adhesion, migration and differentiation. The impact of HA on cell activity was not observed in the Chapter 4 and was hypothesised to its incorporation within the scaffold which may hydrolyse in an *in vivo* model.

The use of a subcutaneous model allows examination of the ability of an engineered construct bone via local recruitment of mesenchymal stem cells. As the subcutaneous site provides a stringent, non-osseous environment, it examines the inherent capacity of the engineered construct to form bone tissue in the absence of *in situ* differentiated osteogenic cells. Finally, the subcutaneous model gives important insight into the inflammatory and immune responses to the engineered scaffolds and coating. The main limitations of this model are the lack of mechanical stimulation and its non-osseous site, distinct from *in situ* MSCs. At present however, the scaffolds

cannot be printed with dimensions small enough to be used in the critical defect model used in Chapter 3.

For a positive control, a polyethylene glycol (PEG) based hydrogels has been used as a carrier of BMP-2. PEG gels are synthetic, flexible and have been demonstrated as effective carrier mechanisms for growth factors(159,236) , particularly when functionalised using a triple helical, $\alpha_2\beta_1$ integrin-specific peptide (GFOGER). A proposed method for this experiment can be found in Appendix 6.4.

5.2 Thesis Conclusions

1. Effect of ethylene oxide as a sterilisation on the osteoinductive capabilities of the technology

Sterilised polymers +/- FN were tested with and without EO sterilisation for topography, FN function and cell behaviour. Non-inferiority was observed between sterilised samples and controls giving rise to the conclusion that FN networks are resilient to EO sterilisation. Subtle behavioural changes were noted following exposure of PMA to EO. Exploration with water contact angle and XPS attributed to these behavioural changes to an alteration of surface chemistry. BMP-2 was not detected following the EO process, which may be as a result of the weeklong duration of process rather than the EO gas specifically. Therefore, the timing of EO sterilisation of this osteoinductive system would be prior to BMP-2 addition.

This bioengineered nanocoating is capable of being sterilised by EO and further *in vitro* experiments can safely use this as a sterilisation technique. Further work specifically comparing the topography and functional difference between EO sterilisation prior to and following addition of FN is warranted before committing to an industrial level of production.

2. Utility of functionalised bone chips

Bone chips were explored for use as a transport scaffold for this osteoinductive nanocoating as the first *in vivo* 3D experiment of this technology. In this critical defect mouse model, bone chips remained present for 8 week duration however quantitative comparison of the utility of BMP-2 fell short of statistical significance. Qualitative histology demonstrated the presence of close bone chip integration and mature bone formation at the 8 week endpoint. Heterotopic ossification was observed even at ultra-low doses of BMP-2.

Further *in vivo* models would require excessive numbers of mice to demonstrate a quantitative difference in the observed additional 10% bone formation attributed to BMP-2.

3. Merits of a customisable 3D printed PCL scaffolds

Supermacroporous PCL scaffolds were 3D printed with various geometries and porosities then evaluated for achieved pore size and porosity, mechanically tested in compression and assessed for biocompatibility. Changes between theoretical and measured pore dimensions demonstrated reduction of between 20% and 70%. Compression testing fell short of cortical bone stiffness or strength, however approached that of metaphyseal bone. Scaffolds were successfully functionalised in 3D and demonstrated biocompatibility with intracellular markers of osteogenesis present up to 4 weeks.

The use of 3D PCL supermacroporous scaffolds are subject to loss of pore morphology when printing. They fall short of the mechanical properties required of a load bearing implant and further work with should focus on use as a load sharing implant. Whilst the nanocoating can be applied in 3D, further work on the use of 3D printed scaffolds with this osteoinductive coating should be evaluated *in vivo* looking specifically for mineralising bone formation.

4. Addition of HA improve mechanical and biological properties

In order to improve mechanical and biological properties of scaffolds, sintered and nano grade HA were mixed with PCL to form composites of differing volume percentages. They were then evaluated mechanically and biologically. Despite even distribution of HA within the PCL, the addition of nano or sintered grades were not found to improve mechanical properties nor demonstrate increased osteoblast function. This is hypothesised to be

due to limited interfacial integration with the PCL matrix and lack of exposure to MSCs on the material surface.

Further work to improve the composite interface could involve an additional interfacial material (e.g. silicone) or surface treatment of HA to increase material interaction. Evaluation *in vivo* may give insight to the osteoinductive effect when surface hydrolysis exposes HA to osteoblasts.

6. Appendix

6.1 List of materials/reagents – Chapter 2

List of materials/reagents	
Methyl Acrylate.....	Sigma-Aldrich
Ethyl Acrylate for spun samples.....	Sigma-Aldrich
Ethyl Acrylate for plasma chamber	Sigma
Medical Grade Polcaprolactone.....	Corbion
Cancellous Chips Canine <1mm Chip.....	Veterinary Tissue UK
Toluene.....	Alfa Aesar
Beonzoin.....	Sigma
Absolute Ethanol.....	VWR Chemical
Dulbecco's phosphate buffered saline (DPBS).....	Life Technologies
MilliQ Water.....	Thermo Scientific (Barnstead Smart2Pure 3)
Formaldehyde.....	Fisher Scientific
Tween 20.....	Sigma
Bovine serum albumin (BSA)	Roche/Sigma
Human plasma fibronectin.....	Sigma-Aldrich
Mouse monoclonal HFN7.1 antibody.....	Santa Cruz Biotechnology
Horseradish peroxidase (HRP) anti-mouse antibody.....	Developmental Studies Hybridoma Bank
Mouse monoclonal P5F3 antibody.....	Invitrogen
Substrate solution.....	R&D Systems
Stop solution.....	R&D Systems
Human BMP-2 (355-BM).....	R&D Systems
Human BMP-2 DuoSet ELISA (DY355).....	R&D Systems
Anti-BMP-2/BMP-4 antibody.....	R&D Systems
Primary antibodies against BMP-2 (ab14933, rabbit polyclonal, 1:2000)	Santa Cruz Biotechnology
Biotinylated anti-rabbit secondary antibody (BA-1100, 1:10000).....	Abcam
Streptavidin-HRP solution (DY998).....	Vector Laboratories
Micro BCA protein assay kit 23235.....	R&D Systems
C2C12 Mouse Myoblasts 91031101-1VL.....	Thermo Scientific
Dulbecco's Modified Eagle Medium (21885-025).....	Sigma-Aldrich
Fetal Bovine Serum.....	Gibco
Penicillin-Streptomycin.....	Sigma
0.04% Trypsin/0.03% EDTA.....	Sigma
Insulin-Transferrin-Selenium (51500-56).....	PromoCell c-41000
MF20 anti-mouse.....	Gibco
CY3 anti-mouse (315-165-003).....	Developmental Studies Hybridoma Bank
Vectashields mounting medium with DAPI.....	Jackson Immunoresearch
	Vector Labaoratories H-1200

Table 21 - Chapter 2 reagents and sources

6.2 List of materials/reagents – Chapter 3

List of materials/reagents	
Polyimide Tube.....	Microlumen
1mm canine bone chips.....	Veterinary Tissue UK
Ethyl acrylate monomer.....	Sigma
Dulbecco's phosphate buffered saline (DPBS).....	Life Technologies
MilliQ Water.....	Thermo Scientific
Bovine serum albumin (BSA)	Roche/Sigma
Human BMP-2.....	R&D systems
Human plasma fibronectin.....	Sigma-Aldrich
Male C57BL/6 Mice.....	Charles River
Isoflurane.....	Zoetis
Hair removal cream	Charles River
Antibiotics.....	Reckitt Benckiser
Buprenorphine (Tamgesic 200ug)	Indivior
Carprofen (Carprieve 5%).....	Norbrook
Betadine.....	Ecolab
Saline.....	Baxter
Suture (Vicryl 5-0)	Ethicon
Decalcification Krajian Solution.....	RICCA
Histo-clear.....	Agar Scientific
Ethanol.....	Fisher Scientific
Mayers hematoxylin.....	Sigma
Scott's solution.....	Sigma
Fast Green Solution (FGF)	Sigma
Acetic acid.....	VWR
Safranin-O.....	Sigma

Table 22 - Chapter 3 reagents and sources

6.3 List of materials/reagents – Chapter 4

List of materials/reagents	
PCL Medical Grade.....	Corbion
Hydroxyapatite sintered (P218R).....	Plasma Biotol
Hydroxyapatite nano grade (677418).....	Sigma
Silicon Carbide Grinding Paper.....	MetPrep
Diamond Polising Compounds (6 µm 560014, 1 µm 541224)	Buehler
Bone Cement – Optipac® Refobacin (4710500394-1)	Biomet
Bone Cement – Antibiotic Simplex (6901-1-009)	Stryker
Hydroset Hydroxyapatite Bone Substitute (397005X).....	Stryker
Penicillin/Streptomysin.....	Sigma
Fetal Bovine Serum.....	Sigma
0.1% sodium pyruvate (S8636)	Sigma-Aldrich
Non-Essential Amino Acids (11140-035)	Gibco
Dulbecco’s Modified Eagle Medium (21885-025)	Gibco
EDTA/trypsin (c-41000)	PromoCell
Human BMP-2 (355-BM010)	R&D Systems
Fibronectin (1918-FN-02M)	R&D Systems
Human Mesenchymal Stem Cells (MSC101)	Promocell
Alamar Blue (BF012A).....	Thermofisher
Osteoimage™ Mineralisation Assay (PA-1503)	Lonza
Ethyl Acrylate.....	Sigma
Bovine serum albumin (BSA)	Roche/Sigma
RNA Extraction Kit (RNeasy ,Micro kit 74004)	Quiagen
RNase-Free DNase Set (1023460, lot 160031631)	Quiagen
RNase-Free Water (lot 160041449).....	Quiagen
QuantiTect Reverse Transcriptase Kit(205310).....	Quiagen
Micro BCA Protein Assay Kit (23235).....	Thermo Scientific
Alkaline Phosphatase Detection Kit, Fluorescence (245-325-0).....	Sigma
Tris-HCL.....	Sigma

Table 23 - Chapter 4 reagents and sources

6.4 Proposed method for subcutaneous mineralisation experiment

6.4.1 Proposed materials/reagents

List of materials/reagents	
PCL Medical Grade.....	Corbion
Hydroxyapatite sintered (P218R).....	Plasma Biotal
Hydroxyapatite nano grade (677418).....	Sigma
Human BMP-2 (355-BM010)	R&D Systems
Fibronectin (1918-FN-02M)	R&D Systems
Ethyl Acrylate.....	Sigma
Isoflurane.....	Reckitt Benckiser
Male C57BL/6 Mice.....	Charles River
Hair removal cream	Indivior
Antibiotics.....	Norbrook
Buprenorphine (Tamgesic 200ug)	Ecolab
Carprofen (Carprieve 5%).....	Baxter
Betadine.....	Ethicon
Saline.....	RICCA
Suture (Vicryl 3-0)	Agar Scientific
Decalcification Krajian Solution.....	Fisher Scientific
Histo-clear.....	Sigma
Ethanol.....	Sigma
Mayers hematoxylin.....	Sigma
Scott's solution.....	VWR
Fast Green Solution (FGF)	Sigma

Table 24 - List of proposed reagents and sources

6.4.2 Sample Preparation

6.4.2.1 Scaffold printing

Scaffolds would be designed using BioCAD (version 1.1 for windows, Regen HU, Switzerland) before exporting to BioCAM (version 1.2 for windows, Regen HU, Switzerland). Scaffold design and printing parameters are outlined in Tables 24 and 25.

Condition	Coating	Layer Orientation (°)	Layer Repetition	Line Spacing (mm)	Extrusion Width (mm)
PCL 0/60 1.0mm gap	pPEA+FN+BMP-2	0,60	Double	1.0	0.3
PCL 0/60 0.7mm gap	pPEA+FN+BMP-2	0,60	Double	0.7	0.3
PCL 0/90 1.0mm gap	pPEA+FN+BMP-2	0,90	Double	1.0	0.3
PCL 0/90 0.7mm gap	pPEA+FN+BMP-2	0,90	Double	0.7	0.3
PCL/20% nanoHA	pPEA+FN+BMP-2	0,90	Double	1.0	0.3
PCL/20% sintered HA	pPEA+FN+BMP-2	0,90	Double	1.0	0.3
PCL 0/90 1.0mm gap	Nil	0,90	Double	1.0	0.3

Table 25 – Proposed nanocoating application and 3D printing design attributes

Condition	Melting Temperature(°C)	Screw Extrusion Temperature(°C)	Extrusion Pressure (MPa)	Extrusion Speed (mm.s ⁻¹)
PCL 0/60 1.0mm gap	68	69	0.40	8
PCL 0/60 0.7mm gap	68	69	0.40	8
PCL 0/90 1.0mm gap	68	69	0.40	8
PCL 0/90 0.7mm gap	68	69	0.40	8
PCL/30% nanoHA	102	100	0.45	6
PCL/30% sintered HA	102	100	0.45	6
PCL 0/90 1.0mm gap	68	69	0.40	8

Table 26 – Proposed printer settings for scaffolds

6.4.2.2 Plasma coating

Scaffolds would be inserted into a clean plasma chamber and a vacuum slowly formed before introduction of radiofrequency (RF) to initiate an ‘air plasma’ treatment at 50 watts for 5 minutes to clean the samples and prime the surfaces for interaction with the impending polymerisation. The air would be shut off after 5 minutes and vacuum allowed to increase once again before the

formal plasma polymerisation. As the vacuum was adjusted for a final time, the EA monomer introduced into the chamber and plasma state was formed using a static radiofrequency. The monomer valve would be adjusted periodically to maintain a consistent vacuum of 1.2×10^{-1} ($\pm 0.2 \times 10^{-1}$). This should be maintained for 15 minutes at 50 watts then RF ceased and vacuum slowly reduced via a filtered air source.

6.4.2.3 FN adsorption

Human plasma FN will be prepared in Dulbecco's Phosphate Buffered Solution (DPBS) ++ (+ calcium + magnesium) to 20 $\mu\text{g}/\text{ml}$ from stock solution of 1.42 mg/ml. Samples prepared on glass slips to be placed on parafilm and 200 μl of fibronectin added to the sample and left covered for 60 minutes. Scaffolds then should be immersed in the FN solution in a vacuum using a vacutainer for 60 mins. Finally, a wash with DPBS and then MilliQ water should be performed before drying the samples with nitrogen.

6.4.2.4 Ethylene oxide sterilisation

Low temperature ($<50^\circ\text{C}$) EO sterilisation could be carried out at the Andersen Caledonia LTD facility. This would precondition samples by warming and humidification to expose any bacterial spores. The batches are then transferred to the EO chamber where they are exposed to the EO gas for >90 minutes at a controlled temperature of $45\text{-}50^\circ\text{C}$. Finally, the samples would require aeration and cooling in order to remove the remaining gas over an 8-hour period. To establish efficacy of treatment, *Bacillus atrophaeus* colonies are placed amongst the batch being sterilised and then cultured for 7 days following sterilisation to confirm sterility of the batch.

6.4.2.5 BMP-2 adsorption

1% w/v BSA in MilliQ water would be inactivated in a 65 °C bath for 10 mins, to block non-specific binding sites, then filtered and added to samples for 30 minutes. Following triple wash with DPBS the samples are incubated with BMP-2 (which displaces albumin due to a higher dissociation constant) at 50 ng/ml in DPBS -- (- calcium - magnesium) for 60 minutes and unadsorbed BMP-2 removed and kept at -80 °C. A final wash with DPBS – would be performed then samples dried with nitrogen flow.

6.4.2.6 Mice preparation

Provisional approval from the home office has been sought and for experimentation within the University of Glasgow Veterinary Research Facility and performed under personal (n°I44130F69) and project license (n°70/8638) issued by the Home Office under the Animals (Scientific Procedures) ACT 1986. Appropriate training on cadaveric specimens prior to *in vivo* experimentation should be undertaken. Intervention groups are paired to appropriate comparison to minimise inter-mouse variability, and where duplicate pairs existed, conditions were implanted in varying sides (as no evidence could be found indicating preferential mineralisation on the left or right side). Furthermore, bias due to observation or any improvement in surgical technique during the series of operations was minimised by a randomised sequence generator (random.org). This resulted in an implantation schedule (Table 27) for sequentially numbered mice which was then concealed following surgery. It was not possible to double-blind via allocation concealment to the surgical team as the scaffolds are visually different, creating a randomised controlled trial, which was not double blinded.

Mouse Number	Left	Right
1	nanoHA	RHA
2	RHA	Control
3	0/90 0.7	PEG
4	nanoHA	PEG
5	RHA	PEG
6	0/90 1.0	nanoHA
7	0/60 1.0	Control
8	0/60 0.7	0/90 0.7
9	0/90 0.7	Control
10	RHA	nanoHA
11	nanoHA	Control
12	0/90 1.0	Control
13	0/60 0.7	0/60 1.0
14	0/60 1.0	PEG
15	0/60 1.0	0/60 0.7
16	0/60 1.0	0/90 1.0
17	0/60 0.7	0/90 0.7
18	0/90 1.0	0/90 0.7
19	0/60 0.7	PEG
20	0/90 1.0	RHA
21	0/60 0.7	Control
22	0/60 1.0	0/90 0.7
23	0/90 1.0	PEG
24	nanoHA	RHA

Table 27 - Implantation schedule to ensure comparison of groups spread between mice to minimise inter-animal variability

6.4.2.7 Surgery

C57BL/6 mice ages 8 weeks require accustomisation to the animal facility for 1 week prior to surgery. On the day of surgery mice would be anaesthetised with isoflurane 3 litres/minute in air then weighed and the skin of the right forelimb removed using hair removal cream. Mice would be transferred to the surgical

table and their faces placed in a constant flow of isoflurane at 2-3 l.min⁻¹ titrated to effect. A heating mat is used with a non-adhesive belt deployed to maintain positioning.

Hair on the dorsal surface will be removed and skin sterilised using an iodine solution. Under aseptic conditions a 20 mm incision is made over the thoracic region of the spine and minimal subcutaneous dissection to the panniculus carnosus performed to create a space for the implant. An implant is then introduced into either side of the thorax as per the implantation schedule (Table 27) taking care to avoid excessive soft tissue tension. The skin is then opposed and sutured using interrupter 4-0 vicryl and mouse transferred to a warm recovery tank.

6.4.2.8 Post-operative procedure

Post operatively mice are transferred to a recovery cage with warm fresh bedding and soft diet. Daily weights were and observations are recorded for the following 7 days including activity levels, food and water consumption, breathing pattern, aggressiveness or fur ruffling. Food should be made available on a daily basis and bedding changed weekly as part of routine care in the animal facility and observation for development of adverse events and infection undertaken.

12 weeks following surgery the mice are to be euthanised using high dose phenobarbital intraperitoneal injection, scaffolds dissected out *en-bloc* and immersed in formalin for 48 hours before a triple wash with PBS—and stored in 70% alcohol. X-Ray Computer Tomography (CT) scans would then be performed using the Bruker Skyscan 1172, using an SHT 11 Megapixel camera and a Hamamatsu 80kV (100 μ A) source. The samples are mounted vertically on a portion of dental wax and positioned 71.24mm from the source. No filter was applied to the X-Ray source and a voltage of 50kV applied for an exposure time of 380 ms. The images generated are 2664 x 4000 pixels with a resolution of 2.97 μ m per pixel. Images are taken in 0.2° steps around one full 360° rotation of the sample with the average of 2 frames taken at each rotation step.

6.4.2.9 Quantification of mineralisation

Prior to implantation, the baseline level of mineral present within the scaffolds should be evaluated and then after explantation. CT data could be visualised using CTan (version 1.12 for windows, SkyScan, Bruker) with the bone formation measured by creating a 'volume of interest' and opened using CTvol (version 2.2 for windows, Skyscan, Bruker). A threshold is required to define areas of density consistent with bone mineralisation and applied to all samples. CTvol is used to calculate volume of mineralised bone using a threshold

attenuation range set to approximately 70-255 for all images. A despeckling process can be applied for black and white to remove noise from the images. BatchManager was then used to measure the volume of radio dense material within the field giving a measured value for mineralised material sample.

Visual 3D reconstructions should be then developed using CTvox (version 3.3 for windows, SkyScan, Bruker). The images produced by the μ CT are based on the level of attenuation through the sample, which is dependent on the thickness of the material and its absorption coefficient.

6.4.2.10 Histological evaluation

Following μ CT the scaffolds could be decalcified in Krajian's Solution (sodium citrate dihydrate, formic acid and deionised water) for 72 hours with change of solution every 24 hours then mounted in paraffin.

Samples are then mounted in paraffin blocks, osteotomed into 5 μ m slices and mounted on microscopy slides. Slides can be deparaffinised and rehydrated in histo-clear and reducing concentrations of ethanol applied. Digital microscopy images would be captured using an EVOS FL Auto (Life Technologies) and Evos FL (Thermofisher v 1.4 for Windows). Images are generally captured at x20 magnification and stitched using the Stitch Image Grid plugin for image J(187)

6.4.2.11 Statistical Analysis

Data will be analysed using Graphpad Prism (version 6 for Macintosh, GraphPad Software, La Jolla California USA) with multiple comparisons performed using Kruskal Wallis test for parametric respectively, with application of the Dunn's correction for incidental significance. A p-value of <0.05 should be considered statistically significant.

References

1. Lozano Picazo P, Pérez Garnes M, Martínez Ramos C, Vallés Lluch A, Monleón Pradas M. New Semi-Biodegradable Materials from Semi-Interpenetrated Networks of Poly(ϵ -caprolactone) and Poly(ethyl acrylate). *Macromolecular Bioscience*. 2015 Feb 1;15(2):229–40.
2. polyethylacrylate [Internet]. polymerdatabase.com. [cited 2019 Oct 28]. Available from: <https://polymerdatabase.com/polymers/polyethylacrylate.html>
3. Beamson G, Briggs D. High Resolution XPS of Organic Polymers. Wiley; 1992. 1 p.
4. Rico P, González-García C, Petrie TA, García AJ, Salmerón-Sánchez M. Molecular assembly and biological activity of a recombinant fragment of fibronectin (FNIII7–10) on poly(ethyl acrylate). *Colloids and Surfaces B: Biointerfaces*. 2010 Jul;78(2):310–6.
5. Annie Zhe C, Andrés AP, Nikolaj G, Mathis R, Matthew D, Manuel S-S. Engineering plasma-polymerised surfaces for synergistic integrin/growth factor signalling to promote mesenchymal stem cell adhesion and differentiation. *Frontiers in Bioengineering and Biotechnology*. 2016;4.
6. Cheng ZA, Alba-Perez A, González-García C, Donnelly H, Llopis-Hernandez V, Jayawarna V, et al. Nanoscale Coatings for Ultralow Dose BMP-2-Driven Regeneration of Critical-Sized Bone Defects. *Adv Sci*. John Wiley & Sons, Ltd; 2018 Nov 19;6(2):1800361–13.
7. Ciullo PA. *Industrial Minerals and Their Uses*. 1996;:115.
8. Brydson JA. *Plastics materials*. 1999. 1 p.
9. Labet M, Thielemans W. Synthesis of polycaprolactone: a review. *Chemical Society Reviews*. Royal Society of Chemistry; 2009;38(12):3484–504.
10. Sinha VR, Bansal K, Kaushik R, Kumria R, Trehan A. Poly- ϵ -caprolactone microspheres and nanospheres: an overview. *International Journal of Pharmaceutics*. 2004 Jun;278(1):1–23.
11. polycaprolactone [Internet]. polymerdatabase.com. [cited 2019 Oct 28]. Available from: <https://polymerdatabase.com/polymers/polycaprolactone.html>

12. Gross RA, Kalra B. Biodegradable Polymers for the Environment. Science. American Association for the Advancement of Science; 2002 Aug 2;297(5582):803–7.
13. Woodruff MA, Hutmacher DW. The return of a forgotten polymer—Polycaprolactone in the 21st century. Progress in Polymer Science. 2010 Oct;35(10):1217–56.
14. Vert M, Li SM, Spenlehauer G, Guérin P. Bioresorbability and biocompatibility of aliphatic polyesters. J Mater Sci: Mater Med. Kluwer Academic Publishers; 1992;3(6):432–46.
15. Tokiwa Y, Calabia B, Ugwu C, Aiba S. Biodegradability of Plastics. International Journal of Molecular Sciences 2009, Vol 10, Pages 3722-3742. Molecular Diversity Preservation International; 2009 Aug 26;10(9):3722–42.
16. Elzein T, Awada H, Nasser-Eddine M, Delaite C, Brogly M. A model of chain folding in Polycaprolactone-b-Polymethyl Methacrylate diblock copolymers. Thin Solid Films. 2005 Jul;483(1-2):388–95.
17. Motala Timol S, Bhaw Luximon A, Jhurry D. Kinetic Study of the Al-Schiff's Base Initiated Polymerization of ϵ -caprolactone and Synthesis of Graft Poly(methylmethacrylate-g-caprolactone). Macromolecular Symposia. WILEY-VCH Verlag; 2005 Dec 1;231(1):69–80.
18. Mosher DF. Fibronectin. New York. 1989.
19. Carsons SE. Fibronectin in health and disease. 1989.
20. Pankov R, Yamada KM. Fibronectin at a glance. Journal of Cell Science. The Company of Biologists Ltd; 2002 Oct 15;115(20):3861–3.
21. Yamada KM. Provisional Matrix In The Molecular and Cellular Biology of Wound Repair.(ed. Clark, R.) pp. 5 1-82. 1996.
22. George EL, Georges-Labouesse EN, Patel-King RS, Rayburn H, Hynes RO. Defects in mesoderm, neural tube and vascular development in mouse embryos lacking fibronectin. Development. 1993 Dec;119(4):1079–91.
23. Yamada KM, Olden K. Fibronectins—adhesive glycoproteins of cell surface and blood. Nature 1981 292:5819. 1978.

24. Theocharis AD, Skandalis SS, Gialeli C, Karamanos NK. Extracellular matrix structure. *Adv Drug Deliv Rev. Elsevier B.V.*; 2016 Feb 1;97(C):4–27.
25. Ingham KC, Brew SA, Migliorini MM. Further localization of the gelatin-binding determinants within fibronectin. Active fragments devoid of type II homologous repeat modules. *J Biol Chem.* 1989 Oct 15;264(29):16977–80.
26. Mao Y, Schwarzbauer JE. Fibronectin fibrillogenesis, a cell-mediated matrix assembly process. *Matrix Biology. Elsevier*; 2005 Sep 1;24(6):389–99.
27. Sechler JL, Corbett SA, Schwarzbauer JE. Modulatory roles for integrin activation and the synergy site of fibronectin during matrix assembly. *Mol Biol Cell. American Society for Cell Biology*; 1997 Dec;8(12):2563–73.
28. Mostafavi-Pour Z. Role of Integrins and Proteoglycans in Cell Adhesion to Fibronectin. 2001.
29. Leikina E, Mertts MV, Kuznetsova N, Leikin S. Type I collagen is thermally unstable at body temperature. *PNAS.* 2002 Feb 5;99(3):1314–8.
30. Lemańska-Perek A, Krzyżanowska-Gołąb D, Pupek M, Klimeczek P, Witkiewicz W, Kątnik-Prastowska I. Analysis of Soluble Molecular Fibronectin-Fibrin Complexes and EDA-Fibronectin Concentration in Plasma of Patients with Atherosclerosis. Inflammation. *Springer US*; 2016 Jun;39(3):1059–68.
31. Baron M, Norman D, Willis A, Campbell ID. Structure of the fibronectin type 1 module. *Nature* 1981 292:5819. *Nature Publishing Group*; 1990 Jun 1;345(6276):642–6.
32. Baron M, Norman DG, Campbell ID. Protein modules. *Trends Biochem Sci.* 1991 Jan;16(1):13–7.
33. Lin F, Zhu J, Tonnesen MG, Taira BR, McClain SA, Singer AJ, et al. Fibronectin peptides that bind PDGF-BB enhance survival of cells and tissue under stress. *J Invest Dermatol.* 2014 Apr;134(4):1119–27.
34. Martino MM, Tortelli F, Mochizuki M, Traub S, Ben-David D, Kuhn GA, et al. Engineering the Growth Factor Microenvironment with Fibronectin Domains to Promote Wound and Bone Tissue Healing. *Science Translational Medicine. American Association for the Advancement of Science*; 2011 Sep 13;3(100):100ra89–9.

35. Martino MM, Briquez PS, Ranga A, Lutolf MP, Hubbell JA. Heparin-binding domain of fibrin(ogen) binds growth factors and promotes tissue repair when incorporated within a synthetic matrix. *Proc Natl Acad Sci USA. National Acad Sciences*; 2013 Mar 19;110(12):4563–8.
36. Martino MM, Briquez PS, Güç E, Tortelli F, Kilarski WW, Metzger S, et al. Growth Factors Engineered for Super-Affinity to the Extracellular Matrix Enhance Tissue Healing. *Science. American Association for the Advancement of Science*; 2014 Feb 21;343(6173):885–8.
37. Salmerón-Sánchez M, Rico P, Moratal D, Lee TT, Schwarzbauer JE, García AJ. Role of material-driven fibronectin fibrillogenesis in cell differentiation. *Biomaterials. Elsevier*; 2011 Mar 1;32(8):2099–105.
38. Llopis-Hernandez V, Cantini M, González-García C, Cheng ZA, Yang J, Tsimbouri PM, et al. Material-driven fibronectin assembly for high-efficiency presentation of growth factors. *Science Advances. American Association for the Advancement of Science*; 2016 Aug 5;2(8):e1600188–11.
39. Ahmed EM. Hydrogel: Preparation, characterization, and applications: A review. *Journal of Advanced Research*. 2015 Mar;6(2):105–21.
40. Amaral M, Lopes MA, Silva RF, Santos JD. Densification route and mechanical properties of Si₃N₄–bioglass biocomposites. *Biomaterials. Elsevier*; 2002 Feb 1;23(3):857–62.
41. Weaver JC, Milliron GW, Miserez A, Evans-Lutterodt K, Herrera S, Gallana I, et al. The Stomatopod Dactyl Club: A Formidable Damage-Tolerant Biological Hammer. *Science. American Association for the Advancement of Science*; 2012 Jun 8;336(6086):1275–80.
42. Lin L, Chow KL, Leng Y. Study of hydroxyapatite osteoinductivity with an osteogenic differentiation of mesenchymal stem cells. *J Biomed Mater Res A. John Wiley & Sons, Ltd*; 2009 May 1;89A(2):326–35.
43. Uzman A. Essential cell biology (2nd ed.). *Biochemistry and Molecular Biology Education. John Wiley & Sons, Ltd*; 2004 Jul 1;32(4):286–7.
44. Snm C, Cancedda R. Cartilage and Bone Extracellular Matrix. *CPD. Bentham Science Publishers*; 2009 Apr 1;15(12):1334–48.

45. van der Stok J, Hartholt KA, Schoenmakers DAL, Arts JJC. The available evidence on demineralised bone matrix in trauma and orthopaedic surgery: A systematic review. *Bone Joint Res.* 2017 Jul;6(7):423–32.
46. Evans MJ, Kaufman MH. Establishment in culture of pluripotential cells from mouse embryos. *Nature* 1981 292:5819. Nature Publishing Group; 1981 Jul 1;292(5819):154–6.
47. Martin GR. Isolation of a pluripotent cell line from early mouse embryos cultured in medium conditioned by teratocarcinoma stem cells. *PNAS. National Academy of Sciences*; 1981 Dec 1;78(12):7634–8.
48. Rippon HJ, Bishop AE. Embryonic stem cells. *Cell Proliferation.* John Wiley & Sons, Ltd (10.1111); 2004 Feb 1;37(1):23–34.
49. Weiss ML, Troyer DL. Stem cells in the umbilical cord. *Stem Cell Rev.* Humana Press; 2006 Jun;2(2):155–62.
50. Horwitz EM, Le Blanc K, Dominici M, Mueller I, Slaper-Cortenbach I, Marini FC, et al. Clarification of the nomenclature for MSC: The International Society for Cellular Therapy position statement. *Cytotherapy.* Elsevier; 2005 Jan 1;7(5):393–5.
51. Gearhart J. New Potential for Human Embryonic Stem Cells. *Science. American Association for the Advancement of Science*; 1998 Nov 6;282(5391):1061–2.
52. Goodell MA, Nguyen H, Shroyer N. Somatic stem cell heterogeneity: diversity in the blood, skin and intestinal stem cell compartments. *Nat Rev Mol Cell Biol.* Nature Publishing Group; 2015 May;16(5):299–309.
53. Friedenstein AJ, Chailakhjan RK, Lalykina KS. The development of fibroblast colonies in monolayer cultures of guinea-pig bone marrow and spleen cells. *Cell Tissue Kinet.* 1970 Oct;3(4):393–403.
54. Uccelli A, Moretta L, Pistoia V. Mesenchymal stem cells in health and disease. *Nature Reviews Immunology* 2008 8:9. Nature Publishing Group; 2008 Sep 1;8(9):726–36.
55. Dominici M, Le Blanc K, Mueller I, Slaper-Cortenbach I, Marini F, Krause D, et al. Minimal criteria for defining multipotent mesenchymal stromal cells. The International Society for Cellular Therapy position statement. *Cytotherapy.* 2006;8(4):315–7.

56. Anderson HC. Matrix vesicles and calcification. *Curr Rheumatol Rep. Current Medicine Group*; 2003 May;5(3):222–6.
57. Lucero CMJ, Vega OA, Osorio MM, Tapia JC, Antonelli M, Stein GS, et al. The cancer-related transcription factor Runx2 modulates cell proliferation in human osteosarcoma cell lines. *J Cell Physiol. John Wiley & Sons, Ltd*; 2013 Apr;228(4):714–23.
58. Komori T, Yagi H, Nomura S, Yamaguchi A, Sasaki K, Deguchi K, et al. Targeted disruption of Cbfa1 results in a complete lack of bone formation owing to maturational arrest of osteoblasts. *Cell*. 1997 May 30;89(5):755–64.
59. Tu Q, Valverde P, Li S, Zhang J, Yang P, Chen J. Osterix overexpression in mesenchymal stem cells stimulates healing of critical-sized defects in murine calvarial bone. *Tissue Eng. Mary Ann Liebert, Inc. 140 Huguenot Street, 3rd Floor New Rochelle, NY 10801 USA*; 2007 Oct;13(10):2431–40.
60. Sinha KM, Zhou X. Genetic and molecular control of osterix in skeletal formation. *Journal of Cellular Biochemistry. John Wiley & Sons, Ltd*; 2013 May 1;114(5):975–84.
61. Nakashima K, Zhou X, Kunkel G, Zhang Z, Deng JM, Behringer RR, et al. The novel zinc finger-containing transcription factor osterix is required for osteoblast differentiation and bone formation. *Cell*. 2002 Jan 11;108(1):17–29.
62. Robert Robison KMS. The Possible Significance of Hexosephosphoric Esters in Ossification: Part II. The Phosphoric Esterase of Ossifying Cartilage. *Biochemical Journal. Portland Press Ltd*; 1924;18(3-4):740.
63. Puchacz E, Lian JB, Stein GS, Wozney J, Huebner K, Croce C. Chromosomal localization of the human osteocalcin gene. *Endocrinology*. 1989 May;124(5):2648–50.
64. Wasi S, Otsuka K, Yao KL, Tung PS, Aubin JE, Sodek J, et al. An osteonectinlike protein in porcine periodontal ligament and its synthesis by periodontal ligament fibroblasts. *Can J Biochem Cell Biol*. 1984 Jun;62(6):470–8.
65. GERDIN AK. The Sanger Mouse Genetics Programme: high throughput characterisation of knockout mice. *Acta Ophthalmologica. John Wiley & Sons, Ltd (10.1111)*; 2010 Sep 23;88:0–0.

66. Harburger DS, Calderwood DA. Integrin signalling at a glance. *Journal of Cell Science*. The Company of Biologists Ltd; 2009 Jan 15;122(Pt 2):159–63.
67. Hynes RO. Integrins: bidirectional, allosteric signaling machines. *Cell*. 2002 Sep 20;110(6):673–87.
68. Humphries MJ, Symonds EJH, Mould AP. Mapping functional residues onto integrin crystal structures. *Curr Opin Struct Biol*. 2003 Apr;13(2):236–43.
69. Humphries MJ. Integrin structure. *Biochem Soc Trans*. 2000;28(4):311–39.
70. Kim C, Ye F, Ginsberg MH. Regulation of Integrin Activation. <http://dxdoiorg/101146/annurev-cellbio-100109-104104>. *Annual Reviews*; 2011 Oct 10;27(1):321–45.
71. Abercrombie M, Dunn GA. Adhesions of fibroblasts to substratum during contact inhibition observed by interference reflection microscopy. *Exp Cell Res*. 1975 Apr;92(1):57–62.
72. Lloyd C. Hot foot. *Nature*. 1980 Nov 6;:13–4.
73. Urist MR. Bone: formation by autoinduction. 1965. *Clinical orthopaedics and related research*. 2002. 7 p.
74. Koenig BB, Cook JS, Wolsing DH, Ting J, Tiesman JP, Correa PE, et al. Characterization and cloning of a receptor for BMP-2 and BMP-4 from NIH 3T3 cells. *Molecular and Cellular Biology*. American Society for Microbiology; 1994 Sep 1;14(9):5961–74.
75. Dijke ten P, Yamashita H, Sampath TK, Reddi AH, Estevez M, Riddle DL, et al. Identification of type I receptors for osteogenic protein-1 and bone morphogenetic protein-4. *J Biol Chem*. 1994 Jun 24;269(25):16985–8.
76. Macías-Silva M, Hoodless PA, Tang SJ, Buchwald M, Wrana JL. Specific activation of Smad1 signaling pathways by the BMP7 type I receptor, ALK2. *J Biol Chem*. 1998 Oct 2;273(40):25628–36.
77. Yamashita H, Dijke ten P, Huylebroeck D, Sampath TK, Andries M, Smith JC, et al. Osteogenic protein-1 binds to activin type II receptors and induces certain activin-like effects. *J Cell Biol*. The Rockefeller University Press; 1995 Jul;130(1):217–26.
78. Rosenzweig BL, Imamura T, Okadome T, Cox GN, Yamashita H, Dijke ten P, et al. Cloning and characterization of a human type II

- receptor for bone morphogenetic proteins. PNAS. National Academy of Sciences; 1995 Aug 15;92(17):7632–6.
79. Kawabata M, Chytil A, Moses HL. Cloning of a novel type II serine/threonine kinase receptor through interaction with the type I transforming growth factor-beta receptor. *J Biol Chem.* 1995 Mar 10;270(10):5625–30.
 80. Even J, Eskander M, Kang J. Bone morphogenetic protein in spine surgery: current and future uses. *Journal of the American Academy* 2012.
 81. Nieden zur NI, Kempka G, Rancourt DE, Ahr H-J. Induction of chondro-, osteo- and adipogenesis in embryonic stem cells by bone morphogenetic protein-2: effect of cofactors on differentiating lineages. *BMC Dev Biol. BioMed Central*; 2005 Jan 26;5(1):1–15.
 82. Daluiski A, Engstrand T, Bahamonde ME, Gamer LW, Agius E, Stevenson SL, et al. Bone morphogenetic protein-3 is a negative regulator of bone density. *Nat Genet. Nature Publishing Group*; 2001 Jan;27(1):84–8.
 83. Sampath TK, Maliakal JC, Hauschka PV, Jones WK, Sasak H, Tucker RF, et al. Recombinant human osteogenic protein-1 (hOP-1) induces new bone formation in vivo with a specific activity comparable with natural bovine osteogenic protein and stimulates osteoblast proliferation and differentiation in vitro. *J Biol Chem.* 1992 Oct 5;267(28):20352–62.
 84. Wolfman NM, Hattersley G, Cox K, Celeste AJ, Nelson R, Yamaji N, et al. Ectopic induction of tendon and ligament in rats by growth and differentiation factors 5, 6, and 7, members of the TGF-beta gene family. *J Clin Invest. American Society for Clinical Investigation*; 1997 Jul 15;100(2):321–30.
 85. Termaat MF, Boer Den FC, Bakker FC, Patka P, Haarman HJTM. Bone Morphogenetic Proteins: Development and Clinical Efficacy in the Treatment of Fractures and Bone Defects. *J Bone Joint Surg Am.* 2005 Jun 1;87(6):1367.
 86. Gautschi OP, Frey SP, Zellweger R. BONE MORPHOGENETIC PROTEINS IN CLINICAL APPLICATIONS. *ANZ Journal of Surgery.* John Wiley & Sons, Ltd (10.1111); 2007 Aug 1;77(8):626–31.
 87. Katanec D, Granić M, Majstorović M, Trampus Z, Pandurić DG. Use of recombinant human bone morphogenetic protein (rhBMP2) in bilateral alveolar ridge augmentation: case report. *Coll Antropol.* 2014 Mar;38(1):325–30.

88. Kang Q, Sun MH, Cheng H, Peng Y, Montag AG, Deyrup AT, et al. Characterization of the distinct orthotopic bone-forming activity of 14 BMPs using recombinant adenovirus-mediated gene delivery. *Gene Ther.* Nature Publishing Group; 2004 Sep;11(17):1312–20.
89. Ong KL, Villarraga ML, Lau E, Carreon LY, Kurtz SM, Glassman SD. Off-label use of bone morphogenetic proteins in the United States using administrative data. *Spine.* 2010 Sep 1;35(19):1794–800.
90. FDA. Panel Executive Summary for P050036 Medtronic’s AMPLIFY rhBMP-2 Matrix (FDA, Silver Spring, MD, 2010).
 . 2010.
91. Woo EJ. Adverse Events Reported After the Use of Recombinant Human Bone Morphogenetic Protein 2. *Journal of Oral and Maxillofacial Surgery.* 2012 Apr;70(4):765–7.
92. Woo EJ. Recombinant human bone morphogenetic protein-2: adverse events reported to the Manufacturer and User Facility Device Experience database. *Spine J.* Elsevier; 2012 Oct;12(10):894–9.
93. Garrison KR, Shemilt I, Donell S, Ryder JJ, Mugford M, Harvey I, et al. Bone morphogenetic protein (BMP) for fracture healing in adults. Cochrane Bone, Joint and Muscle Trauma Group, editor. *Cochrane Database Syst Rev.* John Wiley & Sons, Ltd; 2010 Jun 16;109(6):CD006950.
94. Dai J, Li L, Jiang C, Wang C, Chen H, Chai Y. Bone Morphogenetic Protein for the Healing of Tibial Fracture: A Meta-Analysis of Randomized Controlled Trials. *PLoS ONE.* Public Library of Science; 2015 Oct 28;10(10):e0141670.
95. Friedlaender GE, Perry CR, Cole JD, Cook SD, Cierny G, Muschler GF, et al. Osteogenic protein-1 (bone morphogenetic protein-7) in the treatment of tibial nonunions. *J Bone Joint Surg Am.* NIH Public Access; 2001;83-A Suppl 1(Pt 2):S151–8.
96. Jones AL, Bucholz RW, Bosse MJ, Mirza SK, Lyon TR, Webb LX, et al. Recombinant human BMP-2 and allograft compared with autogenous bone graft for reconstruction of diaphyseal tibial fractures with cortical defects. A randomized, controlled trial. *J Bone Joint Surg Am.* 2006 Jul;88(7):1431–41.
97. Zhang X, Guo J, Zhou Y, Wu G. The roles of bone morphogenetic proteins and their signaling in the osteogenesis of adipose-

- derived stem cells. *Tissue Eng Part B Rev.* Mary Ann Liebert, Inc. 140 Huguenot Street, 3rd Floor New Rochelle, NY 10801 USA; 2014 Feb;20(1):84–92.
98. Myllylä RM, Haapasaari K-M, Lehenkari P, Tuukkanen J. Bone morphogenetic proteins 4 and 2/7 induce osteogenic differentiation of mouse skin derived fibroblast and dermal papilla cells. *Cell Tissue Res.* Springer Berlin Heidelberg; 2014 Feb;355(2):463–70.
99. Granjeiro JM, Oliveira RC, Bustos-Valenzuela JC, Sogayar MC, Taga R. Bone morphogenetic proteins: from structure to clinical use. *Brazilian Journal of Medical and Biological Research.* Brazilian Journal of Medical and Biological Research; 2005 Oct;38(10):1463–73.
100. Groeneveld EH, Burger EH. Bone morphogenetic proteins in human bone regeneration. *European Journal of Endocrinology.* European Society of Endocrinology; 2000 Jan 1;142(1):9–21.
101. Sheikh Z, Javaid MA, Hamdan N, Hashmi R. Bone Regeneration Using Bone Morphogenetic Proteins and Various Biomaterial Carriers. *Materials.* Multidisciplinary Digital Publishing Institute; 2015 Apr 1;8(4):1778–816.
102. Noshi T, Yoshikawa T, Dohi Y, Ikeuchi M, Horiuchi K, Ichijima K, et al. Recombinant human bone morphogenetic protein-2 potentiates the in vivo osteogenic ability of marrow/hydroxyapatite composites. *Artif Organs.* John Wiley & Sons, Ltd (10.1111); 2001 Mar;25(3):201–8.
103. Zambuzzi WF, Fernandes GVO, Iano FG, Fernandes MDS, Granjeiro JM, Oliveira RC. Exploring anorganic bovine bone granules as osteoblast carriers for bone bioengineering: a study in rat critical-size calvarial defects. *Braz Dent J. Fundação Odontológica de Ribeirão Preto*; 2012;23(4):315–21.
104. Lomelino R de O, Castro-Silva II, Linhares ABR, Alves GG, Santos SR de A, Gameiro VS, et al. The association of human primary bone cells with biphasic calcium phosphate (β TCP/HA 70:30) granules increases bone repair. *J Mater Sci: Mater Med.* 2012 Mar;23(3):781–8.
105. Edwards RB, Seeherman HJ, Bogdanske JJ, Devitt J, Vanderby R, Markel MD. Percutaneous injection of recombinant human bone morphogenetic protein-2 in a calcium phosphate paste accelerates healing of a canine tibial osteotomy. *J Bone Joint Surg Am.* 2004 Jul;86(7):1425–38.

106. Dawson JI, Kanczler JM, Yang XB, Attard GS, Oreffo ROC. Clay Gels For the Delivery of Regenerative Microenvironments. *Adv Mater*. John Wiley & Sons, Ltd; 2011 Aug 2;23(29):3304–8.
107. Gibbs DMR, Black CRM, Hulsart-Billstrom G, Shi P, Scarpa E, Oreffo ROC, et al. Bone induction at physiological doses of BMP through localization by clay nanoparticle gels. *Biomaterials*. Elsevier; 2016 Aug;99:16–23.
108. Saito N, Murakami N, Takahashi J, Horiuchi H, Ota H, Kato H, et al. Synthetic biodegradable polymers as drug delivery systems for bone morphogenetic proteins. *Adv Drug Deliv Rev*. 2005 May 25;57(7):1037–48.
109. Winet H, Hollinger JO. Incorporation of polylactide-polyglycolide in a cortical defect: neoosteogenesis in a bone chamber. *J Biomed Mater Res*. 1993 May;27(5):667–76.
110. Lutolf MP, Weber FE, Schmoekel HG, Schense JC, Kohler T, Müller R, et al. Repair of bone defects using synthetic mimetics of collagenous extracellular matrices. *Nat Biotechnol*. Nature Publishing Group; 2003 May;21(5):513–8.
111. Pratt AB, Weber FE, Schmoekel HG, Müller R, Hubbell JA. Synthetic extracellular matrices for in situ tissue engineering. *Biotechnol Bioeng*. John Wiley & Sons, Ltd; 2004 Apr 5;86(1):27–36.
112. Bessa PC, Casal M, Reis RL. Bone morphogenetic proteins in tissue engineering: the road from the laboratory to the clinic, part I (basic concepts). *Journal of Tissue Engineering and Regenerative Medicine*. John Wiley & Sons, Ltd; 2008 Jan 1;2(1):1–13.
113. Osathanon T, Linnes ML, Rajachar RM, Ratner BD, Somerman MJ, Giachelli CM. Microporous nanofibrous fibrin-based scaffolds for bone tissue engineering. *Biomaterials*. 2008 Oct;29(30):4091–9.
114. Kim C-S, Kim J-I, Kim J, Choi S-H, Chai J-K, Kim C-K, et al. Ectopic bone formation associated with recombinant human bone morphogenetic proteins-2 using absorbable collagen sponge and beta tricalcium phosphate as carriers. *Biomaterials*. 2005 May;26(15):2501–7.
115. Saito A, Suzuki Y, Kitamura M, Ogata S-I, Yoshihara Y, Masuda S, et al. Repair of 20-mm long rabbit radial bone defects using BMP-derived peptide combined with an alpha-tricalcium phosphate scaffold. *J Biomed Mater Res A*. John Wiley & Sons, Ltd; 2006 Jun 15;77(4):700–6.

116. Park DJ, Park D-J, Choi BH, Choi B-H, Zhu SJ, Zhu S-J, et al. Injectable bone using chitosan-alginate gel/mesenchymal stem cells/BMP-2 composites. *Journal of Cranio-Maxillofacial Surgery*. Churchill Livingstone; 2005 Feb 1;33(1):50–4.
117. Ramachandran M. *Basic orthopaedic sciences*. 2018.
118. Ong JL, Cardenas HL, Cavin R, Carnes DL. Osteoblast responses to BMP-2-treated titanium in vitro. *Int J Oral Maxillofac Implants*. 1997 Sep;12(5):649–54.
119. Sachse A, Wagner A, Keller M, Wagner O, Wetzel WD, Layher F, et al. Osteointegration of hydroxyapatite-titanium implants coated with nonglycosylated recombinant human bone morphogenetic protein-2 (BMP-2) in aged sheep. *Bone*. Elsevier; 2005 Nov 1;37(5):699–710.
120. Yang DH, Lee D-W, Kwon Y-D, Kim HJ, Chun HJ, Jang JW, et al. Surface modification of titanium with hydroxyapatite-heparin-BMP-2 enhances the efficacy of bone formation and osseointegration in vitro and in vivo. *Journal of Tissue Engineering and Regenerative Medicine*. John Wiley & Sons, Ltd; 2015 Sep;9(9):1067–77.
121. Horasawa N, Yamashita T, Uehara S, Udagawa N. High-performance scaffolds on titanium surfaces: osteoblast differentiation and mineralization promoted by a globular fibrinogen layer through cell-autonomous BMP signaling. *Mater Sci Eng C Mater Biol Appl*. 2015 Jan;46:86–96.
122. Senger DR, Galli SJ, Dvorak AM, Perruzzi CA, Harvey VS, Dvorak HF. Tumor cells secrete a vascular permeability factor that promotes accumulation of ascites fluid. *Science*. 1983 Feb 25;219(4587):983–5.
123. Keramaris NC, Calori GM, Nikolaou VS, Schemitsch EH, Giannoudis PV. Fracture vascularity and bone healing: A systematic review of the role of VEGF. *Injury*. 2008 Sep;39:S45–S57.
124. Figueiredo M, Henriques J, Martins G, Guerra F, Judas F, Figueiredo H. Physicochemical characterization of biomaterials commonly used in dentistry as bone substitutes—Comparison with human bone. *Journal of Biomedical Materials Research Part B: Applied Biomaterials*. John Wiley & Sons, Ltd; 2010 Feb 1;92B(2):409–19.
125. Wong JY, Leach JB, Brown XQ. Balance of chemistry, topography, and mechanics at the cell–biomaterial interface: Issues and

- challenges for assessing the role of substrate mechanics on cell response. *Surface Science*. North-Holland; 2004 Oct 10;570(1-2):119–33.
126. Mourdikoudis S, Pallares RM, Thanh NTK. Characterization techniques for nanoparticles: comparison and complementarity upon studying nanoparticle properties. *Nanoscale*. Royal Society of Chemistry; 2018;10(27):12871–934.
 127. Perren SM, Rahn BA. Biomechanics of fracture healing. *Can J Surg*. 1980 May;23(3):228–32.
 128. Directive C. EU Directive Active Implantable Devices. *Official Journal of the European Communities*. 1990 Jun 20;:1–20.
 129. Directive C. EU Directive Implantable Medical Devices. *Official Journal of the European Communities*. 1993 Jun 14;:1–43.
 130. Andrew JG, Andrew SM, Freemont AJ, Marsh DR. Inflammatory cells in normal human fracture healing. *Acta Orthopaedica Scandinavica*. Taylor & Francis; 2009 Jul 8;65(4):462–6.
 131. Claes L, Recknagel S, Ignatius A. Fracture healing under healthy and inflammatory conditions. *Nat Rev Rheumatol*. Nature Publishing Group; 2012 Mar 1;8(3):133–43.
 132. Robinson CM, Howes J, Murdoch H, Will E, Graham C. Functional outcome and risk of recurrent instability after primary traumatic anterior shoulder dislocation in young patients. *J Bone Joint Surg Am*. The Journal of Bone and Joint Surgery, Inc; 2006 Nov;88(11):2326–36.
 133. Mills LA, Simpson AHRW. The relative incidence of fracture non-union in the Scottish population (5.17 million): a 5-year epidemiological study. *BMJ Open*. British Medical Journal Publishing Group; 2013;3(2):e002276–6.
 134. Mills L, Tsang J, joint GHB, 2016. The multifactorial aetiology of fracture nonunion and the importance of searching for latent infection. onlineboneandjoint.org.uk
 135. Clement ND, Goudie EB, Brooksbank AJ. Smoking status and the Disabilities of the Arm Shoulder and Hand score are early predictors of symptomatic nonunion of displaced midshaft fractures of the clavicle. *Bone Joint* 2016.

136. Elliott DS, Newman K, FORWARD DP. A unified theory of bone healing and nonunion. *Bone Joint* 2016.
137. Moghaddam A, Zimmermann G, Hammer K, Bruckner T, Grützner PA, Recum von J. Cigarette smoking influences the clinical and occupational outcome of patients with tibial shaft fractures. *Injury. Elsevier*; 2011 Dec 1;42(12):1435–42.
138. Zura R, Xiong Z, Einhorn T, Watson JT, Ostrum RF, Prayson MJ, et al. Epidemiology of Fracture Nonunion in 18 Human Bones. *JAMA Surg.* 2016 Nov 1;151(11):e162775–12.
139. Ruedi T, Buckley R. *AO Principles of Fracture Management, Books and DVD.* Thieme; 2007. 1 p.
140. Atalar AC, Kocaoglu M, Demirhan M, Bilsel K, Eralp L. Comparison of three different treatment modalities in the management of humeral shaft nonunions (plates, unilateral, and circular external fixators). *Journal of Orthopaedic Trauma.* 2008 Apr;22(4):248–57.
141. Mills LA, Simpson AHRW. The relative incidence of fracture nonunion in the Scottish population (5.17 million): a 5-year epidemiological study. *BMJ Open.* 2013;3(2).
142. Tsang S, Mills LA, Frantziadis J, Baren JP. Exchange nailing for nonunion of diaphyseal fractures of the tibia. *Bone Joint* 2016.
143. Dahabreh Z, Dimitriou R, Giannoudis PV. Health economics: A cost analysis of treatment of persistent fracture non-unions using bone morphogenetic protein-7. *Injury. Elsevier*; 2007 Mar;38(3):371–7.
144. Kanakaris NK, Giannoudis PV. The health economics of the treatment of long-bone non-unions. *Injury.* 2007 May;38 Suppl 2:S77–84.
145. Patil S, Montgomery R. Management of complex tibial and femoral nonunion using the Ilizarov technique, and its cost implications. *Journal of Bone & Joint Surgery, British Volume. Bone and Joint Journal*; 2006 Jul;88(7):928–32.
146. Perumal V, Roberts CS. (ii) Factors contributing to non-union of fractures. *Current Orthopaedics. Elsevier*; 2007 Aug;21(4):258–61.
147. Perlman MH, Thordarson DB. Ankle Fusion in a High Risk Population: An Assessment of Nonunion Risk Factors. *Foot & Ankle International. SAGE PublicationsSage CA: Los Angeles, CA*; 1999 Aug 1;20(8):491–6.

148. Meidinger G, Imhoff AB, Paul J, Kirchhoff C, Sauerschnig M, Hinterwimmer S. May smokers and overweight patients be treated with a medial open-wedge HTO? Risk factors for non-union. *Knee Surg Sports Traumatol Arthrosc.* Springer-Verlag; 2011;19(3):333–9.
149. Giannoudis PV, Einhorn TA, Marsh D. Fracture healing: the diamond concept. *Injury.* 2007 Sep;38 Suppl 4:S3–6.
150. Dahabreh Z, Calori GM, Kanakaris NK, Nikolaou VS, Giannoudis PV. A cost analysis of treatment of tibial fracture nonunion by bone grafting or bone morphogenetic protein-7. *International Orthopaedics (SICOT).* Springer-Verlag; 2009 Oct;33(5):1407–14.
151. Dimitriou R, Carr IM, West RM, Markham AF, Giannoudis PV. Genetic predisposition to fracture non-union: a case control study of a preliminary single nucleotide polymorphisms analysis of the BMP pathway. *BMC Musculoskelet Disord.* 3rd ed. BioMed Central; 2011 Feb 10;12(1):44.
152. Sulzbacher I. Arthrose – Histologie und pathogenetische Ansätze. *Radiologe.* Springer-Verlag; 2000 Dec 15;40(12):1126–33.
153. DeHeer PA, Catoire SM, Taulman J, Borer B. Ankle Arthrodesis. *Clinics in Podiatric Medicine and Surgery.* 2012 Oct;29(4):509–27.
154. Porter M, Armstrong R, Howard P, Porteous M, Wilkinson JM. Orthopaedic registries - the UK view (National Joint Registry): impact on practice. *EFORT Open Rev.* 2019 Jun;4(6):377–90.
155. Daigle ME, Weinstein AM, Katz JN, Losina E. The cost-effectiveness of total joint arthroplasty: a systematic review of published literature. *Best Pract Res Clin Rheumatol.* 2012 Oct;26(5):649–58.
156. Ellington JK, Gupta S, Myerson MS. Management of failures of total ankle replacement with the agility total ankle arthroplasty. *The Journal of Bone & Joint Surgery.* 2013 Dec 4;95(23):2112–8.
157. Salem KH, Kinzl L, Schmelz A. Ankle Arthrodesis Using Ilizarov Ring Fixators: A Review of 22 Cases. *Foot & Ankle International.* 9 ed. SAGE PublicationsSage CA: Los Angeles, CA; 2016 Jun 27;27(10):764–70.
158. Chen Y, Wang X, Lu X, Yang L, Yang H, Yuan W, et al. Comparison of titanium and polyetheretherketone (PEEK) cages in the surgical treatment of multilevel cervical spondylotic myelopathy: a prospective, randomized, control study with over 7-year follow-

- up. *Eur Spine J*. Springer Berlin Heidelberg; 2013 Apr 9;22(7):1539–46.
159. Shekaran A, García JR, Clark AY, Kavanaugh TE, Lin AS, Guldberg RE, et al. Bone regeneration using an alpha 2 beta 1 integrin-specific hydrogel as a BMP-2 delivery vehicle. *Biomaterials*. 2014 Jul;35(21):5453–61.
 160. Sanders DW, Bhandari M, Guyatt G, Heels-Ansdell D, Schemitsch EH, Swiontkowski M, et al. Critical-sized defect in the tibia: is it critical? Results from the SPRINT trial. *Journal of Orthopaedic Trauma*. 2014 Nov;28(11):632–5.
 161. Schemitsch EH. Size Matters: defining Critical Bone Defect Size. *Journal of Orthopaedic Trauma*. 2017 Oct;31:S20–2.
 162. Rozbruch SR, Pugsley JS, Fragomen AT, Ilizarov S. Repair of tibial nonunions and bone defects with the Taylor Spatial Frame. *Journal of Orthopaedic Trauma*. 2008 Feb;22(2):88–95.
 163. Lenz M, Gueorguiev B, Richards RG, Mückley T, Hofmann GO, Höntzsch D, et al. Fatigue performance of angle-stable tibial nail interlocking screws. *International Orthopaedics (SICOT)*. 2012 Aug 9;37(1):113–8.
 164. Karl M, Kelly JR. Influence of loading frequency on implant failure under cyclic fatigue conditions. *Dental Materials*. 2009 Nov;25(11):1426–32.
 165. Biz C, Iacobellis C. Nailing treatment in bone transport complications. *Strat Traum Limb Recon*. 2014 Jul 24;9(2):89–96.
 166. Zhang Z, Swanson WB, Wang Y-H, Lin W, Wang G. Infection-free rates and Sequelae predict factors in bone transportation for infected tibia: a systematic review and meta-analysis. *BMC Musculoskeletal Disorders*; 2018 Dec 11;:1–9.
 167. K SI, J F, G G, D S, M M. COMPARISON OF ILIZAROV ACUTE SHORTENING AND RELENGTHENING WITH BONE TRANSPORT FOR TREATING INFECTED SEGMENTAL TIBIAL BONE DEFECTS. *Orthopaedic Proceedings. The British Editorial Society of Bone & Joint Surgery*; 2018 Dec 10.
 168. Shekaran A, García JR, Clark AY, Kavanaugh TE, Lin AS, Guldberg RE, et al. Bone regeneration using an alpha 2 beta 1 integrin-specific hydrogel as a BMP-2 delivery vehicle. *Biomaterials*. Elsevier; 2014 Jul 1;35(21):5453–61.

169. Llopis-Hernandez V, Cantini M, Gonzalez-Garcia C, Cheng ZA, Yang J, Tsimbouri PM, et al. Material-driven fibronectin assembly for high-efficiency presentation of growth factors. *Science Advances*. American Association for the Advancement of Science; 2016 Aug 3;2(8):e1600188–8.
170. Holstein JH, Garcia P, Histing T, Kristen A, Scheuer C, Menger MD, et al. Advances in the establishment of defined mouse models for the study of fracture healing and bone regeneration. *Journal of Orthopaedic Trauma*. 2009 May;23(5 Suppl):S31–8.
171. Viateau V, Logeart-Avramoglou D, Guillemin G, Petite H. Animal Models for Bone Tissue Engineering Purposes. In: *Sourcebook of Models for Biomedical Research*. Totowa, NJ: Humana Press; 2008. pp. 725–36.
172. Campbell WC. Interposition of vit allium plates in arthroplasties of the knee: Preliminary report. *The American Journal of Surgery*. Elsevier; 1940 Mar 1;47(3):639–41.
173. Heaton KT, Dorr LD. *The Adult Knee*.
174. Al-Najjim M, Khattak U, Sim J, Chambers I. Differences in subsidence rate between alternative designs of a commonly used uncemented femoral stem. *Journal of Orthopaedics*. 2016 Dec;13(4):322–6.
175. Agarwal R, González-García C, Torstrick B, Guldberg RE, Salmerón-Sánchez M, García AJ. Simple coating with fibronectin fragment enhances stainless steel screw osseointegration in healthy and osteoporotic rats. *Biomaterials*. 2015 Sep;63:137–45.
176. Guerra NB, González-García C, Llopis V, Rodríguez-Hernández JC, Moratal D, Rico P, et al. Subtle variations in polymer chemistry modulate substrate stiffness and fibronectin activity. *Soft Matter*. The Royal Society of Chemistry; 2010 Sep 21;6(19):4748–55.
177. Alba-Perez A. Fibronectin Networks on Plasma Polymerised Poly (ethyl acrylate).
178. Doherty MJ, Mollan RA, Wilson DJ. Effect of ethylene oxide sterilization on human demineralized bone. *Biomaterials*. 1993 Oct;14(13):994–8.
179. Pekkarinen T, Hietalal O, Jämsä T, Jalovaara P. Gamma irradiation and ethylene oxide in the sterilization of native reindeer bone morphogenetic protein extract. *Scand J Surg*. 2005;94(1):67–70.

180. Pekkarinen T, Lindholm TS, Marttinen A, Hietala O, Jalovaara P. Influence of Ethylene Oxide Sterilization on New Bone Formation Induced by Bovine Bone Morphogenetic Protein. *Journal of Musculoskeletal Research*. World Scientific Publishing Company; 2011 Nov 21;04(04):287–95.
181. Lam CX, Teoh SH, Hutmacher DW. Comparison of the degradation of polycaprolactone and polycaprolactone-(β -tricalcium phosphate) scaffolds in alkaline medium. *Polym Int*. 2007;56(6):718–28.
182. Lam CXF, Hutmacher DW, Schantz J-T, Woodruff MA, Teoh SH. Evaluation of polycaprolactone scaffold degradation for 6 months in vitro and in vivo. *J Biomed Mater Res A*. John Wiley & Sons, Ltd; 2009 Sep 1;90(3):906–19.
183. Hollister SJ, Murphy WL. Scaffold Translation: Barriers Between Concept and Clinic. *Tissue Eng Part B Rev*. 2011 Dec;17(6):459–74.
184. Plante I, Stewart MKG, Laird DW. Evaluation of Mammary Gland Development and Function in Mouse Models. *JoVE (Journal of Visualized Experiments)*. 2011 Jul 21;(53):e2828.
185. LeGeros RZ, Lin S, Rohanizadeh R, Mijares D, LeGeros JP. Biphasic calcium phosphate bioceramics: preparation, properties and applications. *J Mater Sci: Mater Med*. 2003 Mar;14(3):201–9.
186. LeGeros RZ. Properties of osteoconductive biomaterials: calcium phosphates. *Clinical Orthopaedics and Related Research*. 2002 Feb;(395):81–98.
187. Preibisch S, Saalfeld S, Tomancak P. Globally optimal stitching of tiled 3D microscopic image acquisitions. *Bioinformatics*. 2009 Jun 1;25(11):1463–5.
188. Bertolai R, Catelani C, Aversa A, Rossi A, Giannini D, Bani D. Bone graft and mesenchymal stem cells: clinical observations and histological analysis. *Clin Cases Miner Bone Metab*. 2015 May;12(2):183–7.
189. Salmerón-Sánchez M, Rico P, Moratal D, Lee TT, Schwarzbauer JE, García AJ. Role of material-driven fibronectin fibrillogenesis in cell differentiation. *Biomaterials*. 2011 Mar;32(8):2099–105.
190. Bateman JP, Safadi FF, Susin C, Wikesjö UME. Exploratory study on the effect of osteoactivin on bone formation in the rat critical-size calvarial defect model. *Journal of Periodontal Research*. John Wiley & Sons, Ltd (10.1111); 2012 Apr 1;47(2):243–7.

191. Kumar S, Ponnazhagan S. Mobilization of bone marrow mesenchymal stem cells in vivo augments bone healing in a mouse model of segmental bone defect. *Bone*. Elsevier; 2012 Apr 1;50(4):1012–8.
192. Skaliczki G, Weszl M, Schandl K, Major T, Kovács M, Skaliczki J, et al. Compromised bone healing following spacer removal in a rat femoral defect model. *Acta Physiologica Hungarica*. Akadémiai Kiadó; 2012 Jul 31;99(2):223–32.
193. Zanchetta P, Lagarde N, Uguen A, Marcorelles P. Mixture of hyaluronic acid, chondroitin 6 sulphate and dermatan sulphate used to completely regenerate bone in rat critical size defect model. *Journal of Cranio-Maxillofacial Surgery*. Churchill Livingstone; 2012 Dec 1;40(8):783–7.
194. Zwingenberger S, Niederlohmann E, Vater C, Rammelt S, Matthys R, Bernhardt R, et al. Establishment of a femoral critical-size bone defect model in immunodeficient mice. *J Surg Res*. 2013 May 1;181(1):e7–e14.
195. Teitelbaum SL. Bone resorption by osteoclasts. *Science*. 2000 Sep 1;289(5484):1504–8.
196. Nauth A, Lane J, Watson JT, Giannoudis P. Bone Graft Substitution and Augmentation. *Journal of Orthopaedic Trauma*. 2015 Dec;29 Suppl 12:S34–8.
197. Ma J, Lin L, Zuo Y, Zou Q, Ren X, Li J, et al. Modification of 3D printed PCL scaffolds by PVAc and HA to enhance cytocompatibility and osteogenesis. *RSC Advances*. Royal Society of Chemistry; 2019;9(10):5338–46.
198. Yang X, Li Y, Liu X, Zhang R, Feng Q. Research Article In Vitro Uptake of Hydroxyapatite Nanoparticles and Their Effect on Osteogenic Differentiation of Human Mesenchymal Stem Cells. *Stem Cells International*. Hindawi; 2018 Jun 19;:1–10.
199. Kim J-W, Shin K-H, Koh Y-H, Hah MJ, Moon J, Kim H-E. Production of Poly(ϵ -Caprolactone)/Hydroxyapatite Composite Scaffolds with a Tailored Macro/Micro-Porous Structure, High Mechanical Properties, and Excellent Bioactivity. *Materials*. Multidisciplinary Digital Publishing Institute; 2017 Oct;10(10):1123–13.
200. Zhang Y, Tanner KE, Gurav N, Di Silvio L. In vitro osteoblastic response to 30 vol% hydroxyapatite-polyethylene composite. *J Biomed Mater Res A*. 2007;81A(2):409–17.

201. Pinto J, Athanassiou A, Fragouli D. Effect of the porous structure of polymer foams on the remediation of oil spills. *J Phys D: Appl Phys*. IOP Publishing; 2016 Apr 13;49(14):145601.
202. Olszta MJ, Cheng X, Jee SS, Kumar R, Kim Y-Y, Kaufman MJ, et al. Bone structure and formation: A new perspective. *Materials Science and Engineering: R: Reports*. Elsevier; 2007 Nov 28;58(3-5):77–116.
203. Malito LG, Arevalo S, Kozak A, Spiegelberg S, Bellare A, Pruitt L. Material properties of ultra-high molecular weight polyethylene_ Comparison of tension, compression, nanomechanics and microstructure across clinical formulations. *Journal of the Mechanical Behavior of Biomedical Materials*. Elsevier Ltd; 2018 Jul 1;83:9–19.
204. Anagnostakos K, Fink B. Antibiotic-loaded cement spacers – lessons learned from the past 20 years. *Expert Review of Medical Devices*. Taylor & Francis; 2018 Feb 14;15(3):231–45.
205. Cimatti B, Engel EE, Nogueira-Barbosa MH, Frighetto PD, Volpon JB. Physical and mechanical characterization of a porous cement for metaphyseal bone repair. *Acta Ortop Bras*. 2015 Jul;23(4):197–201.
206. Zhang W, Gao Y, Yang T, Shen S, Xu L. Supermacroporous scaffolds for three-dimensional culture of tissue cells in disposable bioreactors. *New Biotechnology*. 2016;S(33):S78.
207. Bruyas A, Moeinzadeh S, Kim S, Lowenberg DW, Yang YP. Effect of Electron Beam Sterilization on Three-Dimensional-Printed Polycaprolactone/Beta-Tricalcium Phosphate Scaffolds for Bone Tissue Engineering. *Tissue Engineering Part A*. 2019 Feb;25(3-4):248–56.
208. Bose S, Roy M, Bandyopadhyay A. Recent advances in bone tissue engineering scaffolds. *Trends in Biotechnology*. 2012 Oct;30(10):546–54.
209. Engelberg I, Kohn J. Physico-mechanical properties of degradable polymers used in medical applications: A comparative study. *Biomaterials*. Elsevier; 1991 Apr 1;12(3):292–304.
210. Rouwkema J, Rivron NC, van Blitterswijk CA. Vascularization in tissue engineering. *Trends in Biotechnology*. Elsevier Current Trends; 2008 Aug 1;26(8):434–41.
211. Murphy CM, Haugh MG, O'Brien FJ. The effect of mean pore size on cell attachment, proliferation and migration in collagen–

- glycosaminoglycan scaffolds for bone tissue engineering. *Biomaterials*. Elsevier; 2010 Jan 1;31(3):461–6.
212. Woodard JR, Hilldore AJ, Lan SK, Park CJ, Morgan AW, Eurell JAC, et al. The mechanical properties and osteoconductivity of hydroxyapatite bone scaffolds with multi-scale porosity. *Biomaterials*. Elsevier; 2007 Jan 1;28(1):45–54.
213. Mohanty S, Larsen LB, Trifol J, Szabo P, Burri HVR, Canali C, et al. Fabrication of scalable and structured tissue engineering scaffolds using water dissolvable sacrificial 3D printed moulds. *Mater Sci Eng C Mater Biol Appl*. 2015 Oct;55:569–78.
214. Yousefi A-M, Liu J, Sheppard R, Koo S, Silverstein J, Zhang J, et al. I-Optimal Design of Hierarchical 3D Scaffolds Produced by Combining Additive Manufacturing and Thermally Induced Phase Separation. *ACS Applied Bio Materials*. American Chemical Society; 2018 Dec 31;2(2):685–96.
215. Gloria A, De Santis R, Ambrosio L. Polymer-based composite scaffolds for tissue engineering. *J Appl Biomater Biomech*. 2010 May;8(2):57–67.
216. Rezwani K, Chen QZ, Blaker JJ, Boccaccini AR. Biodegradable and bioactive porous polymer/inorganic composite scaffolds for bone tissue engineering. *Biomaterials*. 2006 Jun;27(18):3413–31.
217. Eshraghi S, Das S. Mechanical and microstructural properties of polycaprolactone scaffolds with one-dimensional, two-dimensional, and three-dimensional orthogonally oriented porous architectures produced by selective laser sintering. *Acta Biomaterialia*. Acta Materialia Inc; 2010 Jul 1;6(7):2467–76.
218. Domingos M, Gloria A, Coelho J, Bartolo P, Ciurana J. Three-dimensional printed bone scaffolds: The role of nano/micro-hydroxyapatite particles on the adhesion and differentiation of human mesenchymal stem cells. *Proc Inst Mech Eng H*. 2017 Jun 22;231(6):555–64.
219. Patrício T, Domingos M, Gloria A, Bartolo P. Characterisation of PCL and PCL/PLA Scaffolds for Tissue Engineering. *Procedia CIRP*. Elsevier; 2013 Jan 1;5:110–4.
220. Huttmacher DW, Schantz T, Zein I, Ng KW, Teoh SH, Tan KC. Mechanical properties and cell cultural response of polycaprolactone scaffolds designed and fabricated via fused deposition modeling. *J Biomed Mater Res*. 2001 May;55(2):203–16.

221. Chuan YL, Hoque ME, Pashby I. Prediction of Patient-Specific Tissue Engineering Scaffolds for Optimal Design. *IJMO*. 2013;:468–70.
222. Zein I, Hutmacher DW, Tan KC, Teoh SH. Fused deposition modeling of novel scaffold architectures for tissue engineering applications. *Biomaterials*. 2002 Feb;23(4):1169–85.
223. Zhou Y, Hutmacher DW, Varawan S-L, Lim TM. In vitro bone engineering based on polycaprolactone and polycaprolactone–tricalcium phosphate composites. *Polym Int*. 2007;56(3):333–42.
224. Barber AH. Mechanical behavior of osteoporotic bone at sub-lamellar length scales. 2015 Feb 9;:1–7.
225. Keaveny TM, Guo XE, Wachtel EF, McMahon TA, Hayes WC. Trabecular bone exhibits fully linear elastic behavior and yields at low strains. *J Biomech*. 1994 Sep;27(9):1127–36.
226. Gebuhr P, Stentzer K, Thomsen F, Levi N. Failure of total hip arthroplasty with Boneloc bone cement. *Acta Orthop Belg*. 2000 Dec;66(5):472–6.
227. Markel DC, Hoard DB, Porretta CA. Cemented total hip arthroplasty with Boneloc bone cement. *J South Orthop Assoc*. 2001;10(4):202–8.
228. Nilsson KG, Dalén T. Inferior performance of Boneloc bone cement in total knee arthroplasty: a prospective randomized study comparing Boneloc with Palacos using radiostereometry (RSA) in 19 patients. *Acta Orthopaedica Scandinavica*. 1998 Oct;69(5):479–83.
229. Deb S, editor. *Orthopaedic Bone Cements*. Woodhead Publishing Limited; 1 p.
230. Nilsen AR, Wiig M. Total hip arthroplasty with Boneloc®: Loosening in 102/157 cases after 0.5–3 years. *Acta Orthopaedica Scandinavica*. Taylor & Francis; 2009 Jul 8;67(1):57–9.
231. MRCS JTE, MSc JPE, MRCS RWW, PhD PAWB, PhD MRW, MSc AS. How long does a hip replacement last? A systematic review and meta-analysis of case series and national registry reports with more than 15 years of follow-up. *The Lancet*. The Author(s). Published by Elsevier Ltd. This is an Open Access article under the CC BY 4.0 license; 2019 Feb 16;393(10172):647–54.

232. Havelin LI, Engesaeter LB, Espehaug B, Furnes O, Lie SA, Vollset SE. The Norwegian Arthroplasty Register: 11 years and 73,000 arthroplasties. *Acta Orthopaedica Scandinavica*. 2009 Jul 8;71(4):337–53.
233. Sabree I, Gough JE, Derby B. Mechanical properties of porous ceramic scaffolds: Influence of internal dimensions. *Ceramics International*. Elsevier; 2015 Aug 1;41(7):8425–32.
234. Maji K, Dasgupta S, Pramanik K, Bissoyi A. Preparation and Evaluation of Gelatin-Chitosan-Nanobioglass 3D Porous Scaffold for Bone Tissue Engineering. *International Journal of Biomaterials*. Hindawi; 2016;2016(4):1–14.
235. Jakus AE, Rutz AL, Jordan SW, Kannan A, Mitchell SM, Yun C, et al. Hyperelastic “bone”: A highly versatile, growth factor-free, osteoregenerative, scalable, and surgically friendly biomaterial. *Science Translational Medicine*. 2016 Sep 28;8(358):358ra127–7.
236. García JR, Clark AY, García AJ. Integrin-specific hydrogels functionalized with VEGF for vascularization and bone regeneration of critical-size bone defects. *J Biomed Mater Res A*. 2016 Apr;104(4):889–900.